EX SITU AND IN SILICO STUDY OF LAYER BUILD-UP AND STRUCTURE FORMATION PHENOMENA DURING CONVECTIVE DRYING OF DEPOSITED DROPLETS

Dissertation zur Erlangung des akademischen Grades

Doktoringenieur
(Dr.-Ing.)

von M.Sc. Manuel Janocha
geb. am 12.08.1991 in Hildesheim
genehmigt durch die Fakultät für Verfahrens- und Systemtechnik
der Otto-von-Guericke Universität Magdeburg

Promotionskommission: Prof. Dr. rer. nat. Julian Thiele (Vorsitz)

Prof. Dr.-Ing. habil. Evangelos Tsotsas (Gutachter)

Prof. Dr.-Ing. Andreas Bück (Gutachter)

Prof. Dr. rer. nat. Franziska Scheffler (Gutachter)

eingereicht am 10.01.2023

Promotionskolloquium am 16.06.2023

Abstract

Drying of solid-laden droplets and associated incremental coating layer formation is an essential sub-process of numerous industrial coating procedures. The quality of the created coating layer and with that the quality of the product is hereby strongly dependent on the layer's properties. Next to layer thickness, this foremost includes layer porosity as well as morphology. In the present dissertation, sessile droplet drying and structure formation under convective conditions are investigated experimentally and simulatively, in order to give further insight into this subject.

The experimental part of this thesis presents an investigation regarding the build-up of small coating layers from deposited droplets dried under forced convection. Herein, the morphological and structural evolution from single droplet residue to multi-deposit coating layer is analyzed, as well as the development of porosity during this incremental layer formation. Three model substances are compared, representing the behavior of spherical nano- and disperse microsuspensions, as well as salt solutions, respectively. The morphologies, porosities and characteristic build-up phenomena of these layers are obtained for every droplet addition. The results of this study on convective drying of sessile droplets and structure formation on a flat, partially wetting substrate are then further set in ratio to layers obtained by fluidized bed coating, in order to relate the phenomena observed for deposited droplets back to a broader field of industrial processes. For this comparison, complementary fluidized bed coating experiments were conducted in a laboratory scale plant and evaluated with regard to layer porosity and morphology. These experiments were carried out under as analogous process conditions as possible, so that the resulting layers can be optimally compared to layers obtained in the course of the experiments featuring deposited droplets and the effects of certain parameters on the coating layers can thus be identified.

In all associated experimental series, focus was laid on the dependency on drying conditions, as well as the development during the consecutive addition of droplets, id est during the incremental build-up. The corresponding characterization of solid residues was performed foremost by white-light interferometry and X-ray micro-computed tomography, with complementary scanning electron microscopy measurements.

In the simulative part of this thesis, a computational fluid dynamics model that incorporates a finite volume approach is presented. It is capable of predicting the influence of gas flow on the evaporation flux profile of sessile droplets during convective drying and is subsequently used to study the impact of convective parameters, droplet properties and setup compositions on the

evaporation, respectively. Evaporation flux distributions originating under a variety of conditions and at various stages in the drying process of water droplets in air are analyzed and quantified. As an extension to already existing models, this numerical simulation takes the advection of vapor in the flow field and the hereby arising shift of the concentration gradient along each droplet's surface into account. This contemplation allows for a representation of not only the overall convective drying process, but particularly the resulting local evaporation under different flow conditions and at different drying stages. Last, the influence of another droplet's presence in the vicinity is analyzed with special regard to surface flux distribution of the droplet pair. Latter, and indices evaluated from it, are seen as indicators for solid transport within the droplets and for deposit formation.

Kurzzusammenfassung

Die Trocknung feststoffhaltiger Tropfen und die damit verbundene inkrementelle Schichtbildung ist ein wesentlicher Teilprozess zahlreicher industrieller Beschichtungsverfahren. Die Qualität der erzeugten Beschichtungen, und damit die Qualität des Produktes, ist hierbei stark von den Eigenschaften der Schicht abhängig. Dazu gehören neben der Schichtdicke vor allem die Schichtporosität und die Morphologie. In der vorliegenden Dissertation wird die Trocknung ruhender Tropfen unter konvektiven Bedingungen und die dazugehörige Strukturbildung experimentell und simulativ untersucht.

Der experimentelle Teil dieser Arbeit stellt eine Untersuchung zum Aufbau kleiner Beschichtungen aus aufgesetzten Tropfen vor, welche unter erzwungener Konvektion getrocknet wurden. Dabei wird die morphologische und strukturelle Entwicklung, sowie die Entwicklung der Porosität während des inkrementellen Schichtaufbaus von einem einzelnen Tropfenrückstand zu einer zusammenhängenden Schicht, bestehend aus mehreren Ablagerungen, analysiert. Es werden drei Modellsubstanzen verglichen, die das Verhalten von sphärischen Nanofluiden, dispersen Mikrosuspensionen und Salzlösungen repräsentieren. Die Morphologien, Porositäten und charakteristischen Phänomene während des Aufbaus dieser Schichten werden bei jeder Addition eines neuen Tropfens ermittelt. Die Ergebnisse dieser Studie zur konvektiven Trocknung ruhender Tropfen und zur Strukturbildung auf einem ebenen Substrat mit partieller Benetzung werden dann weiter ins Verhältnis zu durch Wirbelschichtgranulation erhaltenen Beschichtungen gesetzt, um die beobachteten Phänomene bei aufgesetzten Tropfen auf ein breiteres Anwendungsfeld von industriellen Prozessen zu beziehen. Für diesen Vergleich wurden ergänzende Beschichtungsexperimente in einer Wirbelschichtanlage im Labormaßstab durchgeführt und hinsichtlich Schichtporosität und -morphologie ausgewertet. Diese Versuche wurden unter möglichst analogen Prozessbedingungen durchgeführt, sodass die hieraus resultierenden Schichten bestmöglich mit den im Verlauf der Versuche mit aufgesetzten Tropfen erhaltenen Schichten verglichen werden können und somit der Effekt bestimmter Parameter auf die Beschichtung bestmöglich identifiziert werden kann.

Bei allen zugehörigen Versuchsreihen wurde der Fokus auf die Abhängigkeit von den Trocknungsbedingungen, sowie die Entwicklung während der sukzessiven Tropfenzugabe, also beim inkrementellen Schichtaufbau, gelegt. Die entsprechende Charakterisierung der Feststoffrückstände erfolgte vor allem durch Weißlichtinterferometrie und Röntgen-Mikrotomographie, ergänzt

mit rasterelektronenmikroskopischen Messungen.

Im simulativen Teil dieser Arbeit wird ein strömungsmechanisches Modell nach Finite-Volumen-Methode präsentiert. Dieses Modell ist in der Lage, den Einfluss der erzwungenen Konvektion auf die Trocknungsgeschwindigkeitsverteilung auf der Oberfläche ruhender Tropfen während der Konvektionstrocknung vorherzusagen und wird anschließend verwendet, um den Einfluss von Konvektionsparametern, Tropfenkonstitutionen und Systemkonfigurationen auf die Trocknung zu untersuchen. Trocknungsgeschwindigkeitsverteilungen, welche unter einer Vielzahl von Bedingungen und in verschiedenen Stadien des Trocknungsprozesses von Wassertropfen in Luft entstehen, werden analysiert und quantifiziert. Als Erweiterung zu bereits bestehenden Modellen berücksichtigt die präsentierte numerische Simulation die Advektion des Wasserdampfes im Strömungsfeld und die dadurch entstehende Verschiebung des Konzentrationsgradienten entlang der Tropfenoberfläche. Diese Betrachtung ermöglicht nicht nur eine Darstellung des gesamten konvektiven Trocknungsprozesses, sondern insbesondere der resultierenden lokalen Verdunstung unter verschiedenen Strömungsbedingungen und in verschiedenen Trocknungsstadien. Zuletzt wird der Einfluss der Anwesenheit anderer Tropfen in der Nähe, unter besonderem Fokus auf die Trocknungsgeschwindigkeitsverteilungen auf der Oberfläche von Tropfenpaaren, analysiert. Letztere, und daraus ausgewertete Indizes, werden nachfolgend als Indikatoren für den Feststofftransport innerhalb der Tropfen und für die entsprechende Bildung von Ablagerungsstrukturen genutzt.

Contents

Nomenclature

Latin symbols

A	Area	m^2
a	Viscosity correlation coefficient	–
Bo	Bond number	–
b	Density correlation coefficient	–
C	Capacitance of equiconvex lens	m
Ca	Capillary number	–
c	Concentration	$\mathrm{kg\,m^{-3}}$
D	Diffusivity	$\mathrm{m^2\,s^{-1}}$
d	Diameter	m
f	Drying rate correction factor	–
g	Gravitational constant	$\mathrm{m\,s^{-2}}$
h	Droplet height	m
I	Relative improvement	–
J	Evaporation flux	$\mathrm{kg\,m^{-2}\,s^{-1}}$
k_B	Boltzmann constant	$\mathrm{m^2\,kg\,s^{-2}\,K^{-1}}$
L	Length	m
l	Distance to plate edge	m
M	Mass	kg
$\dot{M}$	Mass flow rate	$\mathrm{kg\,s^{-1}}$
$\tilde{M}$	Molar mass	$\mathrm{kg\,kmol^{-1}}$
m	Mass of one molecule	kg
N	Number	–
Pe	Péclet number	–
p	Pressure	Pa
Q_3	Particle size cumulative distribution	%
q_3	Particle size density distribution	%
R	Contact radius	m
$\tilde{R}$	Universal gas constant	$\mathrm{J\,kmol^{-1}\,K^{-1}}$
Re	Reynolds number	–
r	Radial coordinate	m

S	Surface area	m^2
Sc	Schmidt number	–
Sh	Sherwood number	–
T	Temperature	K
t	Time	s
U	Velocity	$m\,s^{-1}$
V	Volume	m^3
W	Wenzel correction factor	–
X	Lateral coordiante	m
Y	Lateral coordiante	m
Z	Height coordinate	m

Greek symbols

α	Volume fraction	–
β	Mass transfer coefficient	$m\,s^{-1}$
δ	Boundary layer thickness	m
ε	Porosity	–
η	Dynamic viscosity	Pa s
θ	Contact angle	$^\circ$
ϑ	Quarter of mean molecule velocity	$m\,s^{-1}$
$\varkappa$	Vaporization coefficient	–
λ	Deegan correlation factor	–
ν	Kinematic viscosity	$m^2\,s^{-1}$
ρ	Density	$kg\,m^{-3}$
σ	Surface tension	$N\,m^{-1}$
σ_{RSTD}	Relative standard deviation	–
ψ	Evaporative cooling correction factor	–
Ω	Distance between molecule collisions	m
ω	Mass fraction	$kg\,kg^{-1}$

Subscripts

a	Ambient	–
$area$	Area	–
bed	Bed	–
cap	Capillary	–
$channel$	Channel	–
$diff$	Diffusion	–
$drop$	Droplet	–

end	End	–
gas	Gas phase	–
hy	Hydrodynamic	–
hyd	Hydraulic	–
ini	Initial	–
$inlet$	Inlet	–
j	Pixel element identifier	–
$layer$	Layer	–
$liquid$	Liquid phase	–
mar	Marangoni	–
$mean$	Mean value	–
n	Simulation counter	–
net	Net	–
$part$	Particle	–
$plate$	Plate	–
$rough$	Rough	–
sat	Saturated	–
$smooth$	Smooth	–
$sphere$	Spherical	–
$struc$	Structure	–
$surf$	Surface	–
sol	Solution	–
$soli$	Solitary	–
$solid$	Solid phase	–
sus	Suspension	–
$s,theo$	Theoretical solid	–
$s,total$	Enclosed solid	–
tot	Total	–
$vapor$	Vapor phase	–
wb	Wet bulb	–
$Wenzel$	Wenzel	–

Abbreviations

$2-D$	Two-dimensional	–
$3-D$	Three-dimensional	–
B_4C	Boron carbide	–
CB	Cell basis	–
CCA	Constant contact angle	–
CCD	Charged coupled device	–

CCR	Constant contact radius	–
CFD	Computational fluid dynamics	–
DNS	Direct numerical simulation	–
DOS	Domain size	–
DS	Downstream side	–
FBC	Fluidized bed coating	–
FEM	Finite element method	–
FVM	Finite volume method	–
MFC	Mass flow controller	–
Msmt	Measurement	–
NaB	Sodium benzoate	–
PSD	Particle size distribution	–
SDD	Sessile droplet drying	–
SEM	Scanning electron microscopy	–
SiO_2	Silicon dioxide	–
SL	Splitted layers	–
TiO_2	Titanium dioxide	–
US	Upstream side	–
VSI	Vertical scanning interferometry	–
WLI	White-light interferometry	–
μ-CT	X-ray micro-computed tomography	–

Chapter 1

Introduction

Process engineering is the science of transforming raw materials into commercially usable products, through chemical, mechanical or thermal processes (Dal Pont, 2013). Many of these products require some form of protection from interactions with the environment, which ensures that each product's properties are preserved until its usage. Herein, one has two not mutually exclusive options: Packaging and coating. Latter is especially interesting, as its application often is a practical use of process engineering in itself. Moreover, such a coating layer can simultaneously fulfill further purposes, such as improved handling or improved storage properties, or simply addition of another desired property to the final product. This beneficial combination is essential for many products, among others in the food, agricultural and pharmaceutical industry, and, in consequence, controlling the final properties of coating layers through the manufacturing process is a crucial topic in product design and process engineering research.

In nature there are several coating mechanisms that can be observed. Arguably most simple is a reaction of the material's surface with the surrounding medium, as it is the case for example during rust formation on metals. Therein, a new material is formed on the material's surface and therefore blocks further continuation of this interaction. Another mechanism is the purposeful creation of a coating material from the core material. Hereby, the naturally stored substances and energy are used to form a more resistant variation of the core material. Examples for this process are the formation of bark in trees or the formation of skin cells in humans.

However, as per definition these processes involve a reduction of the core materials or a premature partial usage of the ingredients, they are only poorly usable in industry. Furthermore, they limit the possibilities for potential coating materials, as it is always a variation or chemical derivate of the core. Most man-made coating processes therefore get inspiration from another major group of coating mechanisms. Hereby, the coating is created through application of a solid-containing liquid. When this liquid evaporates, the incorporated solids get left behind on the product and therefore cover its surface with a layer. This way, expensive core materials are preserved both during the coating process itself and afterwards. As one can easily deduce from the corresponding

process sequence, the coating layer properties and with this also the properties of the product are hereby dependent on the main stages: Liquid application, drying and structure formation.

The first method of liquid application for coating is to add a sufficient amount of liquid to completely cover the substrate, before the drying process begins to take effect. The liquid application can hereby be carried out using various methods, for example spreading through spin coating or intense spraying. As an alternative to this and in the focus of this dissertation are processes in which solid-containing droplets are steadily applied onto a substrate with a relatively small throughput and at the same time dried. Consequently the three sub-processes of droplet application, droplet drying and structure formation are recurring and overlapping, so that the coating layer is build-up incrementally from dried droplets.

Spray fluidized bed coating is a typical example for such a parallel process. Drops sprayed from a nozzle settle on the surface of fluidized core particles and are subsequently dried. Gradually, this forms a layer whose properties determine the functional properties of the resulting coated particles, exempli gratia solubility or ingredient release behavior. One of its technical applications is the coating of drugs to be taken in the form of pills. Such pills need to release their active ingredients at a specific point in the body, while being protected through all previous steps of the digestion (saliva, stomach acid, et cetera). For this goal to be achieved, the respective coating layer thickness, homogeneity and porosity must be controlled precisely. Similarly to the coating of particles, there are many processes that involve droplet drying and structure formation on flat substrates. Namely, and among others, three-dimensional printing or solar cell anti-refection coating. In its entirety this process is still unexplored. It is therefore of great importance and goal of this dissertation to study and better understand the associated mechanisms and sub-processes as well as their influence on respective coating processes.

In addition to this industrial point of view on the importance of coating layer build-up through solid-laden droplets, the core process of sessile droplet drying and subsequent structure formation can be observed on many occurrences in nature as well. When a colloidal droplet dries on a solid surface, it leaves a ring-like deposit along the perimeter, meaning that the initially dispersed solids get concentrated along the outer rim. These ring patterns often vary in exact morphology, but always feature an increased solid accumulation along the contact line. This phenomenon can be seen in many day-to-day situations. Examples are, among others, residue-rings on washed dishes or laundry, ring-like coffee-stains after spillage or ring-shaped dirt residues on windshields and rooftops of cars. As such a frequently encountered, naturally occurring phenomenon, the formation of these sessile droplet patterns were recognized a long time ago and have been studied ever since.

One particularly expressive example incorporating a naturally occurring ring formation are human tears. Such tears generally show a wide variety of morphologies because their exact composition differs from person to person, but they always feature an increased solid accumulation along the edge. As an enticing introductory example, four different human tears recorded via a light microscope, all featuring ring-pattern formation, are displayed in Figure 1.1.

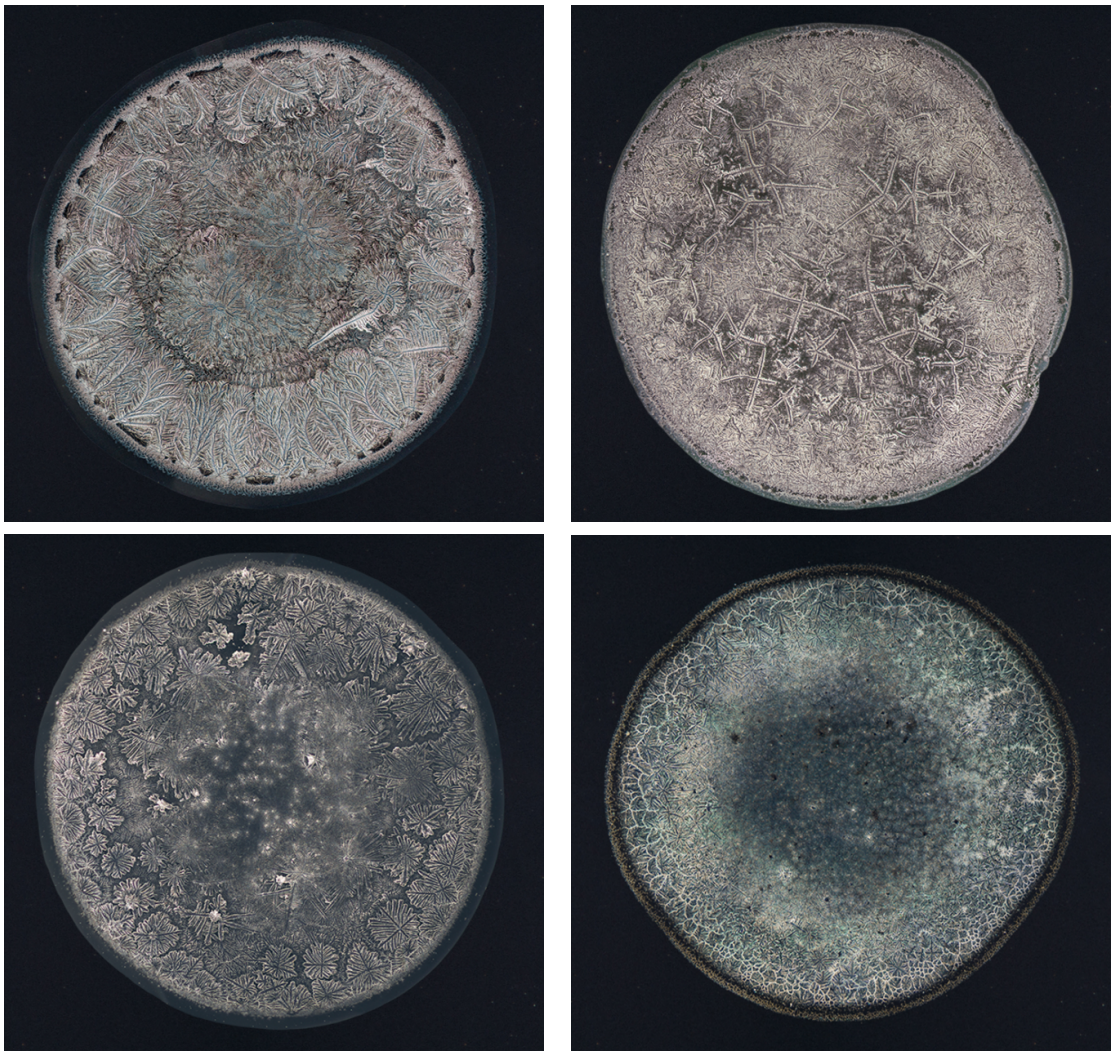

Figure 1.1: Illustrations of human tears recorded via a light microscope. A naturally occurring ring formation, or in other words an increased solid accumulation along the edge, can be seen in all cases. Taken from Imaginarium of Tears (https://imaginariumoftears.com).

1.1 Motivation

The drying of sessile droplets on a substrate is a process that is widespread both in nature and in everyday life. Even if it is not observed directly, one can often inspect the subsequent results, for example in form of annular structures on surfaces formed from solid-containing droplets. In addition to such naturally occurring phenomena, evaporation of nano- and microdroplets is a subprocess of numerous technical applications, from the deposition of thin coating layers on pills through spray-coating, or the spray-on of color droplets during inkjet printing, to the scientific stretching of DNA arrays on biological substrates. However, although sessile droplet drying has been studied for a long time and despite of its apparent simplicity, it is a process that is still not completely explored (Brutin, 2015).

The same statement of unexploredness can be made for the formation of consecutive solid residues

from dried droplets. The included solids hereby form individual residues, driven by each droplet's internal flows (Bhardwaj et al. (2009), Bouchenna et al. (2017)). The arguably most prominent one is the creation of ring deposits, which are resulting from a higher evaporation flux along the pinned contact line of sessile droplets on partially wetting substrates (Kovalchuk et al., 2014) and whose formation was originally described by Deegan et al. (1997). Notwithstanding the widespread basic knowledge on those structures, their exact dependencies on, for example, drying conditions, particle characteristics or droplet properties are still unknown as well. Furthermore, although droplet drying and ring-stain formation are the focus of many scientific investigations, most studies focus on low solid content droplets and purely diffusive drying. Therefore, there is a lack of work involving conditions which are comparable to technical applications, id est high solid content and significant convection.

Moreover, these ring structures are the foundation for any further events in the course of a follow-up coating process (Bhardwaj, 2018), including among others the transition from a solitary deposit to a completed coating layer originating from a multitude of droplets applied one after the other. Although the fabrication of coating layers is a compulsory step in the production of many industrial products - currently significant examples include among others nanoparticle-based silica anti-reflection coatings for photovoltaic applications (Zhang et al., 2017), or salt based anti-fouling layers for foods and cosmetics (Javed and Rahman, 2014) - the specific dependencies of layer porosity or morphology on the drying conditions and used materials are still in question. The reason for this is that a droplet-by-droplet monitoring of the actual layer build-up within technical processes is not feasible. As a result, related studies usually either focus on single droplet structures, or the analysis of finished layers, rather than on the build-up process and the accompanying phenomena themselves. A comparison between single droplets and layers obtained in technical applications, exempli gratia fluidized bed coating, is hereby drawn frequently, but although some comparative studies do exist, the additional mechanisms that take effect during the transition from solitary deposit to multi-deposit layer are always neglected. As of course these mechanisms are significantly influencing layer formation, this neglection is undesirable and further investigation of the matter is necessary. This circumstance was another motivation for the present work.

As described before, the properties of the finally resulting coating layer are an important aspect for the quality of the product that is ultimately sold. In turn, this means that next to the better understanding of natural phenomena, improving the quality of various products is the ultimate motivation behind this dissertation. Naturally, there are numerous examples of day-to-day products that are affected by this, id est were made possible through associated research in the past, or may get improved by future research that builds on the present work. At his point, only one example that is personally important to the author and served as initial motivation for this dissertation and the associated PhD project shall be mentioned. The coating of enteric-coated tablets needs to protect the active substances from destruction through stomach acid on the one hand. On the other hand it needs to enable a controlled release of these ingredients within the subsequent intestines. A contact of the active agent with the stomach's acid is hereby completely ruinous, a release that is too slow greatly degrades the effectiveness of the pill, and a release that is too fast even causes the

opposite of the intended effect on the body. This means that such a coating has to fulfill multiple, complex, partly opposite functions. Consequently, these drugs are completely dependent on their complicated coating, which is why the associated medications have only been on the market for a relatively short time period, although the positive effects of the agents have been known for a long time (Ariyasu et al., 2017). By nature, such a complex coating and the corresponding coating process can always be improved, and this improvement could benefit the daily life of many people, including the author, in turn.

Last, the aspect of natural science shall be mentioned at this point as well. The pattern formation from dried sessile droplets is an important and complex process, that beyond this, is frequently recurring in nature. It is therefore a phenomenon always worth further investigation.

1.2 Scope and outline

The present dissertation consists of five main chapters covering two experimental investigations on drying and structure formation from sessile droplets as well as one experimental study within a fluidized bed setup. These experimental parts are complemented by a simulative investigation on convective sessile droplet drying. In addition to these primary parts of this thesis, first of all, a detailed literature survey on the necessary fundamentals is given. Two more chapters following this survey cover the experimental, material and methodical details of the main analyses.

Chapter 2 deals with the state of the art of droplet drying and structure formation and the theory necessary to understand the corresponding processes discussed in the present thesis. First, the fundamentals of sessile droplets and respective convective drying are presented. Next, the basics of structure formation from such droplets are discussed. Then, the principles of fluidized bed coating processes are explained. Last, the overall goals of this dissertation are composed, based on the state of the art of current research.

Chapters 3, 4 and 5 cover the experimental arrangements, the used materials as well as the experimental methods, respectively. These chapters therefore lay the foundation for understanding and evaluating the results of the subsequent investigations.

Although there have been several experimental studies on sessile droplet drying and solitary deposit formation, involving varying materials, there still is a lack of studies that directly compare structural formation as well as incremental layer build-up for different substances. The aim of Chapter 6 is to characterize this principal behavior and to highlight similarities and differences between the materials. Both, single deposit formation from a dried sessile droplet as well as layer build-up from multiple droplets are investigated herein, exemplarily for a nanofluid, a microfluid and a solution. Special regard hereby is set on morphology, development during the layer build-up (transition from solitary to multi deposit layer) and corresponding development of porosity. In order to study these parameters for each substance, droplet-by-droplet layer build-up processes involving dried deposited microliter droplets during coating are mimicked on a laboratory scale. The principal differences as well as similarities that occur during this replicated layer formation are contrasted

for the three major classes of coating materials. The presented results of these comparisons may contribute to the knowledge on and capability of handling interrelated processes involving such substances. In addition to this, Chapter 6 may provide useful insight on the influence of drying conditions on deposit morphology, the layer formation process and subsequently resulting porosities. Thus, it may contribute to a better understanding and controlling of coating layer fabrication through solid containing droplets, in this regard, too.

The incremental transition from solitary deposit of one sessile droplet to multi-deposit layer is investigated more closely in Chapter 7 for sodium benzoate. Throughout this study, more attention is paid to small details of the droplet-by-droplet layer build-up, including interior structure and surface properties. Same as within the preceding, broader study, three layers of deposits are consecutively applied on a glass substrate and successively dried in a laboratory-scale drying chamber, in order to mimic and closely monitor the build-up process. Furthermore, the influence of droplet characteristics such as volume or solid content is added to the topics of the investigation, and complementary X-ray micro-computed tomography measurements of the deposits are carried out to monitor inner structure development. Through these methods, recurring steps and phenomena throughout the experimental build-up process are identified and characterized. Moreover, these phenomena are linked to specific combinations of droplet positioning and drying conditions.

In Chapter 8, a comparative study on fluidized bed coating is presented. Together with the results of the investigations on sessile droplets in Chapters 6 and 7, this study shall bring insight into the transition from laboratory experiment under controlled conditions to the exemplary process of coating within a fluidized bed, which is closer to processes common in industry, but less suitable for effect isolation. In other words, the complementary study presented in this chapter features an experimental series that varies droplet and convective conditions and an analysis that is focused on layer morphology and porosity. The hereby obtained results for sprayed-on droplets are then compared to the conducted layer build-up with deposited droplets.

Chapter 9 presents a simulative study on droplet drying. A diffusion-limited, quasi-steady-state evaporation of a sessile droplet in laminar airflow is considered and a finite volume method is used to depict the vapor concentration distribution within the droplet's surroundings. This approach allows for an analysis of the flux profile that can also account for the influence of an underlying forced convection around the droplet, further distorting the flux beyond the known non-uniformity. This newly implemented feature is subsequently used to study the distribution of the flux for different ambient flow conditions, setups and at different times or, more specifically, contact angles of the droplet. The simultaneous drying of several droplets under forced convection is also examined. Focusing on convective microdroplet drying, or, more specifically, on the influence of forced convection on the evaporation flux distribution, this chapter is especially fundamental for the understanding of a great number of drying related subprocesses, encountered within technical and scientific applications, respectively. Furthermore, it may contribute to the overall knowledge concerning the drying of sessile droplets.

The results of this dissertation, id est the results of the four main investigations together with the

corresponding conclusions are summarized in Chapter 10 along with an outlook on potentially useful and interesting future research.

Chapter 2

State of the art

The present chapter provides a detailed literature survey of the related scientific subjects and describes the principles of the affiliated phenomena. It therefore establishes a basis for all further deliberations and places the dissertation in the context of scientific research. First, the principles of droplet wetting and drying on planar substrates are discussed. Second, the structure formation phenomena taking place during such processes are explained. Furthermore, the general modeling concepts that were utilized in the respective simulative investigations are covered. Additionally, the underlying mechanisms of the accompanying studies on fluidized bed coating are described.

Finally, based on the presented concepts and considering the available literature, the goals to be achieved by the present dissertation are formulated.

2.1 Drying of sessile droplets on a substrate

2.1.1 Wettability, contact angle and drying behavior

The focus of the present thesis are droplets that are resting on a planar and impermeable surface. When a liquid droplet is applied onto such a substrate in a slow manner, it spreads to equilibrium configuration. Hereby, it forms a specific, macroscopic contact angle θ alongside the three-phase contact line and further attains a specific height h and contact diameter d_{drop}. Figure 2.1 illustrates the spatial dimensions of such a case.

If the droplet is small enough, the corresponding surface tension forces are stronger than the gravitational forces. This in turn means that the droplet is not distorted by gravity, but takes and retains the shape of a perfect spherical cap on the substrate. The ratio of gravitational to surface tension forces is described by the Bond number:

$$Bo = \frac{R_{drop} h \Delta\rho g}{2\sigma_{liquid,vapor}}. \tag{2.1}$$

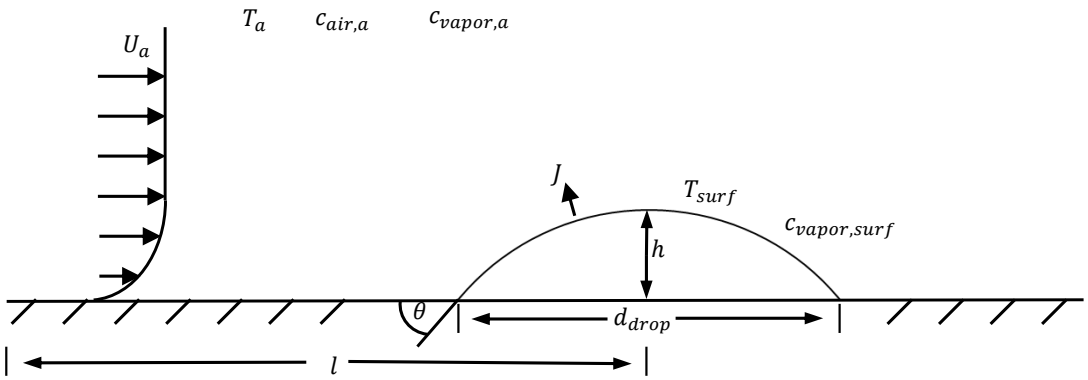

Figure 2.1: Definition sketch of an evaporating droplet on a planar substrate.

Herein, ρ is the density, σ is the surface tension, g is the gravitational acceleration (9.81 m/s^2), h is the droplet's height and R_{drop} the droplet's contact radius ($R_{drop} = d_{drop}/2$). If the Bond number is significantly smaller than unity, the droplet can be assumed to take spherical cap shape (Lubarda and Talke, 2011). Based on Clarke et al. (2002), the initial geometrical dimensions of adhering droplets under spherical cap condition are:

$$\frac{d_{drop}}{2} = \left(\frac{3V_{drop}}{\pi} \frac{\sin^3\theta}{2 - 3\cos\theta + \cos^3\theta} \right)^{1/3}, \tag{2.2}$$

$$h = \frac{d_{drop}}{2} \left(\frac{1 - \cos\theta}{\sin\theta} \right). \tag{2.3}$$

Herein, V_{drop} is the droplet volume. The equilibrium contact angle depends on the surface tensions between the involved components and is specified by Young's equation (Young, 1805):

$$\cos\theta = \frac{\sigma_{solid,vapor} - \sigma_{solid,liquid}}{\sigma_{liquid,vapor}}. \tag{2.4}$$

This means that the tendency of a liquid to spread over a surface depends on both the nature of the surface and the properties of the liquid. Alternatively, from an energetic point of view, it can be said that it depends on the ratio of interaction forces between the liquid and the surface, compared to the cohesive forces that want to bring the droplet into a spherical shape. A contact angle of 0° leads to complete wetting and formation of a monomolecular film (Barthlott et al., 2004). A contact angle of less than 90° is referred to as partial wetting. If a liquid forms a contact angle of more than 90°, this is referred to as non-wetting. Complete non-wetting occurs at a contact angle of 180°.

In an ideal case, the equilibrium contact angle can be determined via Equation 2.4, if the corresponding surface tensions are known. In practice however, any deviations from an ideal surface,

exempli gratia minimal roughness, microporosity or smallest impurities on the surface, quickly lead to deviations from Young's contact angle. Following this realization, Wenzel (1936) investigated the influence of surface roughness on the static contact angle. He found that roughening a hydrophobic surface ($\theta \geq 90°$ for pure water droplets) made that surface behave even more hydrophobic (further increasement of θ). On the other hand, when a hydrophilic surface (water droplet $\theta \leq 90°$) was roughened, it behaved even more hydrophilic (further reduction of θ). He further proposed the incorporation of a roughness factor W_{Wenzel} into Young's equation, representing the ratio of actual surface A_{rough} to apparent surface A_{smooth}, in order to determine a contact angle that is more likely to be formed in practice:

$$\cos\theta_{practice} = W_{Wenzel}\,\frac{\sigma_{solid,vapor} - \sigma_{solid,liquid}}{\sigma_{liquid,vapor}}, \tag{2.5}$$

with

$$W_{Wenzel} = \frac{A_{rough}}{A_{smooth}}. \tag{2.6}$$

As both, the entirety of surface tensions, as well as the roughness factor are rarely known in practice, the Young and Wenzel contact angles are hard to access. Over and above that, these exact contact angles are rarely seen in practice, due to the great number of additional small external influences, which furthermore tend to change from case to case. Instead, it was often observed in the past, that the deviations from an ideal case are leading to a range of possible contact angles that can be attained in equilibrium. This so-called contact angle hysteresis was firstly described by Clayton (1926). The upper bound of this hysteresis is called the advancing contact angle, because it is usually obtained during or directly after the advancing of the contact line. This means, that this angle is the one obtained during liquid addition, in the spreading stage, or, in other words, in case of a droplet deposition onto a surface. Its lower bound counterpart is called the receding contact angle and is formed during the cessation of the contact line. In contrast to the static contact angle described by Thomas Young, which can attain any values between advancing and receding boundary, the advancing and receding contact angle are reproducible and can be seen frequently in nature and practical applications. This also means that these angles can be experimentally determined more easily.

The difference in vapor concentration at the droplet's surface $c_{vapor,surf}$ and the surroundings $c_{vapor,a}$ is the driving force for evaporation J, and, thus, the sessile droplet drying (SDD) process. During this process, the droplet changes its geometrical dimensions, due to the evaporation loss. Picknett and Bexon (1977) presented an experimentally based analysis regarding pendant and sessile droplet evaporation, introducing constant contact angle (CCA) and constant contact radius (CCR) as the two main distinct stages of evaporation. This means, that a droplet counteracts its mass loss either through a reduction in height and contact angle, or through a reduction of contact diameter, while always retaining the spherical cap shape. This is illustrated in Figure 2.2. A

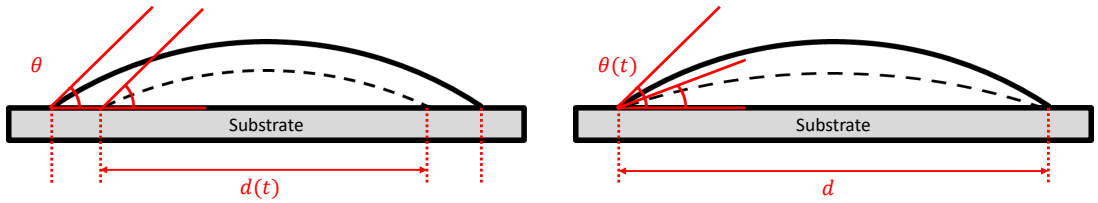

Figure 2.2: Comparison of sessile droplet drying modes: CCA (left), CCR (right).

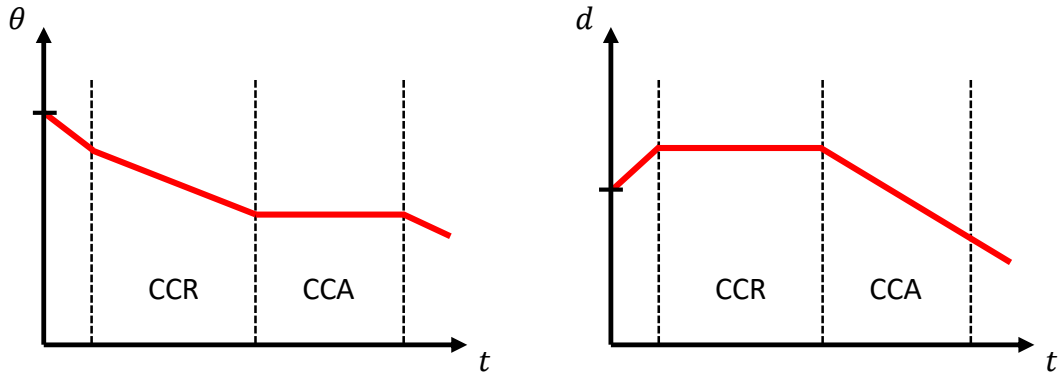

Figure 2.3: Development of contact angle and contact diameter in the course of a drying process on a partially wetting substrate.

combination of these two modes is also possible in rare cases (Sadek et al., 2014).

Further experimental investigations were conducted among others by Birdi et al. (1988), Rowan et al. (1995), as well as Bourges-Monnier and Shanahan (1995), with special regard to the development of contact angle and overall evaporation rate over time. These studies consolidated the distinction between two main drying modes and the representation of a sufficiently small sessile droplet as a perfect spherical cap at all stages of the drying process. They also ascertained that for partially wetting surfaces ($\theta \leq 90°$), the first stage of evaporation always takes place in CCR mode, followed by a receding contact line (CCA mode). At the end of the drying process, an erratic mixture of both modes was observed. The schematic development of contact angle and diameter over the course of the initial spreading and the drying process is shown in Figure 2.3.

The contact angle obtained at the beginning of the CCR mode depends on the properties of the liquid and the substrate and corresponds to the advancing contact angle (Kovalchuk et al., 2014). The point of the drying process at which the droplet undergoes the transition from CCR into CCA mode also depends on these properties. The corresponding θ at this stage conforms to the receding contact angle.

2.1.2 Investigation of the droplet drying process

If a droplet is placed within a surrounding gaseous medium that is not saturated with the droplet's respective vapor, it starts to dry. This means that at the droplet's surface the liquid evaporates and the droplet loses its mass. This evaporation is basically a simultaneous mass and heat transfer process (Shahidzadeh-Bonn et al., 2006). The energy used by the evaporation is transferred as heat through convection and conduction from the surrounding gas and substrate to the droplet. Vapor is transferred into the surrounding gas through diffusion.

Historically, there have been many attempts to mathematically express the mass and heat transfer during droplet drying. Ever since James Maxwell originally described the theoretical evaporation of a perfect sphere within a surrounding medium of infinite volume in 1860, the majority of studies describe the drying of a droplet as a diffusion-controlled process analogous to electrostatic potential fields. Although a number of alternative methods and extensions for the computation of the drying rate have been introduced over the years, namely approaches like characteristic-drying-curve or reaction-engineering (Woo et al., 2008), the classical approach assuming diffusion limitation still remains the most commonly used and effective method for describing the evaporation rate and corresponding heat transfer during sessile droplet drying (Kovalchuk et al., 2014). It shall thus be the focus of the present dissertation, here forth.

The first estimations of the drying rate were done by James Maxwell for large spherical droplets (Maxwell, 1890). He also already postulated that the rate of diffusion and the rate of heat conduction are equivalent, and, thus, can be mathematically expressed through analogous equations. The evaporative mass loss was given as:

$$-\frac{dM_{drop}}{dt} = -4\pi r^2 D \frac{dc}{dr}, \tag{2.7}$$

which can be integrated to

$$-\frac{dM_{drop}}{dt} = 4\pi R_{sphere} D (c_{vapor,surf} - c_{vapor,a}). \tag{2.8}$$

Herein, r is the radial coordinate originating at the droplet center, M_{drop} is the droplet's mass, t is the time, R_{sphere} is the radius of the suspended droplet and D the diffusivity. Later on, Bradley and Fuchs (1959) pointed out that these equations are only valid for droplets whose radius is considerably larger than the mean free path of the vapor molecules. Hence, they proposed a derived, corrective equation for droplets in the micro- and nanoliter range:

$$-\frac{dM_{drop}}{dt} = \frac{4\pi R_{sphere} D (c_{vapor,surf} - c_{vapor,a})}{\frac{D}{R_{sphere}\vartheta\varkappa} + \frac{R_{sphere}}{R_{sphere}+\Omega}}, \tag{2.9}$$

with

$$\vartheta = \sqrt{\frac{k_B T}{2\pi m}}. \tag{2.10}$$

A quarter of the vapor molecule's mean absolute velocity is herein denoted by ϑ. $\varkappa$ is the so-called vaporization coefficient, which means it is equal to the fraction of molecules condensing at equilibrium. Ω is the distance between collisions of molecules, k_B is the Boltzmann constant and m is the mass of one diffusing molecule.

Further simulative investigations regarding drying of spherical droplets were done for example by Huang et al. (2004) and Al-Zaitone et al. (2020). Mezhericher et al. (2010) published a detailed review of the progress of research on droplet drying kinetics.

Corresponding estimations for the drying rate of sessile droplets were established as well. First, Sreznevsky derived Maxwell's equations and showed that the evaporation rate of droplets placed on planar surfaces is approximately proportional to the vapor pressure of the liquid (Erbil, 2012). Further experimental research regarding the drying rate of sessile droplets was conducted by Picknett and Bexon (1977). They discovered that the substrate's presence hinders the evaporation, in comparison to a suspended drop, where no plane is preventing downwards diffusion. They subsequently proposed an equation for the drying rate of sessile droplets that still features a spherical surface expression, but incorporates a correction factor as a function of the contact angle:

$$-\frac{dV_{drop}}{dt} = \frac{4\pi R_{sphere} D}{\rho_{liquid}} (c_{vapor,surf} - c_{vapor,a}) f(\theta), \tag{2.11}$$

with

$$f(\theta) = \frac{1}{2}\frac{C}{R_{sphere}}. \tag{2.12}$$

The capacitance of the equiconvex lens C can hereby be determined via stream functions or polynomial fits incorporating θ. Rowan et al. (1995) later developed a similar correlation, which featured the actual development of the spherical cap surface. In contrast to Picknett and Bexon (1977) however, they neglected the attenuation of the drying rate and assumed the evaporative symmetry of an unsupported droplet:

$$\frac{d\theta}{dt} = -\frac{2\pi D (c_{vapor,a} - c_{vapor,surf}) sin^3(\theta)}{\rho_{liquid} \pi R^2 (1 - cos(\theta))}. \tag{2.13}$$

Next to and derived from these general approaches to the drying rate, there are numerous different approaches to describe the drying kinetics of suspended or deposited droplets depending on the exact conditions. They are most times determined experimentally and therefore account for a variety of other influences, respectively. This includes among others substrate heating (Gleason

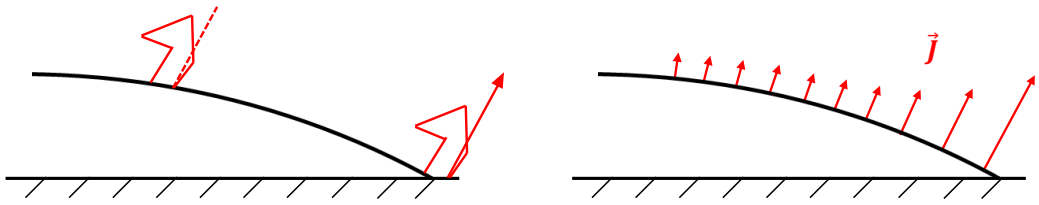

Figure 2.4: Illustration of the same random movement pattern leading to a successful molecule escape at the edge and an unsuccessful escape in the center (left); schematic depiction of evaporation flux enhancement at the edge (right), for systems with $\theta \leq 90°$.

et al., 2016), forced convection (Perdana et al., 2011), the presence of multiple components (Wang et al., 2022), or superhydrophobic surfaces (Dash and Garimella, 2013). Corresponding simulative investigations were conducted by Ruiz and Black (2002) or Guo and Cheng (2019).

2.1.3 Evaporation profile and internal effects

Studies like Picknett and Bexon (1977) and Rowan et al. (1995) correctly assessed that the overall drying rate of sessile droplets is decelerated in comparison to suspended ones. In addition to this phenomenon, there is a number of further effects introduced by the presence of a substrate plane. Above all, the development of an evaporation profile is of great importance. While the evaporation profile on the surface of suspended droplets is spatially uniform, meaning that the evaporation flux is the same on the entire surface, the substrate plane induces a non-uniform flux distribution for sessile droplets. Hereby, the evaporation is greatest at the contact line and is reduced towards the droplet's peak, for partially wetting surfaces.

The flux enhancement along the edge is reasoned in a greater probability of evaporating molecules to escape when exiting from the edge than when leaving from the droplet center. This is illustrated in Figure 2.4, alongside a schematic of the increasing evaporative flux towards the edge.

The resulting flux profile has only a minor effect on overall evaporation rate and droplet drying behavior, and is therefore completely neglected by most studies on such subjects, for example Rowan et al. (1995), Golovko et al. (2009) or Gleason et al. (2016). Other studies, like Picknett and Bexon (1977), naturally account for the profiles overall influence on the droplet's drying rate through their respective correction factors (like the specific fittings for $f(\theta)$ in Equation 2.12), but do not specifically discuss the flux profile itself or the corresponding distribution. However, although the flux distribution is relatively unimportant when discussing the droplet's drying rate, drying behavior or lifetime, this non-uniform evaporation flux profile is the cause for several important phenomena within the droplet. Foremost and directly this includes induced flows such as Marangoni convection or capillary flow (Kovalchuk et al., 2014). Furthermore, this encompasses a number of phenomena resulting indirectly from the profile, for example the pinning of the contact

line during drying that leads to the persistence of the constant contact radius mode, as described in Section 2.1.1.

Figure 2.5 depicts the typical, but not necessarily always applicable or exclusive internal flows and conditions for a droplet drying purely diffusive on a planar, partially wetting and non-porous surface. It can be seen that the capillary flow is directed radially outward from the droplet's central region towards the point of enhanced evaporation along the edge (Gelderblom, 2013). This replenishes the increased mass loss along the contact line and further induces any ring formation phenomena (Kaya et al., 2010), which will be discussed in more detail in Section 2.2. Caused by the evaporation flux profile, the droplet's surface temperature is non-uniform as well. Hereby, energy is withdrawn from the droplet as a result of the phase transition. This means that the droplet is generally cooled through the evaporation, but to varying degrees in the respective areas. However, since heat conduction through the substrate is in most cases significantly higher than the convectively transferred heat through the gas, the droplet's area of highest temperature is located along the contact line, despite the highest evaporation rate's presence. This in turn means that the highest section of the droplet is also the coldest in most applications. This can be attributed to the longest distance to the substrate (Mampallil, 2014). The correspondingly arising temperature gradient on the surface and the unequal distribution of potentially included solids generate a gradient in surface tension ($\nabla\sigma$). In turn, this difference in surface tension creates shear stresses within the droplet, which lead to Marangoni convection. The associated flows are directed away from regions of low surface tension, id est create a backflow from the edge to the center, along the surface. Simultaneously, a balancing current forms further away from the surface. Therefore, the result is a circular flow regime which somewhat counteracts the outward capillary flow (Mokhtari et al., 2021). However, it is comparatively weaker in most drying setups (Hu and Larson, 2006). Nevertheless, this implies that in dependence of the relation of evaporation to heat conduction of substrate and liquid, the thermal Marangoni convection can counteract the evaporation profile's and capillary flow's effects (Tsoumpas et al., 2015). This includes the potential transportation of included solids. It furthermore follows that through Marangoni convection, the substrate's heat conduction properties, or any substrate-related means like heating, can be used as tools to control the net internal flows and any subsequent phenomena (Harris et al., 2007).

2.1.4 Mathematical formulation of the local evaporation flux

Lebedev (1965) derived an analytical solution for the evaporation of a spherical cap on a planar surface. His groundwork consolidated that in contrast to diffusion around suspended spherical droplets, the evaporation flux along the surface of sessile droplets is not uniform. As described in Section 2.1.3, the evaporation profile has a major influence on flows within the droplet and any phenomena resulting from these. In consequence, the flux profile of sessile droplets and the respective mathematical formulation of it, attracted some attention in the past as well.

Deegan et al. (2000) derived an analytic solution for the evaporation flux profile of sessile droplets in case of pure diffusion. They found the following correlation that is valid close to the contact

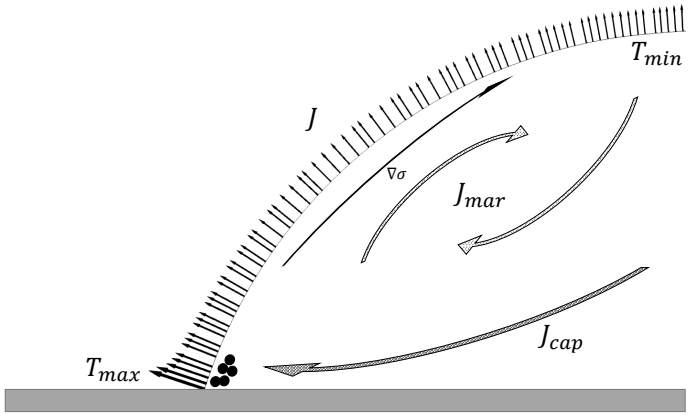

Figure 2.5: Illustration of internal flows and conditions of an evaporating droplet on a partially wetting, planar substrate.

line:

$$J \sim (R - r)^{-\lambda}, \tag{2.14}$$

$$\lambda = \frac{\pi - 2\theta}{2\pi - 2\theta}. \tag{2.15}$$

This correlation again implies that the evaporative flux increases towards the three-phase line and is lowest at the droplet's top.

Hu and Larson (2002) presented a finite element model which is capable of predicting the local evaporation flux in still air and the influence of the droplet's contact angle on it for $\theta \leq 90°$. They proposed a simplified correlation for the case without flow, which is based on the analytical solution of Deegan et al. (2000) and very closely fits to the original approach. This relation for the pure diffusion case describes the local evaporation flux as a function of contact angle and radial coordinate:

$$J = J_{ini}(\theta) \left[\frac{D\,(c_{sat} - c_a)}{R} \right] \left[1 - \left(\frac{r}{R} \right)^2 \right]^{-(0.5 - \theta/\pi)}, \tag{2.16}$$

$$J_{ini}(\theta) = (0.27\theta^2 + 1.3) \left(0.64 - 0.224 \left(\theta - \frac{\pi}{4} \right)^2 \right). \tag{2.17}$$

Later on, Wang et al. (2016) extended these results with a finite volume model without assumption of isothermal conditions. Through this, the evaporative cooling effect could be incorporated. They subsequently proposed the introduction of an additional correction factor ψ for the calculation of J_{ini}, that takes the evaporative cooling into account:

$$J_{ini}(\theta,\psi) = \frac{0.747 - 0.003\psi - 0.967\theta + 0.348\theta^2}{1 + 0.14\psi - 0.005\psi^2 - 1.39\theta + 0.523\theta^2}. \tag{2.18}$$

Popov (2005) derived an expression for the evaporation flux covering a contact angle range of $0° < \theta \leq 180°$. Bhardwaj (2018) later proposed simplified, regionally valid correlations for the pure diffusive case based on a model that incorporated the finite element method.

Additionally to these flux profile correlations of Deegan et al. (2000), Hu and Larson (2002) and Wang et al. (2016) for partially wetting surfaces, as well as Popov (2005) and Bhardwaj (2018) for all contact angles, the local evaporation flux $\overrightarrow{J}$ can be calculated in any diffusion-limited approach to the drying process as a function of the concentration gradient:

$$\overrightarrow{J} = D\,\nabla c. \tag{2.19}$$

The local mass transfer coefficient β can afterwards be obtained utilizing the overall driving force:

$$\beta = \frac{\overrightarrow{J}}{c_{sat} - c_a}. \tag{2.20}$$

From the diffusivity and the local mass transfer coefficient, the corresponding concentration boundary layer thickness δ_c can be evaluated as:

$$\delta_c = \frac{D}{\beta}. \tag{2.21}$$

The total evaporation rate can then be expressed by the integral of the flux over the droplet surface S:

$$J_{tot} = \int \overrightarrow{J}\,\mathrm{d}S. \tag{2.22}$$

2.1.5 Convection around sessile droplets on planar substrates

If a droplet is not drying in still gas, but under the influence of forced convection, there are other parameters that must be taken into account when describing the setup. Foremost, this includes the ambient velocity U_a and the position of the droplet on the substrate. Latter can be specified via the distance l of the droplet from the plate's edge, in direction of the flow, as it is illustrated in Figure 2.1. In contrast to suspended droplets, where the liquid is subjected to a uniform flow field, sessile droplets are subjected to a flow with a velocity profile developed beforehand. The corresponding velocity boundary layer thickness over a flat substrate at distance l from the edge at which the velocity boundary layer starts to develop can be approximated with the Blasius equation:

$$\delta_U(l) = 5.0\sqrt{\frac{\eta_{gas} l}{\rho_{gas} U_a}}. \tag{2.23}$$

In this, η is the dynamic viscosity. The presence of forced convection also means that in addition to gravitational forces, the droplet may also get distorted through the respective drag forces. To describe the ratio of drag forces to surface tension forces and therefore estimate the distortions and verify whether or not the droplet stays in spherical cap shape, the capillary number can be used:

$$Ca = \frac{\eta_{gas}\, U_a}{\sigma_{liquid,gas}}. \tag{2.24}$$

In case $Ca \ll 1$, the droplet retains a spherical cap shape despite the convective drag forces.

The respective properties of the flow, or, more specifically, the laminar or turbulent behavior, can be ascertained via calculation of the Reynolds number. Different characteristic Reynolds numbers can be defined and calculated for the droplet drying setup, each focusing on a different aspect of the forced convection. This can be executed for the general flow over a planar substrate (the characteristic length is equal to the distance l from the substrate edge), a flow within a rectangular flow channel (the characteristic length is equal to the hydraulic diameter d_{hy}), as well as for a flow directly around a sessile droplet (the characteristic length is equal to the droplet's contact diameter):

$$Re_{plate} = \frac{l\, \rho_{gas}\, U_a}{\eta_{gas}}, \tag{2.25}$$

$$Re_{channel} = \frac{d_{hy}\, \rho_{gas}\, U_a}{\eta_{gas}}, \tag{2.26}$$

$$Re_{drop} = \frac{2R_{drop}\, \rho_{gas}\, U_a}{\eta_{gas}}. \tag{2.27}$$

If a flow's external conditions rapidly change, a special and application specific flow behavior occurs for a certain area, until the flow normalizes and can again be categorized by standard Reynolds correlations. This transition area is called hydrodynamic entrance length (Shah and London, 1978). Its length L_{hy} dependents on the spatial dimensions of the transition, the flow's Reynolds number and the hydraulic diameter of the new channel. Consequently a great number of correlations for different situations exists. At this point, only the correlation of Ward-Smith (1980) for the transition taking place for an inflow from a round tube into a quadratic flow channel shall be listed, as this correlation is important for the experimental setup described at a later stage of the present work:

$$L_{hy} = 0.0656\, d_{hyd}\, Re_{channel}. \tag{2.28}$$

Apart from these fluid mechanical processes, another important mechanism taking place in the flow field during droplet drying is the advection of vapor. Assuming a non-turbulent flow and a quasi-steady-state where the vapor concentration distribution and the flow field adjust rapidly to changes in droplet shape, one can express the transport of vapor in the flow field as a function of local velocity U, the concentration gradient ∇c and the diffusivity D (Baines and James, 1994):

$$\nabla(D\,\nabla c) = U\,\nabla c. \tag{2.29}$$

Presupposing spatial independence of the diffusivity yields:

$$D\,\Delta c = U\,\nabla c. \tag{2.30}$$

This equation includes both, the term for convectional transport and the one for transport through diffusion, as it is common. The overall mass transfer rate $\dot{M}$ is therefore accessible through this equation. Since in Maxwell's diffusion limited approach, the droplet's mass loss calculated via Equation 2.8 equals the diffusive mass transfer, the dimensionless mass transfer rate, id est the ratio of convective to diffusive mass transport, can be calculated and expressed through the Sherwood number (Baines and James, 1994):

$$Sh = \frac{\dot{M}}{4\pi RD(c_{vapor,surf} - c_{vapor,a})}. \tag{2.31}$$

In purely diffusive drying cases or at positions of zero velocity, for example at the interfacial boundary, Equation 2.30 is reduced to a purely diffusive transport equation, based on Fick's second law of diffusion for steady-state cases:

$$\nabla(D\,\nabla c) = 0. \tag{2.32}$$

If one again assumes a constant diffusivity, the Laplace equation is obtained:

$$\Delta c = 0. \tag{2.33}$$

This reduction of Equation 2.29 is the norm in all related investigations of the evaporation flux profile up to this point. If the capture of non-purely diffusive mass transport of vapor is desired (buoyancy or forced convection), the convective term in Equation 2.29 cannot be eliminated. Instead, the velocity field must be calculated to obtain the local flow velocity U and in turn solve

Equation 2.29 and describe the advection of vapor. Hence, a corresponding set of momentum transport equations has to be solved. In most related cases, including the simulative part of this dissertation, this comes down to solving the continuity equation and the Navier–Stokes equations for incompressible flows (Schlottke and Weigand, 2008):

$$\nabla U = 0, \tag{2.34}$$

$$\frac{\partial U}{\partial t} + (U\nabla)\, U = -\nabla \frac{p}{\rho} + \nu \nabla^2 U + g. \tag{2.35}$$

Herein, p denotes the pressure and ν the kinematic viscosity. The flow's corresponding ratio of momentum to mass diffusivity is characterized by the Schmidt number:

$$Sc = \frac{\eta_{gas}}{\rho_{gas}\, D}. \tag{2.36}$$

Multiplied with the Reynolds number, the Péclet number is obtained to quantify the ratio between advective and diffusive mass transport within the gas phase:

$$Pe = Sc\, Re = \frac{2R\, U_a}{D}. \tag{2.37}$$

To solve Equations 2.29, 2.34 and 2.35, and therefore in order to investigate the drying of sessile droplets through forced convection and hereby obtain further information on evaporation rate and flux, computational fluid dynamics has proven itself to be a powerful tool.

2.2 Structure formation during sessile droplet drying

Before an individual solid-laden droplet starts to dry, the solids move freely within the liquid phase and are only affected by gravity. For colloidal systems, this free movement is described by Brownian motion. If the included particles are light enough for the Brownian diffusion to counter the gravitational forces, the solids inside the droplet stay distributed homogeneously (Melik and Fogler, 1984). This means that the net flux of solids within the droplet before drying is zero (Sanden, 2003):

$$\begin{aligned} J_{solid,net} = 0 = {} & c_{liquid}\,(U_{liquid} - U_{solid}) \\ = {} & -\frac{D_{liquid,solid}}{1 - V_{liquid}/V_{drop}} \frac{dc_{liquid}}{dh} \\ = {} & -\frac{D_{liquid,solid}}{1 - V_{liquid}/V_{drop}} \frac{dc_{liquid}}{dr}. \end{aligned} \tag{2.38}$$

In such a case, the suspension is considered as stable, which applies to all systems relevant for the present dissertation, at least for the limited lifespan of the droplets before the drying begins, or in other words the time before drying induced phenomena superimpose such deliberations, rendering them insignificant.

In many droplet-drying-based coating procedures the core process comes down to such a solid-laden droplet resting on a comparatively flat, non-porous and partially wetting substrate. During the subsequent drying process a non-uniform evaporation flux arises as described in the previous sections, and the flux distribution acts as the driving force for a number of effects, in particular within the droplet (Zang et al., 2019). Next to, and resulting from the already discussed internal flows, the most prominent of these subsequent effects are arguably the ring-patterns following the deposition of solids, frequently occurring during sessile droplet drying of suspensions or solutions (Deegan et al., 1997). If the droplet is solid-laden, such related shapes originate from the relation of capillary flow and Marangoni convection and are in turn influenced by the droplet drying process (Bhardwaj et al., 2009). This means, that the internal flows which are induced through the evaporation flux transport contained solids with them, as depicted in Figure 2.4. The solids' net flux is consequently non-zero. Soulié et al. (2015) and Xu et al. (2017) presented corresponding visualizations of this particle transport through droplet internal flow imaged via particle tracking velocimetry.

The non-zero net flux also means, that the solid concentration is increasing in direction of the internal flows, id est towards the droplet's contact line, along which, as a result, particles are deposited or crystals are formed (Deegan, 2000). The result are the already referenced, prominent, ring-like formations that are left behind after the drying of sessile droplets. These ring patterns are common wherever drops containing dispersed solids evaporate on a surface, and were scientifically described and reasoned for the first time by Deegan et al. (1997).

Since Deegan et al. (1997) reported the encountered ring morphology for systems that are driven by the higher evaporation flux along the contact line for the first time, many studies on structure formation from deposited droplets have been published (Bhardwaj et al., 2010). Maenosono et al. (1999) investigated the kinetics of this ring formation for semiconductor nanoparticle droplets. Crivoi and Duan (2013a) presented further results on structure formation from nanoparticles and respective morphologies of ring and center basin. This work was followed by investigations from Zhong et al. (2015) and Sanyal et al. (2015), who respectively studied the corresponding formation for droplets containing nanoparticles, as well. Bruning et al. (2020) studied droplets containing salt and Brutin et al. (2011) presented a report about blood droplets containing both soluble and insoluble solids. Willmer et al. (2010), Gorr et al. (2012) and Sadek et al. (2013) focused on structure formation in droplets containing polymers and salt-polymer mixtures. Ring formation dependency on the particle size and concentration was investigated by Shen et al. (2010).

Potential possibilities for coating layer fabrication, resulting from the investigated residue structures, were discussed by Brutin et al. (2011). It was hereby pointed out, that ring-formations could be used to have controlled ingredient releases. Additionally, it was discovered that certain diseases

go hand in hand with changes in structure formation from drying drops of saliva or blood, which in turn means analysis of these structures could be used for diagnosis. Yunker et al. (2011) pointed out different associated problems. They discussed the harming effects ring formation can have on droplet-based industrial painting or printing.

Options to control the resulting deposits were presented in several publications (Mampallil and Eral, 2018). Msambwa et al. (2016) studied structural alterations that can be attained by various additives. External influences on pattern formation such as forced convection (Janocha and Tsotsas, 2021a) or substrate heating (Bouchenna et al. (2017), Sliz et al. (2020)) have also been discussed. As already suggested in Section 2.1.3, control of the ratio of Marangoni convection to capillary flow is the key to controlling ring-formation, be it via convective conditions, additives or substrate heating. A stronger Marangoni convection hereby always means that more particles are transported back from the outer rim into the center, which therefore counteracts ring formation (Bazargan, 2014).

In addition to influences through thermal conditions or droplet properties, Nguyen et al. (2013) discovered dependencies of ring morphology on the substrate roughness and the formed contact angle. Takhistov and Chang (2002) compared morphologies of crystalline structures on hydrophilic and hydrophobic substrates. Deposit morphologies that result under different convective drying conditions of single sessile droplets were experimentally studied by Sondej et al. (2018) for water-based sodium benzoate droplets in air. Furthermore, Sondej et al. (2018) analyzed the influence of drying conditions on the porosity of such solitary sodium benzoate residues. Especially this aspect is of great importance, as drying conditions can be directly and easily controlled in most coating processes. The respective behavior of sodium benzoate structures during the transition stage from single deposit to multi-deposit layer was presented in Janocha and Tsotsas (2021b).

Complementary to these mostly experimental investigations, further simulative studies were conducted to explore contexts of droplet drying and structure formation. Popov (2005) contributed a model that is able to predict formation patterns during sessile droplet drying, based on the problem's finite spatial dimensions. Breinlinger and Kraft (2014) presented a coupling approach of computational fluid dynamics (CFD) and discrete element method (DEM) to incorporate the particle's Brownian motion during ring-formation, while Crivoi and Duan (2014) based their structure formation simulation on a Monte Carlo approach. Larson (2014) utilized the results from his group's previously developed model based on the finite element method (FEM) (Hu and Larson, 2002) for predicting transport and deposition patterns in colloidal droplets. Kaplan and Mahadevan (2014) presented a multi-phase model with the aim to describe the formation of different patterns.

For layer build-up through deposited droplets, the theoretical volume of the solid residues $V_{s,theo}$ can be calculated via the solid mass fraction ω_{solid}, the droplet volume, and the liquid and solid density, respectively:

$$V_{s,theo} = \sum_i \frac{V_{drop,i}\,\rho_{liquid}\,\omega_{solid,i}}{\rho_{solid} + \omega_{solid,i}(\rho_{liquid} - \rho_{solid})}. \tag{2.39}$$

If solid content and droplet volume are constant throughout the application, Equation 2.39 can be simplified to:

$$V_{s,theo} = \frac{N_{drop}\, V_{drop}\, \rho_{liquid}\, \omega_{solid}}{\rho_{solid} + \omega_{solid}(\rho_{liquid} - \rho_{solid})}, \tag{2.40}$$

with N_{drop} as the number of applied droplets. During colloidal or solution based structure formation processes, the solids naturally never form a perfectly homogeneous, compact volume. Instead, an imperfect, id est porous structure that contains voids and cavities is formed. Therefore, a characteristic property of solid residues and corresponding coating layers, that in addition to morphology is particularly significant for the present work, is the porosity. As a measure of the proportion of voids in a structure, the porosity can be determined subsequently to the theoretical volume, with Equation 2.41, if the actual volume of the corresponding structure is known as well:

$$\varepsilon = 1 - \frac{V_{s,theo}}{V_{s,tot}}. \tag{2.41}$$

The cavities and voids leading to the difference between theoretical and actual volume can hereby be completely enclosed within the structure, or feature openings to the surface.

2.3 Drying behavior of sessile solid-laden droplets

As described within the previous section, the pattern formation is a result of droplet drying behavior and thereby arising internal flows. At this point it shall however be noted, that this influence also works vice versa, meaning that the presence of solids inside the droplet influences the drying process. In the constant contact radius stage, the droplet's contact line is pinned, while its contact angle and height are decreasing. Simultaneously, the dispersed solids are accumulating along the edge, forming a respective ring structure. This means that at some point in the drying process of solid-laden droplets, the liquid-gas interface is inevitably meeting the upper edge of the solid deposit. From here on, the ideal CCR mode as depicted in Figure 2.2 is interrupted. Molchanov et al. (2015) reported the further course for most scenarios. When interface and deposit top are meeting, the liquid phase is effectively split into two parts. The first, but smaller part is forming a liquid fringe around the deposit, between the outer rim of the solid structure and the original contact line. This fringe continues to dry and therefore changes from a convex into a concave form until most of the liquid is evaporated and only the wet outer rim of the main deposit remains. The second part of the liquid is placed in the ring's center, forming a new contact line along the ring's crest and retaining a convex, id est spherical cap shaped, form. In the further course of this main liquid part's drying process, again, variants of CCR and CCA mode can be seen. Similar as the initial drying mode was dependent on the substrate-liquid adhesion forces, the subsequent behavior depends on the adhesion forces between deposit and liquid. If these forces are weak, the contact line does not get pinned and the droplet continues to shrink in a constant contact angle

mode, converging towards the center and retaining convex form. If the adhesion forces are strong enough for the contact line to be pinned, the remaining liquid again dries in a constant contact radius mode, as it was the case up to this point. Consequently, the ring's center stays wetted for a comparatively long period, while the remaining droplet shaped part's height is reduced. At some point, as the center is surrounded by rising walls, the droplet's form changes from convex to concave, while still spanning and wetting the enclosed basin, until this liquid fringe is dried as well, leaving only a wet structure. After the main parts of the liquid have dried, the remaining wet solid structure dries similarly to a pore network (Molchanov et al., 2015). The general schematics of the drying process of solid-laden droplets is illustrated in Appendix A.1. Herein, a top view onto a drying sessile droplet is employed. The droplet first is heated up from its initial to wet bulb temperature. It stays at T_{wb} during the entire shrinking stage. Once the crust formation process starts, the temperature slightly increases, as the evaporative cooling effect is becoming more and more diminished (Farid, 2003). After the droplet is evaporated, the remaining liquid evaporates from the wet crust structure. Last, the dry residue structure gets heated up to ambient temperature.

2.4 Fluidized bed technology

Products that incorporate precious or sensitive ingredients often need to be covered with a protective coating layer, in order to preserve the materials from external influences. Other goals of such coatings can be, among others, to improve taste of food related products, improve a product's look, or simply control the product's interaction with the environment (Kleinbach and Riede, 1995). Latter is often the case for pharmaceutical products. Coating properties in all these applications, and with them product quality, are dependent on the coating process itself and its process parameters, respectively.

There is a number of processes that do not involve droplet drying as it was described in Section 2.1. For example sol-gel coating or spin coating do not incorporate droplets, but cover the substrates entirely with the wet coating material, before the drying stage begins. However, processes in which solid-laden droplets are applied to the product and subsequently dried are still important in many areas and the focus of this thesis. One of the most prominent industrial applications among these is fluidized bed coating (FBC), which is widely used for the manufacturing of particulate products, especially in the food (Dewettinck and Huyghebaert, 1999), agricultural (Rieck et al., 2020) and pharmaceutical industries (Liu et al., 2017).

Fluidized bed spray coating is a well established method to coat particles (Peglow et al., 2011). In this process, core particles are placed within a process chamber on a permeable medium (perforated plate) and subjected to an upwards directed gasflow opposing gravity (Atarés et al., 2012). When a certain airflow velocity, namely the minimum fluidization velocity, is exceeded, the particles are fluidized (Schmidt, 2018). Depending on the fluid flow, or, more specifically, the flow velocity, the fluidization behavior of this particle bed can hereby be controlled. Conceivable regimes and with them the basic principle of the method are depicted in Appendix A.2. At low gas flow rates, the particles remain in contact with each other to form a fixed bed (Figure A.2a). Once the point of

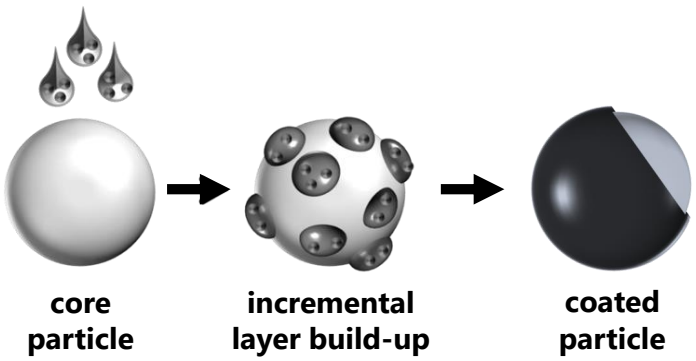

Figure 2.6: Schematic illustration of the principles of droplet based particle coating.

minimum fluidization is reached, the forces of resistance, buoyancy and gravity are in equilibrium (Rieck et al., 2016). This means that the particles begin to float, as depicted in Figure A.2b. After further bed expansion with increasing flow rates, these stable process stages are followed by several other regimes arising at higher flow velocities (Figure A.2d to h), which shall not be part of the present overview.

When the fluidization of the core particle bed corresponds to the desired process conditions, the coating material (usually suspensions or solutions) is sprayed into this fluidized bed. Hereby, the sprayed droplets get applied onto the particles' surface and dried through the fluidization gasflow. The liquid part evaporates and the solids contained in the coating material remain, get deposited on the surface and coating layers incrementally form around the core particles (Uhlemann and Mörl, 2000). The enclosing layers are therefore built around the core particles by repeated droplet deposition and drying. This is illustrated in Figure 2.6, and means that droplet drying on a surface, as described in Section 2.1, and corresponding structure formation, as described in Section 2.2, are important subprocesses of this industrial application. The corresponding study on fluidized bed coating therefore forms the practical reference to the investigations of these naturally occurring processes.

Similar as for carefully deposited droplets, the exact morphology and porosity of sprayed droplets and associated coating layers is dependent on the drying process. A corresponding study of fluidized bed coating with sodium benzoate was presented by Rieck et al. (2015). Herein, the coating layer properties mainly depended on drying conditions, droplet characteristics and the structure formation mechanisms taking place. Latter naturally depend on the used materials. An additional related study was conducted by Bachmann et al. (2020), who investigated deposit structures and the subsequently resulting layers during fluidized bed spray coating processes with regard to layer-thickness and its distribution. Sondej et al. (2016) analyzed coating porosities within a fluidized bed for various materials. Hampel et al. (2013) contributed a related study on coating within a Wurster fluidized bed.

Additionally, such layering processes were simulatively investigated among others by Jiang et al. (2019) or Li et al. (2012). Haferl et al. (2000) and Attinger et al. (2000) developed a finite element

model simulating droplet impact and predicting splash behavior. Bhardwaj et al. (2009) extended this simulation of pure liquid droplets by incorporating heat transfer.

2.5 Comparison of sessile droplet drying and spray coating

As described in the previous section, drying and pattern formation of single droplets is an important part of many spray based coating processes. As such, there has also been a number of studies that incorporate some sort of comparison between the two systems.

Monse et al. (2006) and Sloth et al. (2009) added complementary droplet drying experiments to their investigations on spray drying, stating general differences and offsets. Perdana et al. (2011) studied drying kinetics for deposited and sessile droplets. Sondej (2019) conducted experiments with a salt solution within a fluidized bed as well as a sessile droplet drying chamber and analyzed arising morphologies. On the basis of such insights, Schutyser et al. (2012) and Tran et al. (2016) presented new options for design and process control of spray dryers.

Although the process of subsequent sessile droplet drying and deposit formation is important for the resulting coating layer, the great number of concurrent effects during fluidized bed coating complicates the search for exact scientific correlations and the segregated observation of parameter influences. Additionally, fluidized bed design prevents continuous observing of one particle, which in turn prevents the monitoring of incremental layer build-up. This means that notwithstanding some studies do compare coating layers from sessile droplets and spayed droplets, the comparison itself and the corresponding transition from residue to layer is seldom the main focus of the investigations. It is therefore usually handled very briefly and many details of the process are continuously neglected.

2.6 Conclusion

Following Maxwell's original studies, the drying of suspended and pendant droplets and the resulting solid deposition patterns as well as layer formation from solid-laden droplets have been studied extensively, with many important insights into the mechanisms at work. However, several aspects of these complex processes are still relatively unknown today.

Among these unknowns are the influences of several process parameters, foremost drying conditions, as well as the influence of droplet properties. Furthermore, for both simulative and experimental studies on droplet drying and structure formation, conditions typically investigated in research feature large droplets with only little solids and purely diffusive or very slow drying processes, which are far from the conditions of technical processes. The porosity of sessile droplet deposits, as one of the most important three-dimensional morphological features, is investigated only very rarely. Even more limiting regarding structure formation, however, is the sparseness of experiments on the incremental build-up of layers from initial droplet residues. Such experiments and simulations are therefore at the heart of the present project.

2.7 Aim of the thesis

This dissertation is intended to contribute to the expansion of knowledge about droplet drying and layer formation. More precisely, the goal of the experimental part of the project is to mimic the build-up of layers from deposited and dried, solid-containing droplets, in a droplet-by-droplet manner. During this ex-situ layer build-up, morphology and porosity are to be measured incrementally. This is expected to yield new insights into the build-up and structure of porous coatings created by simultaneous spraying and drying, which in turn are decisive for the performance properties of the coating. Aiming at results that are as generally valid as possible under well-defined conditions, such experiments cannot fully reproduce the technical process of coating in spray fluidized beds, which serves as an important practical example. However, coming as close as possible to the drying conditions of this process, they will still allow a distinction to be made between effects specific to the spray fluidized bed and actual structure formation in the layer build-up.

In the course of this, the present research shall identify and investigate phenomena that are native to the build-up process and further assess their influence on the resulting layers. As such phenomena taking place during the incremental layer build-up, or in other words the transition from solitary residue to layer, are frequently neglected in literature, one goal of the present work is to further explore these mechanisms. Focusing exactly on this transition from single ring structure to multi-deposit layer, these processes shall be investigated in depth within the present experimental studies. The current contribution is therefore essential for understanding the layer build-up encountered in many industrial processes and scientific applications. In addition to that, it may contribute to the overall knowledge on deposit formation from sessile droplets dried under convective conditions and in turn lead to a more purposeful design of coating layers and processes.

It was shown by Tsotsas (2012) and Rieck et al. (2015), that drying and droplet conditions strongly influence structure formation and coating layer morphology and porosity in spray fluidized bed coating. To follow-up this research, mechanisms and conditions influencing layer formation and their interactions are to be identified and analyzed in the present experimental study, with the aim of finding at least regionally valid trends. Additionally, droplet properties and drying conditions shall be chosen as closely to industrial conditions as possible. This goal extends and stands in contrast to most previous studies, which usually feature gentle drying and relatively dilute colloids or solutions with low solid concentration.

As described in Section 2.5, there are various studies that frequently draw a comparison between single droplet structure formation and creation of coating layers. However, all these comparative studies were conducted in spite of the further mechanisms taking effect or the unexplored phenomena taking place during droplet addition. Consequently, one goal of this thesis is to help close this gap in knowledge and give further insights into the mechanisms that take place during the transition stage. In order to pursue this goal of a better understanding of layer build-up processes within a fluidized bed further, layers created therein are to be compared with the ex-situ layers created from deposited droplets.

Regardless of the great number of simulative investigations on droplet drying and structure formation, the great majority of related simulative studies can be sorted into two categories. Either droplet internal phenomena are investigated with a presupposed flux distribution, or the diffusion limited evaporation is investigated neglecting buoyancy-induced convection and not addressing forced convection. This means that up to this point, the drying profile of sessile droplets was only analyzed for cases without a surrounding flow field. Consequently, one goal of the simulative part of the present dissertation is to investigate the influence of forced convection on the evaporation flux distribution during sessile droplet drying. Thereof, one hopes to draw additional conclusions regarding structure formation and give reasons to arising morphologies and porosities.

As droplet drying and structure formation are influencing each other, and as they are in turn important aspects of fluidized bed coating, the respective studies in the present thesis are reasoned in this practical application and vice versa. Furthermore, the determined values and trends are intended to help draw conclusions regarding connections between laboratory scale and industrial processes. In consequence, this means that all investigations presented in this dissertation are reasoned in each other and are contributing to the same goal of a better understanding of droplet-based coating processes.

Chapter 3

Experimental arrangement

The aim of the planned experimental investigations was to investigate and clarify layer formation analogous to the processes taking place in fluidized bed coating, with regard to finally resulting and incremental development of layer morphology and porosity. The most important mechanisms to be realized are the serial placement and controlled drying of solid-laden individual droplets in a laboratory setup outside, as well as coating experiments directly within a fluidized bed. The present chapter describes the experimental setups that were designed, built and utilized to achieve this goal.

3.1 Sessilde droplet drying

3.1.1 Drying chamber

The application of sessile droplets and their subsequent convective drying were executed in a cuboid glass drying chamber. The chamber has a length of 100 mm and a $20 \times 20\,\mathrm{mm}^2$ cross-sectional area for the forced convection. The chamber's sides and ceiling are made of float glass to enable monitoring the droplet application process as well as the drying of applied droplets from the sides and the top through a charged coupled device (CCD) camera system. On the front and back side of the chamber, tube connections for the gas inlet and gas outlet are installed. These are connected to the air control unit described in detail in Section 3.1.3. In the direction of flow, directly in front of the area designated for application, there is a small drill-hole for a respective temperature sensor incorporated in the connected airflow temperature control circuit. The height of the hole is selected in such a way that the inserted thermocouple has not any decisive influence on the flow conditions around the deposited droplets. The chamber's ceiling features an aperture with 10 mm diameter, through which the micropipette of the droplet dispenser described in Section 3.1.2 can be inserted and droplets can be placed in the application area. On the ceiling, another glass plate is placed, which is used to close the opening during the convective drying process and accordingly prevents a mixture of the atmosphere inside and outside the chamber, as well as a deviation in the flow. The removable bottom plate of the drying chamber is used as the substrate's basis and is made of

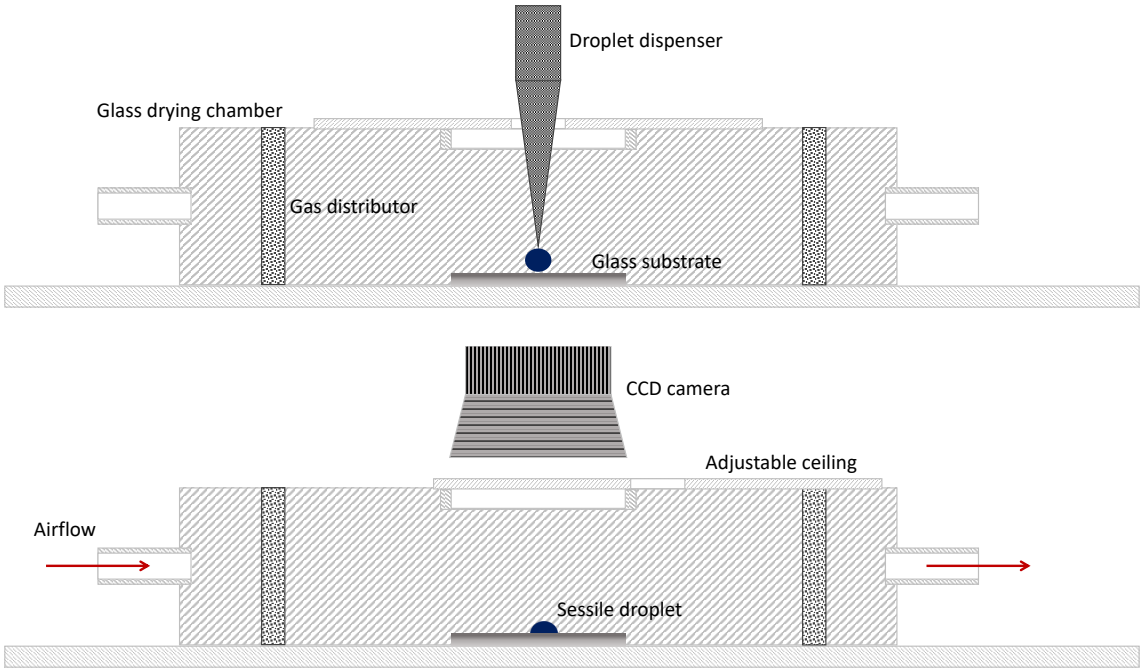

Figure 3.1: Schematics of the sessile droplet drying chamber and the two-step droplet application and convective drying process.

borosilicate glass. Chamber's walls, ceiling and bottom plate have a wall thickness of 4 mm and are not further insulated.

Based on Equation 2.26, the chosen experimental plan (Tables 6.2 and 7.1), as well as the material properties in Appendix C, the maximum Reynolds number within the drying chamber's flow channel amounts to 1896. This value would result in a hydrodynamic entrance length of 2.49 m, according to Equation 2.28, which is naturally not feasible. Instead, gas distributors made of sintered metal with a mean pore size of 200 μm are placed at the chamber's inlet and outlet, in order to act as flow straighteners after the tube inflow, ensure a uniform velocity entry into the drying region and in turn promote a laminar flow within the chamber and especially around the droplets, even at the highest velocity tested. These distributors were purchased from Tridelta Siperm GmbH (brand name B200). The respective tubes leading in and out of the chamber feature an inner diameter of 4 mm. The described chamber for convective sessile droplet drying as well as the two phases of droplet application and drying are schematically shown in Figure 3.1, furthermore, a detailed description of this equipment can be found in Janocha and Tsotsas (2021b).

3.1.2 Droplet application process

In order to exclude the influence of droplet momentum, one requirement on the application device was that the droplets should be depositable with as little momentum as possible. Furthermore, a high accuracy regarding dispensed droplet volume is a basic requirement. The chosen droplet dispenser for the application of sessile droplets was a micropipette-based droplet injector type

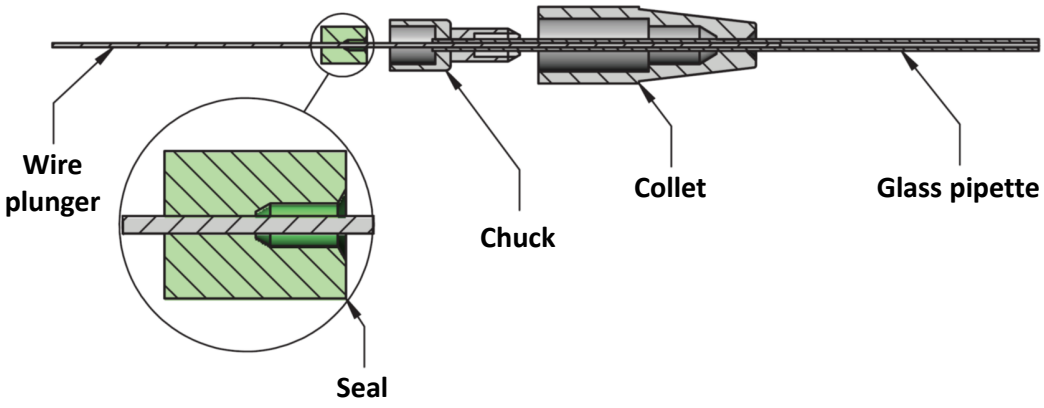

Figure 3.2: Schematic working principle of the plunger-based Nanoject III droplet dispensing setup, adapted from Nanoject III instruction manual.

Nanoject III from Drummond Scientific Company. This nanoliter injector works with specifically pulled borosilicate glass pipettes and produces droplets with preset volume. Before the experiment, the glass pipettes are pre-filled with oil and then put onto the device. Silica oil with a kinematic viscosity of 1000 cSt proved to be a dependable displacement medium that results in accurate dosage without boosting clogging phenomena or drying inside the capillary tube. Thereafter, a wire plunger is automatically inserted into the cannula part of the pipette via a precise actuator. This plunger is able to extend and retract exact distances within the glass pipettes and hereby pushes out liquid for droplet dispensing or sucks in material for backfilling. Figure 3.2 illustrates the schematic working principle of such a plunger-based droplet dispensing system. Further on, an injection speed of 100 nanoliter per second was applied in all experimental series. This relatively high dispensing speed makes observation of the dispensing process difficult, especially for 100 nl droplets, but was deemed necessary to counteract disturbing phenomena accompanying a pipette-based dispensing, which are explained in more detail later on in this section.

The necessary pipettes for the device were pulled with a micropipette puller type P-1000 Flaming-Brown from Sutter Instrument Company prior to each experiment. Corresponding borosilicate capillary tubes with an inner diameter of 0.53 mm and an outer diameter of 1.14 mm were used as base material. Depending on the dispensed substance, different types of pulled pipettes were found to be suited best, id est resulting in accurate droplet dosing while simultaneously avoiding clogging related problems or instability of the tip. The created pipettes' characteristics that were found feasible for the three substances described in Section 4.2 are summarized in Table 3.1. The taper's optimal opening size was hereby determined to be smallest for sodium benzoate, since the solutes are present in a dissolved state and thus do not block the tip. The small opening simultaneously prevents early crystallization, as it limits the contact with ambient air. In case of colloidal systems the taper tip needs to be larger in order to prevent blockage by accumulated particles or agglomerates. In the course of the present investigation, this was especially the case for the disperse boron carbide microsuspension.

Table 3.1: Results of the suitability study on micropipettes and respective tips for the used substances.

Material	Inner diameter	Taper length	Taper tip	Taper morphology
Silica-based	0.53 mm	2 – 3 mm	0.9 – 1 μm	stubby
nanofluid				non-beveled
Boron carbide	0.53 mm	3 – 4 mm	8 – 10 μm	stubby
microfluid				non-beveled
Sodium benzoate	0.53 mm	5 – 8 mm	5 – 6 μm	stubby
solution				non-beveled

The droplet dispenser is inserted through the closeable aperture in the drying chamber's ceiling. On the side of chamber, a camera type JAI GO-5000M-USB (62 fps, 5 MP, monochrome) enables optical control of the application process, which is executed manually for all droplets. An adjustable objective lens is installed on the camera to keep the pipettes in focus at different application positions and enable an in real time visual assessment of the distance from pipette tip to substrate. Through this method, side effects that inevitably accompany a nozzle-based dispensing, such as hysteresis, variable droplet volume, or splash, could be prevented.

After successful application of a droplet, the dispensing pipette is removed, the chamber's ceiling closed and the drying airflow is applied. The consecutive droplet application and convective drying process is schematically illustrated in Figure 3.1 as well. The dispenser's insertion, droplet application and dispenser removal are executed manually via a micromanipulator type MM33-L from Drummond Scientific Company.

The accuracy achieved with the Nanoject III droplet dispenser, the pulled micropipettes with the configurations listed in Table 3.1 and the chosen workflow was determined before the main experimental investigation. For this purpose, exemplary single droplet residues of all later used coating materials at known solid content were weighed with a laboratory scale with an accuracy of 10 μg (Sartorius LC 4800P). A droplet size of 1 μl was set as a target volume. Through the known solid mass, the dispensed droplet volume can be calculated via the following equation:

$$V_{drop} = \frac{m_{solid}}{\rho_{drop}\,\omega_{solid}}. \tag{3.1}$$

The droplet density can hereby be calculated through the known solid content. Respective values can be found in Appendix C. The results of these weight measurements and the resulting droplet volumes are listed in Appendix B.2. In the first 12 tests in Table B.1 an injection speed of 50 nl/s was set. One can see that there is a systematic error and the dispensed droplet volumes are naturally fluctuating around a too low average value. This error was identified to be due to the dispensing process with micropipettes. In this process, an initial part of each droplet is pulled upwards on the outside of the pipette tip, before a stable droplet hanging from the tip is formed. Hence, a

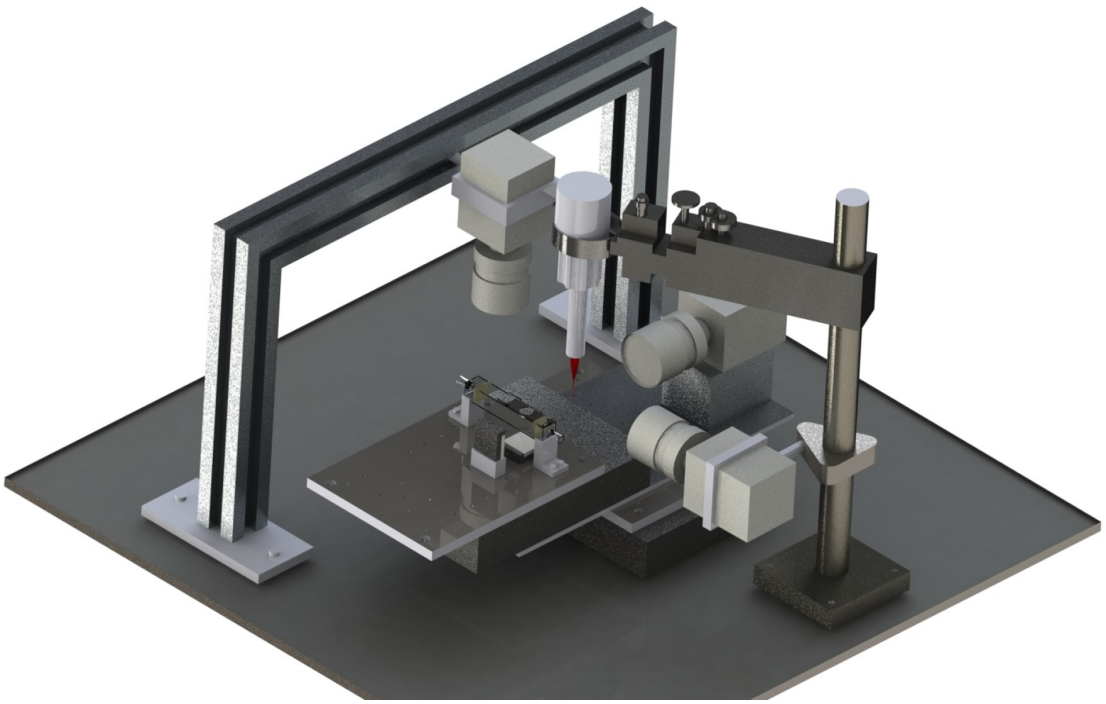

Figure 3.3: Schematic illustration of the sessile droplet drying setup, comprised of drying chamber, droplet dispenser, positioning system and cameras.

certain percentage of the dispensed volume is always lost to this effect. This systematic error was identified through the present study and was successfully countered through an enhancement of dispensing velocity to the Nanoject's maximum injection speed of 100 nl/s. The results after this adjustment can be viewed in test 13 to 24 of Table B.1. As the mean droplet volumes calculated through weight measurement were a better fit afterwards, this adjustment was kept for the main experimental series.

3.1.3 Positioning, in situ visualization and convective drying

The laboratory setup for sessile droplet drying is schematically illustrated in Figure 3.3. The droplet dispenser itself is stationary in its position above the substrate plate and can only be adjusted in height for the droplet deposition procedure. To execute the layer build-up mimicking positioning scheme described in Section 5.1.1, the entire drying chamber, including the bottom plate, is placed on a positioning system. This positioning table comprised of two positioning axes type CXN-80150 from GMT Europe GmbH has a step accuracy of 0.1 μm, a repeatability accuracy of 1 μm and enables the precise placement of droplets at different predefined positions on the substrate plane or an already existing layer.

To prevent a premature drying of the droplets, for example in the suspended state or during the spreading and dosing phase, the entire application process is carried out in nearly saturated air. In order to prevent any condensation of water vapor on the inner surfaces of the drying chamber, saturation of the airflow is not carried out completely. Instead, the dew point is set about two degrees

below the actual gas temperature, as in preliminary tests a humidity that was too close to saturation showed phenomena that were difficult to control and consequently the experimental procedure was unreliable. For this reason, the compressed airflow of 21 °C and a density of 1.293 kg/m^3 first is saturated and afterwards heated-up by about two degrees (till 23 °C) before entering the drying chamber. All deposition processes are therefore carried out at temperatures close to room temperature and at airflow velocities of 0.1 m/s. The particular part of the air supply unit that is responsible for handling this saturated airflow for droplet application consists of a Bronkhorst Mättig mass flow controller type F-201CV-500 and a saturator coupled with an Optidew dew-point hygrometer from Michell Instruments GmbH and a thermostat system from Julabo GmbH type F25-HE, as well as a circulation heater type CHF01499 from Omega Engineering GmbH.

Once the individual droplets have been deposited at the desired position and the dispenser has been removed from the chamber, the convective drying airflow is started (as illustrated in the bottom part of Figure 3.1). Hereby, the flow conditions are set via an air supply setup installed in parallel to the one described above. This unit is comprised of two Bronkhorst Mättig mass flow controllers type F-201CV-20K, working with compressed air of low humidity. A combination of two electrical heaters (Enda type ETC4420-230), each with an independent temperature sensor (thermoelement type K) positioned inside the drying chamber is set up within the air supply system, in order to dynamically control and adjust the convective airflow's temperature. The first one is used to preheat the airflow to a temperature closely below the desired value of the gas. The second heater is positioned directly in front of the drying chamber and connected to a temperature sensor that is placed above the droplet. This two-step preheat configuration enables the application and preservation of a predefined temperature during the entirety of the process. The respective control is especially important, as the drying chamber itself is not insulated or heated, since this would prevent the monitored droplet application. Instead, heat losses at the walls and ceiling are compensated through the integrated air supply control loop. In order to minimize disturbing heat losses, all tubes after and in between the two heaters are insulated and wrapped with heating jackets. A respective four-way valve is placed in front of the drying chamber to enable quick switching between application and drying airflow. The schematics of the designed air supply unit are illustrated in Appendix B.1.

During the drying process, the droplet is monitored via two CCD cameras type JAI GO-5000C-PMCL (107 fps, 5 MP, color) with telecentric lenses type SILL TZM 1007/1,0-C and two DALSA XTIUM-CL-MX4 frame-grabbers. These cameras enable an optical assessment of the experimental progression after the droplet deposition. This includes foremost the droplets' individual positioning (central, non-central, spanning), as described in Chapter 7 and the drying behavior of the droplets (CCR, CCA and point of transition). The necessary illumination is achieved via a set of thin LED panels type CCS-LFL-612SW2 from CCS Inc. attached below and next to the chamber.

3.2 Fluidized bed coating

3.2.1 Fluidized bed plant

The comparative coating experiments were performed in a fluidized bed plant type GPCG 1.1 from Glatt Ingenieurtechnik GmbH. The laboratory-scale setup with its cylindrical fluidization chamber with a height of 450 mm and a diameter of 150 mm is illustrated in Figure 3.4. Same as the sessile droplet drying chamber, this fluidized bed plant utilizes a supply of compressed air in combination with Bronkhorst Mättig mass flow controllers in order to obtain constant values for gas flow rate. The compressed air is heated to the desired temperature by a system of three electric heaters, enters the plant's inlet chamber and then passes through the distributor plate and the particle bed, fluidizing the particles. The sinter metal gas distributor plate placed at the bottom of the fluidization chamber has a mean pore size of 100 μm and ensures uniform flow conditions, or in other words an evenly distributed flow over the cross sectional area of the apparatus. The corresponding flow rate was measured with a Bronkhorst Mättig mass flow meter type F-112AC, alongside with temperature measurements at the inlet, outlet and within the fluidized bed (thermocouples type K), as well as measurements of the gas moisture content. Afterwards, the air enters a calming zone with an inner diameter of 450 mm and is then cleaned by a textile filter with a mean pore size of 7 μm. This filter removes incorporated dust and remaining particles, before the gas can exit the apparatus. After this filtration, the air passes through an exhaust chamber and is blown out.

A two-fluid nozzle (Düsen-Schlick GmbH, type 970/0S4) was installed within the fluidization chamber in top-spray configuration. The nozzle's distance to the bottom plate was chosen to be 150 mm. The coating material was pumped towards this nozzle by a piston valve pump type LDP-31 from Labortechnik-Sewald GmbH and the nozzle's liquid tube orifice diameter was adjusted to

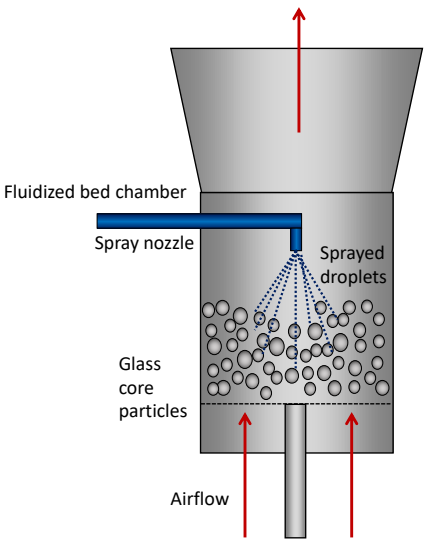

Figure 3.4: Schematic illustration of the fluidized bed coating setup.

be 0.8 mm, with an atomization air pressure of 2 bar. Latter results in a mean droplet diameter of 40 μm (Hampel, 2010). This spray system dispensed the coating material during all experiments. A further description of the entire laboratory scale plant and equipment can be found among others in Rieck (2020).

Chapter 4

Materials and preparation

In the following, the materials used in the experimental parts of the present work are discussed. In order to cover a wide variety of coating substances and corresponding processes that involve these substances, one exemplary coating material for each of the three major classes was chosen. Namely, this means one nanosuspension, one microsuspension and one salt solution.

The coating properties of nanosuspensions are represented by an aqueous mixture of silicon dioxide and titanium dioxide nanoparticles, explained in more detail in Section 4.2.1. The developments during layer build-up featuring microparticles were investigated based on a boron carbide microsuspension, which is described in Section 4.2.2. The characteristics of solution-based coatings and their respective layer build-up were examined by means of sodium benzoate, which is outlined in Section 4.2.3.

4.1 General treatment and material fabrication

Essential material properties of all substances involved in the experimental or simulated in the in silico study, were determined prior to the main investigations. Material properties at the respective conditions were taken from or calculated with correlations of Marrero and Mason (1972), Glück (1991), Poling et al. (2000), Jang et al. (2001) and Lide (2004). In addition to this, manufacturer information was obtained and complementary measurements were conducted. The results of the determination of basic material properties are listed in Appendix C. The properties and measurements that are especially important for the main investigations of this thesis are explained in greater detail in the further course of this chapter.

The suspensions and the solution were prepared using a Sartorius AG scale type FV-120C. The two colloidal substances were afterwards sonicated at 20 kHz and 500 W for five minutes, before each experimental series. For this process, an ultrasound probe consisting of a model U500 sonic dismembrator from Thermo Fisher Scientific company and a 3 mm microtip sonotrode were used. An amplitude of 20 % of the sonotrode tip diameter was set for all treatments. This ultrasound

Table 4.1: Material properties and theoretical volumes of single droplet structures.

Material	Density [kg/m^3]	V_{drop} [μl]	ω_{solid} [wt%]	$V_{s,theo,drop}$ [nl]
SiO_2/TiO_2	2650/4260	1	40	181.6
B_4C	2510	1	5	20.5
NaB	1440	0.1	5	3.5
NaB	1440	1	5	35.2
NaB	1440	0.1	20	14.8
NaB	1440	1	20	147.6
NaB	1440	0.1	30	22.9
NaB	1440	1	30	228.8
$Water$	997	1	–	–
$Ethyleneglycol$	1110	1	–	–

sonication ensures a homogeneous dispersion of particles and breakage of any agglomerates that were potentially formed prior to droplet deposition.

Table 4.1 lists the densities that were set for any involved substances, respectively, as well as the resulting theoretical volumes for one droplet residue structure, according to Equation 2.40. These particular properties and deliberations are used later on to calculate the porosities of the experimentally created structures.

The viscosities of the aqueous suspensions and solution were determined via a rheometer measurement with a rotational rheometer type MCR-502 from Anton Paar GmbH. Surface tensions were measured with a Du Noüy tensiometer. The results are listed in Table 4.2. Three measurements were conducted for each substance and mass fraction, the average was used for all follow-up calculations.

Table 4.2: Measured viscosities and surface tensions of the aqueous coating materials at 25 °C and the solid mass fractions used in the main experimental investigations.

Coating material	ω_{solid}	η[Pa s]	σ[mN m^{-1}]
SiO_2/TiO_2	40 wt%	$42.47 \cdot 10^{-4}$	79.84
B_4C	5 wt%	$14.61 \cdot 10^{-4}$	76.66
NaB	5 wt%	$11.98 \cdot 10^{-4}$	71.35
NaB	20 wt%	$16.24 \cdot 10^{-4}$	57.83
NaB	30 wt%	$26.21 \cdot 10^{-4}$	57.03

4.2 Coating materials and specific pre-treatment

4.2.1 Nanofluid

The nanoparticle experimental series was conducted on the basis of a monodisperse colloidal silica ($Si0_2$) nanosuspension. Such silica nanoparticles have many industrial applications. Among others they are used for anti-reflection coatings, organic dyes or contrast agents in medical imaging. The nanoparticles for the present experimental series were purchased from Sigma-Aldrich in a water-based, suspended and stabilized state. The brand name of this 40 wt% silicon dioxide nanofluid product is Ludox TM40. The therein included nanoparticles are created via a Stöber synthesis and consequently are almost perfectly spherical, with a mean particle size of 22 nm and a very narrow particle size distribution.

While both, the microparticle-based and the crystalline substance require no further preparation, the droplet residues incorporating nanoparticles naturally develop drying-induced instabilities and structural tensions within the deposit. This often results in the formation of cracks followed by fracture of the deposit. As described by Lee and Routh (2004) or Dufresne et al. (2006), this crack phenomenon is reasoned in the relatively high normal stress that is imposed by the interfacial tension, compared to the particle-particle bonds. The initially tested pure silica nanofluid showed both, a radial crack pattern as described by Dufresne et al. (2003), as well as circular crack patterns as described by Jing and Ma (2012). This is illustrated in Figure 4.1.

The drying-induced formation of fractures intensifies with a faster drying process (Maurice et al., 2015) and an increase in solid content (Prosser et al., 2012). At a similar solid content as the other substances that were used in this study, or in other words at around 30 wt%, the initial pure silica nanofluid did not only show crack formation, but entire parts of the residue structures broke apart from the main deposit. In addition to this problem with structural stability, commercial silica nanofluids are negatively charged in order to make the individual particles repel each other. Through this, agglomeration is prevented and the nanosuspension is stabilized. The glass substrate's surface, being an amorphous silica solid itself, is by nature slightly negatively

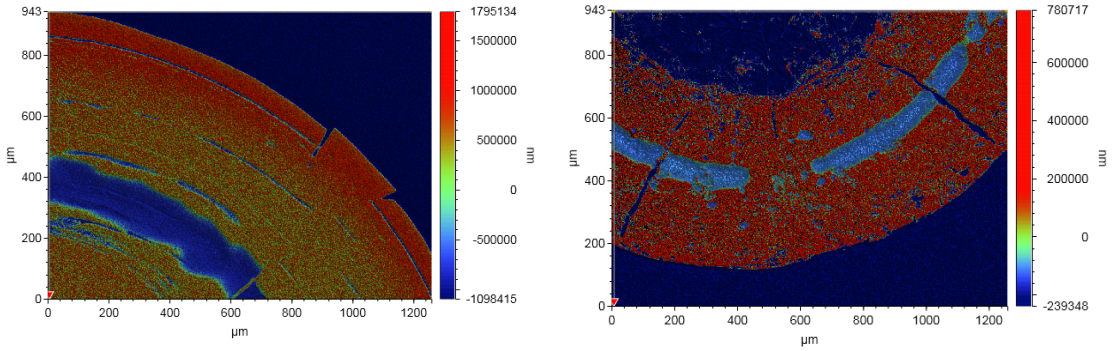

Figure 4.1: Exemplary white-light interferometer scans of radial (left) and circular (right) fracture patterns of silica deposits.

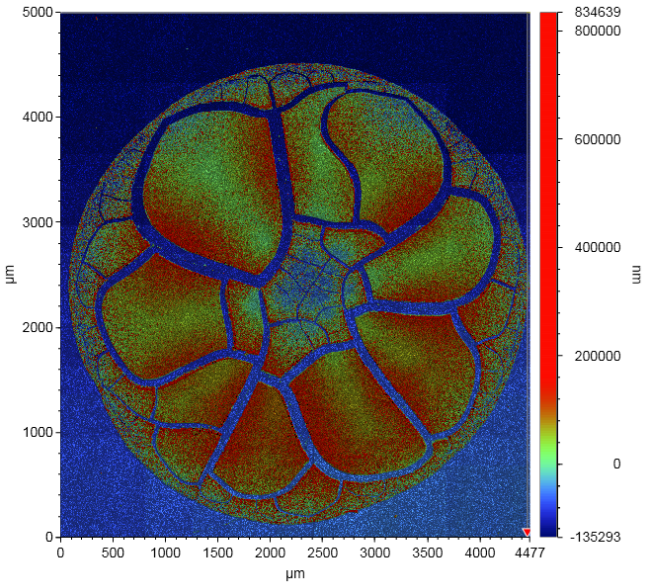

Figure 4.2: White-light interferometer image of a SiO_2/TiO_2 deposit without further dilution or additions, showing strong basin formation.

charged as well. Thus, the nanoparticles and the glass substrate naturally repel each other. This phenomenon caused a relatively loose positioning of the residue on the substrate and subsequently resulted in deposit sliding, similar as reported by Sanyal et al. (2015). In combination with drag forces imposed by forced convection and structural break-up, this combination of effects further led to partial abrasion. Since both, a deceleration of the drying process as well as any significant solid content reduction oppose the purpose of the present investigation, several substances were added in order to stabilize the coating nanomaterial on the substrate and reduce crack formation.

The first augmentation to the silica nanosuspension were titanium dioxide nanoparticles with a corresponding primary particle size of 21nm. These additional nanoparticles were purchased from Merck Chemicals GmbH as Titanium(IV)oxide nanopowder with 99.5 % purity. This supplement slightly improved the adhesion properties of the nanofluid, as described by Widati et al. (2019), but did not prevent the formation of fractures. Rather, the deposits showed strong basin formation.

The entire SiO_2/TiO_2 nanosuspension was then diluted with 99 % pure ethylene glycol from Grüssing GmbH. This ethylene glycol ($C_2H_6O_2$) acts as a plasticizer and proved to enhance stability significantly. The resulting suspension is therefore comprised of 30 wt% SiO_2 nanoparticles, 10 wt% TiO_2 nanoparticles, 10 wt% $C_2H_6O_2$ plasticizer and 50 wt% deionized water as main solvent. After these outlined additions and dilutions, or in other words with this new nanofluid composition, the initially formed solid deposits adhered to the substrate as an undivided whole, without any major cracks within the structure and without any parts of the deposit detaching from the main deposit. Instead, the residues from that point on showed a branched structure as described by Crivoi and Duan (2013b) and Zhong et al. (2015) for copper nanofluid droplets. This morphology will be discussed in more details within Section 6.3. The impact of sample preparation

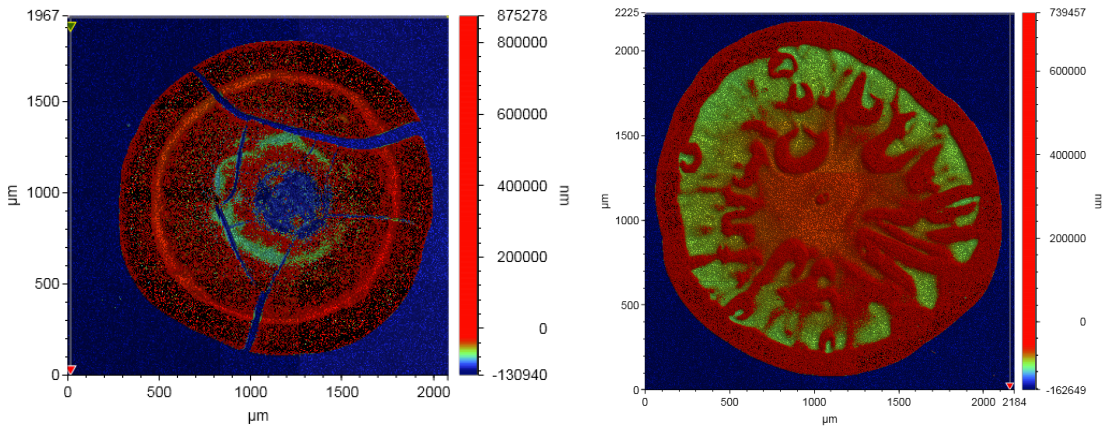

Figure 4.3: Exemplary white-light interferometer images of a silica deposit before sample preparation (left part). Scan of an intact residue of silica and titaniumoxide nanoparticles after pre-treatment (right part).

is illustrated in Figure 4.3, showing an exemplary untreated deposit with fractures and ongoing abrasion (left part), contrasted to an intact branched structure after the additions described above (right part).

For any affiliating analysis, this pre-treatment result indicates that on the one hand, the characteristic morphology and deposition patterns are retained and can be analyzed, on the other hand a calculation of porosity is now feasible, as all solids are retained and remain part of the same structure. Hence, and considering the experimental procedure and analysis described within the subsequent section, this means that a stable layer build-up can be conducted, a convective drying process can be realized without any parts of the structure breaking off due to drag forces and, thus, an ensured calculation of porosity can be done. The persisting effects of a faster drying process and the consecutive addition of solids are discussed in Section 6.3.2.

4.2.2 Microfluid

As exemplary substances for microsuspension behavior during coating, boron carbide (B_4C) microparticles were chosen. Boron carbide is a high hardness ($\geq$ 30 GPa) ceramic material and consequently used mainly in the arms and military industry, for example for bulletproof vests or tank armor (Gray and Mann, 2012). The boron carbide microsuspension was purchased as a dry powder from Artur Glöckler GmbH (brand name B_4C 3000F). It is manufactured through grinding and correspondingly contains disperse, non-spherical particles with a mean particle diameter of 0.8 μm according to the manufacturer. The exact particle size distribution density q_1 and cumulative distribution Q_1 were determined via laser scattering (HORIBA Europe GmbH, Laser scattering particle size distribution analyzer type LA-960) and can be seen in Figure 4.4. Hereby, the respective microfluid was created with deionized water from Merck Chemicals GmbH (conductivity of $< 0.1\,\mu$S/cm), same as for the actual experiments. A sample of the suspension was fed to the particle sizing instrument and analyzed via laser diffraction. This means that laser

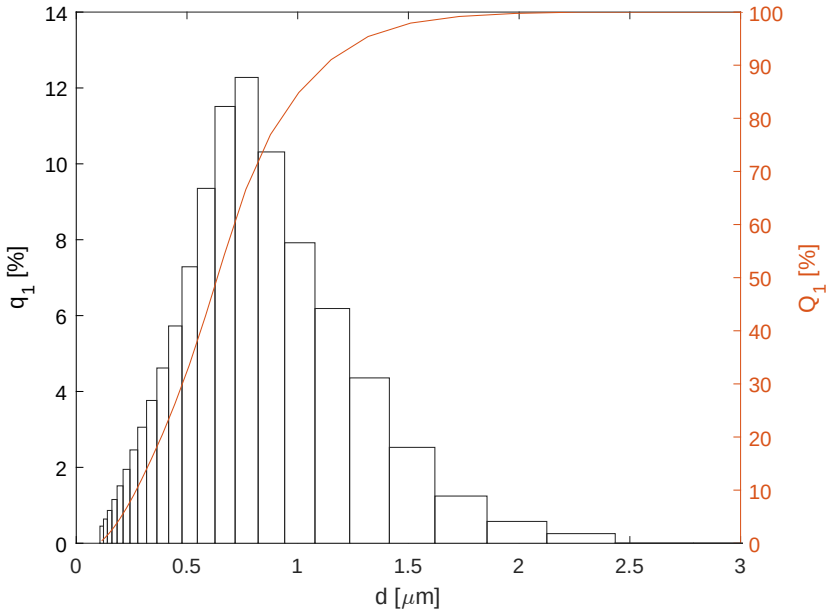

Figure 4.4: Particle size distribution of the boron carbide powder as obtained via laser scattering.

beams are passed through the sample and the angular variation of the intensity of scattered light is measured, as among others reported by Black et al. (1996). The mean particle size was hereby determined to be 0.67 μm with a standard deviation of 0.33 μm.

4.2.3 Solution

Sodium benzoate (NaB) was chosen to create an exemplary salt solution. NaB is the sodium salt of benzoic acid ($C_7H_5NaO_2$), and mainly used as an anti-fouling, or in other words anti-microbial additive in the food (additive number E211) and pharmaceutical industry (Yadav et al., 2016). It is a natural ingredient in many fruits and vegetables and is produced industrially through neutralization of sodium hydroxide with benzoic acid. When dried, sodium benzoate solutions form needle-shaped crystal structures with a typical length of circa $2-4\,\mu$m (Butterhof et al., 2012). It is strongly hygroscopic and has a high solubility in water. The dry, white salt powder was purchased from Merck Chemicals GmbH (brand name BIOXTRA) at 99.5 wt% purity. The corresponding solution was produced with deionized water (same as for the microsuspension). The NaB solution's saturation concentration at room temperature (21 °C) was determined to be circa 40 wt%.

4.3 Substrates

4.3.1 Glas plates for sessile droplet drying

20 mm × 20 mm × 1 mm borosilicate glass slides were used as substrates for the sessile droplet application. Borosilicate glass was chosen, because it features a relatively smooth surface, is almost completely non-porous and inert. In addition to this, its low refractive index facilitates both the

in situ observation during the drying process as well as the subsequent white-light interferometer measurements.

The deposition process was preceded by a thorough isopropanol cleaning of the glass slides for sodium benzoate and boron carbide, and an additional sulfuric acid (H_2SO_4, 96 wt%) cleaning for colloidal silica. Latter results in a glass surface that is slightly positively charged, which helps with silica deposit stability (Lee et al., 2007).

Each substance's contact angle on these pre-treated borosilicate glass slides was experimentally measured prior to the main experimental series. As described in Section 2.1.1, both advancing and receding contact angle and with this also the contact angle hysteresis can be obtained in order to characterize the wetting behavior of a sessile droplet. However, for droplet deposition as well as subsequent drying and structure formation, the advancing contact angle, id est the angle the droplet obtains after the wetting stage and with which it starts its drying process, is of far greater importance. In addition to this, the receding contact angle is likely not reached in the drying processes of the main experimental series, since solids are incorporated and accumulating along the contact line. In comparison with the advancing angle's value, the value of the receding contact angle thus plays a subordinate role and is furthermore far more error-prone in the experiment, especially for materials with incorporated solids. This is due to first solid accumulations taking place at the surface and contact line during the liquid addition stage, which results in an alteration of the surface-droplet interactions during the liquid removal stage. Consequently, determination of the receding contact angle was not the focus of the present contact angle measurement series and the corresponding data must be handled with this in mind. For all systems, the integer average of three contact angle measurements was later used for calculation of the application area diameter (Section 5.1.1). The results for pure water were set as parameters for the simulation of drying droplets in Section 9.

A dynamic, sessile drop contact angle measuring method similar as reported by Yuan and Lee (2013) was conducted. For this procedure, an OCA25 contact angle measuring system from Dataphysics GmbH was utilized. In the course of the experiment a droplet was deposited onto the borosilicate glass plates. The droplet dispenser, a 100 μl syringe from Hamilton Company, was left within the droplet (Figure 4.5, left part). After the initial deposition, additional liquid is added to the droplet. Afterwards, this liquid is retracted. Hereby, the droplet is constantly monitored via a CCD camera and the formed contact angle is obtained optically via a grayscale matching and a correspondingly fitted tangent which is placed on the droplet's edge (Figure 4.5, right part). The initial droplet volume was set to 1 μl and the dosing speed was chosen to be 0.1 μl/s. Both values were kept constant over the course of all experiments. The measuring system automatically adjusts the time for liquid addition and retraction, until the three phase line is clearly moving and in turn, a clear advancing or receding angle can be made out. This resulted in measurement times between 120 to 180 seconds, with an optical input of the CCD camera of ten frames per second.

During the present experimental series, it was found that the sodium benzoate solution's contact angle depends on the solid mass fraction to a certain extent. Therefore, the experiments were

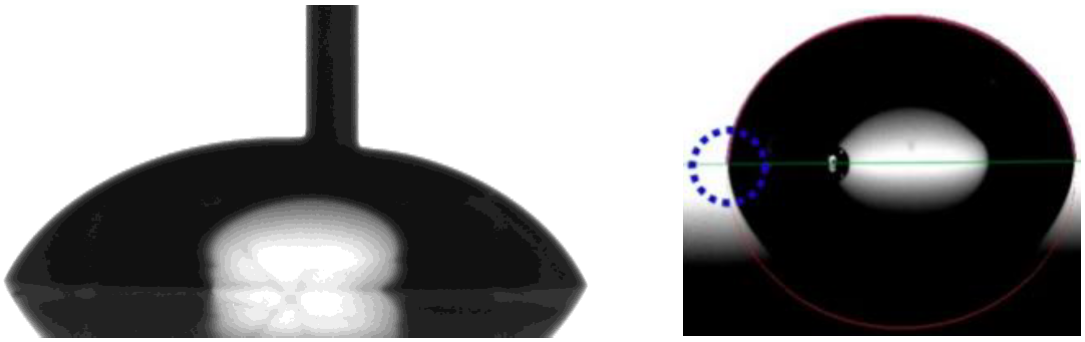

Figure 4.5: Working principle of a dynamic contact angle measurement via sessile droplet method.

conducted for every solid content used in the main experimental study. The slight dependency of contact angles on ambient conditions was neglected, meaning that the up- and down-titration of the droplets' volume was always done at atmospheric conditions. Table 4.3 lists the measured contact angles on borosilicate glass for the different materials and corresponding solid mass fractions, respectively. Corresponding data sets of the contact angle measurements over time are given in Appendix C.8. The general data accuracy and consistency for contact angles on the utilized pre-cleaned glass slides can be rated as good. However, signs of stick-slip behavior resulting in CA outliers could be observed frequently.

Table 4.3: Contact angles of the three exemplary substances on borosilicate glass at different solid mass fractions.

Material	ω_{solid} [wt%]	θ [°]
H_2O	–	72.1 ± 1.5
SiO_2/TiO_2	40	48.3 ± 1.6
B_4C	5	36.9 ± 1.9
NaB	5	60.3 ± 1.3
NaB	20	58.1 ± 1.2
NaB	30	56.9 ± 1.5

4.3.2 Glas particles for fluidized bed coating

The fluidized bed coating experiments were performed with non-porous borosilicate glass beads from Sigmund Lindner GmbH. The particles obtain a mean diameter of 0.75 – 1.0 mm, with a standard deviation of 0.058 mm and a sphericity of 0.8. The particle density was 2400 kg/m^3. The glass particles' surface is very homogeneous and smooth, which is why they are usually used as grinding and dispersing material (Sondej, 2019).

Chapter 5

Experimental methods and ex-situ analysis

The experimental methods and procedures that were conducted and applied in the framework of this dissertation are described in the present chapter. This includes the procedures executed as part of the experiments themselves, or in other words used within the laboratory setups described in Chapter 3, as well as the structural and morphological analysis and the image processing that was conducted in order to obtain the desired data from the created structures and collected samples.

5.1 Sessile droplet drying

5.1.1 Deposition procedure

The droplet deposition takes place within a small circular area inside the drying chamber. This area's diameter was established for each substance, respectively, to be 2.25 times the contact diameter of a corresponding sessile droplet. The individual sessile droplet contact diameters for all substances were determined prior to the experiments, as described in Section 4.1, and the geometry relation for droplets not distorted by gravity from Clarke et al. (2002) (Equation 2.2) was used to calculate the corresponding diameters. The results for all substances, corresponding solid mass fractions and droplet sizes used in the experimental series in Chapters 6 and 7 are listed in Table 5.1. The solid content is hereby essential, as it influences the specific contact angle and therefore the geometry, as shown in Table 4.3.

A self-developed algorithm simulating a random positioning determines the deposition procedure, or in other words, the droplets' feasible positions within the calculated, predefined application area for one layer. Hereby, the droplets were not allowed to extend over the domain boundary. For the remaining positions within the area, 20 % of the droplet diameter was set as a maximum overlap constraint. An individual layer is declared as finished when no more droplets can be fitted onto the area without violating these aforementioned constraints. The limited application area hereby

Table 5.1: Droplet footprint and resulting deposition area in dependence of material and droplet size.

Material	ω_{solid} [wt%]	V_{drop} [μl]	d_{drop} [μm]	d_{area} [μm]
SiO_2/TiO_2	40	1.0	2200	4950
B_4C	5	1.0	2450	5513
NaB	5	0.1	926	2084
NaB	5	1.0	1995	4489
NaB	20	0.1	941	2117
NaB	20	1.0	2028	4563
NaB	30	0.1	949	2135
NaB	30	1.0	2044	4599

reduces the number of droplets required to mimic a small layer by eliminating the possibility of two droplets being positioned with too much distance to each other, or in other words, without notable interaction. The moderate overlap constraint on the other hand forces a distribution of the droplets in the available area, which in turn promotes the formation of small layers instead of centralized piles. The random placements are handled by generating random numbers for each position's distance from the center ($0 - 0.5\,[d_{area} - d_{drop}]$) and angle ($0° - 360°$). The first is hereby always restricted to a corresponding maximum value, in order to comply with the individual application area of each series.

For the first droplet there is no possibility of invalid overlap. Consequently, its generated position is always feasible and thus, can always be virtually occupied. After this first random position within the application area has been established, a follow-up position is created and tested for feasibility. If this second set of coordinates is viable as well, meaning it has no invalid overlap with the priorly established position, the respective droplet virtually gets placed. Its coordinates then are added to the maximum overlap condition, to be met by all positions that are tested afterwards. However, if the position is not viable, it is deleted instead. This procedure of creating and testing of random positions is then continued further, until one million follow-up coordinate sets have been created and tested for feasibility, one after another.

After the test of all generated follow-up positions is completed and the respective feasible coordinates have been identified, the first layer is declared as finished. The next layer is then generated, following a new individual pattern in the same area, calculated according to the same algorithm. In Figure 5.1 an example of such a positioning pattern for one virtual layer can be viewed. Over the course of the entirety of build-up experiments, three layers were applied within the same area, which means that the entire procedure was executed three times for every conducted experiment. The number of droplets within each layer however varies, depending on the randomly determined positions. After the three virtual layers had been created, the corresponding experiment and analysis were executed. The positioning procedure and the corresponding algorithm are also explained in Janocha and Tsotsas (2021b). The resulting droplet numbers within each experiment or rather

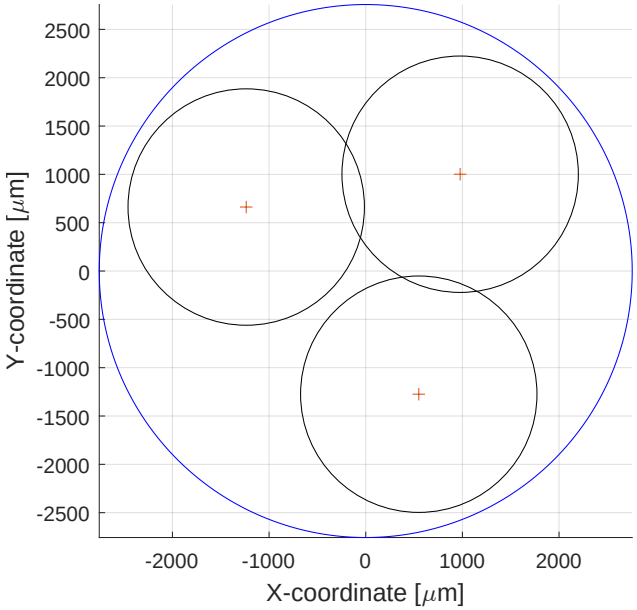

Figure 5.1: Example of a positioning pattern for one layer of SiO_2/TiO_2 droplets (1μl). Three viable positions were identified by the pseudo-random positioning algorithm for this case.

each layer are listed in Tables 6.2 and 7.1.

5.1.2 Fabrication of small coating layers

After the positions for all layers have been calculated via the algorithm, the droplets are manually deposited and subsequently dried one after the other. The average drying airflow velocity U_a as well as the drying airflow's inlet temperature T_a were varied throughout the experimental series, though constant during each experiment. Through this procedure small coating layers could be incrementally manufactured and the respective build-up monitored.

5.2 Fluidized bed coating

During the fluidized bed coating experiments, the fluidized bed chamber's inlet air velocity and temperature were set to match the associated conditions of the sessile droplet drying chamber (U_a and T_a). Same goes for the droplets' solid content. Other process conditions, such as bed mass, spray rate and process time, were kept constant throughout the experiments. Samples were taken after 15, 20 and 60 minutes, respectively. With this, layer build-up as well as resulting layers could be analyzed.

5.3 Morphological and structural analysis

Analysis of solid residues and coating structures created with deposited droplets as well as those manufactured within the fluidized bed was performed ex-situ, with three high-resolution, non-

destructive methods. Each of these methods has its own working principle, as well as corresponding strengths, weaknesses and application areas, which are described in the following. The ultimate aim of this morphological and structural analysis was to develop a strategy that would enable the structures of the deposits to be systematically recorded and characterized.

5.3.1 White-light interferometry

White-light interferometry (WLI) is a versatile and non-destructive optical tool for acquisition of surface structure and topographical data. WLI as a surface capturing method was first utilized for the measurement of sessile droplet residues by Dam and Kuerten (2008). Other examples for studies including a characterization of sessile droplet residues with white-light interferometry are the studies of Dugyala and Basavaraj (2014) and Sondej et al. (2018). The optical method is contactless and therefore preserves the sample's integrity. This not only allows for repetitive scans of the same structure to be conducted, in order to reduce errors, but most importantly allows for a continuation of the experiment with the same, unaltered structure afterwards, which is essential for the present experimental study. A disadvantage, however, is that the internal structure such as pores or the like is not recorded.

The colloidal droplets in the present experimental investigation are applied and subsequently dried in a droplet-by-droplet manner. After the addition of each new solid residue via an additional droplet, the entire structure was scanned by means of a white-light interferometer type Contour GT K0G from Bruker Corporation and the corresponding control and analysis software Vision64. This kind of microscope emits broadband white light with a short coherence length through a collimating lens onto a beam splitter, id est a partially reflecting mirror. By means of this mirror, the light is splitted to follow two paths. One path leads to a flat reference mirror, the other part of the light is directed onto the sample structure. The reference mirror inside the interferometer is hereby adjusted to be in the same focal plane as the sample, or in other words to have the same distance to the beam splitter as the sample's base. The reflected light from both surfaces is afterwards recombined within a CCD camera sensor. On the way back, the two parts of the beam overlap and form an interference pattern. The two beams' interference difference is then used to obtain height data of the sample surface and thereby create a three-dimensional (3-D) image of the sample, including its summits and indentations. The functional principle of the WLI is therefore based on the coherent superimposition of reference waves generated by the light source with object waves reflected by the sample. Figure 5.2 illustrates the working principle of such a white-light interferometer.

The used interferometer Contour GT K0G features several working modes with different measurement speeds and accuracies. Vertical scanning interferometry (VSI) mode was chosen, as a compromise between sufficient vertical resolution, enough vertical range and acceptable measurement time. In this mode, the interferometer scans the structure's surface with a 10 nm vertical and 0.38 μm lateral resolution. Hereby, the WLI lens is moved vertically in order to take a complete scan of the surface profile in a rectangular section. This procedure works incrementally, by as-

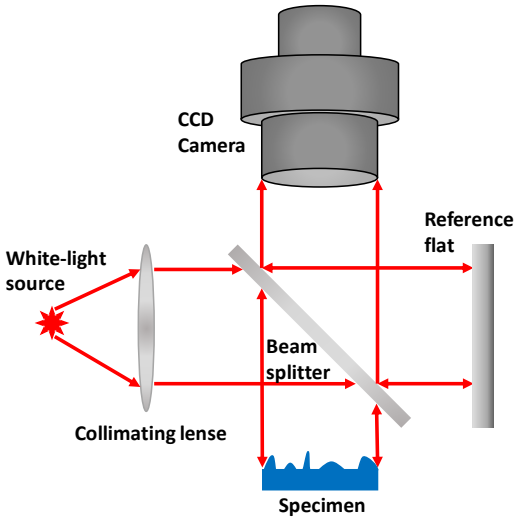

Figure 5.2: Working principle of a white-light interferometer.

signing a specific height for every pixel and thus creating a three-dimensional height profile of the residue's section. As described above, and as described in more detail by Groot and Deck (1995), the height data of the solid structure in such a section is obtained through optical path differences. Through a stitching-like method with overlapping edge scans, the obtained images of the sample's sections are put together, creating a three-dimensional profile of the entire sample. This scan procedure is schematically illustrated in the left part of Figure 5.3. Each scan's framework is controlled and its parameters can be adjusted via the incorporated software Vision64. Important parameters hereby are the vertical distance to be scanned, the handling procedure for dead pixels (due to unexpected reflection phenomena) and the threshold for height values to be included into the profile (signal-to-noise level). The first parameter naturally has to be adjusted depending on the size of the sample structure. The latter two were adjusted manually for every sample to obtain a consistent height profile without indeterminate regions. A rescan of dead pixels combined with a threshold of $1 - 3\,\%$ hereby proved to provide good results for most samples. Rescans were done with a lower than standard intensity for sodium benzoate, which is highly reflective, and with a higher than standard intensity for SiO_2/TiO_2 and B_4C, whose surfaces are not that reflective. It shall however be noted that such a redundant scan method greatly increases the measurement time and is therefore only suited for relatively small samples as the ones investigated in the present dissertation, and not feasible for scanning of larger surfaces. The corresponding right part of Figure 5.3 shows an exemplary profile of a solitary sodium benzoate ring structure obtained via the used white-light interferometer with the described parameters and scan method. Resulting measurement times were between 30 to 90 minutes.

This enables both, an analysis of residue morphology and the calculation of the enclosed volume V_{total} of the observed deposit, as reported by Sondej et al. (2018) for solitary ring structures. Hereby, this total volume is obtained through surface integration of the corresponding height data

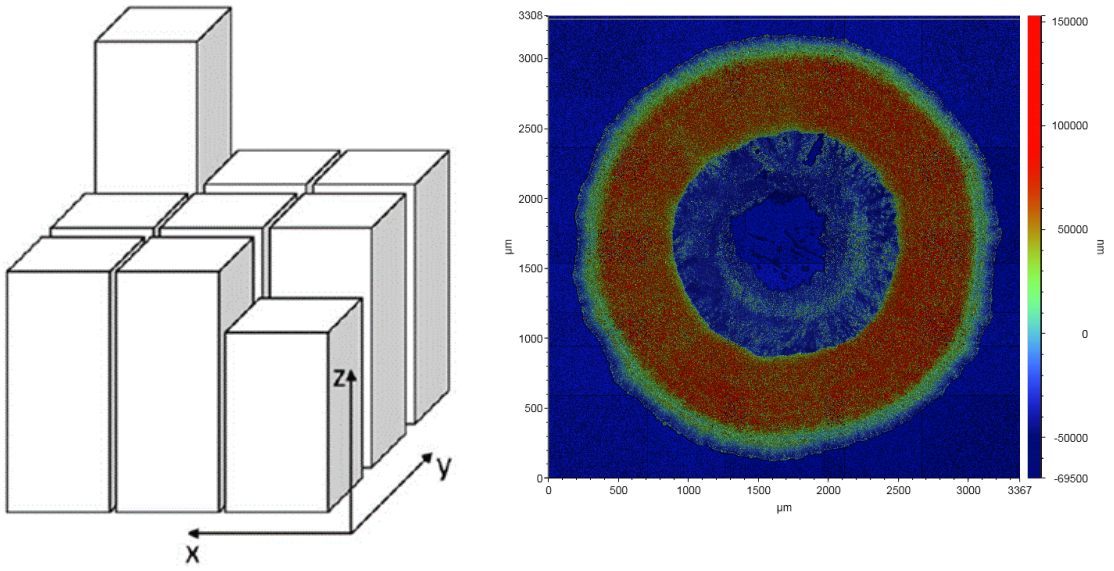

Figure 5.3: White-light interferometer scan schematics (left part) and exemplary scan of the NaB residue structure of one sessile droplet (right part).

and size of each pixel j:

$$V_{total} = \sum \Delta X_j \Delta Y_j \Delta Z_j. \tag{5.1}$$

The lateral size $(\Delta X, \Delta Y)$ of each pixel depends on the individual zoom settings and the used lens. Therefore, it varies between scans. One obstacle in the calculation of the structural volume is the definition of the substrate's height ($Z = 0$). Each scan's reference substrate height was calculated individually by averaging the minimum values of each column of the acquired height-data matrix. As white-light interferometry obtains height values through each point's distance to a reference mirror, small irregularities in the glass plate's flatness or a general tilt of the sample on the microscope's table, meaning a deviation from the horizontal, can change this height profile. Especially latter proved to be a phenomenon that can disturbingly influence the results. In order to address this issue, the average of three measurements was taken for each structure. For each of these measurements the tilt of the microscope's table was manually adjusted, trying to be as horizontal as possible each time. Herewith, this problem is converted into a random error and thus can be countered by repetition.

Since the number of droplets, the droplet volume and the droplets' solid content are priorly known, the theoretical solid volume (calculated with Equation 2.40) and the enclosed volume of the structure can be determined at each point of the droplet-by-droplet build-up process. The corresponding porosity can subsequently be calculated with Equation 2.41 after each droplet addition. The development of porosity over the course of layer build-up can thus be monitored.

To assess the accuracy of WLI measurements with the chosen scan parameters described above, specifically for the present application of sessile deposit volume determination, repeated scans of several sample structures were conducted. The results of the test of this method are listed in Appendix B.3. After this test the present white-light interferometer was deemed sufficiently accurate in order to analyze residues of all materials and both low volume as well as high volume solid structures, with a maximum relative standard deviation of circa 10 %.

5.3.2 X-ray micro-computed tomography

X-ray micro-computed tomography (μ-CT) is a non-destructive method that creates cross-sections of a physical object and with this can be used to reconstruct a virtual, three-dimensional model. Historically, it was first used as a medical application. Farber et al. (2003) however presented uses for the analysis of other porous structures in particle technology. In the following, it was mostly used for quality control of pharmaceutical products (Schomberg et al., 2021). For example Tokudome et al. (2009) used μ-CT measurements to assess pills regarding integrity, layer thickness and homogeneity. Examples for works in the field of scientific research have been provided by, among others, Perfetti et al. (2010), who quantified coating layer morphologies via μ-CT scans, or Dadkhah et al. (2012), who investigated the inner structure of agglomerates produced within a fluidized bed. The main advantage over white-light interferometry is the visualization of inner structure, including for example the cavities influencing porosity. Among its disadvantages, however, is the greatly increased measurement effort, which is the reason why white-light interferometry has been preferred regarding the accompanying droplet-by-droplet analyses.

In the present dissertation, the layer porosity of particles coated in the fluidized bed experiments was measured with an X-ray micro-computed tomograph type CT-ALPHA 2000 from ProCon X-ray GmbH. The general working principle of this tomograph is schematically illustrated in Figure 5.4. For the measurements, the particles were placed on a polyvinyl chloride (PVC) sample holder and positioned between an X-ray source (maximally 160 kV) and a $120 \times 120\,\mathrm{mm}^2$ detector (Hamatsu, type C7942Sk-25). The X-ray source emits a conical beam of radiation which penetrates the sample to a degree that depends on the absorption capacity of the material (Sun, 2014). The unabsorbed residual radiation is recorded by the detector and converted into a two-dimensional (2-D) grayscale image. The X-ray source was operated at 50 kV and 100 μA. In the course of the measurement, the sample was rotated stepwise and X-ray intensity after permeation was determined by the detector after every step. Similar as reported by Dadkhah et al. (2012), randomly selected particles were completely scanned (360°) in 1600 rotational steps and an exposure time of 1 s per step. For each step, three intensity profiles were obtained. The respective first profile was discarded and the other two were averaged. This procedure reduces the influence of background noise and counteracts small movements of the sample on the movable PVC sample holder. Based on the obtained averaged intensity profiles for each rotation step, 1600 two-dimensional images of one particle and its surroundings were calculated. A three-dimensional model was then constructed for each particle from the corresponding stack of 2-D images.

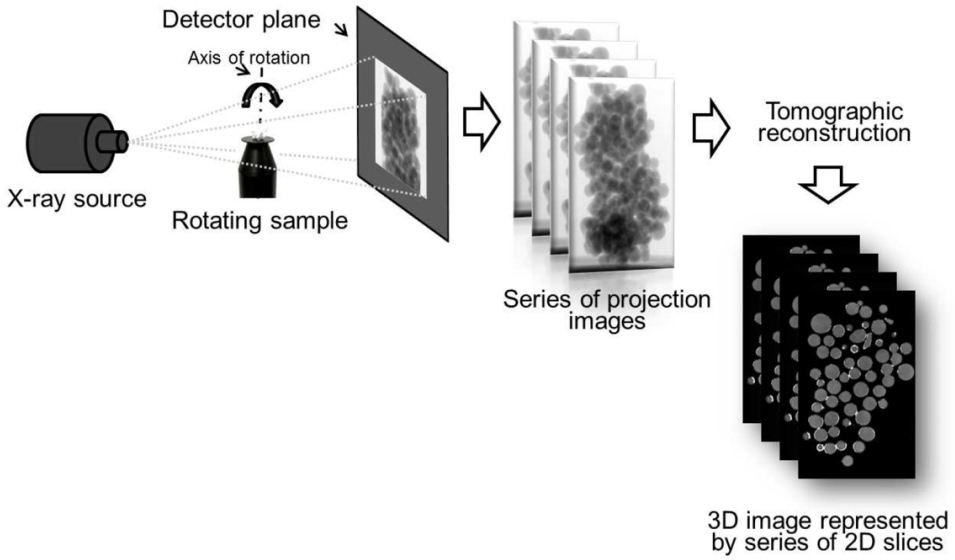

Figure 5.4: General working principle of X-ray micro-computed tomography (Dadkhah, 2014).

The measurements were controlled via the software Volex 2.0 from Fraunhofer Institute for Integrated Circuits (Erlangen, Germany), and took approximately 1.5 hours, respectively. Before each measurement, a warm-up procedure was carried out, including a test and adjustment of all related control parameters and an adjustment of the X-ray filament. After this preparation, measurements were conducted for three particles from each sample and their average was taken for the respective porosity value. In order to further facilitate good measurement results, or in other words accurately measured porosities, also a suitable distance from sample holder to detector had to be found for each sample. In the course of the measurements, a sample distance of 660 mm and a voxel size of 64 μm^3 were determined to be suitable in almost all cases.

After the physical image acquisition process, the coating shell image was separated from the core particle section through binarization. For this, the image processing software MAVI from Fraunhofer Institute for Technical and Industrial Mathematics (Kaiserslautern, Germany) was used. The entire procedure consisted of: Cropping of the 3-D image to cut off non-relevant surrounding areas, application of a median filter to reduce background noise, final binarization. Via an Otsu method, the binarization threshold was selected in a way that well seperated the coating material (white voxels) from the core substance and the surroundings (black voxels). Hence, this procedure provided the solid volume of the coating layer, corresponding to $V_{s,theo}$. Afterwards, a closing operator within the same software framework was used to fill structural cavities. Through this operator a filled structural volume was obtained (corresponding to $V_{s,tot}$) and the coating layer porosity could be calculated according to Equation 2.41. The measurement and subsequent image processing parameters are summarized in Table 5.2, the image processing procedure is visualized in Figure 5.5.

In addition to the calculation of layer porosity from FBC particles, X-ray micro-computed to-

Table 5.2: μ-CT measurement and image processing parameters.

Parameter	Value
Control software	Volex 2.0
Rotation	360°
Rotation steps	1600
Skip	1 image
Averaging	2 images
Voltage	50 kV
Current	100 μA
Energy	5 W
Exposure time	1 s
Detector distance	660 mm
Voxel length	4 μm
Voxel size	64 μm^3
Measurement time	4800 s
Image processing software	MAVI
Filter	Median filter
Threshold	Otsu based
Closing operator	1000 μm^3 cube

mography was used for further visualization of structural morphology of sessile droplet residues. Complementary measurements of selected samples were conducted especially for the in-depth investigation in Chapter 7. The specific measurement parameters in these cases strongly varied due to the major differences in size and morphology of the sessile droplet residues. However, and in contrast to the analysis of FBC results, in case of sessile droplet residues μ-CT was just used for visualization purposes and not for porosity calculation. Herein, the μ-CT gives insight into the internal layer structure that is forming in different drying and positioning cases. Thus, there is no risk of a strong variation of measurement parameters having affected any quantitatively determined results.

5.3.3 Scanning electron microscopy

Further visualizations of layers created through fluidized bed coating were conducted via scanning electron microscopy (SEM). This imaging procedure does not incorporate a visualization of inner structure, but depicts the coating's surface in more detail as the mainly used X-ray micro-computed tomography. Furthermore, it can visualize small structural details on the particles' surface, which proved to be difficult to execute with the μ-CT, due to the naturally present noise-disturbances that accompany an X-ray radiation based method.

SEM images are produced by scanning a sample's surface with a focused electron beam. Interactions of this beam with atoms on the sample's surface result in different reflected signals that are

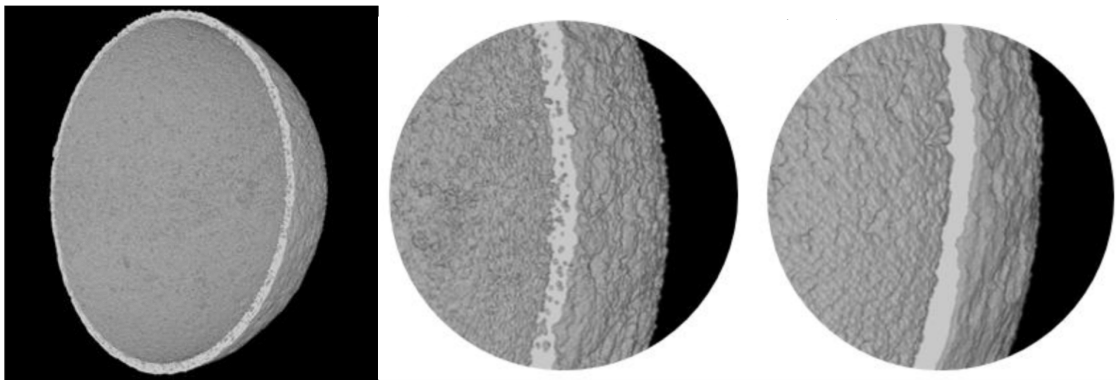

(a) Binarization **(b)** Seperated porous shell **(c)** Closed shell

Figure 5.5: Illustration of results of the image processing procedure after μ-CT measurements as described by Sondej (2019).

used to compose an image of the surface topography in that region. Multiple scans are conducted in a raster pattern, in order to acquire an image of the entire particle. Through different foci, different details on the surface of a sample can be emphasized. A scanning electron microscope type Phenom G2-Pro from Phenom-World BV was utilized for all scans incorporated in the present project. Each original image was taken at a resolution of 1024×1024 pixels and a voltage of 10 kV. Prior to the image acquisition, the samples were put under vacuum and coated with a thin layer of gold, making the entire sample surface a conductor, thereby preventing charge accumulation and increasing contrast, as described by Dewettinck et al. (1998). The images covered a sample that contained around ten particles. Solitary, clearly visible particles were chosen to be put in greater focus for further analysis of coating structure, coating surface topology and morphological details of the surface. Hereby, a maximum magnification of 12,000 times was used. The entire scanning procedure was similar as described by Hede et al. (2008) and Rieck et al. (2015).

5.4 Interim conclusion

An experimental setup in which the incremental layer build-up from dried deposited droplets can be conducted droplet-by-droplet under controlled environmental conditions was compiled and designed. Pre-treatment strategies for all coating materials were developed and a corresponding characterization of the involved substances was undertaken. Furthermore, a stochastic algorithm was developed to handle pseudo-random placement of droplets during the sessile droplet experiments. With this algorithm, the creation of small coating layers can be mimicked and analyzed.

A strategy for systematic structural investigation was established. Therein, white-light interferometry was chosen as the measurement method for a droplet-by-droplet monitoring of structure formation from deposited droplets. In addition to this established main analysis strategy, complementary measurements have been conducted with μ-CT for inner structure visualization purposes.

In order to contrast the coating layers originating from sessile droplets under associated conditions with industrial processes, a suitable fluidized bed plant was chosen for exemplary comparative

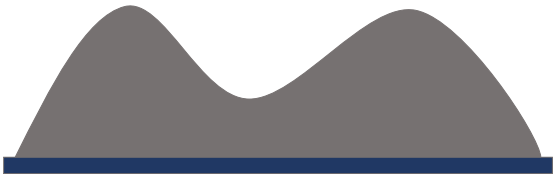

(a) Structural volume as determined via WLI

(b) Solid volume as determined via μ-CT

(c) Structural volume as determined via μ-CT

Figure 5.6: Principal differences of the structural volumina determined via white-light interferometry and X-ray micro-computed tomography, affecting the porosities calculated in turn.

coating experiments. The layers resulting from fluidized bed coating were analyzed via X-ray micro-computed tomography and scanning electron microscopy regarding morphology and porosity.

After the separate analyses of layers created via sessile droplet deposition as well as fluidized bed coating, the resulting structures of these two processes can be compared. In addition to many distinct physical differences that will be discussed later on, at this point it shall be noted, that porosity values which are obtained by WLI (conducted for SDD) and μ-CT (conducted for FBC) are also methodically not exactly the same. Since white-light interferometry does not ascertain inner structure, the obtained volume covers the entire deposit including all pores and all cavities no matter the size. Calculation of porosity is subsequently done with the theoretical solid volume as determined through the number of involved droplets and their respective solid mass content (as described in Section 2.2). The μ-CT however does not yield the overall volume of the structure, but the actual solid volume instead. The closing operator used to determine the structural volume, and with this the porosity, does integrate small pores, but does not include larger cavities. This principal difference is illustrated in Figure 5.6. The porosity calculated for sessile droplets through results of the WLI measurements therefore methodically includes sizeable cavities, while the shell porosity determined from μ-CT measurements for particles coated within the fluidized bed resembles a

porosity excluding such large cavities. Further distinctions regarding porosity determination by these two methods were done by Sondej (2019).

Chapter 6

Experimental investigation of layer build-up from dried deposited droplets

In this chapter, an experimental series featuring layer build-up from dried deposited droplets is presented. The experiments were conducted within the laboratory setup described in Section 3.1, following the methods explained in Section 5.1. The respective analysis was conducted featuring the imaging methods elucidated in Section 5.3. This chapter is an extended version of the experimental publications Janocha and Tsotsas (2021b) and Janocha and Tsotsas (2022). The respective study on sessile droplets is designed to fundamentally improve the understanding of layer build-up from dried, solid-laden droplets in order to explore industrial coating processes, for example within a fluidized bed, in more depth, and with this improve the ability to optimize these processes based on the new knowledge.

6.1 General preliminary deliberations and calculations

The experiments were carried out with the three exemplary materials outlined in Chapter 4. The structures resulting from the three respective experimental series were analyzed in a droplet-by-droplet manner. Evidently, such an in-depth analysis of a relatively small number of applied droplets shows somewhat unique morphologies and porosities for every experiment. This is due to the slightly varying droplet deposition patterns due to natural variations in single deposit morphology caused by small variations in shape and size of the involved particles, as well as the individual positioning of every droplet. In combination, these phenomena henceforth lead to the development of a different structure. This of course means that a comparison of the experiments described hereafter has to be handled carefully and therefore stands in contrast to the subsequent analysis of fluidized bed coating layers in Chapter 8, where a structure consisting of a far greater number of droplets is analyzed, less attention is paid to small structural details, and the effect of an individual droplet is thus negligible. However, despite the undeniable uniqueness of every created structure, common characteristics regarding both morphology and porosity as well as

Table 6.1: Maximum capillary, Reynolds and Péclet numbers for the present sessile droplet drying experiments, or in other words the materials' solid content and contact angle.

Material	ω_{solid} [wt%]	d_{drop} [μm]	Ca_{max}	$Re_{drop,max}$	Pe_{max}
SiO_2/TiO_2	40	2200	$3.52 \cdot 10^{-4}$	214	141
B_4C	5	2450	$3.67 \cdot 10^{-4}$	238	157
NaB	30	2044	$4.93 \cdot 10^{-4}$	198	130

their respective development over time were found for every material. These similarities and corresponding differences are discussed and compared hereafter.

Each experiment's first deposited droplet results in a solitary residue that lays the foundation for any structure formation follow-up. The spreading and wetting behavior of the droplets herein conforms to the description of Picknett and Bexon (1977) for partially wetting surfaces, or in other words a contact angle of less than 90°. The respective spatial dimensions of the droplets created in both the present and the subsequent experimental investigation as well as the simulative study are listed in Appendix D.1. The droplet volumes that were chosen for the present experimental series (1 μl, together with the chosen maximum airflow velocity of 1.5 m/s), result in a maximum Bond-number of 0.0486 (Equation 2.1) and a maximum capillary number of $4.93 \cdot 10^{-4}$ (Equation 2.24). This means that all droplets investigated over the course of this thesis take the shape of a perfect spherical cap and are not distorted by gravity or convective drag forces (Lubarda and Talke, 2011). Furthermore, the droplets were observed to dry in a constant contact radius mode as described by Schönfeld et al. (2008) or Perdana et al. (2011).

At the combination of highest airflow velocity (1.5 m/s), highest droplet volume (1 μl) and lowest temperature (21 °C), the selection of drying parameters results in the maximum Reynolds numbers that are listed in Table 6.1, defined with sessile droplet contact diameter (Equation 2.27, with properties from Appendix C, and the contact diameters in Table 4.3). At the greatest contact angle (B_4C), this results in a maximum Reynolds number of 238. Since this value is still below the critical Reynolds number for flow around spherical-cap shaped objects (Mikulencak and Morris, 2004), this means that all experiments took place in a laminar regime.

The systems characteristic Schmidt numbers can be calculated to be $Sc_{21°C} = 0.66$, $Sc_{50°C} = 0.61$ and $Sc_{75°C} = 0.53$, respectively. This in turn results in the characteristic maximum Péclet numbers ($U_a = 1.5$ m/s and $T_a = 21$ °C) which are listed in Table 6.1 as well.

As the droplets are deposited onto a partially wetting substrate and drying in CCR mode, the droplets' initial residues thus form variants of the associated ring-structures that were described among others by Deegan et al. (2000) and Hu and Larson (2002). Recordings of the progression of such a ring formation process taken by the installed top-view camera are shown in Appendix D.2, Figure D.1. It can be seen that crust formation starts along the contact line and then proceeds inwards while forming a spanning, annular structure. Herein already, one can see the importance of drying conditions, as they determine the drying rate and with this the speed with which the liquid

and incorporated solids are transported towards the liquid-gas interface, where crust formation starts. The overlap limitations in one layer, as prescribed by the positioning algorithm, additionally cause the follow-up droplets within the first layer to show a behavior similar to the solitary ones. As described in Section 2.7, the focus of this study is laid on layer build-up rather than on solitary droplet residues, as the latter have already attracted much attention in literature (Erbil (2012), Nguyen et al. (2017)). Nevertheless, the initial droplets and residues of each experiment provide the basis for any further structural formation, and their morphology and porosity are therefore essential for every further development. These initial deposits of each substance will therefore be discussed first, before the respective build-up and development are analyzed. Besides, due to the uniqueness of all further arising structures, solitary droplet residues are the only ones that are directly reproducible and therefore can be used to broadly assess the repeatability as well as the error margin of the obtained porosities.

Once the initial residues are discussed, the further development can be investigated and common and characteristic phenomena that occurred with different materials during the incremental layer build-up can be investigated. Since only neglectable interactions occur in the first layer, due to the limited overlap prescribed by the positioning algorithm (more details can be found in Section 7.2), follow-up investigation droplets (second and third layer) were deposited onto a set of one or more already existing, more or less pronounced ring-like structures placed next to each other on the glass substrate. Same as for the first layer, the follow-up deposition is controlled by the algorithm described in Section 5.1.1. Despite this same procedure, the positions of droplets in the first and second layer can differ from the originally determined one, as droplets may be pulled towards another pre-existing structure due to enhanced adhesion forces between existing residue and droplet, compared to droplet and substrate. Hence, the spreading stage as well as the finally obtained shape of such droplets may differ significantly from the first layer. In consequence, the layer morphology and build-up also strongly depend on positioning as described in more detail in Chapter 7. This includes both, each droplet's original position predetermined by the positioning algorithm, as well as the adhesion dependent actual position each droplet obtains during the experiment. As described above, this gives each sample a unique morphology. Possibilities herein include a central positioning (in the center region of an already existing ring) or a positioning on the side of one or amid several structures (adjoining to the outer rim of one or more existing rings). A detailed investigation of possible cases of droplet positioning was executed for sodium benzoate and is described in Section 7.3 and Section 7.4. Further deliberations on this subject were published in Janocha and Tsotsas (2021b). In Janocha and Tsotsas (2022) a comparison of the three exemplary substances was conducted. In this context, differences and similarities regarding structural build-up, porosity development and so forth were highlighted.

At this point it shall also be noted, that a direct comparison of layer build-up and especially porosity development of specific layers or resulting structures in all sessile droplet drying experiments is only possible to a limited extent. This is due to the already discussed uniqueness of every deposit resulting from unpredictable positioning effects, particularly after the first layer. Both local drying conditions and droplet positioning patterns lead to small deviations, which are in turn amplified

with any further addition and finally lead to a unique structure. Nevertheless, a number of general trends regarding the development of porosity were identified over the course of the conducted experiments, and will be discussed hereafter.

6.2 Experimental plan

In general, the solid content of each material was selected to be as high as possible in order to mimic industrial conditions (where the amount of energy necessary to evaporate the water is to be minimized), but without disturbing the overall process or altering the present system. However, further experiments were conducted at lower mass contents (Chapter 7), in order to contrast these conditions and analyze the influence of solid concentration. Furthermore, the point of a disturbingly high solid mass fraction was naturally different for each substance and therefore the maximum solid content tested varies between the substances.

The microsuspension quickly showed sludge-like behavior, which is why a relatively low solid content of up to $\omega_{solid} = 5\,\mathrm{wt\%}$ was chosen. Especially compared to the nanosuspension, which can be applied at up to 40 wt% without problems. The sodium benzoate solution was applied with a maximum solid content near the solubility limit ($\omega_{solid} = 30\,\mathrm{wt\%}$).

The convective conditions were set as high as possible as well, in order to represent conditions that can be found in technical processes. As described before, displacement or deformation of the droplets is undesirable, which limits the convective conditions that can be safely applied. Table 6.2 summarizes the conducted experiments, the experimental parameters and the corresponding conditions.

For the studies regarding solitary deposit porosity, two additional single sessile droplet drying experiments were carried out for every experiment in Table 6.2. The results are tabulated in Appendix D.3. They deliver two other samples, respectively, making a total of three solitary residues that can be analyzed for each combination of drying conditions. The theoretical solid volume and the measured structural volume for all experiments is listed in Table 6.3, alongside with the calculated individual porosities of the solitary layers and the structures' cumulative porosities.

Table 6.2: List of conducted sessile droplet experiments for a comparison of nanofluid, microfluid and solution.

Exp. No.	Material	ω_{solid} [wt%]	V_{drop} [μl]	U_a [m/s]	T_a [°C]	N_{drop} 1^{st} layer	N_{drop} 2^{nd} layer	N_{drop} 3^{rd} layer
1	SiO_2/TiO_2	40	1.0	0.1	21	3	3	2
2	SiO_2/TiO_2	40	1.0	1.0	21	2	2	3
3	SiO_2/TiO_2	40	1.0	1.5	21	2	3	3
4	SiO_2/TiO_2	40	1.0	1.5	50	3	2	3
5	SiO_2/TiO_2	40	1.0	1.5	75	1	2	2
6	B_4C	5	1.0	0.1	21	3	1	3
7	B_4C	5	1.0	1.0	21	2	1	3
8	B_4C	5	1.0	1.5	21	3	2	2
9	B_4C	5	1.0	1.5	50	2	2	2
10	B_4C	5	1.0	1.5	75	1	3	3
11	NaB	30	1.0	0.1	21	2	3	1
12	NaB	30	1.0	1.0	21	3	3	3
13	NaB	30	1.0	1.5	21	2	1	3
14	NaB	30	1.0	1.5	50	3	2	1
15	NaB	30	1.0	1.5	75	2	3	3

6.3 Investigation: Silica-based nanofluid

6.3.1 Initial deposit

As already shown in the right part of Figure 4.3 (after pre-treatment), the drying of solitary colloidal nanofluid droplets results in typical ring structures along the droplets' contact lines. Due to the enhanced evaporation flux along the edge, the majority of particles is transported outward. Simultaneously to the receding of the contact angle, these particles accumulate in a circular spanning structure or in other words a hollow ring. However, inside this classical ring, id est in the central part of the deposit, variously shaped branched structures arise. This is again illustrated in Figure 6.1. During this experimental series (experiments No. $1-5$), it was observed that a portion of the included solids does not accumulate in the outer ring. Instead, it covers the center basin with a uniformly distributed, thin layer of particles. After the receding contact angle reaches the top of the ring, this central basin starts to dry. During the second drying stage, tensions arise within this layer and result in a bulging of the structure, similar as described by Xu et al. (2009). This bulging produces elevated branches (though not as high as the surrounding ring), as well as areas with a relatively low height profile. Areas without solid accumulation, id est uncovered parts within the deposit, were not spotted for silica nanofluid deposits under normal conditions. The outer ring itself is always clearly visible, but not as pronounced as for the tested sodium benzoate salt solution. It furthermore obtains a relatively even morphology of the surface, which may be reasoned in the uniformity and sphericity of the involved nanoparticles.

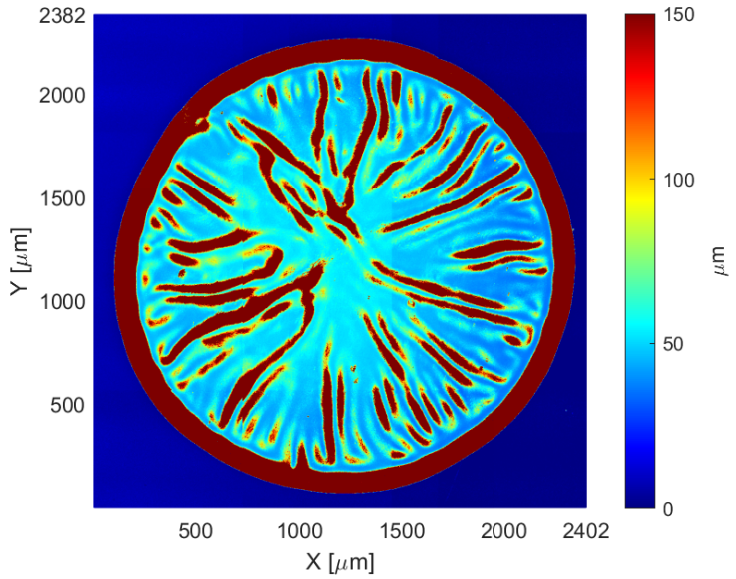

Figure 6.1: White-light interferometer scan of a SiO_2/TiO_2 solitary deposit from a sessile droplet showing an enclosing ring and a branched center. This WLI scan corresponds to the first droplet of experiment number 2.

The corresponding solitary deposit porosities and the respective fluctuation are illustrated in Figure 6.2, corresponding to Appendix D.3. Solitary nanoparticle residues form the least porous structures, in comparison with the other two substances (Figures 6.7 and 6.11). Despite some data spread, first correlations regarding a dependency of SiO_2/TiO_2 porosity on the convective conditions can already be made out. In the left part of Figure 6.2, one can see that the average porosity is increasing, alongside an increase in drying airflow velocity. Same can be stated for the increase in temperature (Figure 6.2, right part), but in an attenuated manner. Consequently, process parameters resulting in a fast drying process seem to produce more porous SiO_2/TiO_2 structures. This in turn can be reasoned in less time for the involved particles to sort themselves into a complex structure.

The spread itself in this case is due to random crystallization or structure formation behavior, as well as natural contact angle hysteresis on the substrate (Eral et al., 2013), in addition to the common inaccuracies in experimental execution and data acquisition. Thus, it is relatively similar under all drying conditions. It is furthermore quite similar for all materials, as can be seen if one compares the belonging error bars in Figures 6.2, 6.7 and 6.11. This consistency coincides with the study of Sondej et al. (2018), who investigated the same repeatability for the drying process of solitary sodium benzoate droplets.

6.3.2 Layer build-up

Once further droplets get placed onto the branched nanoparticle structures of the first layer that were illustrated in Figure 6.1, various phenomena take place. If a follow-up droplet or even only part of one droplet gets in contact with the fingering structures in an existing basin, the basin's area

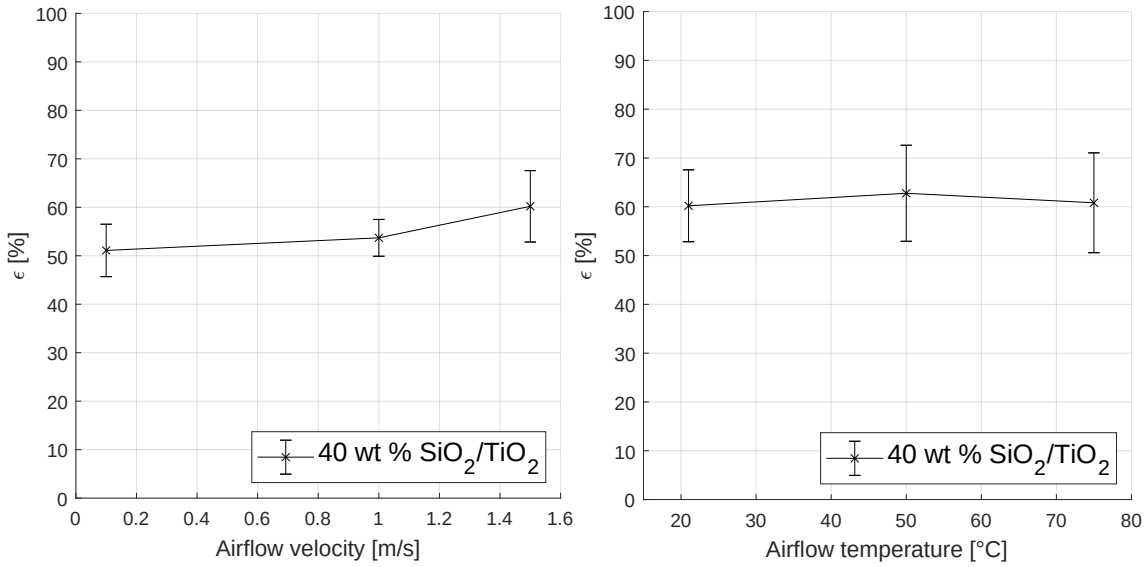

Figure 6.2: Solitary SiO_2/TiO_2 droplet porosities in dependence of airflow velocity at 21 °C (left) and in dependence of drying temperature at 1.5 m/s (right).

gets rewetted. Hereby, the bulged surface first redissolves and then arises again during the second drying stage. Although the individual branches naturally get altered during this process, the overall bulged morphology is retained. This results in a generally higher elevation of the branched basin and can be viewed in the bottom right part of Figure 6.3. The structure's enclosing ring features too much solid accumulation to be significantly rewetted during the addition of follow-up droplets. In consequence, the first layer's ring structures are retained and only enhanced in size. Since the ring around dried SiO_2/TiO_2 nanosuspension droplets is relatively slim (at least compared to sodium benzoate), cases in which a part of the droplet positioned itself outside, while the other part simultaneously placed itself inside an existing ring were spotted during the experiments as well. This phenomenon results in a new ring structure that partially overlaps with the existing ones. This can be seen in the upper left part of Figure 6.3. Furthermore, one can also recognize how additional droplets between the basic ring-like deposits result in a merging of the structure through solid bridges (Figure 6.3 middle section). These bridges show relatively similar morphology to ring structures, id est are comprised of an elevated surrounding boundary with a branched central basin.

During most experiments the executed pre-treatment described in Section 4.2.1 sufficiently stabilized the bulging areas. However, at high airflow velocities and high temperatures, or in other words for a very fast drying process, the formation of cracks kept persisting to a degree. This occurred mainly during the addition of the second and third layer and relates to experiments No. 4 and 5. Herein, as shown in Figure 6.4, the outer ring stays mainly intact, while the branched structures in the center show points of breakage.

The porosity development during layer addition, obtained by means of white-light interferometry as described in Section 5.3.1 and Equations 2.40 and 2.41, is shown in Figure 6.5. Since the white-

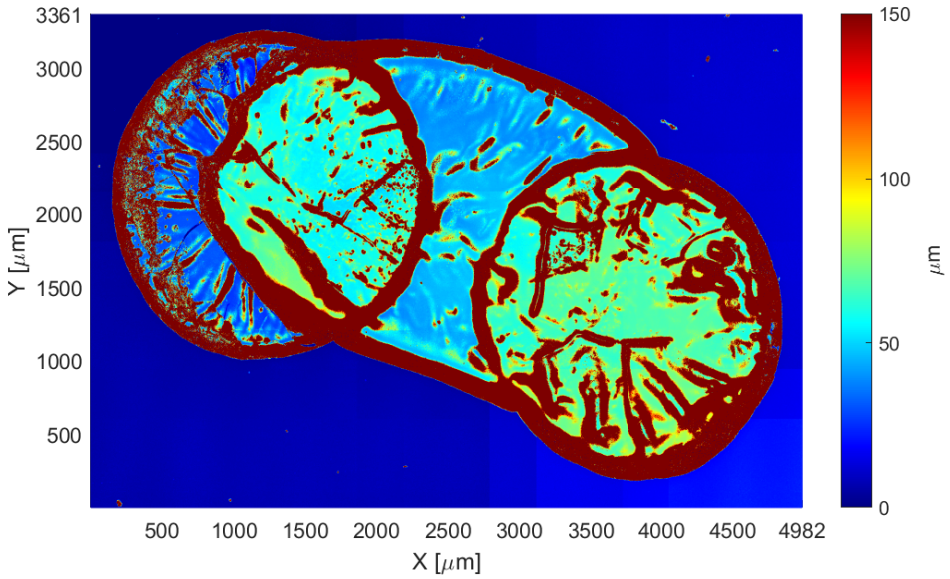

Figure 6.3: Multi-droplet SiO_2/TiO_2 nanofluid residue structure with elevated, branched basins, corresponding to experiment No. 3, 4^{th} droplet, 2^{nd} layer.

light interferometer always detects the entirety of the structure that exists at a specific timepoint of the experiment, the layer porosities in Figure 6.5 and all following figures are cumulative. This means that the porosity at layer number two is the average porosity of the entire structure developed until this point in time, or in other words, it comprises the porosities of layers one and two. The corresponding value at layer No. three represents the average after addition of the third layer, id est the average of layers one, two and three.

One can see that the dried nanofluid's porosity is generally lower than for the microfluid or the solution (compared to Figure 6.9 and Figure 6.12). Nevertheless, it is still relatively high, attaining values between 50 % and 75 %. This phenomenon is due to the fact that the careful application of sessile droplets is naturally associated with high porosities, especially when compared to other process environments like for example a fluidized bed.

An important trend that could be identified for all involved materials is an increase in porosity over the course of layer build-up. For the present nanoparticle mixture, the increase tends to be strongest from the first to the second layer and then continues in a slightly attenuated manner. This development is reasoned in the substrate's receding influence. The first layer is forming on a smooth and flat area, while other layers are deposited onto an already porous and uneven surface. Furthermore, this progression is a natural and expected phenomenon. If the layer is viewed as a sum of dried deposits of individual drops, it should always obtain a higher porosity than each individual deposit, similar to the higher overall porosity of a bed consisting of already porous particles. However, the increase itself was generally lower for the SiO_2/TiO_2 colloid than for the microfluid and salt solution, making the dried nanofluid to the densest of the materials tested in this experimental study.

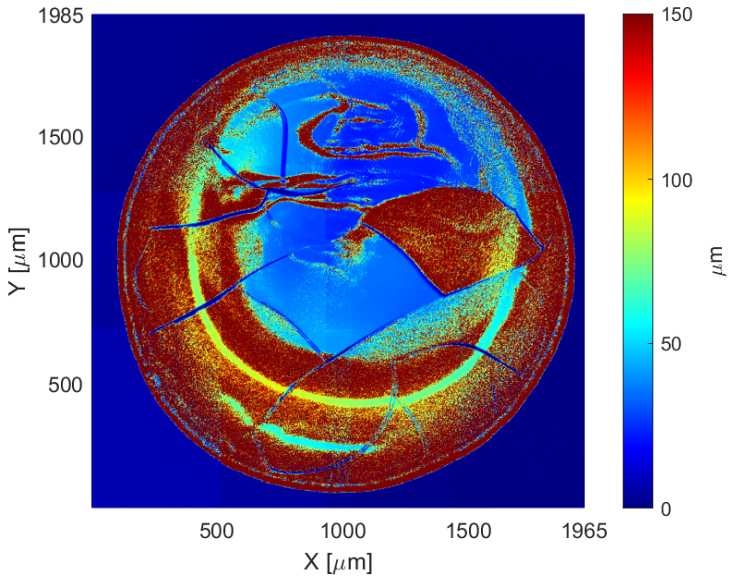

Figure 6.4: Stacked nanofluid residue dried at 50 °C and 1.5 m/s, corresponding to experiment No. 4, showing formation of cracks inside the center basin with an intact outer ring.

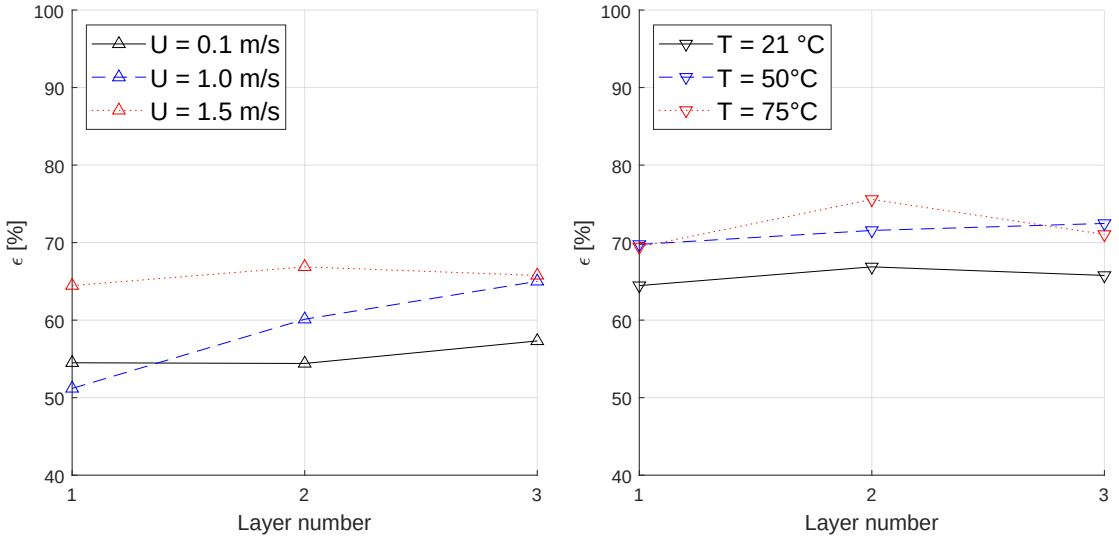

Figure 6.5: Average porosity during layer build-up from dried colloidal SiO_2/TiO_2 droplets in dependence of drying airflow velocity at 21 °C (left), corresponding to exp. No. 1 (solid Δ), 2 (dashed Δ) and 3 (dotted Δ); and drying airflow temperature at 1.5 m/s (right), corresponding to exp. No. 3 (solid ∇), 4 (dashed ∇) and 5 (dotted ∇).

Similar as observed for solitary deposits, the cumulative porosity generally increases with an increase in velocity as well as temperature, id est for a faster drying process of the droplets. The rather atypical drop in porosity of experiment No. 5 (between layers 2 and 3) may be reasoned by the aforementioned crack formation under severe drying conditions.

6.4 Investigation: Boron carbide microfluid

6.4.1 Initial deposit

In contrast to the other substances, solitary microfluid residues already showed two distinct kinds of structural morphology. The solitary deposit morphologies hereby depend on the drying conditions. At low airflow velocities and temperatures, or in other words when the droplet was dried slowly, the solids accumulated in a rather classical ring structure. Contrary to the silica-based nanofluid, there were no signs of crack formation or other indications of high internal tensions. Instead, the center was covered relatively evenly, with no points without solid accumulation and no branched structure. Especially compared to the sodium benzoate solution discussed in Section 6.5, less solids accumulated within the outer ring and more particles remained within the central basin. This also naturally means that the outer ring structure is usually not as distinct as for sodium benzoate. In consequence, the slowly dried microsuspension on average obtained the most even height profiles of the three materials tested. This result conforms with the experimental findings of Yunker et al. (2011) and Dugyala and Basavaraj (2014), as well as the results of the simulative investigation of Xu et al. (2017), who described that the ring pattern formation of colloids is dependent on the particle shape. In their investigations, respectively, spherical particles showed the strongest ring formation tendency, while disperse or ellipsoid particles showed significantly less strive to form rings. This phenomenon is due to the distortion of the air-water interface that accompanies the transportation of disperse particles (Mampallil, 2014).

With an increase in airflow velocity and temperature, id est a fast drying process, an untypical accumulation trend dominates. In such a fast drying case, more and more particles are settling in

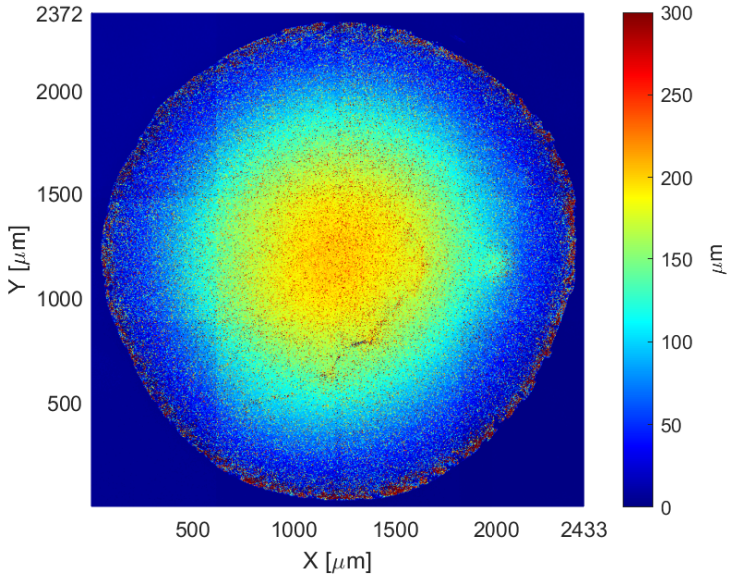

Figure 6.6: White-light interferometer scan of a solitary boron carbide deposit from a sessile droplet dried at 1.5 m/s and 75 °C, showing central elevation and thin accumulation along the edge, corresponding to experiment No. 10.

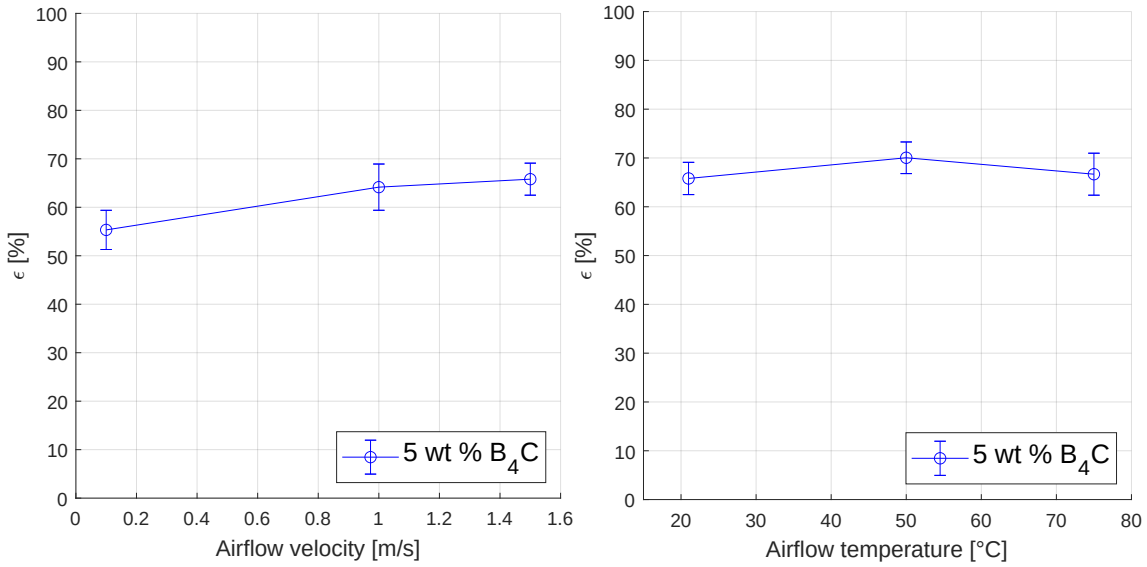

Figure 6.7: Solitary B_4C droplet porosities in dependence of airflow velocity at 21 °C (left) and in dependence of drying temperature at 1.5 m/s (right).

the droplet's center and are therefore only insignificantly transported towards the edge. This results in a central, symmetrical elevation which is flattening towards the edge, where only a small fringe of particles is accumulating. The thus arising height profile is exemplarily illustrated in Figure 6.6, corresponding to experiment No. 10. This distinct morphology is reasoned in the different particle size distribution (PSD) of the deposited solids. Compared to the SiO_2/TiO_2 nanoparticles, the boron carbide's PSD is very broad. Additionally, some particles of this microsuspension are always likely to be present in small agglomerates, even despite the prior ultrasound sonication. This formation of agglomerates is also different from the nanofluid, as therein particles are more likely to naturally repel each other.

One can see that during the drying process bigger particles tend to remain close to the center, while smaller particles are transported faster by the outbound capillary flows inside the droplet. If the drying process is relatively slow, this behavior simply results in less accumulation in the ring and more in the center, as initially described in this subsection. However, if the droplet is drying quickly, the majority of particles, or in other words a greater part of the PSD, are not significantly transported towards the edge and in turn do not accumulate in an outer ring, but form a raising in the droplet's center. Only a small fraction of light particles is transported fast enough to accumulate at the edge, before the droplet reaches the second drying stage. This small particle fraction is responsible for the slim fringe that is visible for example in Figure 6.6. The ring-shaped area in between the edge and the central elevation showed little to no solid accumulation for initial droplets under these drying conditions.

The porosity of single B_4C deposits is illustrated in Figure 6.7. If compared to the other substances, one can see that solitary boron carbide deposits comprised of disperse particles obtain the highest porosities. On top of that, the correlations regarding dependency on the convective conditions that

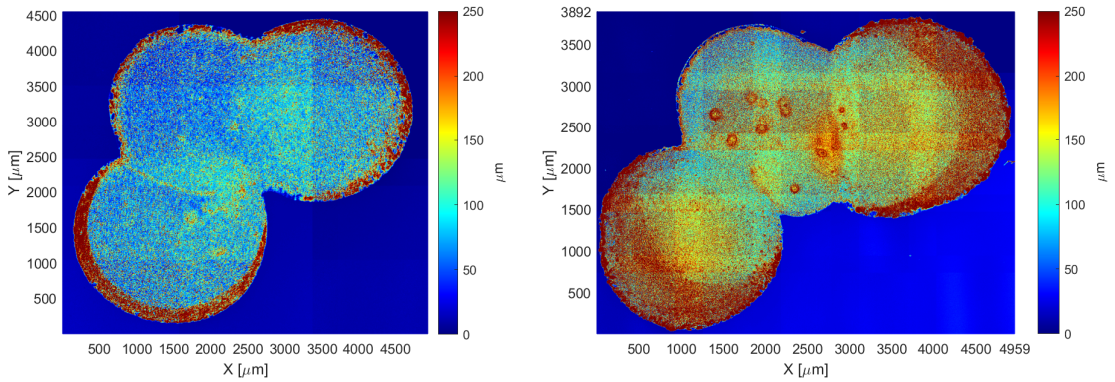

Figure 6.8: Exemplary B_4C microfluid residue structures during layer build-up, corresponding to a slow droplet drying (exp. No. 7, 3^{rd} droplet, 2^{nd} layer, left); as well as a fast droplet drying process in exp. No. 9 (6^{th} droplet, 3^{rd} layer, right).

were made for single SiO_2/TiO_2 nanoparticle residues can also be noted here. This includes the increase in average porosity alongside an increasing airflow, visible in the left part of Figure 6.7, as well as the attenuated increase with higher temperatures (Figure 6.7 right part). In consequence, process parameters that promote a fast drying process with little sorting time for the particles again seem to produce more porous structures.

6.4.2 Layer build-up

Further deposition of B_4C microparticle layers results in morphologies as exemplarily illustrated in Figure 6.8. As had already been observed for solitary residues, the basic morphology presented itself to be dependent on the drying conditions. As described in Section 6.4.1, the morphology of solitary deposits already changes significantly with the particles' available time to be transported by the droplet's internal flows. Although subsequent solid deposition results in a certain leveling of the height profile, as follow-up droplets are primarily positioning themselves in basins and sinks, differences in morphology and its development can still be spotted.

The first part of Figure 6.8 shows a structure that arose during a slow drying process. It can be seen that despite the fact that several droplets were already stacked upon the original ring structures, the rim surrounding the deposit remains relatively slim compared to other materials. This in turn results in a great extent of rewetting and redeposition within the overlap areas. One can see that the result is no definite ring structure that can be made out, but rather a slightly higher average elevation in those areas. Instead of individual rings, and contrary to the nanoparticles, the entire coated area is surrounded by an elevated perimeter, without steep increases or sudden elevations present inside. Thus, the central parts are quite uniformly covered and the microsuspension consequently resulted in the most leveled height profiles of created layers.

Although the previous statement remains true for layers that were created under fast drying conditions, one can still make out the different development hinted by corresponding solitary deposits. The second image of Figure 6.8 shows the associated elevations towards the center of each respec-

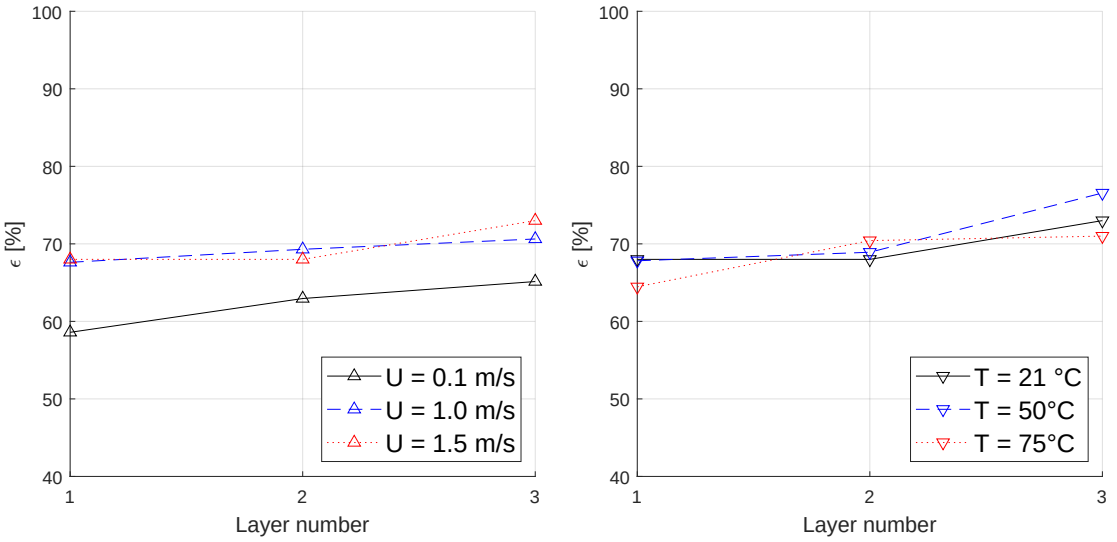

Figure 6.9: Porosity average during layer build-up from colloidal boron carbide droplets. Illustrated at 21 °C in dependence of drying airflow velocity (left), corresponding to exp. No. 6 (solid Δ), 7 (dashed Δ) and 8 (dotted Δ); and at a drying airflow velocity of 1.5 m/s dependent on drying temperature (right), corresponding to exp. No. 8 (solid ∇), 9 (dashed ∇) and 10 (dotted ∇).

tive deposition, due to bigger particles not being distinctively transported outward. Though not as steep as sodium benzoate ring structures or silica fingering structures, these central elevations do result in a slightly more uneven height profile of the enclosed area compared to slowly dried B_4C layers. It can also be seen that the outer rim shows relatively sparse accumulation, even though several droplets have already been deposited.

The cumulative porosity that was obtained during B_4C layer build-up can be viewed in Figure 6.9. Same as for the other materials, porosity increases alongside layer number and higher airflow velocity or temperature. However, in comparison with the nanosuspension and solution, the influence of drying conditions on porosity seems relatively small. This in turn means, that the respective datapoints at each layer number are close together. This behavior can be reasoned by the rather even height profile compared to the more protrude structures of SiO_2/TiO_2 nanoparticles and especially NaB salt crystals.

Furthermore, the early leveling that results in a fairly uniform height profile in succession causes a relatively similar porosity increase between first and second, as well as second and third layer. This development is especially different from sodium benzoate structures (Figure 6.12), which recorded a steep increase that flattened latter on. Due to this rather consistent increase coupled with reduced influence of drying conditions, boron carbide particles were overtaken by sodium benzoate as the most porous structure over the course of the executed layer build-up. The high dispersity of the involved micrometer-particles, however, consistently produced higher porosities than the more coherent, spherical SiO_2/TiO_2 nanoparticle mixture.

6.5 Investigation: Sodium benzoate salt solution

6.5.1 Initial deposit

The sodium benzoate solution shows the most clear ring formation compared to the other, colloidal materials. The solids, being present in a dissolved state and thus at a molecular level, easily get transported by the internal flows that replenish the enhanced water-loss along the edge. However, in contrast to the colloidal systems, this does not directly result in a solid accumulation. Instead, the nucleation probability gets enhanced towards the contact line, forming an area of local supersaturation (Shahidzadeh et al., 2015). The vast majority of solutes is hereby accumulating in the outer ring, leaving a center with almost no solid residues. Due to this increased outbound accumulation and the crystalizing behavior of sodium benzoate, the enclosing ring structure is higher and wider compared to the particle-based substances that were experimentally investigated in this study. Consequently, the central basin is relatively small compared to the previous materials and the difference in height between center and ring is more substantial. This refutes any postulates which claim that the back-diffusion may be more pronounced for molecules and smaller particles and the respective residues would therefore be less annular. The NaB's crystallization can hereby result in different structural patterns of the ring. These patterns were categorized in detail by Sondej et al. (2018). Figure 6.10 shows the most common phenomenon of a rounded, relatively symmetrical ring structure that forms the basis for most further droplet depositions. Small morphological details of and deviations from this basic ring morphology of sodium benzoate structures are discussed in-depth in Chapter 7, but shall not be the focus of the current comparison between solution and colloidal substances.

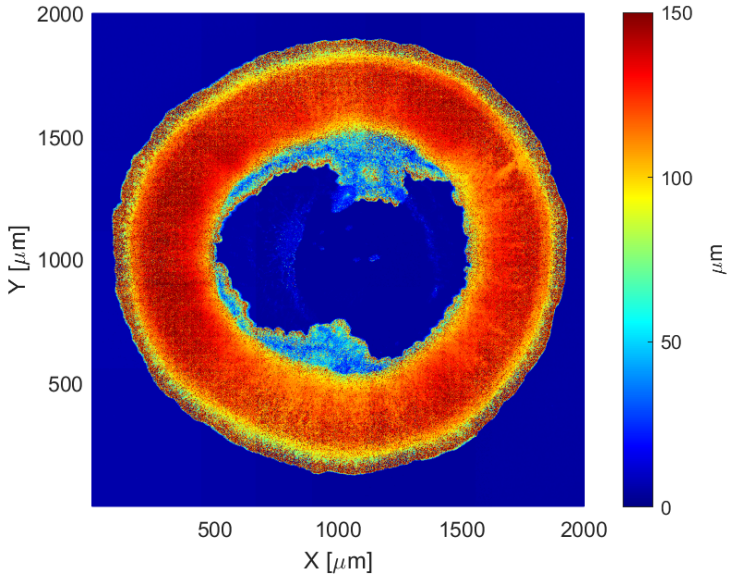

Figure 6.10: White-light interferometer scan of a solitary sodium benzoate residue structure showing a strong accumulation to a ring with a relatively small center basin with little to no solid accumulation, corresponding to experiment No. 11.

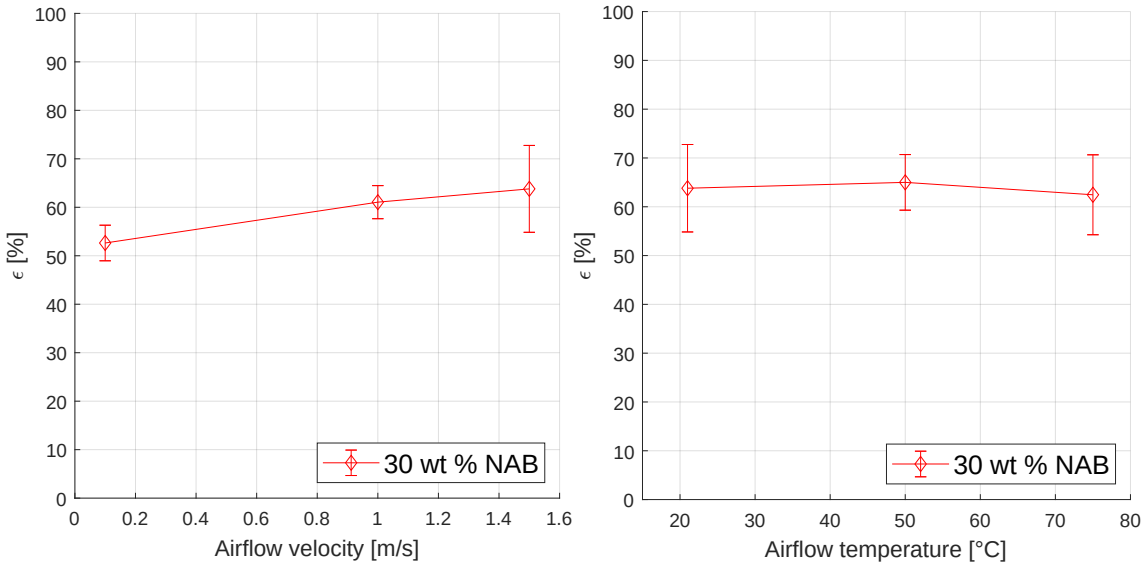

Figure 6.11: Solitary NaB droplet porosities in dependence of airflow velocity at 21 °C (left) and in dependence of drying temperature at 1.5 m/s (right).

The corresponding solitary NaB deposit porosities can be viewed in Figure 6.11. If one compares the values to the other substances (Figure 6.2 and Figure 6.7), one can see that single sodium benzoate deposits comprised of solids dissolved at a molecular level obtain the second highest porosities, lower than the B_4C microfluid but higher than the SiO_2/TiO_2 nanosuspension. Again, one can make out trends regarding the influence of drying conditions. Similar as for the other two substances porosity tendentially increases with a faster drying process, whereby the dependency on airflow velocity seems more pronounced, as can be seen when comparing the left and right part of Figure 6.11. Another observation that must be noted is that the spread slightly increases at more severe conditions. This can be reasoned in the crystallization behavior, which is naturally different and slightly less predictable than structure formation involving particles, especially during fast drying.

6.5.2 Layer build-up

For the sodium benzoate solution, continued deposition resulted in conical structures that tend to merge into a grown together layer at some point. These conical structures arise from stacked deposits, which are in turn obtained from droplets placing themselves in the center of an already existing ring-structure. If this happens, the lower ring gets extended inwards and the entire structure rises in the height with decreasing diameter. Id est, a second ring with smaller diameter is formed on top of the one underneath. As the resulting cone increases in height, this scenario becomes less probable and additional droplets are more likely to slide down the cone's side, creating another adjacent ring-structure that acts as the foundation for an additional cone. After several cones came into existence next to each other, these structures merged into a layer either through droplets sagging in between and resulting in solid bridges between the tapers, or through a merging of the

cones' outer rims at the basis. The development of morphology of NaB structures over the course of layer build-up is discussed in more detail in Chapter 7 and was also presented in Janocha and Tsotsas (2021b).

This layer build-up mechanism and respective development of morphology is quite different from the previously discussed observations involving colloidal materials. It is possible because in comparison to the nano- or microfluid, solitary sodium benzoate deposits have significantly less solid accumulation within their center. Accompanied by a higher and broader ring structure, as described in Section 6.5.1, it is possible for follow-up droplets to be completely entrapped in the central basin while leaning on the inner rim of the existing structure. In addition, the mixed case observed in Figure 6.3, in which an additional droplet simultaneously deposits in the center of an existing structure as well as next to it, could not be spotted for the salt solution because of sodium benzoate's different initial deposit morphology. In other words this means that droplets are either sliding outward or inward of a present ring, but never span over or take place directly on it. The conical development of resulting structures additionally makes this material to the one that produces the most uneven height profile. Compared to the other two substances, which spread, merged and leveled relatively fast on the substrate, the sodium benzoate solution rather produced individual substructures that used to grow together only later on in the process. This also implies that, compared to the colloids, the solution's layer build-up showed a relatively high amount of uncovered spots within the deposition area.

The porosity development over the course of the conducted layer build-up is illustrated in Figure 6.12. Again, it can be seen that the porosity increases with addition of further layers. This is a behavior that colloids and salt solution have in common. Moreover, sodium benzoate shows the strongest increase of the three materials. While the first layer exhibited values of porosity that were between those of nanosuspension and microsuspension, sodium benzoate structures attained the highest porosities on average after three layers were deposited. This comparatively strong increase during layer addition is again reasoned in the NaB's crystallization behavior, which produces large, ring-shaped cavities that can easily be stacked on top of each other and quickly result in relatively voluminous structures that are mostly hollow inside. Sodium benzoate thus forms a highly porous network of large cavities.

In most conducted experiments, the increase from first to second layer was significantly higher than the one from second to third. This flattening of the porosity increase is due to the substrate's receding influence and is similar to the trend for nanoparticles. Moreover, it was observed in many of the present experimental series (sessile droplet as well as fluidized bed) and is especially pronounced for sodium benzoate. Another trend NaB has in common with the colloidal systems is the influence of drying conditions, which likewise caused a higher porosity when associated with faster drying, for this substance.

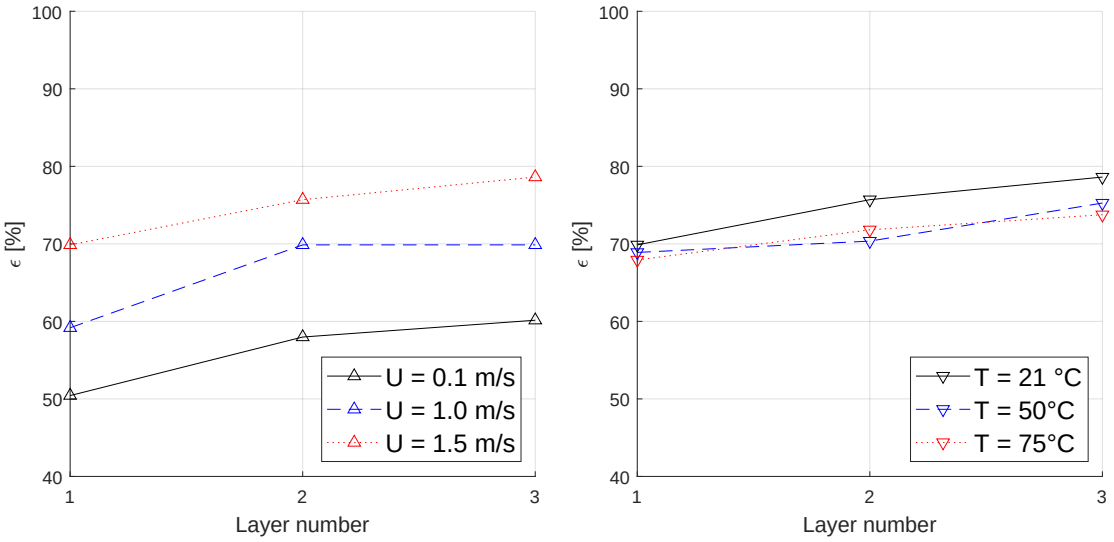

Figure 6.12: Average porosity during sodium benzoate layer build-up. Displayed in dependence of drying airflow velocity at 21 °C (left), corresponding to exp. No. 11 (solid Δ), 12 (dashed Δ) and 13 (dotted Δ); as well as drying airflow temperature at 1.5 m/s airflow velocity (right), corresponding to exp. No. 13 (solid ∇), 14 (dashed ∇) and 15 (dotted ∇).

6.6 Further investigation on porosity evolution from sessile droplets

Up until now, all shown porosities were related to residue structures as a whole. This contemplation is naturally expedient, because the properties of a coating are of course evaluated in the same manner. Nevertheless, the detailed monitoring of the incremental build-up process presents opportunities to investigate not only the entirety of the coating structure, but also the nature of individual layers and their origins. Since droplet addition is done in a controlled, predetermined way and the solid residue structures are measured after every droplet addition, it is possible to calculate not only the porosity of the entire structure, but also the layers' individual porosities. For this calculation, the theoretical solid volume of only one applied layer $V_{s,theo,layer}$ is used instead of the theoretical volume of the structure. Additionally, the structural volumes of the previous layers are subtracted from the newly attained volume. This results in the following equations, adjusted from Equation 2.41:

$$\varepsilon_{2^{nd}layer} = 1 - \frac{V_{s,theo,2^{nd}layer}}{V_{s,tot} - V_{s,tot,1^{st}layer}}, \tag{6.1}$$

$$\varepsilon_{3^{rd}layer} = 1 - \frac{V_{s,theo,3^{rd}layer}}{V_{s,tot} - V_{s,tot,2^{nd}layer}}. \tag{6.2}$$

The results of the respective calculations of the non-cumulative layer porosities are listed in Table 6.3, alongside the measured structural and calculated theoretical volumes.

Table 6.3: Theoretical solid volumes, measured structural volumes and corresponding individual as well as cumulative porosities attained during layer build-up from sessile droplets.

	1^{st} layer			2^{nd} layer				3^{rd} layer				Structure			
Exp. No.	$V_{s,theo}$ [nl]	V_{struc} [nl]	ε_{layer} [−]	$V_{s,theo}$ [nl]	V_{struc} [nl]	$V_{s,tot}$ [nl]	ε_{layer} [−]	$V_{s,theo}$ [nl]	V_{struc} [nl]	$V_{s,tot}$ [nl]	ε_{layer} [−]	N_{drop} [−]	$V_{s,theo}$ [nl]	V_{tot} [nl]	ε [−]
1	544.8	1197	0.54	544.8	2390	1193	0.54	363.2	3403	1014	0.64	8	1453	3403	0.57
2	363.2	744	0.51	363.2	1821	1077	0.66	544.8	3632	1811	0.70	7	1271	3632	0.65
3	363.2	1022	0.64	544.8	2741	1719	0.68	544.8	4244	1503	0.64	8	1453	4244	0.66
4	544.8	1802	0.70	363.2	3194	1392	0.74	544.8	5278	2084	0.74	8	1453	5278	0.73
5	181.6	594	0.69	363.2	2231	1636	0.78	363.2	3137	907	0.60	5	908	3137	0.71
6	61.5	149	0.59	20.5	221.3	72.8	0.72	61.5	412	190	0.68	7	143.5	412	0.65
7	41.0	127	0.67	20.5	200.3	73.7	0.72	61.5	419	219	0.72	6	123.0	419	0.71
8	61.5	192	0.68	41.0	320.3	12.8	0.68	41.0	532	211	0.81	7	143.5	532	0.73
9	41.0	127	0.68	41.0	263.8	13.6	0.70	41.0	525	261	0.84	6	123.0	525	0.77
10	20.5	57.7	0.65	61.5	277.2	21.9	0.70	61.5	495	218	0.72	7	143.5	495	0.71
11	457.6	923	0.51	686.4	2723	1799	0.62	228.8	3445	722	0.68	6	1373	3445	0.60
12	686.4	1681	0.59	686.4	4556	2875	0.76	686.4	6832	2276	0.70	9	2059	6832	0.70
13	457.6	1519	0.70	228.8	2825	1306	0.83	686.4	6420	3595	0.81	6	1373	6420	0.79
14	686.4	2207	0.69	457.6	3859	1652	0.72	228.8	5550	1691	0.87	6	1373	5550	0.75
15	457.6	1427	0.68	686.4	4059	2632	0.74	686.4	6975	2916	0.77	8	1830	6975	0.74

Once again one can see the tendential increase of layer porosity at faster drying conditions. If the individual layer porosities are averaged over all experiments with one substance, reasons for the development of cumulative porosity can be spotted. The average porosity of SiO_2/TiO_2 single layers amounts to 0.62, 0.68 and 0.66 for the first, second and third layer, respectively. This means that the porosity of all layers on the one hand is relatively similar and on the other hand conforms with the porosities attained by the resulting structures (average of 0.66), which in turn suggests the amount of inclusions of larger cavities is not significantly increased at high layer numbers. In contrast to this, a different behavior can be recognized for B_4C and especially NaB. For these substances, the average porosity of the first layer is lower as the resulting structure's, the individual porosity of the second layer lies in the same range and the third layer's individual porosity tends to be even higher than the cumulative structural porosity. For example, the average porosity of third layers of sodium benzoate amounts to 0.76, while the cumulative porosities of the same experiments have a mean value of 0.71. This suggests that an increasing amount of cavities or highly porous transitions is included during incremental layer addition, raising the cumulative porosity. The first postulation at this point is reasoned in the structure of the first deposits, which already yield relatively high porosities. The latter is deduced from the structural similarity (ring formation) of all residues, including those not deposited on the original substrate. As these phenomena are affiliated with the receding influence of the substrate, it can again be seen that the greatest difference always occurs between layers one and two, while the third layer often behaves similarly to the second one.

Generally, the fluctuation of individual layer porosities still tends to be relatively high, similar as for the cumulative porosities, which is again due to the quite unique morphology of each sample that was discussed beforehand. The latter, however, combined with the phenomena and postulates made regarding porosity evolution of both the entire structure as well as individual sublayers, led to a further, more detailed study, which will be presented in the next chapter.

6.7 Conclusions

A series of experiments focusing on layer build-up from dried deposited droplets was presented. Three layers of three representative materials, namely a silica-based nanoparticle suspension, a boron carbide microparticle suspension and a sodium benzoate solution, were applied onto a small area of a glass substrate, respectively. These layers consisted of up to three droplets each, and every droplet was subsequently dried after its deposition to mimic an incremental structure formation. In order to study layer structure dependencies on convective conditions, gas velocity and temperature were varied between the experiments. White-light interferometer scans were conducted in a droplet-by-droplet manner, in order to obtain morphology and porosity over the course of the mimicked build-up process. Through this experimental procedure, principal similarities and differences in morphology could be identified for solitary deposits, the transitional stage including first interactions of several droplets, as well as the resulting small coating layers. In addition to this, the deposits' porosity and its development were obtained in each experiment, and could thus be analyzed and compared between the three exemplary materials.

Deposits of the sodium benzoate solution show a generally strong solid accumulation within a surrounding ring along the droplets' edge, or in other words a classical coffee-ring formation. The result is a broad ring structure with only minor depositions in its center. The addition of further solids firstly results in the assembly of conical structures and a comparatively uneven height profile. Later, these arising cones are connected through the formation of solid bridges or a merging of their outer rims. Nanoparticle based residues show a comparatively smaller ring, with branched accumulations within the central basin. Therefore, corresponding incremental layer build-up also features more overlapping scenarios than observed for sodium benzoate. The central fingering structures as well as the individual outer rings, however, are mostly retained. The boron carbide colloid featured the least accumulation along the droplets' contact line and thereby naturally the most accumulation of solids within the central part. The result of this is a relatively slim ring structure in comparison with the other substances, especially sodium benzoate. In turn, the solitary deposits as well as any further layers displayed the most even height profiles. Moreover, an almost complete disintegration of ring structures in overlap areas could be observed. Consequently, it could be shown that lighter incorporated solids go hand in hand with stronger ring formation.

Solitary deposits consisting of disperse microparticles (boron carbide) attained the highest initial porosities. SiO_2/TiO_2 nanoparticle residues resulted in the least porous structures. All materials showed an increase in porosity alongside the deposition of further layers, though the characteristics of this increase varied. The nanoparticle mixture showed the slightest increase on average. In consequence, the corresponding structures remained the ones with lowest porosities over the course of incremental deposit addition. The boron carbide microparticles showed a stronger and consistent increase in porosity over layer number, while sodium benzoate structures showed an initially very strong increase that continued in an attenuated manner later on. Due to this still generally strong increase, the experiments involving sodium benzoate resulted in the most porous final coating layer structures. All materials tendentially developed higher porosities when dried at high airflow velocity and temperature. Thus, it can be deduced that a faster drying process and corresponding sparse time for solids to sort themselves produces more porous structures.

Chapter 7

In-depth investigation of sodium benzoate layers from sessile droplets

While the aim of Chapter 6 was to highlight general differences and similarities, this chapter's goal is to illuminate specific details of the layer build-up process from deposited droplets, id est the transition from single deposit to finished layer. This transition, though being an essential part of any coating process that features droplets, has attracted much less attention in literature than its respective starting point (solitary deposit) and end stage (coating layer). The results in this chapter are an extended version of Janocha and Tsotsas (2021b) and deal with structural build-up from sodium benzoate droplets. In the course of this in-depth analysis, further influences of process parameters than already discussed in Chapter 6 are investigated as well. This includes foremost the alteration of droplet volume and solid mass fraction.

The obtained structures were analyzed via white-light interferometry (same as in the previous chapter) and X-ray micro-computed tomography, in order to obtain results regarding the development of morphology and porosity as well as additional insight into inner structure.

7.1 Experimental plan

For the in-depth analysis of sodium benzoate structures, several supplementary experimental series were conducted in addition to the experiments No. $11 - 15$ in Table 6.2. Same as for the previous trials, the average velocity in the cross-sectional area of the drying chamber and the corresponding temperature were varied between the experiments, but kept constant during each layer build-up, and again three layers were deposited onto the substrate following the positioning algorithm.

With these experiments, the behavior of sodium benzoate droplets at a droplet volume of 100 nl and a solid content of 5 wt% and 20 wt% was investigated, respectively. Furthermore, the behavior in the purely diffusive case is checked for the present experimental setup as well. Other experimental parameters are oriented on the previous series, id est experiments No. 11 to 15. Table 7.1

Table 7.1: List of conducted sessile droplet experiments for an in-depth analysis of sodium benzoate layer build-up.

Exp. No.	Material	ω_{solid} [wt%]	V_{drop} [μl]	U [m/s]	T [°C]	N_{drop} 1^{st} layer	N_{drop} 2^{nd} layer	N_{drop} 3^{rd} layer
16	NaB	5	1.0	0.0	21	2	1	2
17	NaB	5	1.0	0.1	21	3	2	1
18	NaB	5	1.0	1.0	21	3	2	2
19	NaB	5	1.0	1.5	21	2	3	2
20	NaB	5	0.1	0.0	21	1	2	2
21	NaB	20	1.0	0.0	21	3	3	3
22	NaB	20	1.0	1.5	75	2	3	3
23	NaB	20	0.1	0.0	21	3	3	3
24	NaB	20	0.1	1.5	75	1	2	2
25	NaB	30	1.0	0.0	21	1	3	2
26	NaB	30	1.0	1.0	50	2	3	3
27	NaB	30	0.1	0.0	21	2	2	2
28	NaB	30	0.1	1.5	21	1	2	3
29	NaB	30	0.1	1.5	50	2	1	3
30	NaB	30	0.1	1.5	75	2	3	3

lists the experiments that were conducted in this framework. As the reduction of solid content and droplet volume also results in a decreasing Reynolds, Bond and Péclet number, the general deliberations of the previous experimental series regarding laminar flow and spherical cap droplet shape (Section 6.1), still remain true. Same as for experiments No. 1 to 15 the spread of initial droplet porosity was estimated through conduction of two additional droplet drying experiments, respectively. The results are tabulated in Appendix D.3.

The detailed morphological analysis of resulting structures from the experiments listed in Table 7.1 shows, expectedly, that due to the individual deposition patterns and the individual positioning effects discussed hereafter, every deposit is unique when examined at this level. The exact repetition of a particular morphology is thus impossible and comparison between the individual deposits must therefore be handled carefully. That having been said, during build-up and in-depth comparison of these individual structures, a number of recurring occurrences and characteristic substructures were identified. Those phenomena can thus be quantified and, additionally, are further linked to specific droplet, positioning or drying conditions, hereinafter.

7.2 Investigation of first layer interactions

The first droplet of the first layer is by definition a solitary droplet. As described in Chapter 6, the selection of glass as substrate means that it rests on a flat, impermeable, partially wetting surface

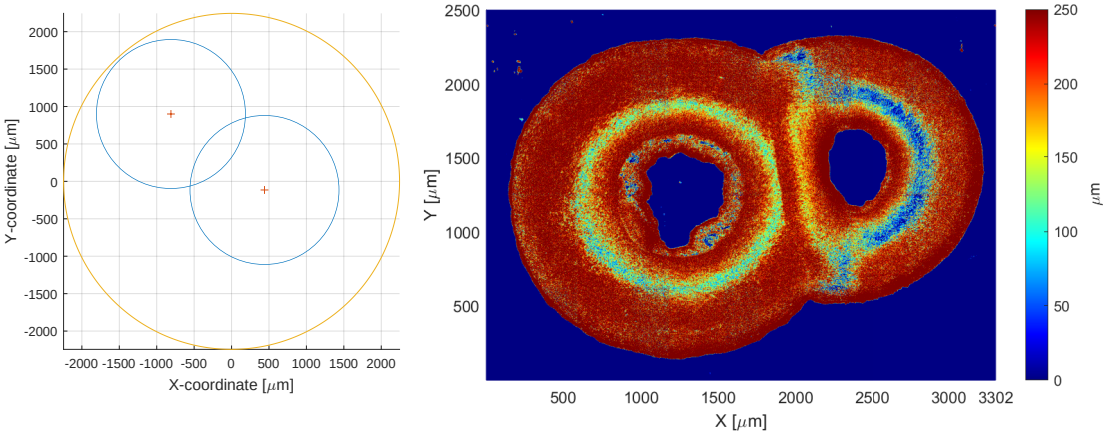

Figure 7.1: Positioning coordinates (left) and WLI scan of the resulting two-droplet structure (right) for $\omega_{solid} = 30\,\text{wt\%}, V_{drop} = 1\,\mu\text{l}, U = 0.1\,\text{m/s}, T = 21\,^{\circ}\text{C}$, corresponding to exp. No. 11.

and dries in a dominant CCR mode as described by Picknett and Bexon (1977). The constant contact radius mode with its associated higher evaporation rate along the pinned contact line was observed for all droplets in this study, even beyond the first layer and at low and high solid content and droplet volume. The capillary flow towards the edge consequently forms the characteristic ring structures by transporting any contained solids. This strive to ring formation was again seen for all droplets in the first, second and third layer, respectively.

For all solid contents tested in this study, even as low as 5 wt%, CCR mode was still persisting by the time the liquid-air interface reached the upper edge of the ring. Since from there on the droplet edge is made up by the solid residue itself rather than by the initial droplet-substrate contact line, other distinct stages of sessile droplet evaporation (like CCA) were not observed during first layer droplets drying in experiments 16 to 30. The reason for this is that any follow-up droplets of the first layer are still mainly resting on the glass substrate.

Nevertheless, as described in Section 5.1.1, edges of the droplets are allowed to overlap in order to quickly mimic realistic layer build-up behavior. This means that first droplet-droplet interactions can already be viewed for the first layer. The typical interactions of two exemplary droplets in the first layer are illustrated in Figure 7.1. The left part of the figure shows the prior determined individual positions with corresponding overlap. The droplet on the left was placed first, followed by the one on the right. The white-light interferometer scan of the resulting structure can be seen in the right part of Figure 7.1. Both droplets were dried at the same temperature of 21 °C and 0.1 m/s airflow velocity (experiment number 11).

It can be seen that the low airflow velocity results in the classical, symmetrical ring structure of the first droplet. For the second droplet's placement, there are not only adhesion forces between substrate and liquid, but also between liquid and already existing residue. As a result, parts of the liquid are adhering to the outer ring of the previous structure and the spreading of the second droplet

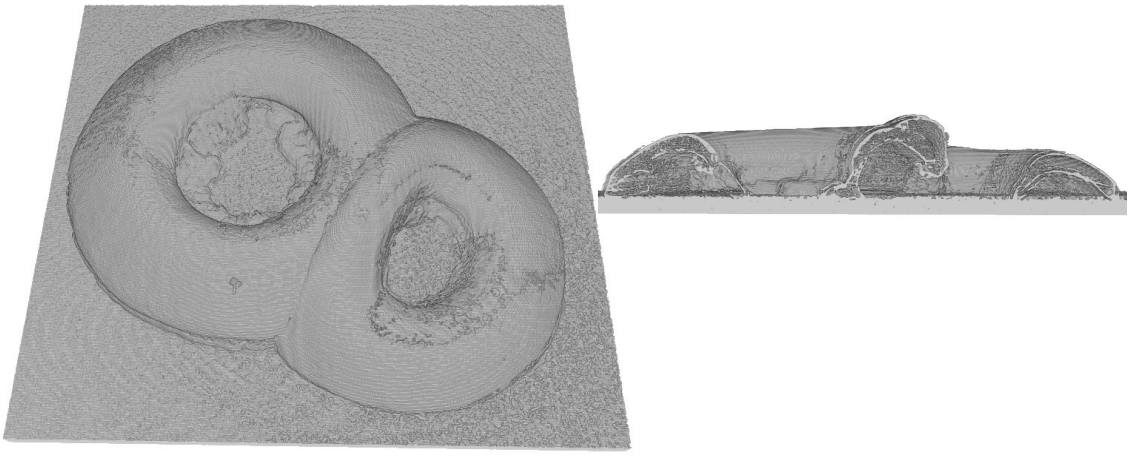

Figure 7.2: X-ray micro-tomography scan of the two exemplary droplets in the first layer (left) and a clipped view in flow direction (right), corresponding to experiment number 11, $\omega_{solid} = 30\,\mathrm{wt\%}, V_{drop} = 1\,\mu\mathrm{l}\,, U = 0.1\,\mathrm{m/s}, T = 21\,^{\circ}\mathrm{C}$.

on the substrate is less pronounced. Hence, the actual formed contact angle is higher than for the initial droplet and the diameter of the second deposit is significantly smaller, despite the droplets' consistent volume. The addition of a second droplet results in an attachment on the existing ring within the overlap area, which can be viewed in the μ-CT scan presented in Figure 7.2. Thus, this deposit section in turn acquires the highest altitude and the steepest slope towards the center of the second residue. Further addition of droplets to the first layer results in the same effects as described: Incremental coverage of the substrate with ring-like structures that merge in the overlap sections.

The right part of Figure 7.2 shows a clipped view of the deposit. Herein, one can see that instead of a consistent structure, the applied rings are comprised of large cavities that are spanned with a thin, porous layer. This insight was made possible through μ-CT analysis, which, in contrast to white-light interferometry, also penetrates the deposits and illuminates inner structure.

7.3 Investigation of centered higher-layer deposition

The second and third layer droplets are placed quasi randomly onto the first layer's structures by utilizing the same algorithm as before. This means that these droplets are not placed on a smooth substrate but on an irregular layer formed from ring structures of previous residues. Hence, further mechanisms take effect. In the course of this procedure different cases of droplet positioning with regard to the existing structures presented themselves. These cases were characterized and could be sorted into two groups: Centered and non-centered positioning.

The first group of build-up possibilities incorporates follow-up droplet positions near the center of already existing ring structures. This group, together with the enclosing case discussed later on, was the most commonly observed one during the experiments. The reason for this frequency is a relatively low contact angle that results in ring structures with a relatively high diameter. This is

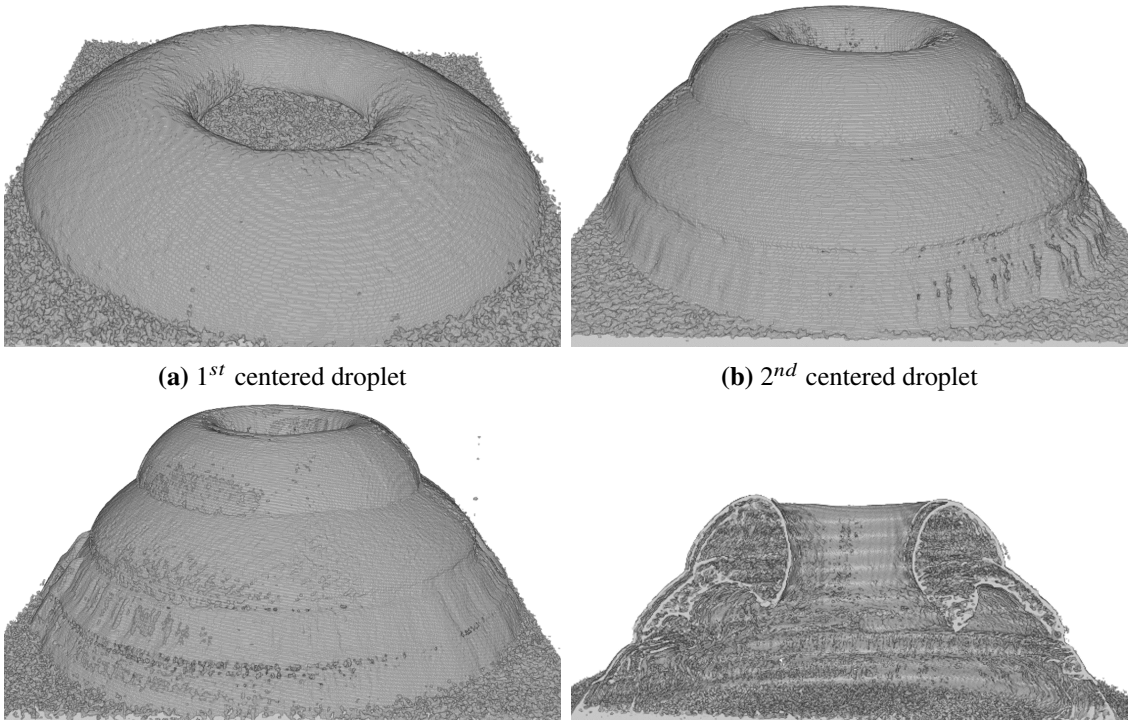

(a) 1^{st} centered droplet

(b) 2^{nd} centered droplet

(c) 3^{rd} centered droplet

(d) Interior structure

Figure 7.3: μ-CT images of conical structures, created through centered positioning or sliding of 30 wt% NaB droplets with 1 μl volume, dried at $U = 0\,\mathrm{m/s}$ and $T = 21\,^{\circ}\mathrm{C}$ (exp. No. 25).

an observation made not only for sodium benzoate, but for all substances investigated in this study. Though in case of NaB, this deposition type results in a particularly distinct set of morphologies. It can either occur if the droplet is placed centered in relation to the already existing ring, or in case it is deposited on an elevation that leans towards the center, in which case the droplet slides down the inner rim as a result.

In the experimental series with high NaB solid content ($\omega_{solid} = 20,\ 30\,\mathrm{wt\%}$), the existing ring structure is too big to significantly redissolve during the drying stage of any additional droplets. Apart from the increased size of the base structure, droplets with higher solid content show faster crust formation and the dissolution is slower, which also results in a negligible amount of rewetting of existing structures. The combination of these effects means that any existing ring structures stay largely intact during follow-up depositions.

Especially for 30 wt% NaB, the deposition structures are very sizeable and, due to the solid content's proximity to the maximum saturation concentration, nearly nothing of the existing solid residues redissolves during the drying process. For a central positioning case involving these profound structures, additional droplets cover the entirety of the predecessor's central area, maintain a relatively spherical shape and rest on the existing ring. During the drying stage, the bulk of solutes accumulates along the inner rim of the existing structure and effectively extends the rim inwards. Hereby, the overall structure increases greatly in height, but is simultaneously reduced

in diameter, id est it forms a stacked cone. Such a conically shaped accumulation as a final result of three centered depositions is exemplified in Figure 7.3. The conical structure consisting of multiple rings stacked on top of each other is in its basic nature similar to morphologies reported by Willmer et al. (2010) for salt solutions containing polyethylene oxide. They observed that the contained polymers are constricting droplet and crystal formation, which in turn results in the formation of two rings from one multi-component droplet. The salt-based ring is hereby placed within the enclosing polymer structure, resulting in a conical pattern. In Figure 7.3d one can again see that the stacked rings individually comprise large cavities. This means that the pattern of an inner structure which consists of enclosed, ring-shaped cavities, persists beyond the first layer.

Although it was the most common phenomenon for the second and third NaB layer, the piling of droplets to conical deposits is not likely to continue furthermore, as the tip of the cones gets smaller and smaller over time. In other words, top deposits incrementally form smaller diameters and a centered position becomes less likely. Rather than being positioned in the center, additional droplets are expected to slide to the side of the conical structure and thus result in non-centered depositions to be discussed in Section 7.4.

The spreading of droplets on the substrate slightly fluctuates. As reported by Eral et al. (2013), this is a natural result of contact angle hysteresis. In addition to this, the spreading is dependent on the overlap and interaction with other residues, as already described in Section 7.2. For ring structures with a relatively large diameter, or in other words droplet residues after large initial spreading and only minor interaction with other droplets, the case of a ring-like deposit forming inside of another larger ring during layer addition was observed occasionally. This particular phenomenon could be spotted only for 20 wt% sodium benzoate droplets of the second layer and is favored at high drying airflow velocity and temperature, id est a fast drying process. In consequence of this, this pattern was also seen more frequently for 100 nl droplets than for microliter range droplets. For such small droplets undergoing a fast drying process, ring formation is not as strong as for 1 μl droplets. This means that the height profile is more leveled and the ring-center difference is less severe.

This can be observed in Figure 7.4, or, more specifically, the teal areas within the left subfigure. In the corresponding right part of Figure 7.4, one can see that these minor accumulations in the central region of the first droplet halt the spreading during the second droplet's application. Afterwards, these low solid areas dissolve again to some degree, forming a new ring structure with smaller diameter and new central point.

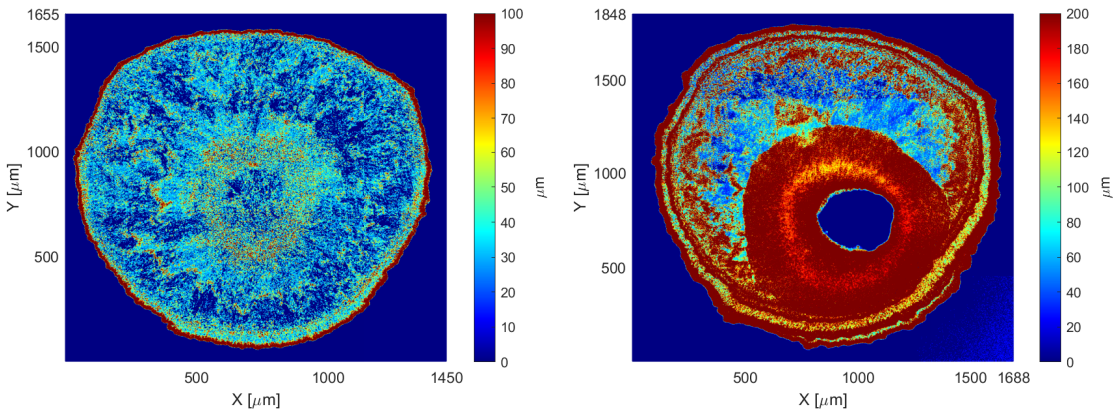

Figure 7.4: White-light interferometry images after first (left) and second (right) deposition of 20 wt%, 100 nl sodium benzoate droplets dried at $U = 1.5\,\mathrm{m/s}$ and $T = 75\,^{\circ}\mathrm{C}$ (experiment number 24).

7.4 Investigation of non-centered higher-layer deposition

In the first non-centered positioning case, the respective droplet takes a position at the side of an already existing structure. This can either happen deliberately, if the positioning algorithm determines a set of coordinates on the existing structure's edge with minor overlap, or, if the droplet gets deposited onto an elevation and subsequently slides down the outer rim of an already existing ring to an unoccupied side, resulting in only minor overlap, as well. The outcome of both of these positioning effects is relatively similar to the addition of a droplet in the first layer. During drying, the main part of the new droplet is in contact with the glass substrate and is only merging with the existing sodium benzoate residue in a relatively small area which is still pinned onto the outer rim. If one side of the additional droplet has a larger overlap with an existing structure, one can observe a new characteristic effect. In this case, the droplet addition does not lead to the common spherical-cap droplet shape and associated ring structure as reported by Deegan et al. (2000) or Lubarda and Talke (2011), but instead the droplet tends to enclose an already existing ring. The accompanying change in sessile droplet shape is due to the increased adsorption along the contact line of substrate, old deposit and new droplet. During the drying stage, this newly formed liquid fringe adds the contained solutes to the edge of the existing structure. This in turn results in a steadier slope and an enlarged diameter of the entire deposit. The enclosing effect during droplet addition is the most common case among non-centered depositions. A noteworthy side effect of this phenomenon is the transition from a smooth morphology of the outer rim to a corrugated surface. In Figure 7.5, such corrugated and extended rim structures around an existing ring are illustrated via μ-CT images. While this reoccurring phenomenon takes place in both centered (as discussed in the previous section) and non-centered droplet addition cases, it was rarely observed during deposition of the first layer. This missing of the enclosing effect during first layer placements can be attributed to the limited overlap prescribed by the placement procedure.

Same as initially non-centered deposits, droplets that slide down the outer rim of an existing

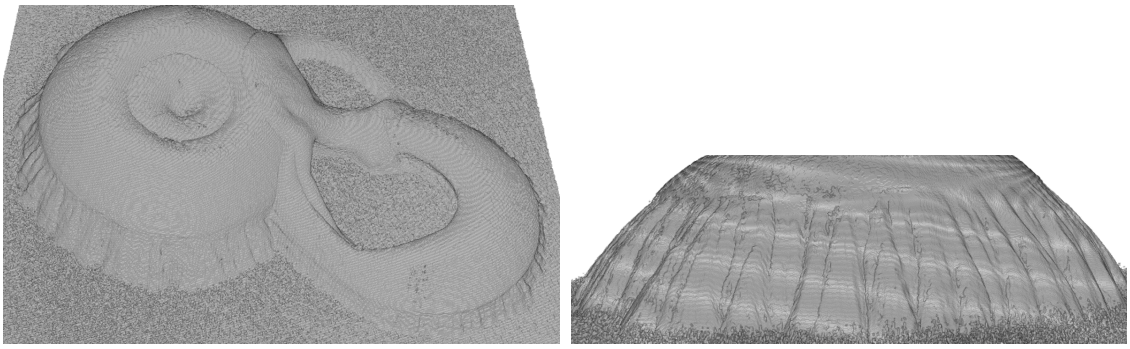

Figure 7.5: μ-CT scan of a droplet pinned in a corner of the previously existing layer, corresponding to exp. No. 21 (left subfigure). μ-CT visualization of a rim that was repeatedly extended and corrugated by droplet additions to an existing ring structure, corresponding to exp. No. 26 (right subfigure).

central positioning cone broaden the layer and create new foundations for more conical elevations. Furthermore, it could often be seen that parts of the centrally positioned droplet extend to the outer rim as well and therefore simultaneously result in a similar effect as the enclosing of non-centered additions. However, the extension and corrugation of the outer rim was reduced compared to the non-centered case.

The last recurring case that was identified for this group of positioning cases can be seen in the left part of Figure 7.5, as well. This case is a mixture of the previous two. On this occasion, a small part of the additional droplet's solution is pulled along the existing deposit's edge and encloses its outer rim. In contrast to this, the other part maintains a spherical-cap shape similar as for undisturbed droplets, and leans on the rim of the deposit. The enclosing part of the liquid results in the corrugated rim decoration described beforehand. The part of the droplet that retains its form applies a new ring, which is significantly smaller in diameter and height. This shrinkage is due to the reduced contact area between droplet and glass, the reduced amount of involved liquid and the steeper contact angle of the remaining part. Consequently, the effects described above are magnified. This hybrid case was most commonly observed if the droplet gets pinned in a surrounded edge or a tapered corner. Such a corner-pinned situation in which this kind of behavior was typically seen is further illustrated in Figure 7.6, corresponding to experiment 11. Herein, the second layer's first droplet (indicated with a black circle, Figure 7.6, left part) on the one hand extended the outer rim of one droplet of the first layer (left blue circle), and on the other hand added a smaller ring-like deposit in the tapered corner. Looking at the contact area between all three deposits in experiment number 21 (Figure 7.5, left part; Figure 7.6, right part), one can also see the common side effect in which addition of droplets with greater overlap in one area is accompanied by slight partial rewetting. This often ablates the previous ring structures in that particular area only and hereby creates surface irregularities and distortions. Either through these distortions, or through partial rewetting, minor parts of the follow-up solution can get stuck within the center of the other involved ring. This results in a small amount of solids accumulating in this adjacent ring's center.

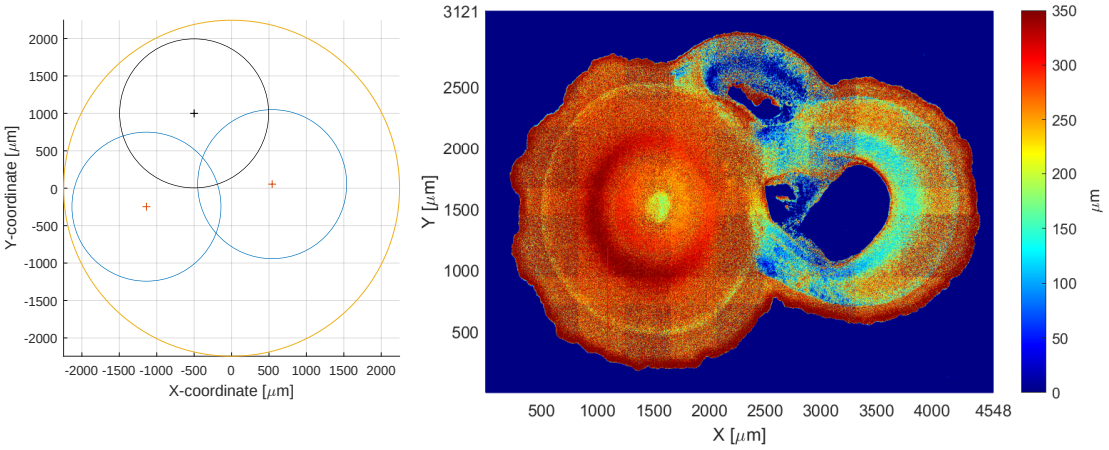

Figure 7.6: Positioning coordinates (left) and WLI scan of the resulting two-droplet structure (right) for $\omega_{solid} = 30\,\mathrm{wt\%}, V_{drop} = 1\,\mu\mathrm{l}, U = 0.1\,\mathrm{m/s}, T = 21\,°\mathrm{C}$, corresponding to exp. No. 11.

7.5 Transition from individual substructures to a grown together layer

In the course of the first few sodium benzoate droplet depositions and additions, the applied solids rather merged into a couple of substructures that can be individually identified and characterized, such as stacked cones or side by side rings, instead of forming a connected layer. In order to create one coherent deposit which can be compared to layers produced in industry, for example by spray fluidized bed coating, the addition of more droplets in this area is necessary. During the present experimental series with NaB droplets, such a comprising structure could only be identified after eight or more droplet applications. The respective experiments showed two different processes that were ultimately leading to this result.

The first possibility corresponds to the rim enclosing effect described in the Section 7.4. Through repeated broadening of the outer rim of one or multiple conical towers, these substructures start to increasingly merge together. First, the individually underlying structures merge into a continuous base. Then, further overlying deposits start to merge and overlap as well. The result of this merging is a grown together deposit. The left-hand side of Figure 7.7 shows two conical structures merging through rim extension.

The second possibility for the transition to a small layer are droplets that position themselves in between two or more of the individual conical tower structures, adhering at the elevations on the side, sagging in between them and thus forming a liquid bridge when dried. In consequence, this solid bridge between the tower structures connects the involved individual cones to one another. Following the bridge-like shape of the droplet, the deposit takes a similar form and hereby merges the cones or rings into a comprised structure. This phenomenon is visible in the right-hand side illustration of Figure 7.7. In case of this exemplary layer, three individual deposits existed.

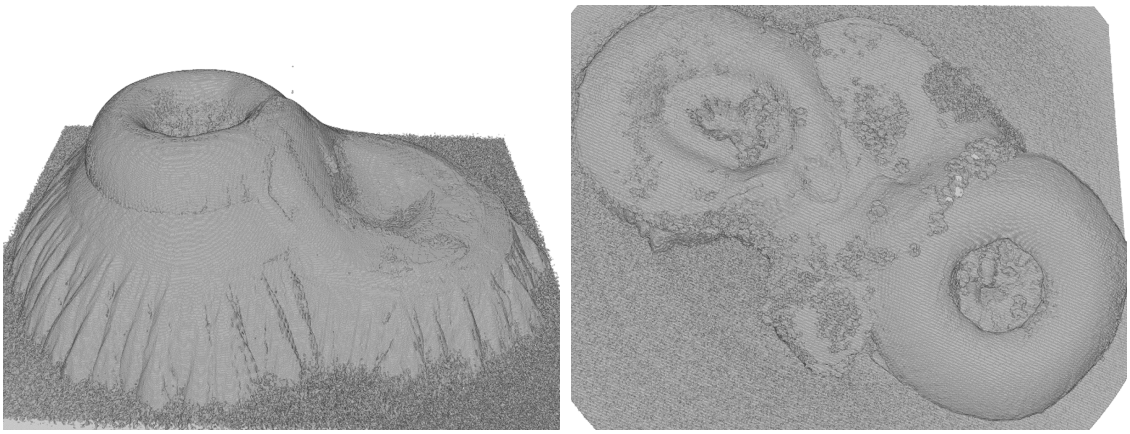

Figure 7.7: μ-CT recording of a layer structure created through a bridge formed between individual elevations corresponding to exp. No. 15 (left); rim extension of two conical structures corresponding to exp. No. 26 (right).

Two of them originated from the first layer (top left and bottom right). A third ring-like elevation, belonging to the second layer, has arisen in the corner between the previous two. During the further process of deposit addition, those three structures got extended mainly in height. In addition to this, other droplets got placed between the three main elevations, providing respective residue bridges. Through this process, the enclosed basins got filled, the height profile of the layer was leveled, and instead of quasi-independent substructures, a relatively uniform elevation was created. Hence, the end result is a relatively uniform layer in which all solids are connected and that completely encloses the substrate.

7.6 Interim conclusion

Through the conducted X-ray micro-computed tomography measurements several new observations and further insights on droplet behavior as well as layer morphology were achieved. This mainly includes the comprehension of the previously unknown inner structure. It was found that positioning has a great influence on morphology for layers created within the present experimental setup, id est a relatively low number of applied droplets. Furthermore, details like rim corrugation were visualized. However, most importantly it could be shown that large cavities form within the deposits in the case of sessile droplet deposition, by examining the deposit structures using the structure penetrating μ-CT. These cavities are responsible for the height of attained porosities and the majority of morphology related observations. They occur when the concentration of the solid at the liquid-gas boundary is very high, causing saturation and crystallization at the outer edge. The solid then covers the droplet's surface like a shell. Sondej (2019) further investigated this phenomenon utilizing coulometry measurements of the structure and moisture content measurements of the exhaust air. It was discovered that because the rate of crystallization proceeds rapidly and the shell frequently completely surrounds the remaining droplet, it is also possible for water that has not yet evaporated to be trapped inside. In this case it greatly reduces the rate of diffusion, as the trapped water has to diffuse through the microporous solid shell. In any case, this structure formation

beginning outside leaves large voids inside the residue.

7.7 Influence of forced convection on deposit and layer morphology

The absence of airflow (diffusive cases) or very small air flow velocity (0.1 m/s) during the drying process results in formation of very symmetrical ring structures, as shown in Figure 7.1, or symmetrical cones, as shown in Figure 7.3. In contrast to this, the presence of significant forced convection during the drying, or, in other words, during the stage of solid transportation, introduces an amount of systematic asymmetry in the structures. This asymmetry influences the morphology in addition to the degree of random asymmetries observed in any case. Convective flow over a droplet shifts the evaporation flux distribution over the droplet's surface in upstream direction, as described in the course of the simulative investigation in Section 9.2.1 and as reported by Janocha and Tsotsas (2021a). As postulated in Section 9.2.5, this flux shift goes hand in hand with an increased intrinsic flow to the side which is subjected to increased evaporation, in order to replenish the liquid loss. In turn, more solids are transported to the droplet's upstream side, creating an asymmetrical deposit.

During the present experimental series, it was observed that this effect is most noticeable in the first layer. For low solid content this shift results a wider and higher ring structure on the side facing the flow. However, the area of low solid accumulation stays in the center of initial droplet application. For high solid contents, this deposit basin is shifted in flow direction, which impacts the subsequent layer build-up. WLI images of clearly shifted sodium benzoate deposits resulting from drying under high airflow velocity are shown in Figure 7.8. Moreover, this shift effect could be seen among others in Figure 6.4 for the silica based nanofluid, or the right part of Figure 6.8 for the boron carbide microfluid, as well. Corresponding to the size of the included solids, the shift effect is strongest for sodium benzoate, slightly attenuated for SiO_2/TiO_2 nanoparticles and significantly weakened for B_4C microparticles. This relation is again due to the fact that smaller and lighter solids are transported by internal flows more easily. The magnitude of the effect therefore also corresponds to each substance's degree of ring formation.

The solid shift effect is most clear for 1 μl droplets dried at low temperatures but high velocities. For 100 nl droplets it is not as significant. The reason for this behavior is that the shift in evaporation flux distribution increases with an increase in Reynolds number, as can also be deduced from Table 9.3. Thus, the solid transport to the upstream side is magnified, as well. In contrast to this, a generally faster drying process, either due to increased temperature or decreased droplet size, simultaneously reduces the amount of time available for the directed solid transport and in turn acts oppositionally, creating more symmetrical deposits.

Especially for high solid mass fractions, this shift effect towards one side and the accompanying displacement of the center had a significant impact on the overall morphology of the created deposits and the further development of morphology during layer build-up. The drying of such droplets on the substrate results in more crescent than ring-shaped deposits. A corresponding μ-CT

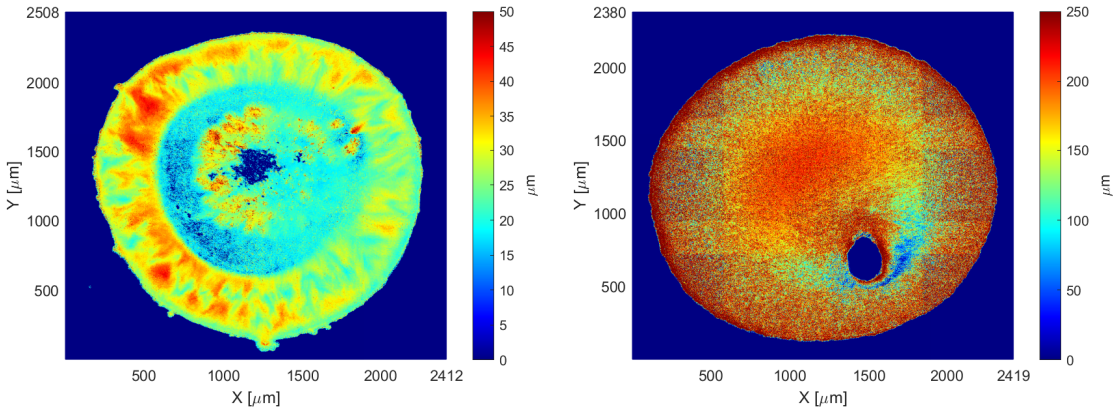

Figure 7.8: White-light interferometry surface analyses of asymmetrical ring structures from 1 μl droplets dried at 1.5 m/s. 5 wt% NaB (left), corresponding to the first droplet of exp. No. 19; 30 wt% NaB (right), corresponding to the first droplet of exp. No. 13.

illustration can be viewed in Figure 7.9a. Analyzing a clipped view in flow direction (Figure 7.9b), one can see an increased height and width of the structure's flow facing side. Recordings of the crescent formation process are shown in Appendix D.2, Figure D.2. Herein, it can also be seen that the crystallization starts on the upstream side of the contact line. From the point of the contact line that faces the flow, the structure formation moves to the downstream side, along the three-phase-line, in an enclosing manner. The outer ring is then closed on the downstream facing point of the droplet. From this point on, the structure formation proceeds inwards, as was described in the previous chapter. However, structure formation progresses faster on the upstream side. Hence, a crescent shaped structure results from these different start times and progression speeds.

The resulting distortion in the ring further prevents the creation of symmetrical conical structures, as were shown in Figure 7.3. The positioning of additional droplets in the center is hereby hindered, id est less common, and follow-up droplets are rather leaning on the downstream rim in addition to being pulled towards the displaced central basin. The combination of these phenomena results in a structure that attaches to both, the center and the thin part of the crescent. It hereby covers both areas, respectively. During drying, the droplets again stay in relatively spherical shape and subsequently form a distorted ring with its center positioned over the one of the deposit that already existed. The resulting morphology is shown in Figure 7.9c and Figure 7.9d. Similarly to the symmetrical cones, a droplet placement on top of the deposit becomes less likely with an increase in already involved deposits. In case of a strong forced convection, this probability decreases even more, due to the drag forces on the still fresh droplets, making them slide to the side, even when initially positioned directly on the structure. Regardless of this low probability, an example of such a three-droplet structure is illustrated in Figure 7.9e. Hereby again, the added deposit on the one hand sticks to the distorted central basin, and on the other hand is attached to the side that has the greatest downwards slope.

Due to the low probability of three droplet asymmetrical cones, most solids simply form a rela-

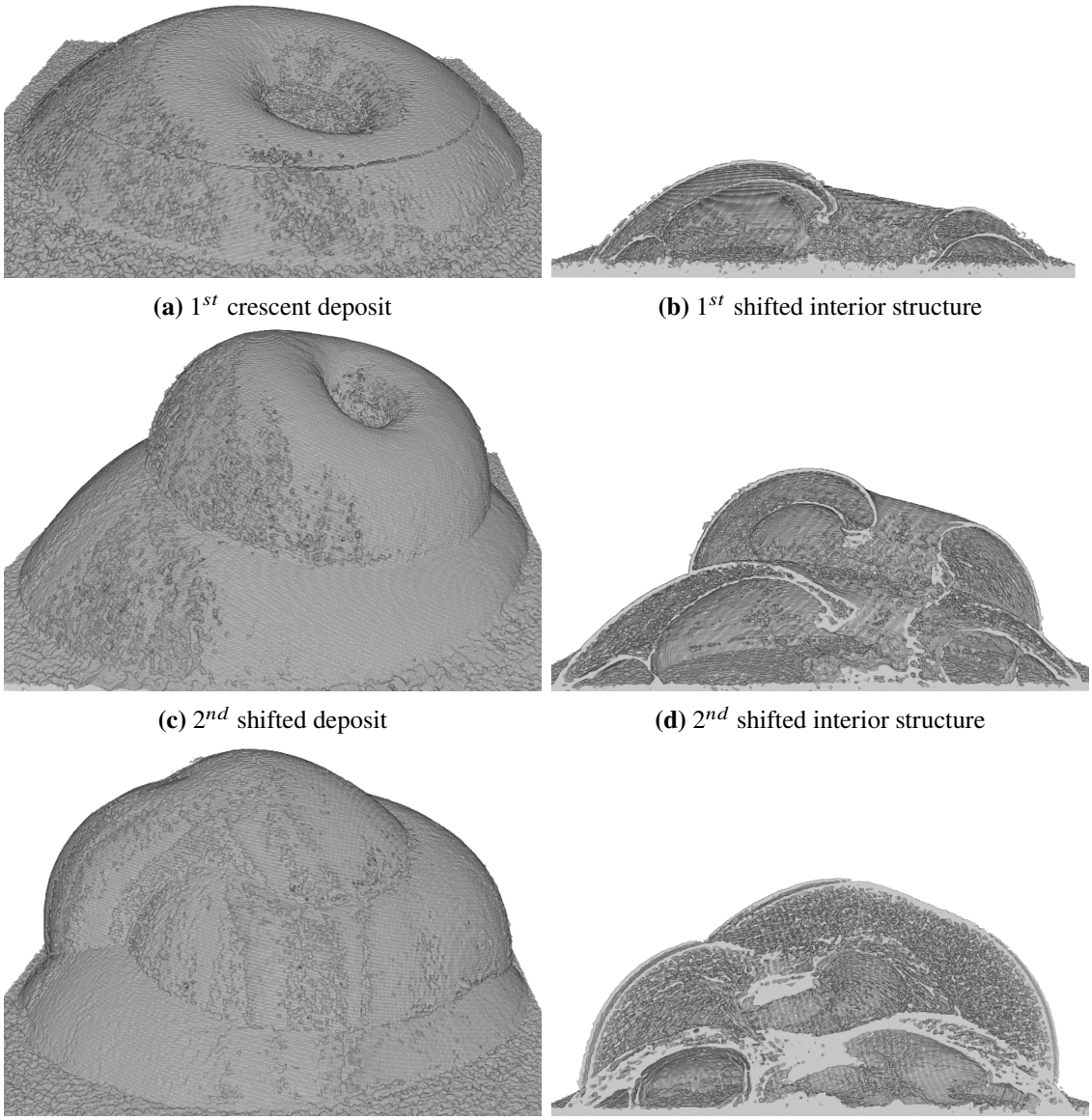

(a) 1^{st} crescent deposit

(b) 1^{st} shifted interior structure

(c) 2^{nd} shifted deposit

(d) 2^{nd} shifted interior structure

(e) 3^{rd} shifted deposit

(f) 3^{rd} shifted interior structure

Figure 7.9: μ-CT scans of shifted 30 wt%, 1μl conical NaB structures on glass (a, c ,e) and clipped views in flow direction (b, d, f), dried at $U = 1.5\,\mathrm{m/s}$ and $T = 21\,^{\circ}\mathrm{C}$, corresponding to experiment No. 13.

tively spherical attachment on the downstream side. At this point, the residues return to a more symmetrical morphology. This effect can be attributed to the small slipstream that is given to the respective droplets by the existing structure. In other words the existing cone (symmetrical or not) increases the velocity boundary layer in its wake and therein reduces the influence of forced convection on the follow-up droplet. This situation can also be compared to the relations for binary droplet setups simulatively investigated in Section 9.2.4. Therein, the downstream droplet also experiences a reduced flux shift.

7.8 Influence of solid content

In Chapter 6 all substances were applied at relatively high solid content, respectively. This configuration is of course also common in industrial processes and therefore of great importance for any investigations regarding coating layer build-up. The present section however shall investigate the structural build-up at low solid content, in order to set the characteristics in relation to developments at high solid concentration.

The development of sodium benzoate morphology has been discussed up to this point based on observations made during experiments with 20 wt% and 30 wt% NaB droplets. In experiments $16 - 20$ though, some differences regarding behavior of morphology and porosity were identified at a relatively low solid content.

With 5 wt% sodium benzoate, the residues are significantly smaller in volume, as can naturally be expected. Moreover, the ring structures are much flatter in comparison to the geometrical relations of high solid content droplets. This means that residue structures are not simply scaled down if less solids are available, but the spatial dimensions are altered to some degree as well.

Although the classic formation of ring structures is retained, the flattening of the outer rings means that no sliding or sliding-dependent positioning occurs in the follow-up layer formation. Instead, the applied droplets often completely cover the existing ring, independently of their centered or non-centered positioning. Through the enhanced adhesion forces along the existing deposit's edge, the follow-up droplet is pulled along the substrate-deposit contact lines, similar to the partially enclosing case for higher solid content. Hereby the droplet's spreading on the substrate is increased. Therein, the droplets contact angle is effectively decreased, which may cause the general flattening of the emerging residues.

Since the new droplets themselves have a high water content, their drying process also takes significantly longer compared to 20 wt% and 30 wt% droplets, under the same conditions. This, in combination with the lower amount of deposited solids, results in almost complete rewetting of the previous structure and the formation of a new ring that contains a greater amount of solids. In Figure 7.10 one can see several white-light interferometry images of such a process. Therein, one can monitor a deposit that grows in a droplet-by-droplet manner, while retaining its classic ring morphology. It can be observed, that the rim significantly grows in height and also increases in width through this process. While there is some accumulation of solids in the center, the majority of solids are still accumulating in one single ring. As a result of that, the characteristic ring morphology remains largely the same over the course of several droplet additions. This in turn means, that positioning patterns which lead to adjacent or piled ring structures at high solid content, can result in one single ring deposit for low solid concentration cases. This is again due to constant rewetting of existing structures. Thus, the number of deposited droplets in the current experimental series was not enough to form small layers comparable to Figure 7.7, when using 5 wt% sodium benzoate droplets. Nevertheless, the characteristic ring morphology was found to be the determining phenomenon at this mass fraction as well. This conforms with the results of

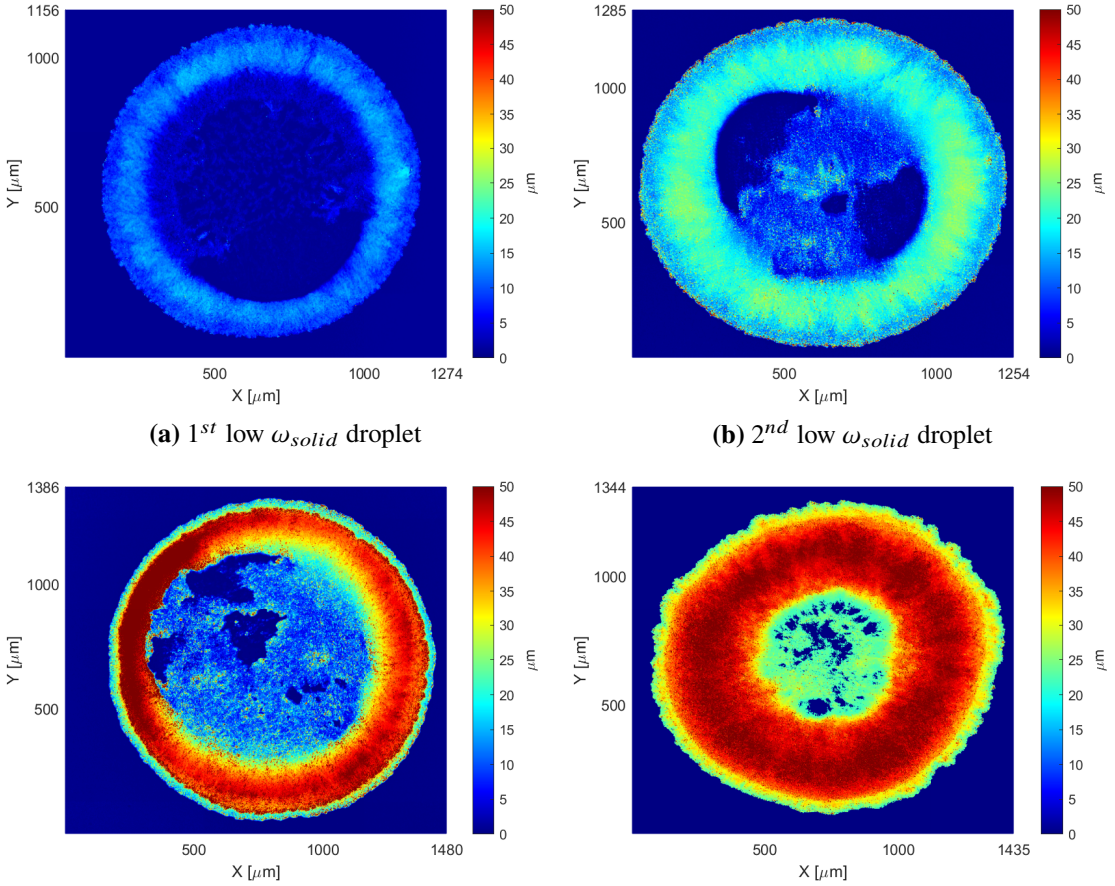

(a) 1^{st} low ω_{solid} droplet

(b) 2^{nd} low ω_{solid} droplet

(c) 3^{rd} low ω_{solid} droplet

(d) 4^{th} low ω_{solid} droplet

Figure 7.10: White-light interferometer images of the consecutive deposition of four relatively dilute (5 wt%) sodium benzoate droplets at $T = 21\,°C$ without convection, corresponding to experiment No. 20.

Soulié et al. (2015), who reported an inhomogeneous deposition of solids for concentrations higher than $0.001\,\mathrm{mol/m^3}$, for different crystalline systems, as well as Kaya et al. (2010), whose results indicated that for very low salt concentrations a nucleation starting in the center can be observed.

A part of the additional data for porosity of 5 wt% droplets is illustrated in Figure 7.11. The influence of solid content on solitary deposit porosity can be most disctintively estimated if one compares the results for this present low solid content series to the already known data for droplets near the solubility limit ($\omega_{solid} = 30\,\mathrm{wt\%}$) under the same convective conditions, as this comparison covers the entire range of NaB mass fractions tested. For this continuative study of initial deposit porosity, again two additional experiments were carried out for specific parameter combinations listed in Table 7.1, namely experiments No. 17 till 19. With these additional results and the corresponding first droplet's value from the associated build-up experiments, the spread of initial droplet porosity was estimated same as for Section 6.5.1.

Comparing the spread in Figure 7.11 to the one in the left part of Figure 6.11, it can be seen that it does not significantly change with the variation of solid content. And, it is similar for both, low air

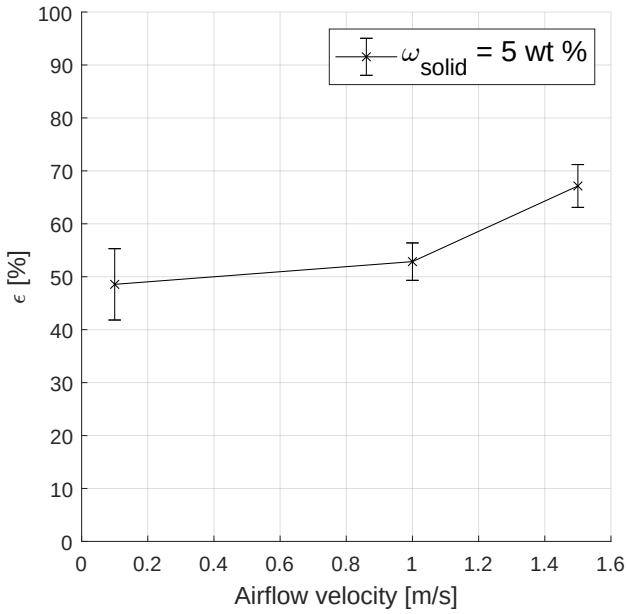

Figure 7.11: Repeatability of single sodium benzoate droplet porosities at 5 wt% solid content in dependence of airflow velocity at 21 °C.

velocities and temperatures, id est slow drying, as well as high velocity and temperature, associated with fast drying, and for 5 wt% and 30 wt% droplets, respectively. This implies that the amount of unavoidable porosity fluctuation caused by contact angle hysteresis and unique morphology details is independent of the droplets' NaB concentration and consequently reproducibility and repeatability of initial droplet porosity are not affected.

The results illustrated in Figure 7.11 are in the same data range as the porosities reported by Sondej et al. (2018), who obtained values between 0.4 and 0.6 for solitary sodium benzoate droplets on glass within a different experimental setup. Looking at the dependency on process parameters, an increase in airflow velocity or temperature, or, in other words, a faster drying process, tends to increase the porosity of the initial deposit. This means that although the initial structures obtained slightly different spatial dimensions, similar basic influences of convective conditions are apparent.

If one compares this porosity of 5 wt% droplets to 30 wt% ones (Figure 6.11), a slight increase of porosity at higher solid mass fraction can be observed. These results conform with the findings of Rieck et al. (2015) for fluidized bed coating with NaB on glass beads and the trends observed by Sondej et al. (2018).

The development of porosity during layer build-up with 5 wt% droplets is plotted in Figure 7.12. Similar as for build-up with high solid content droplets (Figure 6.12), the values feature a generally high porosity. Since the same can be stated for the 100 nl droplets in Figure 7.14 as well, this can be identified as a general characteristic of all sodium benzoate related datapoints independent of droplet size, solid content and drying conditions. Values on the one hand never reach below the 0.4 mark and on the other hand regularly rise above 0.7. As was proven through μ-CT scans, these across the board very high values are reasoned in the extensive formation of cavities within the

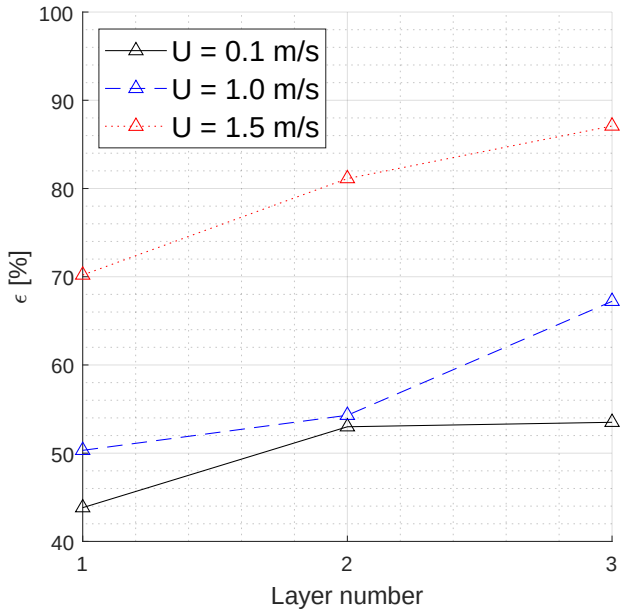

Figure 7.12: Development of porosity during layer build-up at $T = 21\,°\mathrm{C}$ and $\omega_{solid} = 5\,\mathrm{wt\%}$, corresponding to exp. No. 17 (solid Δ), 18 (dashed Δ) and 19 (dotted Δ).

deposits. This can again can be observed in the clipped illustrations in Figure 7.3 and Figure 7.9. These cavities constitute the majority of the inner structure, hence, the analyzed residues rather resemble a network of enclosed cavities than a uniform network of small pores. In turn, it can be stated that the obtained porosity largely depends on cavity size, while the porosity of the enclosing solid walls is of less importance.

The second correlation that can identified in Figure 7.12 is an increase in porosity with the addition of more layers, similar as observed for high solid content droplets. Again, the reason for this development is that only the first layer in every experiment is applied onto a smooth substrate and follow-up layers are deposited on an uneven and porous base from previous structures. The corresponding trend in cumulative porosity is preserved, despite the very different morphological development. The same statement can be made for an increase of porosity alongside an increase of drying airflow velocity, as deposits experiencing the highest drying rate, id est $1.5\,\mathrm{m/s}$, have the highest porosity values over all three layers, same as the respective initial deposits.

Comparing the first layer values for 5 wt% droplets to the corresponding ones for 30 wt% in Figure 6.12, the slight increase with higher solid content that was already observed for solitary residues can be confirmed. This effect is reasoned in faster crust formation, which is in turn due to the higher supersaturation at the liquid-gas phase boundary and corresponding rapid onset of crystallization. This faster crystallization results in an increased slope and height of the deposits, thus defining the external geometry of the deposition structure at a point in time where the droplets still have a higher contact angle. This phenomenon was among others reported by Handscomb et al. (2009) and is also commonly known in spray drying processes, where it was studied among others by Mezhericher et al. (2008) and Bück et al. (2012). However, this trend for initial droplets

is not clearly visible beyond the first layer, which may be attributed to the significantly different structural development of low and high solid content solution that was already discussed.

7.9 Influence of droplet volume

Regarding the influence of droplet volume it can first of all be stated that all experiments with a droplet size of 100 nl showed similar structural details and height-profiles as their 1μl counterparts. This means that in contrast to a reduction of solid content, a reduction in volume has no significant effect on basic morphology and layer build-up mechanisms. Instead, the structures are simply scaled down. An exception to this similarity is the upstream side shift of solids at high airflow velocities, which is reduced for smaller droplets. The reason for this is the deeper placement within the substrate's velocity boundary layer.

In experiments 28 to 30, the size of 30 wt% droplets was changed to 100 nl. Through this, a comparison to experiments 13 to 15 is enabled and an investigation regarding the influence of droplet volume on porosity can be conducted. The additionally acquired porosities can be viewed in Figure 7.13 and compared to the right part of Figure 6.11. Again, one can see the reduced influence of temperature in comparison with velocity. Furthermore, it can be stated that a reduction in droplet size does not noticeably effect the general values of porosity or the corresponding spread. The further evolution of porosity under different temperatures is shown in Figure 7.14. Again it can be observed that the trend of higher porosity alongside faster drying kinetics, which could be identified for an increase of flow velocity, is not as clear with an increase of temperature. All datapoints, especially first-layer porosities, are located close together, which again might be explained by the utilized experimental setup without insulated walls or substrate heating, or in other words

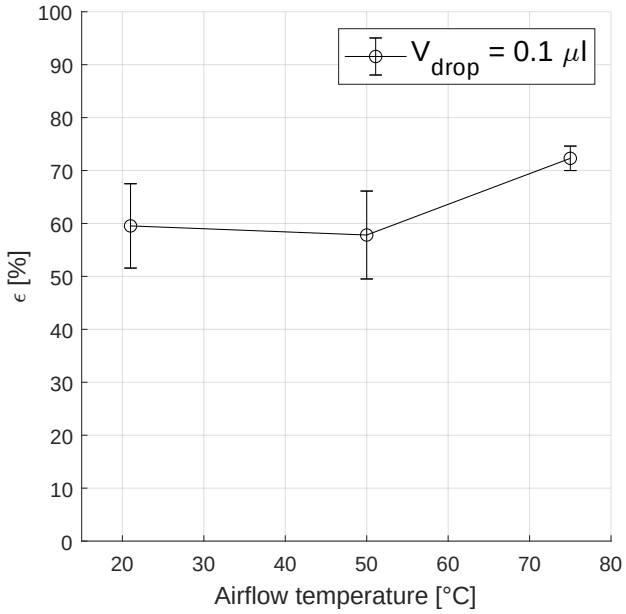

Figure 7.13: Repeatability of solitary 100 nl sodium benzoate droplet porosities in dependence of drying temperature at 1.5 m/s airflow velocity.

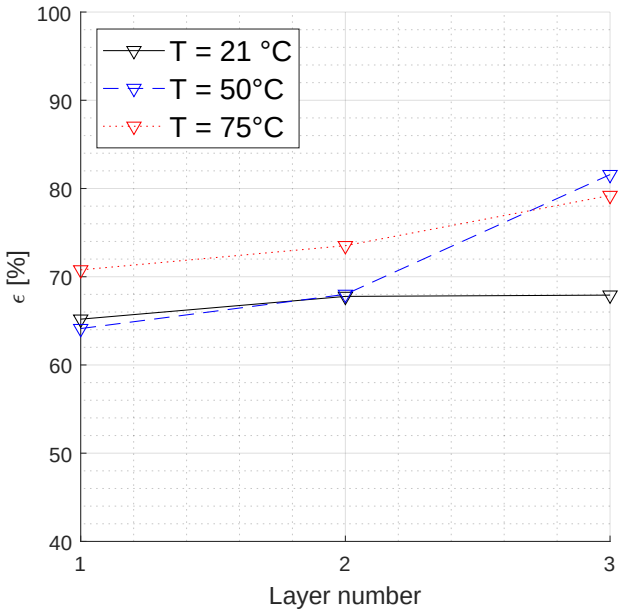

Figure 7.14: Development of porosity during layer build-up at $U = 1.5\,\mathrm{m/s}$. $V_{drop} = 100\,\mathrm{nl}$, corresponding to exp. No. 28 (solid ∇), 29 (dashed ∇) and 30 (dotted ∇).

the non-perfect adiabatic conditions. Indeed, intensified heat input was observed to have much less effect on droplet drying times than a comparable increase in flow velocity. Regarding the comparison of droplet size, one can see that the values of porosity lie in the same range. Therefore, no clear correlation between droplet size and porosity could be determined from the corresponding experiments.

7.10 Further investigation on porosity evolution from sessile sodium benzoate droplets

Corresponding to Section 6.6, the structural volumes and layer porosities of the present experimental study are presented in Table 7.2. Same as discussed before, third layer porosities tend to be higher than the cumulatively obtained ones. This behavior persists for 100 nl droplets and could be confirmed to be due to enhanced cavity inclusion of the second and third layer through the conducted μ-CT measurements. Furthermore, the trend towards comparably low porosities at slow drying conditions could be clarified again through the purely diffusive experiments. The fluctuation which can be seen in both cumulative as well as individual layer porosity in Table 7.2 is yet again due to structural uniqueness.

Table 7.2: Theoretical solid volumes, measured structural volumes and corresponding individual as well as cumulative porosities attained during layer build-up from sessile sodium benzoate droplets.

	1^{st} layer			2^{nd} layer				3^{rd} layer				Structure			
Exp. No.	$V_{s,theo}$ [nl]	V_{struc} [nl]	ε_{layer} [−]	$V_{s,theo}$ [nl]	V_{struc} [nl]	$V_{s,tot}$ [nl]	ε_{layer} [−]	$V_{s,theo}$ [nl]	V_{struc} [nl]	$V_{s,tot}$ [nl]	ε_{layer} [−]	N_{drop} [−]	$V_{s,theo}$ [nl]	V_{tot} [nl]	ε [−]
16	70.4	98	0.28	35.2	228	130	0.73	70.4	438	209.8	0.66	5	176	438	0.60
17	105.6	188	0.44	70.4	374	186	0.62	35.2	454	79.8	0.56	6	211.2	454	0.54
18	105.6	213	0.50	70.4	385	173	0.59	70.4	752	366.4	0.81	7	246.4	752	0.67
19	70.4	236	0.70	105.6	932	696	0.85	70.4	1908	975.4	0.93	7	246.4	1908	0.87
20	3.5	5.78	0.39	7.04	25.6	19.8	0.64	7.04	54.8	29.18	0.76	5	17.6	54.8	0.68
21	442.8	906	0.51	442.8	2017	1111.4	0.60	442.8	3611	593.5	0.72	9	1328.4	3611	0.63
22	295.2	876	0.66	442.8	2468	1592	0.72	442.8	4542	2073	0.79	8	1180.8	4542	0.74
23	44.3	66.6	0.34	44.3	201	134.73	0.67	44.28	359	157.5	0.72	9	132.8	358.8	0.63
24	14.8	44.1	0.67	29.5	174	129.55	0.77	29.52	369	195.4	0.85	5	73.8	369	0.80
25	228.8	544	0.58	686.4	3469	2925	0.77	457.6	5868	2399	0.81	6	1373	5868	0.77
26	457.6	1420	0.68	686.4	3750	2331	0.71	686.4	7192	3441	0.80	8	1830	3441	0.75
27	45.8	83.2	0.45	45.8	168	85	0.46	45.8	288	120	0.62	6	137	288	0.52
28	22.9	65.7	0.65	45.8	213	147	0.69	68.64	428	214	0.68	6	137	428	0.68
29	45.8	128	0.64	22.9	215	87	0.74	68.64	745	531	0.87	6	137	745	0.82
30	45.8	157	0.71	68.6	432	275	0.75	68.64	881	448	0.85	8	183	880	0.79

7.11 Conclusions

An experimental series that replicates successive layer built-up from dried sodium benzoate-laden droplets was presented. Sessile droplets were successively applied onto a glass substrate in a droplet-by-droplet manner and dried under various conditions up to technical. Hereby, a simplified coating layer was incrementally created. The morphology of the simplified layer structure that incrementally forms from individual deposits was analyzed via white-light interferometry and X-ray micro-computed tomography. As already described in Section 6.5, ring structures as commonly observed for single deposits were identified to be the recurring and determining pattern during the entire layer build-up, even at low solid content and droplet volume. In the course of the present investigation, the interior structure of these rings was made visible through the conducted μ-CT experiments in addition to the general surface profile. Hereby, it was discovered that the sodium benzoate rings rather are spanning structures with large cavities in the middle, than a homogeneous porous network. Individual structures emerging at the start of the process are made up of several rings, either stacked over one another, or positioned next to another. This creates conical, simultaneously arising tower-like substructures. Therein, each ring's main cavities are retained, resulting in construction of several spanning structures stacked on top or next each other and, thus, in a very high overall porosity.

Droplet positioning in respect to the rings at the basis, or in other words central or non-central positioning, was identified as the key parameter influencing morphology during this stage of layer build-up. In the further course of the addition process, the previously formed individual substructures merge either by extension of their rims or by formation of solid bridges in between the substructures. Both options result in a grown layer.

Drying conditions, or more precisely high airflow velocities, showed influence on morphology as well. Solids are hereby increasingly transported to the upstream side, forming an asymmetrical, crescent shaped deposit, instead of symmetrical ring-like structures. Through the associated experiments, the simulatively obtained evaporation flux profiles that will be discussed in Chapter 9 could thereby be proven experimentally as well. Nonetheless, the asymmetries in conical deposits caused by this overflow finally played a subordinate role towards the end of overall layer formation.

With respect to porosity development, several conclusions can be drawn in addition to the ones made in Chapter 6. The obtained porosities were relatively high in all experimental series. This circumstance was confirmed to be due to the recurring inclusion of large cavities for sodium benzoate. As the other colloidal substances, namely B_4C and SiO_2/TiO_2, showed similarly high porosities, it can be deduced that the respective ring structures made from nano- or microparticles also contain large, spanned cavities. The same can be said for the preservation of these cavities during layer build-up, since monitoring of porosity over the course of incremental deposit addition revealed a consistent increase with increasing layer number for all substances. This phenomenon can only be reasoned by more frequent inclusion of cavities for growth on already existing residues, instead of growth on a smooth substrate. The postulates made in the previous chapter regarding inclusion and inclusion frequency of such cavities could thus be confirmed.

Same as before, the highest drying rates within the miniature drying chamber could be imposed through amplification of airflow velocity, while variation of temperature did not show such a significant influence. In addition to these known variations of convective conditions, also the droplet conditions, namely solid content and droplet volume, were varied in this study. The reduction of solid content naturally resulted in a slower drying process and different structure formation with a significantly higher amount of rewetting and a correspondingly increased retaining of basic ring shapes on the substrate. This coincided with generally lower porosities than obtained with high solid laden droplets, which can be reasoned in slower crust formation and drying compared at same convective conditions. The variation of droplet size naturally speeds up the drying as well, yet since solid amount and distances for solid transport are simultaneously scaled down, morphology and porosity did not show notable differences. This fact may however only be true because the basic microliter droplets are already at a scale where gravitational or other macroscopic forces are insignificant. This means that the application of less droplets with higher volume is recommended to create a less porous coating layer with the same amount of material, and, consequently, the operation with smaller droplets during sessile droplet deposition as well as during spray on in fluidized bed is expected to result in more porous layers.

Chapter 8

Fluidized bed coating experiments

In addition to analyzing layer build-up from dried sessile droplets containing solids on planar surfaces, coating of particles within a fluidized bed was also examined in order to improve understanding of layer formation. The results of this undertaken coating series within the fluidized bed plant described in Section 3.2.1 represent the third part of the experimental investigation in this dissertation. They are presented in this chapter.

Although fluidized bed coating is not the focus of this study, these complementary experiments were carried out in order to illustrate the main trends in FBC and highlight the differences between sessile droplets and droplets sprayed on core particles in a fluidized bed. This includes both, the development during layer build-up as well as the properties of resulting layers.

8.1 Experimental execution and plan

A series of fluidized bed coating experiments with sodium benzoate on glass particles was conducted in batch mode. Hereby, naturally, the layer build-up cannot be observed in a droplet-by-droplet manner. Instead, samples were taken at specified times during the coating process, or in other words after the entry of certain amounts of NaB coating solution into the fluidization chamber. Three exemplary particles were randomly selected from each sample and analyzed with regards to porosity via μ-CT, as described in Section 5.3.2. Self-evident, also not all drying conditions could be equally selected. Drying airflow velocities of 0.1 m/s were insufficient to fluidize the core particles. Consequently, only 1 m/s and 1.5 m/s were tested. This corresponds to a volume flow rate of 63.62 m^3/h and 95.43 m^3/h, respectively. In addition to that, at a temperature of 21 °C the dominant process within the bed was agglomeration, not coating. This phenomenon is described by Strenzke et al. (2020). Therefore, corresponding experiments at room temperature failed due to production of oversized agglomerates, before the desired process runtime was reached. Table 8.1 lists the complementary fluidized bed experiments that were conducted and the corresponding drying conditions in comparison to the sessile droplet series. Apart from the drying conditions, all other parameters, like bed mass M_{bed}, coating material spray rate $\dot{M}_{sus}$ and process time t_{end},

Table 8.1: List of conducted fluidized bed coating experiments and used parameters.

Exp. No.	Material	ω_{solid} [wt%]	U_{inlet} [m/s]	T_{inlet} [°C]	M_{bed} [kg]	$\dot{M}_{sus}$ [g/h]	t_{end} [min]
31	NaB	30	1.0	50	1	500	60
32	NaB	30	1.0	75	1	500	60
33	NaB	30	1.5	50	1	500	60
34	NaB	30	1.5	75	1	500	60
35	NaB	05	1.0	50	1	500	60
36	NaB	05	1.0	75	1	500	60
37	NaB	05	1.5	50	1	500	60
38	NaB	05	1.5	75	1	500	60

were kept constant.

8.2 Results and discussion

In Figure 8.1, the shell porosities of particles coated with $\omega_{solid} = 30\,\text{wt\%}$ NaB after 15, 20 and 60 minutes are displayed, respectively. In comparison to the results in Section 6.5.2, one can see that the acquired values are significantly lower. While the sessile droplet porosity lies between 0.7 and 0.8 (Figure 6.12, right), the shells produced within the laboratory fluidized bed plant obtain a porosity in the region of 0.3 to 0.4. There are several conceivable reasons for this general offset. First, sprayed droplets have an initial impact period including a greater spread on the substrate before they reach the spherical cap equilibrium shape (Delele et al., 2016). Since drying and solid accumulation already take place during this stage and the small sprayed-on droplets dry quickly, the resulting residues are likely to occupy a larger area, but not extend as high. Second, other core particles may touch or skim the resting droplet. In both cases, shape and spread of the droplet are altered; the process is significantly disturbed and, therefore, may deviate from drying and accumulation of sessile droplets outside the fluidized bed. In addition, one should note that during the sessile droplet layer build-up every droplet was carefully deposited. This means that, apart from slight rewetting, the pre-existing structures remained unchanged. Within a fluidized bed though, already existing parts of a coating layer are subjected to interparticle collisions and collisions with the fluidization chamber. These collisions certainly affect the existing structures and are likely to act in a compressing manner. Especially the characteristic network of structural cavities inside the ring structures with a relatively thin outer wall, as described in Section 7, is likely to be destroyed and condensed to some degree by such collisions.

Despite the general offset in porosity, similar trends regarding its development can be identified. Same as for the sessile droplets, porosity increases in the earlier stages of layer build-up. After a certain amount of material has been deposited, this increase flattens. After 20 min, the shell porosity remains roughly the same. This is again reasoned by the receding influence of the

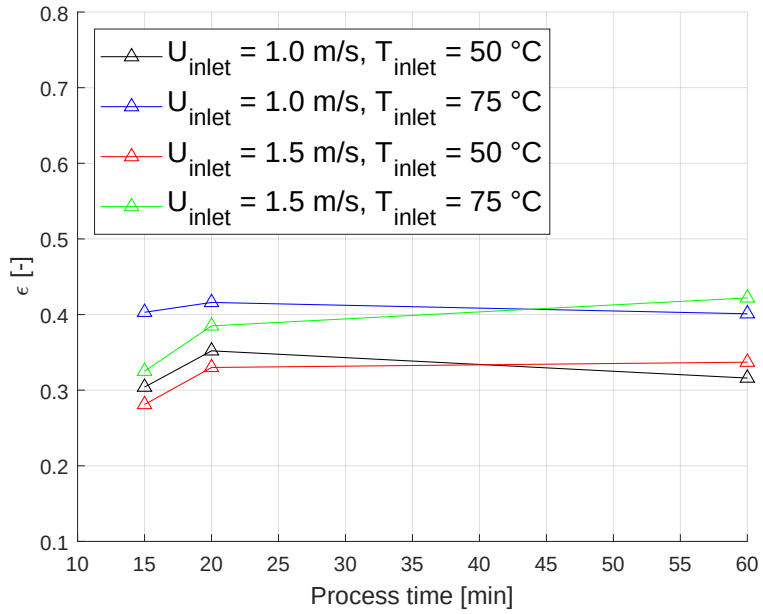

Figure 8.1: Shell porosity over the course of fluidized bed coating experiments with 30 wt% sodium benzoate on glass particles under different drying conditions.

substrate. While the first deposits rest on a flat surface (or relatively flat compared to the droplet size), follow-up residues are built on already existing exaltations and indentations and therefore behave very differently. After a while, all deposits emerge on an irregular surface. From then on, they only expand the layer, but do not alter the overall surface morphology, which remains similarly irregular. Thus, porosity stays relatively constant. This phenomenon is therefore confirmed via the fluidized bed coating experiments, as herein a much larger number of droplets was deposited and the substrate's influence at the end of the process became negligible, compared to equivalent sessile droplet experiments with much less droplets.

Once more, in fluidized bed coating, the resulting porosity increases with conditions enabling a faster drying. In the present FBC experiments, however, an alteration of temperature seems to have more impact on coating layer porosity than a change in airflow velocity, contrary to the relation found in the sodium benzoate sessile droplet drying series. Consequently, the two experimental series with 75 °C inlet temperature yielded the highest porosities, while the experiments at 50 °C resulted in porosities of circa 0.1 less. The alteration of airflow velocity in both cases resulted only in a minor porosity change (about 0.02). A reason for this may be that an increase in air flow velocity certainly increases the coefficients of gas-side heat and mass transfer in the sessile droplet drying chamber. In the fluidized bed though, expansion is increased at higher air velocity, whereas the interface transfer coefficients remain nearly constant.

The surface morphology of sodium benzoate layers as obtained via scanning electron microscopy is depicted in Figure 8.2. It shows different surface structures of the coating layer. First of all, it can be seen that after the amount of deposited coating material, no classical ring-structures or the like are remaining. This means that from here-on, surface morphology rather refers to the

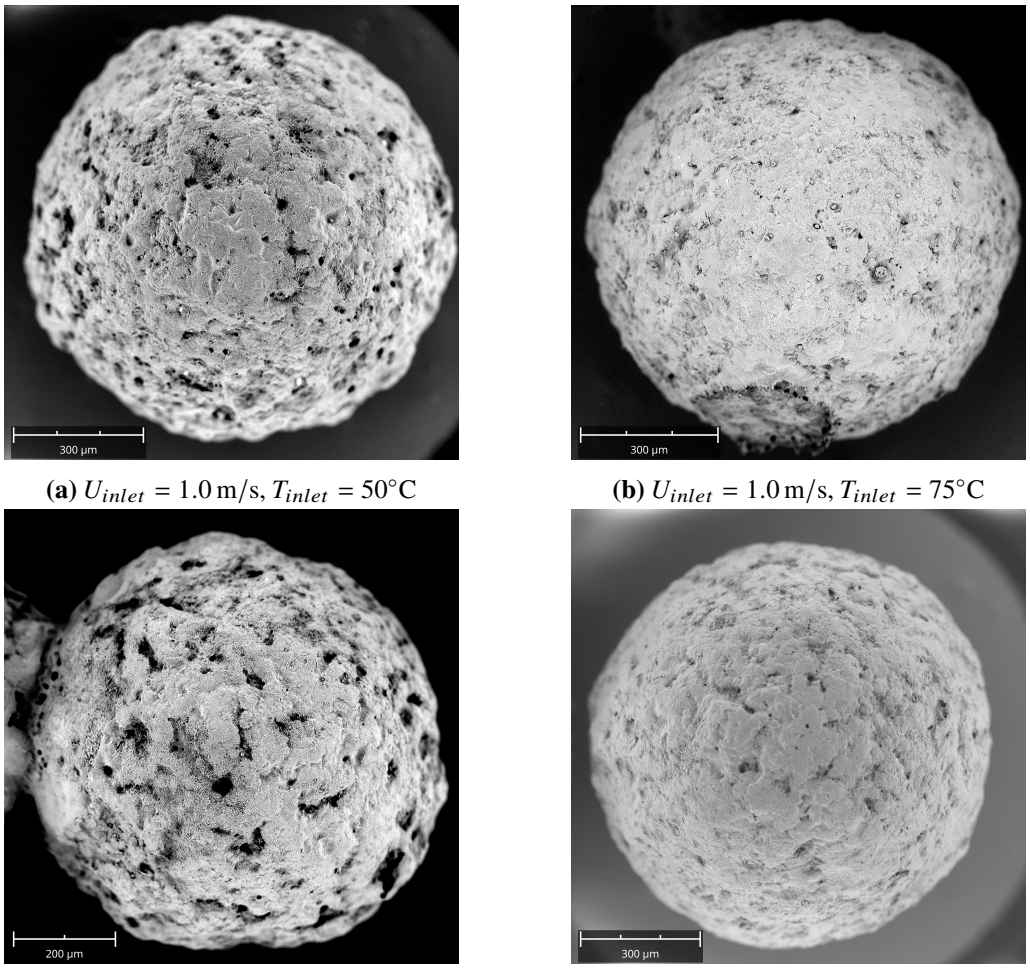

(a) $U_{inlet} = 1.0\,\mathrm{m/s}$, $T_{inlet} = 50°\mathrm{C}$

(b) $U_{inlet} = 1.0\,\mathrm{m/s}$, $T_{inlet} = 75°\mathrm{C}$

(c) $U_{inlet} = 1.5\,\mathrm{m/s}$, $T_{inlet} = 50°\mathrm{C}$

(d) $U_{inlet} = 1.5\,\mathrm{m/s}$, $T_{inlet} = 75°\mathrm{C}$

Figure 8.2: Scanning electron microscope images of surface morphologies of glass beads coated with 30 wt% sodium benzoate at different convective conditions within a fluidized bed.

existence of gaps or fissures, as well as the distribution of coating thickness. If one compares the SEM measurements at 50 °C (left) to the ones at 75 °C (right), it can be noticed that the layers at higher temperature appear to be more uniform, or in other words their height profile seems to be more leveled, with less gaps or fissures.

The layer porosities from spray coating experiments featuring a 5 wt% sodium benzoate solution are listed in Table 8.2. The solid content used for this experimental series proved to be too low to obtain feasible porosity values after 15 and 20 minutes, respectively. The cause for this is that the amount of solid residues is not enough to form a consistent layer with a thickness great enough that it can be safely distinguished from the core particle within the μ-CT and in turn sensibly evaluated. Rather, so-called island coating takes place, meaning that certain areas are covered while others remain completely uncoated. Consequently it was not possible to monitor the layer build-up over time, as done for experiments No. 31 – 34. Nevertheless, after 60 minutes, the covered areas were large enough and featured sufficient amounts of solids for a porosity to be calculated, though

Table 8.2: Porosities obtained for fluidized bed spray coating experiments with low solid content NaB coating solution.

Exp. No.	ω_{solid} [wt%]	U_{inlet} [m/s]	T_{inlet} [°C]	t_{end} [min]	ε [−]
35	5	1.0	50	60	0.28
36	5	1.0	75	60	0.33
37	5	1.5	50	60	0.28
38	5	1.5	75	60	0.38

uncovered spots still remained. The average porosity of these coated areas can thus be compared to the previously obtained layer porosities of the corresponding high solid content cases.

The porosity offset to sessile droplet drying that was identified for high solid content cases still persists for the 5 wt% sodium benzoate solution. Id est the porosities in Table 8.2 are significantly lower than the layer porosities discussed in Section 7.8 (experiments No. 16 to 20). In addition to this general offset and compared to the final results in Figure 8.1, all porosities of 5 wt% FBC cases are lower than their 30 wt% counterparts at the same convective conditions. This can again be reasoned in a slower crust formation and a longer time period of wet residues during which compressing effects can take place. Consequently, layers created via spray fluidized bed coating with low solid content droplets were the least porous of all experimental series conducted in the course of this dissertation.

Regarding dependency on drying conditions, the same observations as for fluidized bed coating with 30 wt% droplets can be made. Again, temperature seems to have a greater effect on porosity than airflow velocity, resulting in higher porosities of the experiments at 75 °C. Nevertheless, the values obtained in experiments No. $35 - 38$ need to be cautiously handled, due to their disperse nature and the low amount of solids available for μ-CT scanning and follow-up image processing.

SEM images of glass particles coated with 5 wt% sodium benzoate are depicted in Figure 8.3. One can see that in contrast to the corresponding experiments at high solid content, completely uncoated areas remain. In addition to this, the described tendency to island coating is much more severe at lower temperatures. Especially coatings produced at low temperatures and low airflow velocities (Figure 8.3a) show extensive concentration differences between areas. This leads to the conclusion that island coating is enhanced for conditions promoting slow drying processes. This observation may be explained by the higher possibility of two or more droplets adjoining into one on the core particle's surface, which in turn results from the fact that prior applied droplets in the vicinity are less likely to be already dried when further droplets are spayed on the surface.

Figure 8.3a shows extensive island coating. This means that for such particles areas that are only slightly sprinkled can be spotted. Moreover, some individual solid deposits can clearly be made out in these areas. If these solid residues are small enough, it is safe to assume that they arose from only one or a very small number of droplets and were not significantly extended or connected to

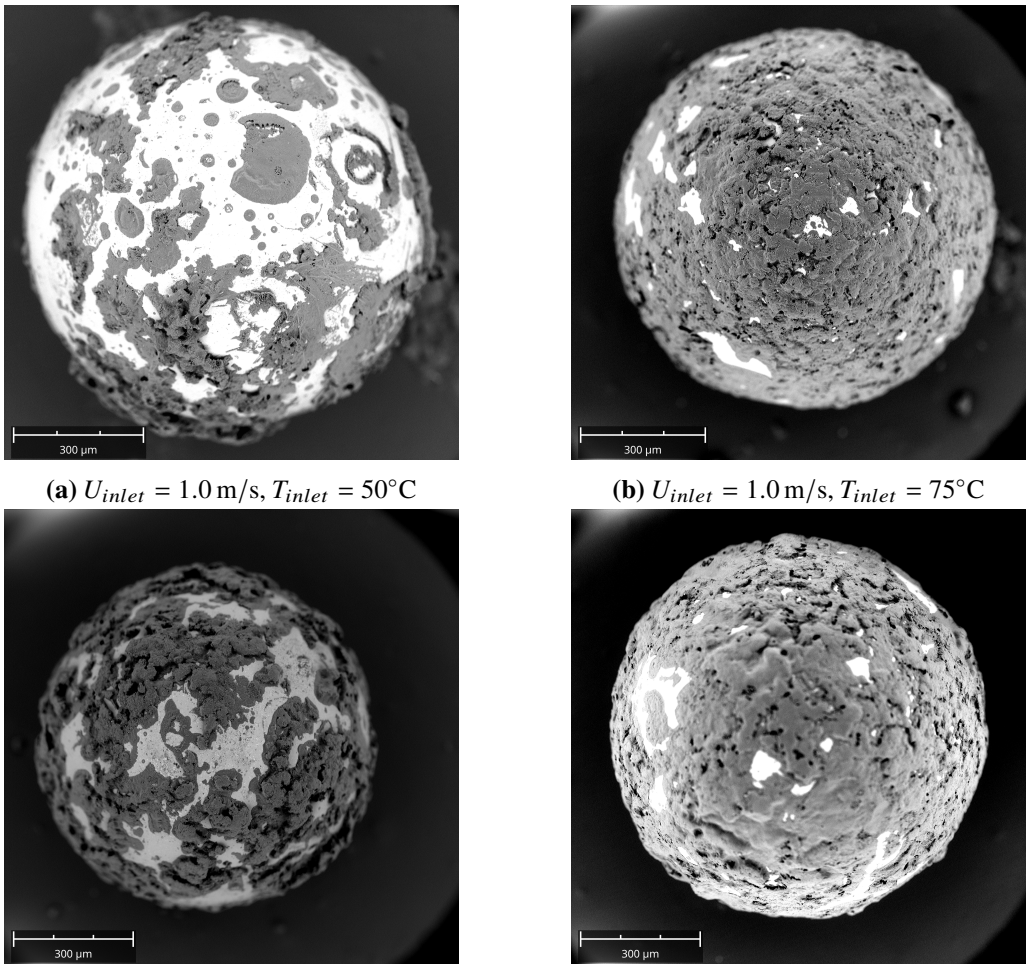

(a) $U_{inlet} = 1.0\,\mathrm{m/s}$, $T_{inlet} = 50°\mathrm{C}$

(b) $U_{inlet} = 1.0\,\mathrm{m/s}$, $T_{inlet} = 75°\mathrm{C}$

(c) $U_{inlet} = 1.5\,\mathrm{m/s}$, $T_{inlet} = 50°\mathrm{C}$

(d) $U_{inlet} = 1.5\,\mathrm{m/s}$, $T_{inlet} = 75°\mathrm{C}$

Figure 8.3: Scanning electron microscope images of surface morphologies for 5 wt% sodium benzoate coatings on glass beads at different convective conditions produced in a fluidized bed, after 60 minutes.

a greater coating material deposit by the time the process was terminated. Thus, these individual deposits on a core particle's surface can be compared to the low solid content sessile droplet residues that were analyzed in Section 7.8. Figure 8.4 depicts SEM images of such small solitary deposits created during experiment No. 35.

The formation of ring-structures observed for sessile droplets is clearly also present for a nozzle-based droplet dispensing. This can be deduced from the round deposits in the left part of Figure 8.4. Apparently, this morphology is only distorted if the droplet gets smeared before the drying is finished. This can be the case for example through an interparticle collision at the droplet's position. If the droplet is not disturbed during drying, similar structures as illustrated in Figure 7.10 for sessile droplets arise. They feature strong signs of ring formation with few accumulations in the center. The various ring sizes that can be observed are hereby most likely due to variations of droplet volume, or in other words the droplet volume fluctuation that naturally accompanies a nozzle-based dispensing. The outer ring often shows signs of corrugation and is therefore usually less smooth as

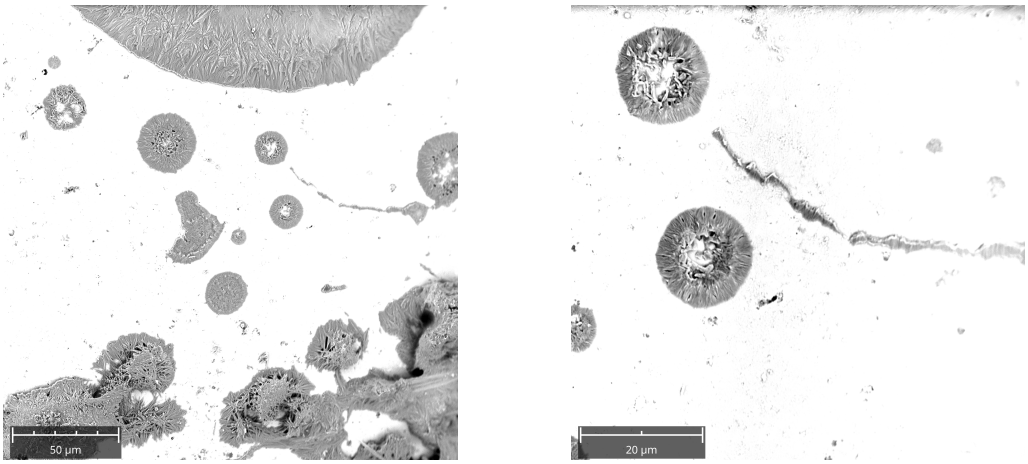

Figure 8.4: SEM images of small deposits in sprinkled areas on a core particle's surface from 5 wt% NaB solution droplets. The experiment was executed at 1.0 m/s airflow velocity and a temperature of 50 °C (exp. No. 35).

for most sessile droplets. It hereby shows similarities to the corrugated rim structures observed for a partial second wetting of an initial sessile droplet residue (Figure 7.5). This fact may suggest that either smaller or heavily smeared follow-up droplets might have touched and partially rewetted the existing ring deposits, resulting in the same mechanism as discussed in Section 7.4.

The general results of porosity trends and the offset to sessile droplets, as well as the morphology hereby conform with the findings of Rieck et al. (2015), who investigated coating processes with sodium benzoate within the same fluidized bed plant, but under different drying conditions and with smaller particles. The presence of ring structures on the core particles' surface somewhat contradicts the general estimations of Hu and Larson (2006), who assessed that substrate heating would reduce ring-formation tendencies. This, however, is quite probably due to the relatively low temperatures, the reduced heat conduction from air to core particles compared to a continuous substrate heating in the sessile droplet case, and the correspondingly intensified effect of evaporative cooling on the core particles than on a heated substrate.

8.3 Conclusions

Complementary experiments were carried out within a fluidized bed, in addition to the prior series with deposited droplets. Herein, glass particles were coated with a sodium benzoate solution and analyzed via X-ray micro-tomography and scanning electron microscopy. In comparison to the prior investigated NaB layers originating from sessile droplets, porosities were significantly lower, but followed similar trends regarding evolution during layer build-up and dependency on drying conditions. The offset can hereby be reasoned in the different conditions within a fluidized bed, especially the presence of significantly more droplets simultaneously on the surface, some of which already beginning to dry on the way to the particle, or uniting and forming completely new structures. Additionally, the offset can be reasoned in different spray-on wetting behavior and interparticle collisions. It can furthermore be attributed to the different structural analysis

methods, as with the white-light interferometry a pore- and cavity-free volume was determined, which contains no information about the internal structure of the deposit, while the porosity via X-ray micro-tomography is calculated without including the volume of such large cavities in the structural volume, because the applied closing operator only fills the included pores (as depicted in Figure 5.4).

The comparison of morphologies turned out to be relatively difficult, because of the very different conditions of origin and droplet numbers involved. Nevertheless, similar structural details, such as ring-shaped deposits, could be identified in some places.

Chapter 9

In silico study on sessile droplet drying

In the following simulative study, quasi-steady-state evaporation in laminar flow above a sessile droplet is considered and a finite volume method is used to depict the vapor concentration distribution within the droplet's surroundings. This method allows for a flux profile analysis that can also account for an underlying forced convection around the droplet, further distorting the flux beyond the known non-uniformity. The newly implemented feature subsequently is used to study the flux distribution for different ambient flow conditions and at different times, or, more specifically, contact angles. The simultaneous convective drying of several droplets is also examined. This chapter is an extended version of Janocha and Tsotsas (2021a).

9.1 CFD simulation setup

9.1.1 Simulation approach

A pure water droplet is resting on a flat, impermeable and partially wetting surface, with a distance l from the substrate's edge, as illustrated in Figure 2.1. Based on the CA determining experiments in Section 4.3.1 with pure water on glass plates, the initially formed contact angle θ is set to 72 degrees. This corresponds to the experiments of David et al. (2007). The droplet is overflown by air with temperature T_a, velocity U_a, and humidity ϕ that corresponds to the partial pressures of vapor $p_{vapor,a}$ and air $p_{air,a}$. The droplet's surface is considered isothermal at wet bulb temperature. Heat transfer is otherwise not considered. At the droplet-air interface, vapor concentration is assumed to correspond to saturation concentration at wet bulb temperature, according to the diffusion-limited approach. Furthermore, the Kelvin effect is neglected, and thus, saturated vapor concentration c_{sat} at the surface is also considered uniform.

As a result of these simplifications, the saturated vapor pressure is described as a uniform boundary condition over the entire droplet-air interface and the entire simulation time. It can be calculated via the Antoine equation (Appendix C.1.5). The corresponding saturation concentration can be determined via the ideal gas law:

Table 9.1: Main simulation and material parameters.

Parameter	Value	Unit
c_{sat}	8.24	$\mathrm{g\,m^{-3}}$
D	$26.1 \cdot 10^{-6}$	$\mathrm{m^2\,s^{-1}}$
l	9 – 45	mm
p	101.3	kPa
R	0.9	mm
$\tilde{R}_{vapor}$	461.5	$\mathrm{J\,kg^{-1}\,K^{-1}}$
T_a	25	°C
T_{wb}	8.3	°C
U_a	0 – 1.5	$\mathrm{m\,s^{-1}}$
V_{drop}	1	μl
η_{air}	$1.837 \cdot 10^{-5}$	Pa s
η_{water}	$8.91 \cdot 10^{-4}$	Pa s
θ	72 – 10	°
ρ_{air}	1.1839	$\mathrm{kg\,m^{-3}}$
$\sigma_{water,air}$	0.0741	$\mathrm{N\,m^{-1}}$
ϕ	0	–

$$c_{sat} = \frac{p_{sat}}{\tilde{R}_{vapor}\,T}. \tag{9.1}$$

Herein, $\tilde{R}_{vapor}$ is the specific gas constant of vapor. This calculation results in a saturation concentration of $8.24\,\mathrm{g\,m^{-3}}$ at the corresponding wet bulb temperature T_{wb} and system pressure p listed in Table 9.1. The difference to vapor concentration c_a in the surroundings is the driving force for the evaporation. Table 9.1 summarizes the tested parameters and used material values.

The material properties that were not specifically investigated experimentally were taken from Glück (1991). D is the diffusion coefficient of vapor in large excess of air, taken from Marrero and Mason (1972). In order to keep the simulation as focused as possible, the temperature dependence of D in the flow field is neglected. At this point it shall be noted that alteration of temperature and humidity while keeping the ambient velocity constant has very limited influence on the flux profile. Studies certainly show influence on the overall evaporation rate of the droplet (Korenchenko and Zhukova, 2022), however, the local flux distribution is affected only marginally. This means that although the flux profile is certainly dependent on the advection to diffusion ratio, its dependency on the ambient velocity is far greater than on the other parameters of ambient air that affect the overall evaporation rate, but not the boundary layer. This statement is valid for both single and binary droplet setups within the tested range of velocity, position and contact angle. Because the overall evaporation rate of sessile droplets was discussed extensively in literature (Erbil, 2012), and the influence of air temperature and humidity can be accounted for in the respective driving

force, these quantities are not in the focus of the analyses hereafter.

Under the conditions from Table 9.1, the maximum capillary number for the adhering droplet is $3.72 \cdot 10^{-4}$, based on Equation 2.24. The calculation of the maximum Bond number of the droplet (Equation 2.1) yields 0.039. Same as in the preceding experimental investigations, these characteristic values in turn mean that all droplets take the shape of a spherical cap and stay in this shape, even at the severest conditions tested in this in silico study (Lubarda and Talke, 2011). The maximum Reynolds number for the droplet overflow in the simulated cases amounts to $Re_{drop,max} = 174$ (Equation 2.27), which is below the critical Reynolds number for an overflow of semi-spherical objects (Mikulencak and Morris, 2004). Within the present analysis, a maximum distance l of $50R$ in upstream direction of the droplet is chosen. At the chosen maximum velocity ($1.5\,\mathrm{m\,s^{-1}}$), this results in a Reynolds number of the flow over the plate of 9667 at the position of the droplet, calculated with Equation 2.25. This is significantly below the critical value of 10^5 for a flow over a planar surface. Therefore, all flows and the corresponding boundary layers within the presented model stay in the laminar regime. A simulation of higher velocities or higher contact angles was consciously refrained, in order to avoid random turbulences in the flow field or instabilities in droplet shape. These effects would render the present quasi-steady-state contemplation unusable. The chosen simulative setup therefore is represented by a Schmidt number of $Sc = 0.59$ and a maximum Péclet number of $Pe = 103$.

One obtains a minimum velocity boundary layer thickness of 1.5 mm at the droplet's position, when inserting the highest simulated ambient velocity and the minimum distance from the plate's edge (Equation 2.23). Since the initial droplet height can be calculated to be 0.66 mm (based on Equation 2.3 and listed in Appendix D.1), all droplets in this simulation are completely submerged in the velocity boundary layer of the flow and therefore fully subjected to the developed velocity profile alongside the substrate. This fact will later on be seen to lead to a significantly different drying behavior than the one of, exempli gratia, suspended hemispheres within a uniform flow.

9.1.2 Computational approach

The computational fluid dynamics software OpenFOAM V7 was used to obtain the solution for the three-dimensional problem described above. This CFD software incorporates the finite volume method (FVM) as the numerical technique. A cuboidal computational domain was chosen, in order to represent the conditions of the corresponding experimental setup and allow for a straightforward application of the initial velocity at the rectangular inlet. A uniform velocity is prescribed at the domain inlet and further coupled with an atmospheric pressure outlet. The substrate is assumed to be adiabatic. At the domain bottom, id est the substrate, a no-slip condition is applied to allow for velocity boundary layer development. Slip conditions are prescribed at the top and the sides of the cuboid domain to simulate a free flow over the substrate plane. The vapor concentration at the domain's borders is set to have a gradient of zero.

The finite volume method which is used to acquire the surface gradient tracks the volume fraction α rather than the corresponding concentration. Applying the ideal gas law, Equation 2.19 is

transformed to:

$$\overrightarrow{J} = D \frac{p}{\tilde{R}_{vapor} T w b} \nabla \alpha. \tag{9.2}$$

At this point it shall be noted that Equation 9.2 refers to the droplet's surface and does not account explicitly for the influence of a forced flow field. Rather, the presence of forced convection influences the development of the boundary layer over the droplet and, in turn, the resulting gradient at the interface in steady-state, id est $\nabla \alpha$. This gradient differs greatly, depending on the surrounding macroscopic flow conditions. It is solved via a FVM jointly with the corresponding mass and momentum transport equations, namely Equations 2.29, 2.34 and 2.35, from which the local flow velocity U and the advection of vapor are obtained.

For cases with little to no ambient velocity (purely diffusive benchmark cases), the domain has to be large enough to ensure that the field values reach the ambient conditions sufficiently accurately. Furthermore, it must be ensured that the target gradient is insignificantly affected by the domain size (DOS). To ascertain the necessary minimum domain size, the relative improvement I of a simulation n with regard to its predecessor with smaller computational domain is calculated and the changes in the individual results regarding total evaporative flux are compared:

$$I_n = \frac{|J_{tot,n} - J_{tot,n-1}|}{J_{tot,n-1}}. \tag{9.3}$$

These tests regarding size showed that a domain that spans a distance of $50R$ in every direction from the center of the droplet generates evaporation flux values with sufficient accuracy, meaning an improvement of less than 1 % in case of any further domain enlargement. This result corresponds to the outcome of a similar domain study from Bhardwaj (2018). This distance furthermore ensures that errors due to numerical residues caused by the proximity of the outer boundary can be prevented, as for example documented by Girard et al. (2008).

The computational grid is comprised of hexagonal cells and consists of a cell basis (CB) of 200 cells in each direction, id est a $50R$ distance. The mass transport and flow around the droplet are not approximated via add-on models. Instead, a direct numerical simulation (DNS) approach is taken and a mesh that is fine enough to completely resolve processes in the flow and boundary layer is employed. To adequately resolve the boundary layer around the droplet, the grid is subjected to a further refinement process that originates at the phase boundary. In the course of this, additional mesh layers are added through adaptive splitting of cells at the interfacial boundary. These additional splitted layers (SL) are set to expand with a factor of 1.1 until they reach the size of the non-splitted cells, in order to ensure a smooth transition and avoid computational problems or numerical artefacts. An amount of 10 inserted layers proved to supply a sufficient resolution of the boundary layers and, therefore, the evaporation flux around the droplet, meaning less than 1 % improvement in case of further refinement.

Table 9.2: Results of domain and mesh size convergence studies.

Domain size	I	Number of layers split for droplet boundary resolution	I	Number of base mesh cells for $50R$ distance	I
$10R$	–	5	–	200	–
$25R$	13.6 %	10	1.6 %	300	0.1 %
$40R$	6.4 %	15	0.4 %		
$50R$	1.4 %				
$60R$	0.6 %				

In case of the presence of forced convection, tests proved the postulation that convective setups require less domain size for equivalent convergence. Herein, the results are independent from the domain size even at a domain size of $10R$. However, the distance l from the front edge of the substrate to the center of the droplet is a significant operating parameter in presence of flow. As such, it will be discussed later on. Additionally, for setups with flow, the domain's basic cell size needs to be small enough to adequately resolve the flow field and the flow's velocity boundary layer that forms on the substrate and above the droplet. In consequence, the original number of cells within the grid was increased to confirm a sufficient resolution of the velocity field and the corresponding evaporation flux profile at maximum ambient velocity. Hereby, the initially chosen cell size proved to be accurate enough (less than 1 % improvement upon refinement). The results of the mesh and domain size convergence studies are listed in Table 9.2.

Although the development of vapor concentration in the surrounding flow field shall not be the main focus of the present study, it was also observed in order to ensure a correct display of the diffusion process within the field. Figure 9.1 shows the resulting concentration fields of the last step of the study on convergence. One can see the corresponding insignificant change with further domain enlargement or mesh refinement.

The grid resulting from these tests and the corresponding refinements is structured similarly to most approaches in literature, for example Bouchenna et al. (2017). A section of this mesh is shown in Figure 9.2.

9.1.3 Validation of the model

Hereafter, the presented model is validated against available literature. In contrast to pendant droplets, sessile drops develop a distribution of the evaporation flux even in absence of forced convection, id est in a purely diffusive case without overlaying gas flow. This means that a validation of the present model is possible by comparing the results of diffusion dominated cases calculated with this model to existing solutions in literature. For this validation, the FEM based fitting of Hu and Larson (2002), according to Equations 2.16 and 2.17, was set as a benchmark for the present FVM model. Figure 9.3 displays the good agreement between both solutions. For the studies of convective conditions hereafter, this solution is not applicable. However, it is used for

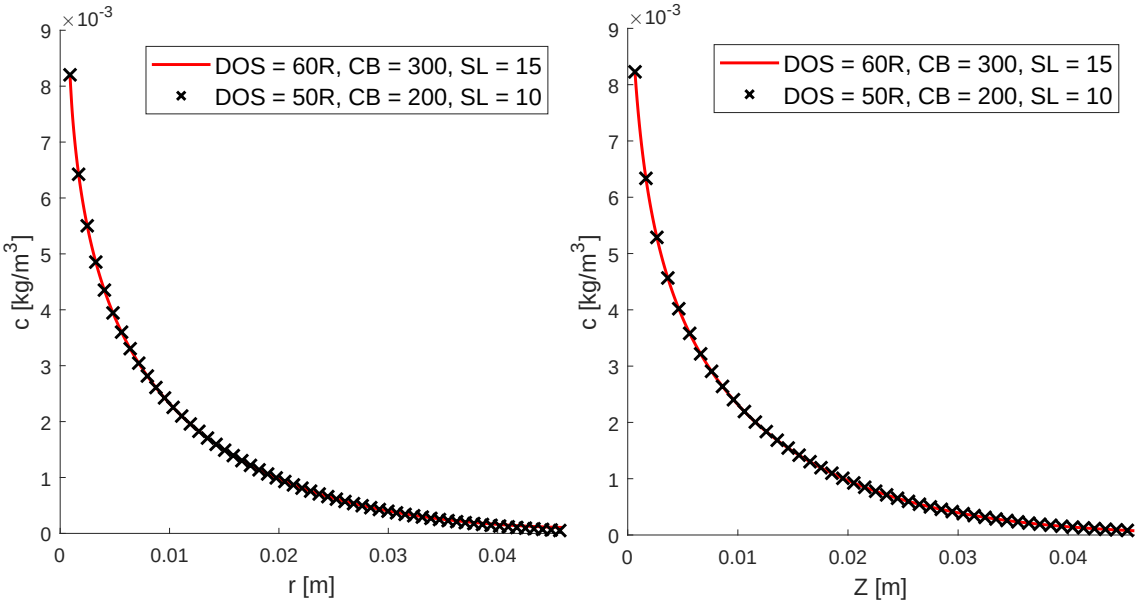

Figure 9.1: Distribution of vapor concentration alongside the r- (left) and z-coordinate (right). A similar development can be seen despite further increased base cell number, number of split layers and domain size.

validation of the model on hand, since the resulting flux distribution shall converge to this solution with decreasing ambient velocity. The sufficient agreement with Hu and Larson (2002), together with the results of the study on necessary grid and domain size (Section 9.1.2) are taken as evidence that the created model delivers physically accurate results in the frame of the deliberately made simplifications.

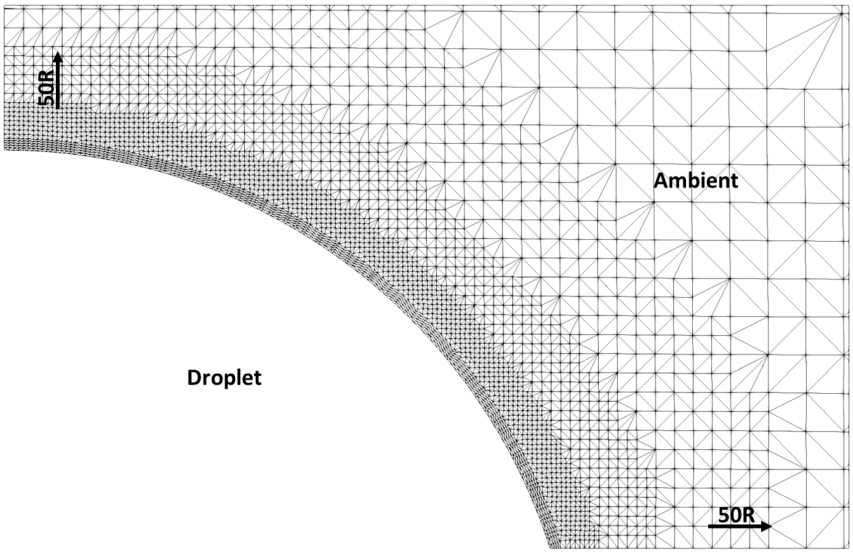

Figure 9.2: Slice of the finite volume mesh above the droplet.

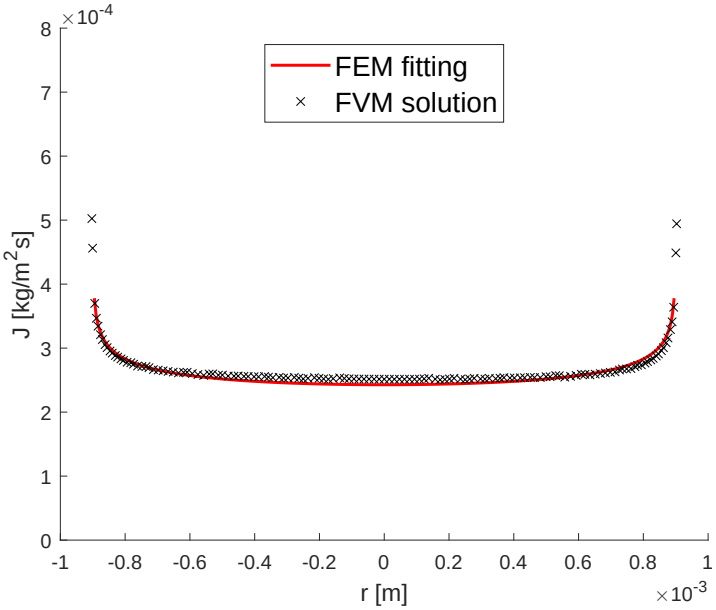

Figure 9.3: Comparison of evaporation flux profiles from FEM simulation data of Hu and Larson (2002) with results of the present model.

9.2 Simulation results and discussion

In the course of this section, the developed model is utilized to study the effect of different convective conditions, droplet properties and ambient parameters on flux distribution. Namely this includes ambient velocity, droplet contact angle and droplet position. Last, the evaporation flux distribution for two adhering droplets drying under forced convection in close proximity to each other are presented and discussed. Same as for Equation 2.14 and Equation 2.16, a coordinate system with its origin at the droplet's center is used for the expedient presentation of the simulations' three-dimensional results. The height coordinate z is used to specify a distance to the substrate plane and the angular coordinate γ specifies the deviation from flow direction, taking a value of $\gamma = 0°$ when parallel and $\gamma = 90°$ when orthogonal to the flow. The radial coordinate r specifies a distance from the droplet center aligned in flow direction. In case studies involving two sessile droplets, also two coordinate origins are placed, therefore enabling a direct comparison of any developments along each droplet's radius or height.

9.2.1 Influence of drying airflow velocity

If an overlaying flow field is present, the transport of vapor in the surrounding air is generally accelerated. Thus, the overall mass transfer within the gas phase and in turn the drying speed is increased. On the upstream side (US) of the droplet, the drying airflow is directed towards the droplet and increases the transport of vapor away from the surface. Therefore, it reduces the local concentration boundary layer thickness. Similarly to the commonly known boundary layer for a flow around a sphere, the concentration boundary layer in the present case increases in thickness in the wake of the droplet. This means that on the one hand, the local evaporative flux is increased on the upstream side, on the other hand the local evaporation flux on the downstream side (DS) gets less increased by this phenomenon and thus is always lower than its upstream side counterpart. Correspondingly, the concentration gradients on the droplet's surface are generally steeper on the upstream side.

A series of simulations was performed in order to investigate the influence of different ambient airflow velocities. The droplet's contact angle was set to 72° and the distance to the substrate edge was 10R in this set of simulations. Alongside greater air velocities, the effect of the evaporation flux shift to the upstream side intensifies. Hence, the mirrored flux distribution that corresponds to the diffusive case shifts in opposite direction to the air flow. This converts the symmetrical evaporative flux distribution for pure diffusion into a downstream-tailed distribution, if a flow field is present. This effect is visualized in Figure 9.4, along a two-dimensional slice in flow direction. Within the droplet this means that an enhanced flow towards the upstream side can be expected, in order to replenish the evaporation loss.

The vector size in Figure 9.4 illustrates the magnitude of the flux. Herein, the classical maximum of local flux along the contact line can be viewed in Figure 9.4a. Again, this enhancement is due to a higher escape probability of evaporating molecules along the edge, or in other words a greater availability of volume for diffusion within this area (Deegan et al., 2000). Particularly in

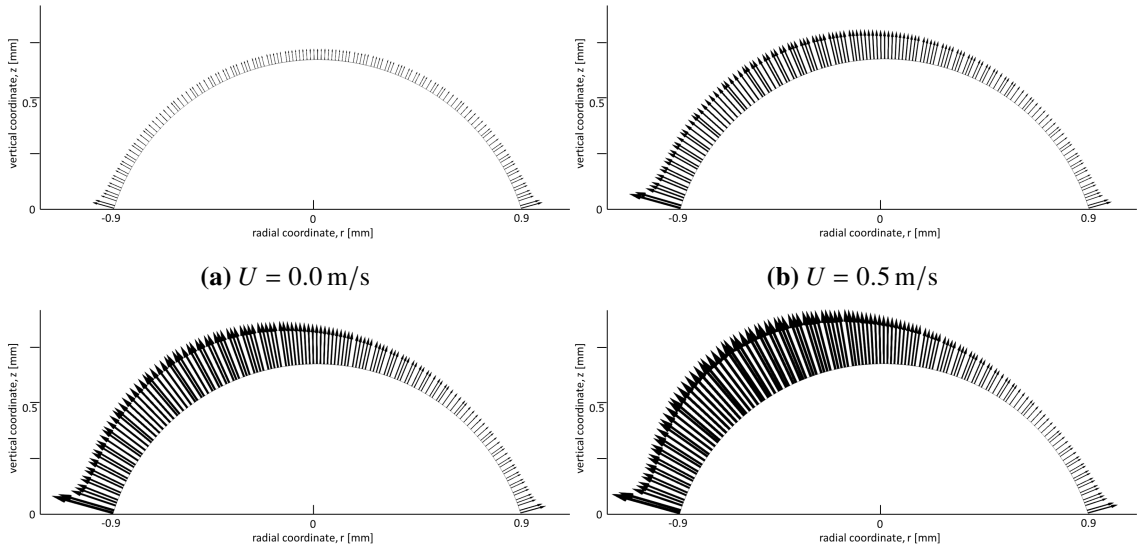

(a) $U = 0.0\,\mathrm{m/s}$ **(b)** $U = 0.5\,\mathrm{m/s}$

(c) $U = 1.0\,\mathrm{m/s}$ **(d)** $U = 1.5\,\mathrm{m/s}$

Figure 9.4: Evaporation flux along a single droplet's surface for different airflow velocities at $\gamma = 0°$.

Figure 9.4d one can see that the forced convection results in a new local maximum that appears in addition to the known maximum at the droplet's edge. This new maximum is located at approximately $R/2$ towards the upstream side. This in turn means, that in addition to the line of locally greatest mass transfer coefficient, id est the droplet-substrate contact line, the overlaying flow profile results in a second area in which a maximum, accompanied by a corresponding local minimum in concentration boundary layer thickness, is formed. To further illustrate this arising of a new maximum, Figure 9.5 (left) shows the flux distribution along the radial coordinate at $\gamma = 0°$ of the droplet's footprint at different flow velocities. To further visualize the shift to the upstream side, one can make the flux dimensionless and put further emphasis on the distribution itself. For this purpose, it makes sense to normalize the evaporation flux by relating all values to the evaporative flux at the droplet's center ($r = 0$). At the same time, the flow velocity can be represented in terms of Reynolds number. The result is shown in the right part of Figure 9.5.

The newly observed local maximum is specific to sessile droplets drying on a substrate. It cannot be seen with suspended spherical or hemispherical objects, as in these cases the boundary layer is smallest at the stagnation point and afterwards increases monotonously. In contrast to the flux increase along the edge, the phenomenon of a new local maximum is not the result of enhanced escape probability, but of the non-uniform velocity field approaching the droplet. Through the velocity boundary layer forming above the substrate, the flow reaches the droplet with an already developed velocity profile with increasing magnitude alongside a rise of the height coordinate. The new maximum's location hereby conforms with the point of greatest orthogonal velocity to the droplet's surface. Consequently, this effect is magnified with increasing ambient velocity, as can be seen in the left part of Figure 9.5, but reduced with a decrease in the droplet's contact angle, as can be observed in Figure 9.10. The latter can be explained by the fact that with diminishing

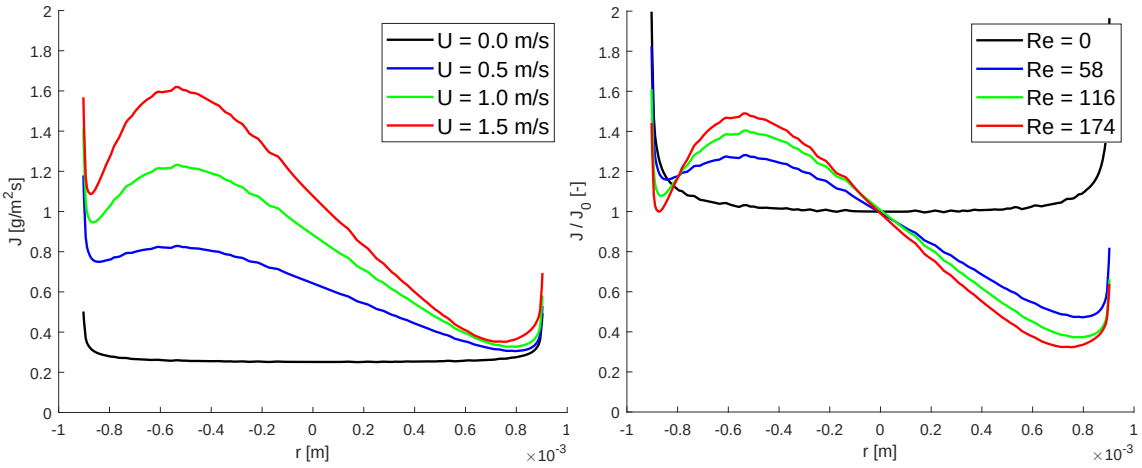

Figure 9.5: Radial profiles of evaporative flux at different flow velocities (left) and normed flux values at corresponding Reynolds numbers (right).

height and contact angle, the droplet quickly becomes a smaller obstacle in the flow, with less local congestion and smaller perpendicular component of the velocity. This logically converges to the case of a flat surface on which there is no local mass transfer maximum.

Excluding the enhancement effect along the contact line, similarities between the described development of local mass transfer and local heat and mass transfer around a sphere in natural convection, as it was shown by Lee and Chung (2017), can be detected. Although the droplet is subjected to a flow, the mass transfer distribution less resembles known profiles of forced convection around a sphere, as for example described by Zhang et al. (2008). This similarity to mass transfer through natural convection is due to the velocity boundary layer developing over the substrate, as convective velocities diminish at the bottom, especially directly in front of the droplet, forming an area of very low local Péclet numbers and a relatively high velocity boundary layer thickness.

To visualize the rotational asymmetry in convective cases, Figure 9.6 displays the flux distribution along different angles to the flow direction (left part). In this contemplation for an exemplary case of $Re = 116$ and $\theta = 72°$ it is evident that the local maximum described above is reduced towards the droplet sides and moved towards the droplet's peak. At $\gamma = 90°$, id est orthogonal to the flow, the flux distribution is symmetrical and the local maximum is centered. This uniform distribution is reached by an upstream side flux reduction and a corresponding increasing on the downstream side. The maximum at an orthogonal angle decreases with lower Reynolds number, as can be seen in the right part of Figure 9.6. This converges to the purely diffusive case, in which there is no centered peak in the flux.

The thickness of the concentration boundary layer δ_c that is formed in the present scenario progresses in opposite direction to the flux. Its development is shown in Figure 9.7a and was calculated via Equation 2.20. The associated local mass transfer coefficient β behaves similarly to the flux, as can be seen in Figure 9.7c and compared with Figure 9.5 (left). Both properties again

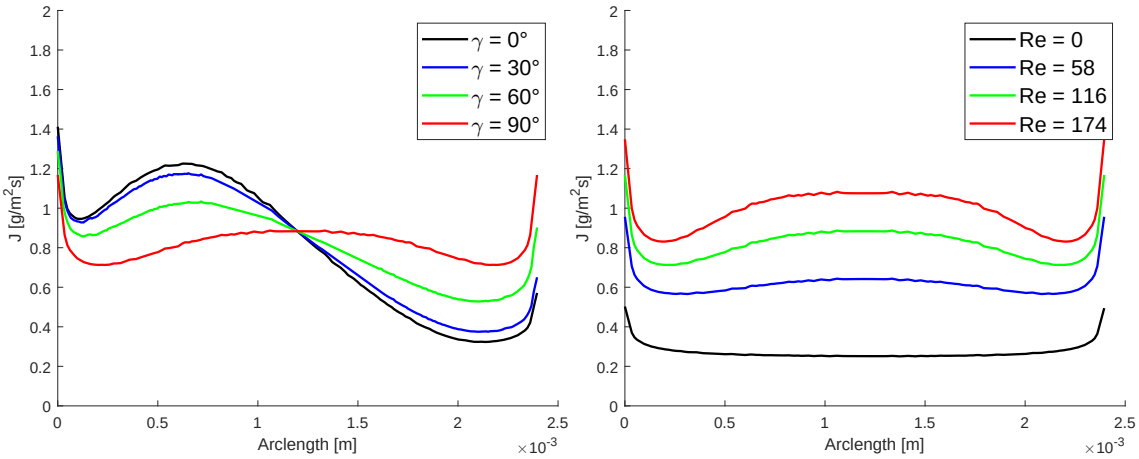

Figure 9.6: Flux development at different angles to the flow direction for $Re = 116$ and $\theta = 72°$ (left). Flux development along $\gamma = 90°$ at different flow velocities for $\theta = 72°$ (right).

can be normed with regard to their respective value at $r = 0$ (Figures 9.7b and 9.7d).

Corresponding to the development of the concentration boundary layer, also the concentration field behavior greatly differs for diffusive and convective cases, as well as for a contemplation alongside the r- and z-coordinate. In Figure 9.8 one can see that the decline in concentration over the vertical and radial position is similar for setups solely involving diffusion ($Re = 0$). Furthermore, one can observe that the vapor concentration along the vertical coordinate above the droplet decreases significantly faster in convective cases. Profiles over the radial coordinate show a similar but attenuated trend, compared to the pure diffusion profile. This means that in the wake of the droplet, a tail of increased vapor concentration establishes, while the distribution above the droplet is diminished relatively quickly. This shift in flow direction is to be expected and due to the mass transport within the flow field.

Table 9.3 quantifies the concentration gradient shift for different droplet contact angles and Reynolds numbers. Flux on the upstream half of the droplet (negative r-coordinate) is compared to the droplet's total evaporation flux to obtain an upstream percentage. Secondly, the evaporation flux taking place in the outer ten percent of the droplet area is extracted and set in relation to the total flux, in order to obtain an edge evaporation ratio. The evaporation flux in the outer ring is then further subdivided into a portion taking place within the upstream half and the corresponding downstream share. These two evaporative fluxes are set in relation to each other.

The evaporation shifts more and more to the upstream side by an increase in either contact angle or Reynolds number. At the limit of stable conditions, this results in an evaporation portion of maximally about 66 % on the upstream side. In contrast to this, the edge evaporation is reduced down to circa 16 % for the combination of high Reynolds number and contact angle. In the pure diffusion case, flow within the droplet is primarily induced through the enhanced evaporation flux at the pinned contact line (Bhardwaj et al., 2009). This can also be deduced from Figure 9.4a or Figure 9.5, $Re = 0$. Utilizing the present model, one ascertains that around 20 % to 30 % of the

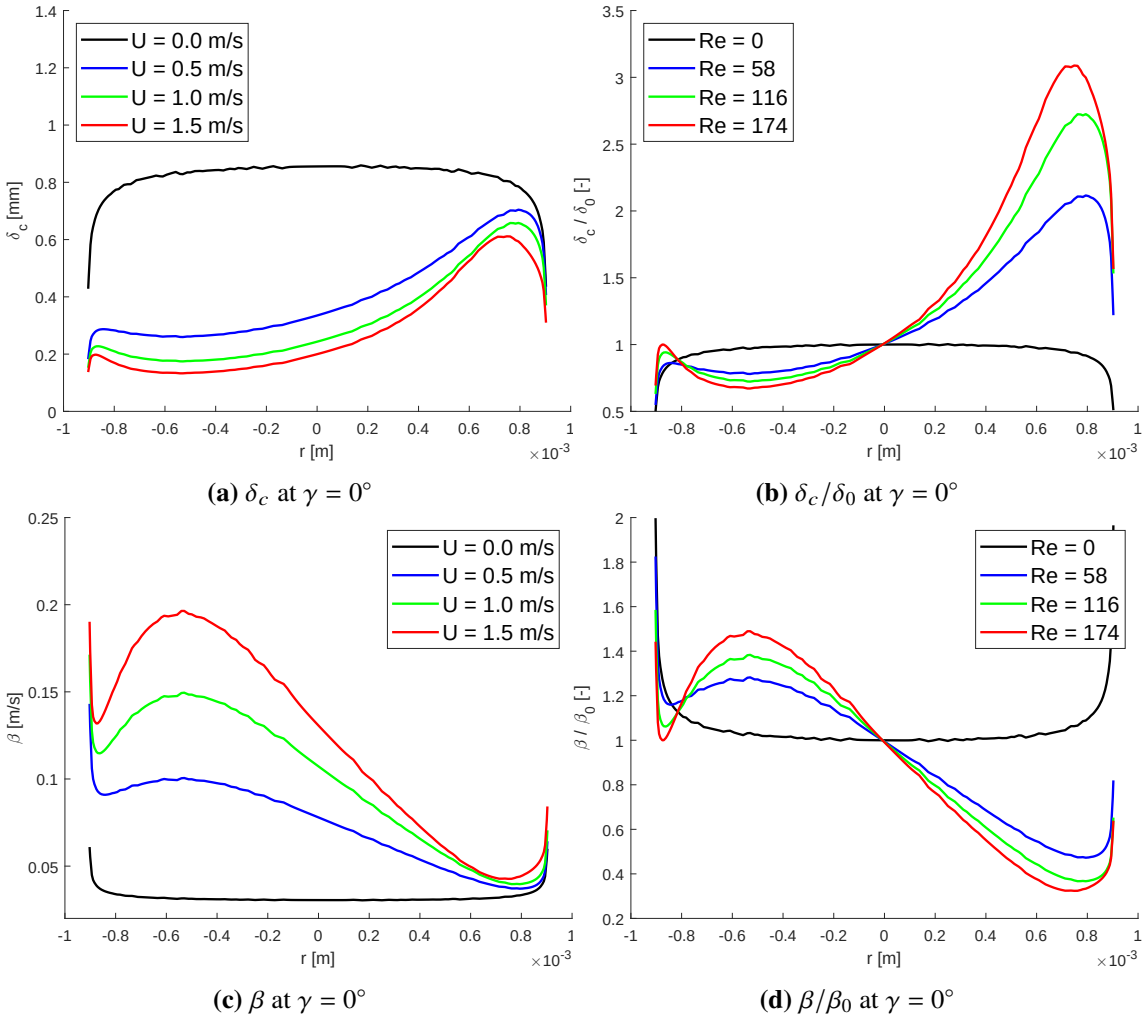

(a) δ_c at $\gamma = 0°$

(b) δ_c/δ_0 at $\gamma = 0°$

(c) β at $\gamma = 0°$

(d) β/β_0 at $\gamma = 0°$

Figure 9.7: Development of boundary layer thickness and local mass transfer coefficient at different flow velocities along the maximal cord in gas flow direction.

total evaporation takes place along the outer 10 % of the droplet's surface, if there is no external flow present. Due to the arise of the new local maximum described above, this edge evaporation is increasingly reduced for higher Reynolds numbers. The evaporation ratio along the edge itself however is gradually shifted to the upstream side, similarly to the entire evaporation flux.

9.2.2 Influence of droplet position

In the diffusive case the droplet's position on the substrate has no influence on the evaporation profile, because there is no forced convection or ambient velocity. In the convective case a velocity boundary layer forms on the plate. Since all droplets studied in this contribution are submerged within this boundary layer, the velocity around the droplet is not only a function of the applied ambient velocity, but also of the individual droplet position within the boundary layer. More specifically, the resulting flux profile is dependent on the droplet's position with regard to the starting point of velocity layer development. Figure 9.9 shows the difference in flux distribution in dependence of the droplet center's distance to the front of the substrate plane. The corresponding

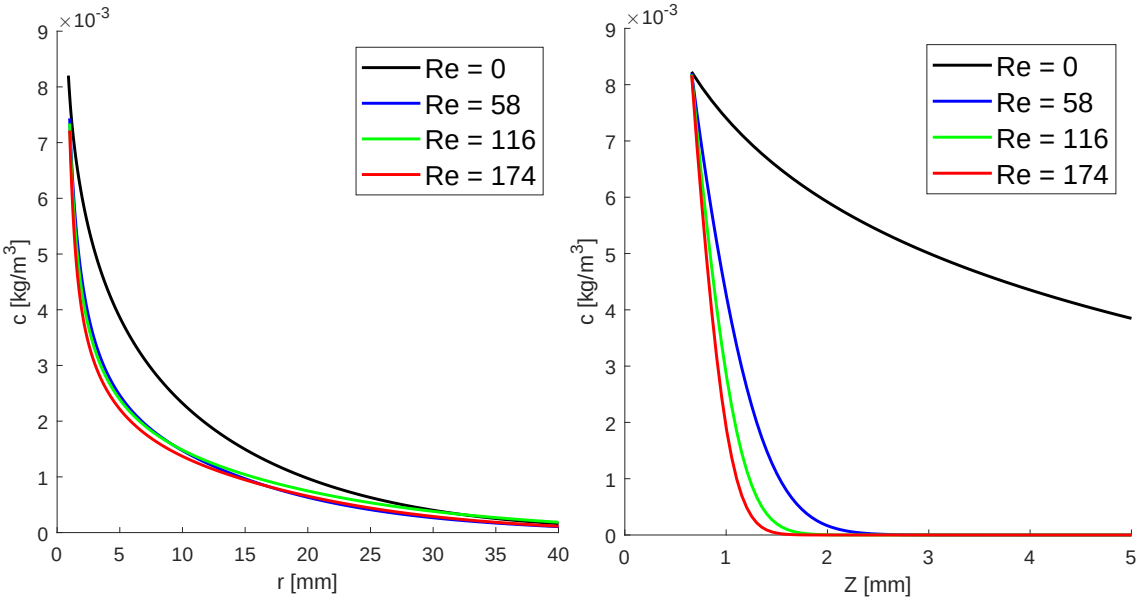

Figure 9.8: Vapor concentration development along the r-coordinate downstream of the droplet at $z = 0$ (left) and along the z-coordinate at $r = 0$ (right) for different Reynolds numbers.

developments of concentration boundary layer and mass transfer coefficient can be viewed in Appendix E.1.

It is evident that the evaporation flux decreases with increasing distance from the front of the substrate, especially on the upstream side and around the local maximum at $-R/2$. The downstream side, in particular the downstream edge, is only marginally affected. This constancy goes hand in hand with a reduction of the upstream shift. As the boundary layer thickness is a square root function of distance, effects related to it become less severe for droplet positions further away from the edge of the plane.

9.2.3 Influence of droplet contact angle

The dominating drying behavior of sessile droplets on partially wetting surfaces, id est $0° < \theta < 90°$ (Yuan and Lee, 2013), consists of a pinned contact line with a decline in the droplet's contact angle and height (Semenov et al., 2013). Therefore, it is sensible to examine the respective flux profiles not as subjected to time but as a function of the formed contact angle. Due to a usually observed depinning of the contact line at the end of the drying process, followed by a rather erratic behavior at low contact angles as described by Dunn et al. (2008), the focus of the following analysis is laid on the constant contact radius stage. The contact angle is chosen to recede from from 72° to 10°. The lower boundary of this span, or in other words the static receding contact angle, was selected based on the preceding contact angle experiments and is in good agreement with the statements of Gatapova et al. (2018).

Figure 9.10 shows the emerging flux distributions over the course of the drying process, for

Table 9.3: Quantification of upstream evaporation, edge evaporation and comparison to the downstream counterparts.

Re	θ [°]	US evap.	Edge evap.	US-/DS edge
0	72	50.00 %	21.04 %	1.00
58	72	61.45 %	18.26 %	1.59
116	72	64.17 %	16.85 %	1.67
174	72	66.19 %	15.93 %	1.69
0	40	50.00 %	22.45 %	1.00
58	40	59.81 %	20.03 %	1.57
116	40	61.91 %	18.69 %	1.72
174	40	63.10 %	17.79 %	1.79
0	10	50.00 %	28.58 %	1.00
58	10	58.90 %	25.98 %	1.55
116	10	60.52 %	24.48 %	1.73
174	10	61.30 %	23.48 %	1.84

30° decreasing difference, respectively. The belonging profiles of δ_c and β are illustrated in Appendix E.2. One can see that the upstream side's local maximum ($r \approx -R/2$) of the flux profile is less pronounced for reduced contact angles. In contrast to that, the increase at the droplet's edge is generally intensified, especially in opposite flow direction. This combination means that an increasing portion of the evaporation takes place along the edge, as can also be seen in Table 9.3. As elaborated within Section 9.2.2, the first effect is due to decreased velocities perpendicular to the droplet's surface at lower contact angles. In other words, with diminishing contact angle and height, the droplet becomes a smaller obstacle for the forced convection and thus less local congestion is taking place. The latter phenomenon is attributed to the increase of available volume along the edge and in turn the higher probability of escape of evaporating molecules, coinciding with a contact angle decrease. Both effects logically converge to the case of a flat surface, with strong increase at the edges but without any other local maxima, similar as in the diffusive setup.

The specific simulation results are listed in Table 9.3. By comparing US evaporation for decreasing contact angle at the same Reynolds number, it can be seen that the combination of effects also slightly reduces the shift of evaporation flow to the upstream side. This decreasing shift results in slightly more symmetrical profiles at lower contact angles. Nevertheless, the influence of velocity is significantly stronger and the evaporation on the upstream side remains at circa 60 % for the tested cases. Table 9.3 also quantifies the previously described deduction of an increasing portion of the evaporation taking place along the edge at lower angles. One can see that with diminishing contact angle, the edge's percentage of evaporation rises significantly, exempli gratia from about 17 % at 72° to circa 25 % at 10° for a Reynolds number of 116. In contrast to this, an increase in ambient velocity makes the evaporation more centered. This also means that the asymmetry between the edge on the upstream side compared to the downstream side slightly decreases with decreasing

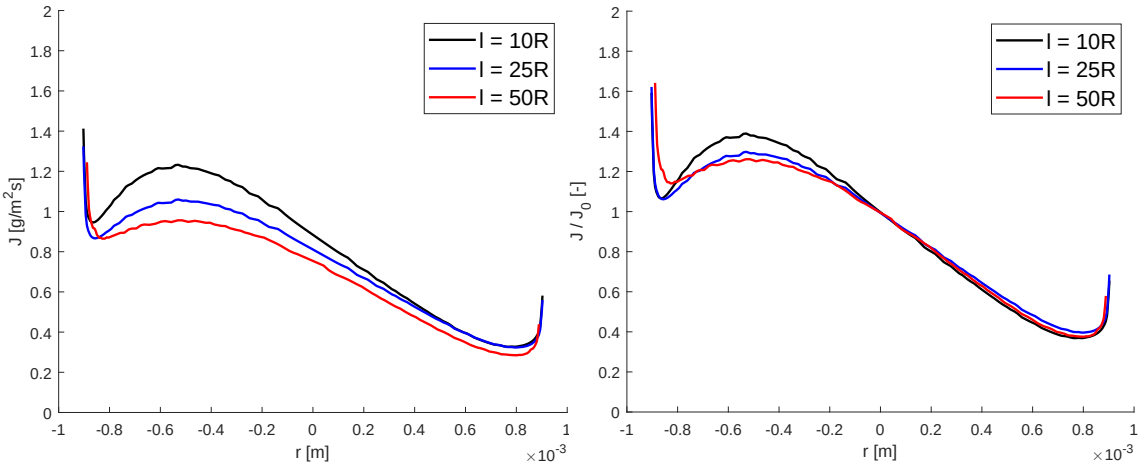

Figure 9.9: Surface flux distribution at $Re = 116$, $\theta = 72°$, $\gamma = 0°$, for droplets placed at different distances from the front of the substrate plane and corresponding normalization with the flux on the droplet's peak ($r = 0$).

contact angle, but increases in case of larger ambient velocity. This in turn can be attributed to higher gas velocities along the downstream side, followed by a decrease of the concentration boundary layer in the wake, with the droplet being a gradually smaller obstacle over time.

It shall be noted that the individual arclength over the radial coordinate of the droplet decreases with decreasing contact angle. This in turn means, that despite the overall slight increase of flux values, due to a significant increase of evaporation along the edge, the surface integral or in other words the total evaporation flow in consecutive stages is approximately constant. Moreover, this implies that the relative consistency in drying speed of the entire droplet over time, as it is described among others by Schönfeld et al. (2008) and Kelly-Zion et al. (2011), can be ascribed to the diminishing of available surface area combined with a tendential enhancement of local drying flux at the edge.

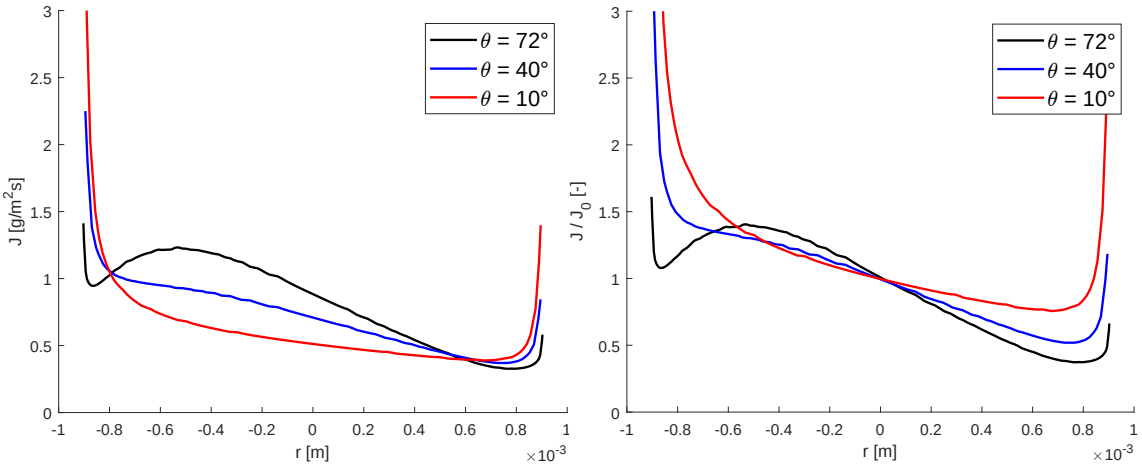

Figure 9.10: Surface flux distribution at $Re = 116$, $\gamma = 0°$, for several contact angles (left) and corresponding normalization with the flux at $r = 0$ (right).

9.2.4 Interaction of binary droplet systems

Although the drying of a solitary micro- or nanodroplet is certainly of scientific importance and has many applications in nature, it often is just an entry case for processes that involve multiple droplets, as they are common in industry. In order to extend the basic contemplation of a solitary droplet, further simulative studies were directed towards binary droplet systems drying in close vicinity to each other. With literally infinite possibilities to place such droplets on a surface, the investigation had to be reasonably restricted. Logically, all interaction effects will fade away with an increase in distance between the droplets. However, a very close placement, or an other words the case of nearly joining droplets, is also not in the sense of the present study. Generally, a placement incorporating an offset perpendicular to the direction of the flow decreases droplet interactions. As a result of these deliberations, an exemplary case setup of two droplets placed one after the other in flow direction, with a distance of about one contact radius (1 mm) has been chosen for all studies hereafter. This representative binary configuration thus shows all relevant effects in a clear manner, while simultaneously avoiding side effects. Over the course of the following analysis, the droplet placed upward and closer to the flow source shall be denoted as first or upstream droplet. The one further in the direction of the flow shall be denoted as second or downstream droplet. The principally arising flux profiles of this configuration are visualized in Appendix E.3, for diffusive and convective setups, respectively.

In contrast to the solitary droplet setup, the individual flux distributions of each droplet are asymmetrical even without an overlaying airflow. As it can be observed in Figure E.3a and E.3b, the droplets' maximum evaporation flux shifts to the side which is most remote from the respective other droplet. In turn, this means that the flux distributions of the two droplets are exactly mirrored. This phenomenon is illustrated in Figure 9.11 (left part). It can further be observed that in the binary setup the flux magnitude is generally reduced, but more severely on the side facing the neighboring droplet. The edge facing away from the respectively other droplet is basically not affected. The right part of Figure 9.11 further compares solitary to binary flux distribution for a case incorporating forced convection. Again, one can see that the solitary droplet always obtains the highest local flux. Furthermore, in the binary case with forced convection, the shift effect is slightly enhanced for the upstream droplet, compared to the corresponding solitary one. This is the result of the distorted velocity field and the in turn enlarged velocity and concentration boundary layers in between the two droplets. Additionally, there are modest circulation phenomena in the area between the two droplets, especially at high contact angles and velocities. The corresponding circulating backflow in the first droplet's wake and the accompanying transport of vapor from the upstream side of the second droplet to the downstream side of the first one increases the concentration boundary layer thickness and, hence, the asymmetry within the flux profile compared to the convective single-droplet setup. For the downstream droplet, the evaporation flux distribution is on the one hand shifted to its downstream side due to the other droplet's presence, on the other hand it is conveyed upstream as a result of the forced convection. In consequence, both the velocity and the concentration boundary layer develop in a distinctly different way around the second droplet than around an upstream or solitary droplet.

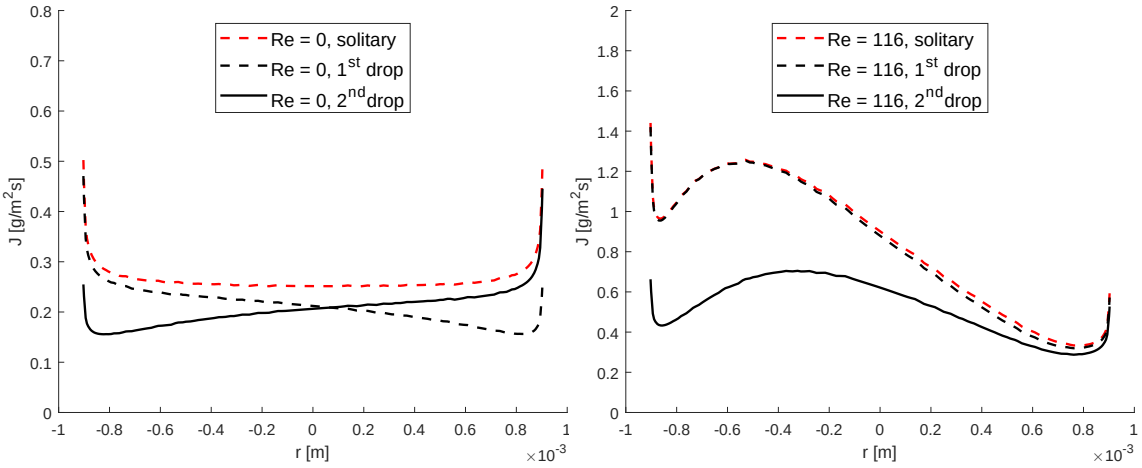

Figure 9.11: Comparison of surface flux distribution along $\gamma = 0°$ of binary and solitary droplet setups for the purely diffusive case (left) and under forced convection at $Re = 116$ (right).

The combination of effects described above further indicates that the dominant evaporation side for the downstream droplet changes between diffusive and convective setup, as can be seen in Figure E.3b and E.3d. The influence of forced convection in this matter is very significant and therefore this change in dominant evaporation side occurs very quickly with the application of ambient gas flow. Profiles of evaporation flux at different airflow velocities for the binary setup are shown in Figure 9.12. In this figure one can also see that the local maximum for the second droplet is no longer located at $-R/2$, but is instead formed at circa $-R/3$. This location change results from the altered velocity field around the droplet, which in turn is the result of the upstream droplet's distortion of the flow. The point of greatest orthogonal velocity is thereby moved further towards the droplet's peak.

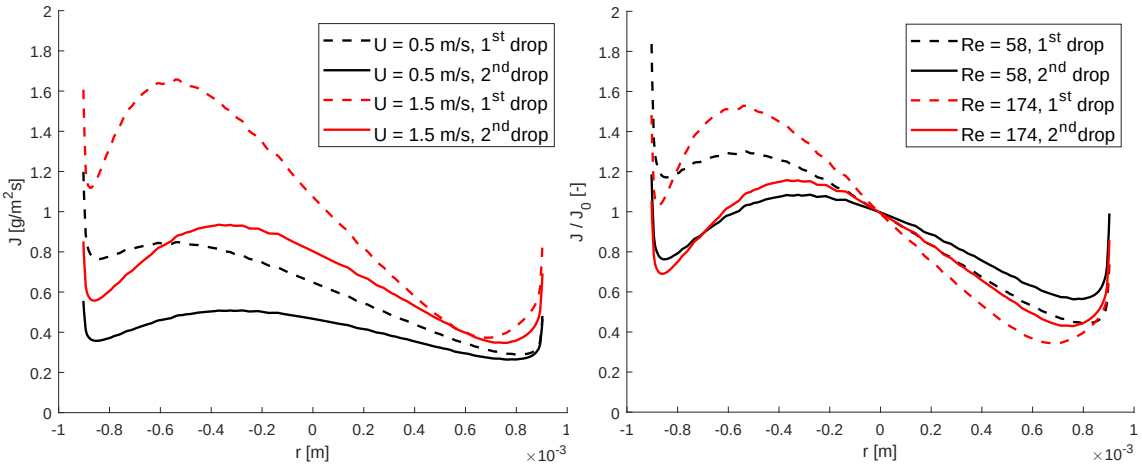

Figure 9.12: Flux profiles in dependence of forced convection for the binary droplet case along the $\gamma = 0°$ cord.

Table 9.4: Comparison of upstream side to downstream side flux and edge flux for binary droplet setups.

		1^{st} droplet			2^{nd} droplet		
Re	θ [°]	US evap.	Edge evap.	US-/DS edge	US evap.	Edge evap.	US-/DS edge
0	72	55.4 %	20.6 %	1.34	45.2 %	20.6 %	0.76
58	72	62.2 %	18.1 %	1.60	55.4 %	18.5 %	1.17
116	72	65.0 %	16.7 %	1.66	57.5 %	17.8 %	1.21
174	72	66.6 %	16.1 %	1.67	58.9 %	17.5 %	1.26
0	40	54.1 %	22.2 %	1.23	46.4 %	22.2 %	0.77
58	40	60.2 %	19.9 %	1.60	56.0 %	20.3 %	1.28
116	40	62.3 %	18.6 %	1.75	57.8 %	19.2 %	1.39
174	40	63.6 %	17.7 %	1.83	59.1 %	18.3 %	1.43
0	10	53.3 %	28.4 %	1.19	47.0 %	28.4 %	0.81
58	10	59.2 %	25.9 %	1.57	56.4 %	27.6 %	1.33
116	10	60.8 %	24.4 %	1.75	57.9 %	25.0 %	1.48
174	10	61.6 %	23.4 %	1.87	59.5 %	24.1 %	1.57

The results of the studies on velocity and contact angle dependencies for binary droplet setups are quantified in Table 9.4. If one compares the values of the upstream droplet of the binary setup and the corresponding values for a solitary droplet in Table 9.3, only relatively small differences in US-evaporation proportion in dependence of velocity can be noticed. A slightly greater share of the evaporation compared to a solitary droplet takes place along the upstram side and edge of the first droplet. The upstream side itself however is barely influenced by the second droplet's presence, as can be seen in the right part of Figure 9.11. Consequently this shift increase is the result of decreased downstream-side evaporation due to the second droplet, which is again due to the modest vortices forming in between the droplets under forced convection. The effect however is relatively minor and generally it can be said that the first droplet of a binary setup behaves similarly to a solitary droplet under the same conditions.

Analyzing the values of the downstream droplets in Table 9.4, the unique behavior indicated prior in Figures E.3 to 9.12 is further confirmed. The change in dominant side for the evaporation flux is indicated by a transition in the US evaporation fraction from less than 50 % without convection to more than 50 % with convection and a change in the ratio of upstream to downstream edge from below to above unity. In addition to this, the considerable reduction of all upstream related portions compared to the first droplet is visible.

Same as for the previous flux profiles, the thickness of the concentration boundary layer and the local mass transfer coefficient in the binary configuration develop correspondingly to the drying flux distribution, as can be seen in Figure 9.13 and Appendix E.5.

In order to study the binary cases' dependency of the evaporative flux on the contact angle,

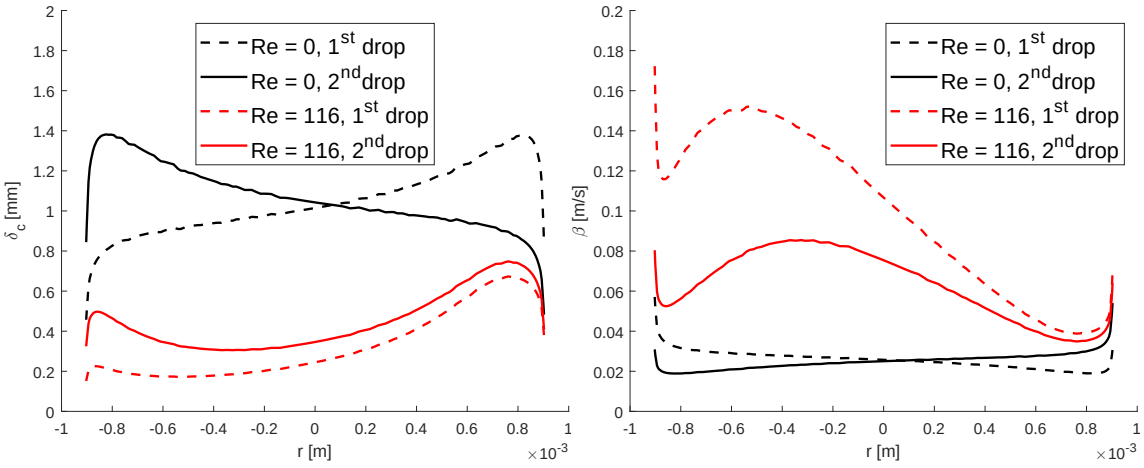

Figure 9.13: Exemplary boundary layer thickness (left) and local mass transfer coefficient (right) for binary droplet cases at different Reynolds numbers along the $\gamma = 0°$ cord.

again one needs to find a representative case. As can be seen in Figure 9.8, vapor is transported in flow direction towards the downstream droplet. Additionally, the velocities surrounding the second droplet are reduced. Local concentration gradients and therefore the entire drying speed of downstream droplets are thus significantly decreased compared to single droplet evaporation. For this reason, the reduction in contact angle happens slower and the heights of the first and second droplet are offset in time. In addition to this phenomenon, in most technical applications, the different droplets are not applied simultaneously, but at randomly varying times closely after each other. Furthermore, contact angle hysteresis influences the relation of the individual initial contact angles as well, making any combination a possible scenario. As exemplary investigations, a simulation series was carried out for the case of a simultaneous start of the drying process with a resulting contact angle offset, as well as for a drying process that is chronologically displaced, resulting in the same contact angle of both droplets at specific timepoints within the drying process.

The results for setups of same contact angles can be seen in Table 9.4, for the tested ambient velocities. Herein, one can see that the simulation predicts opposite trends in upstream evaporation development for the two droplets. While a smaller contact angle reduces the shift to the upstream side for the first one, the subsequent droplet's upstream percentage is slightly increased. This outcome may be explained by fewer distortions of the flow field and the correspondingly reduced influence of the upstream droplet on the velocity boundary layer at lower contact angles. A rising amount of gas passes over both, the first and the second droplet, without being significantly deflected by the obstacle. The expansion of the velocity boundary layer in the upstream droplet's wake is therefore less severe. By the time it reaches the second droplet its influence is consequently reduced compared to a droplet with greater contact angle. Nevertheless, the overall concentration gradient on the downstream droplet's surface is greatly diminished at all contact angles.

The presence of another droplet on the flow side also significantly changes the velocity profile applied to the droplet placed further in the direction of the flow. The binary setup hereby effectively

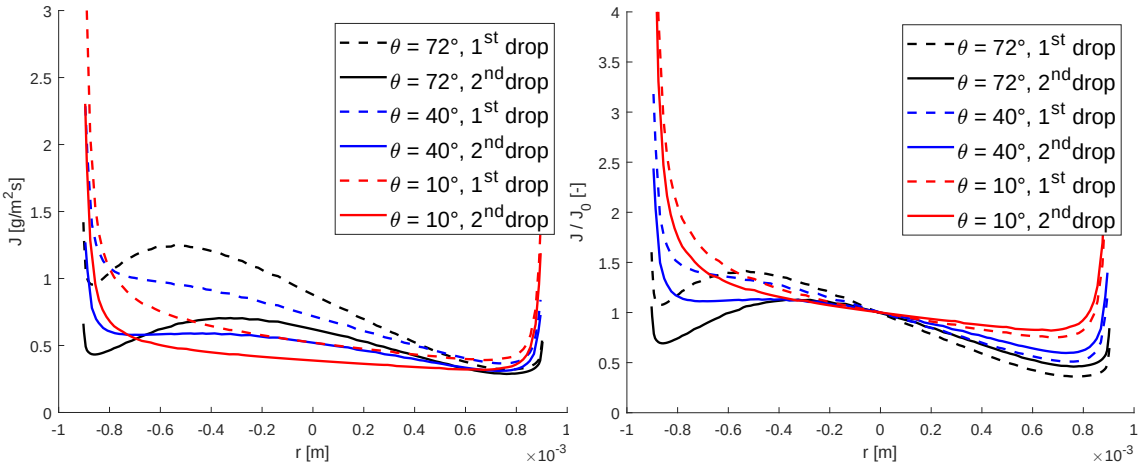

Figure 9.14: Evaporation flux profiles for binary combinations of droplets for various but same contact angle at $Re = 116$, $\gamma = 0°$.

eliminates the second droplet's local maximum on the upstream side, which could be spotted for solitary droplets. Thus, and in contrast to the previous cases, the gain along the upstream side is not reasoned by the new formation of a maximum, but results from a monotonous decrease. This effect can be detected very clearly if one plots the local flux over the maximal cord, as in Figure 9.14, and is further the reason for the reduced upstream to downstream evaporation ratio compared to a solitary sessile droplet setup. Similar as before, the evaporation along the edge increases with diminishing contact angle. Further glyph illustrations of evaporation flux profiles for different contact angles can be found in Appendix E.6. The respective boundary layer and mass transfer profiles are listed in Appendix E.7.

During the simulations of droplet pairs with same initial contact angle and the particular distance investigated in this analysis, it was discovered that the second droplet dries with approximately half the speed of its predecessor, id est in twice the time. This occurrence turned out to be adequately valid for the entire range of tested gas velocities and is again based on a reduction of the local concentration gradients on the surface due to changes in the velocity field and local concentration surrounding the second droplet. Over the course of the drying process, the contact angles therefore diverge from each other. Starting with $\theta = 72°$ for both droplets, the upstream one forms an angle of 40° at the same time the second droplet forms an angle of about 59°. With $\theta = 10°$ in the upstream droplet's last stage of the drying process, the second sessile droplet still obtains a contact angle of about 48°. Those two moments in time during the drying process were chosen for a follow-up investigation. The influence of the two different contact angles on the flux distribution was analyzed by keeping the ambient velocity constant, as usual. The resulting shift and distribution of the evaporative flux are quantified in Table 9.5.

If this data is compared to the values from Table 9.4, it is evident that the upstream droplet's US-evaporation is fairly independent of the properties of the droplet applied in its wake. The same statement is true from the downstream droplet's point of view, in an attenuated manner. However,

Table 9.5: Comparison of upstream side to downstream side flux and edge flux for binary droplet setups with an offset in contact angle.

	1^{st} droplet				2^{nd} droplet			
Re	θ [°]	US evap.	Edge evap.	US-/DS edge	θ [°]	US evap.	Edge evap.	US-/DS edge
116	40	62.4 %	18.6 %	1.76	59	58.8 %	17.1 %	1.34
116	10	60.8 %	24.4 %	1.75	48	59.2 %	18.0 %	1.43

in the later stages of the drying process, the second droplet's flux profile converges more and more towards solitary droplet behavior, with the droplet beforehand diminishing faster and being a smaller obstacle for the flow. This logically converges to a solitary droplet setup once the upstream droplet is dried. Thereby, the slight development of eddies, which was previously observed in between the two droplets for high velocities at initial contact angle could not be detected anymore.

9.2.5 Influence of flux profile on structure formation

One reason for the importance of the evaporation flux distribution on sessile droplets' surfaces is the influence on internal flows and thereby on any structure formation processes. An increase in upstream evaporation hereby means, that an enhanced flow towards the upstream side takes place, in order to replenish the higher mass loss in the respective area. In consequence, residue structures, such as coffee-ring depositions, are not distributed symmetrically. Rather, an increased accumulation of particles or solutes occurs along the side that faces the flow and therefore forms the slimmer velocity and concentration boundary layers. Thus, a more voluminous deposit compared to the downstream facing part is formed, as the majority of solids is transported in the corresponding direction to some degree.

In addition to this transfer due to a general evaporation shift, also the altered flux development is expected to influence solid deposition. The local maximum that was distinctly observed for solitary and upstream droplets is hereby expected to result in an internal flow that, contrary to purely diffusive cases, is not only streaming towards the outer edge, but instead is also directed towards the upper area on the upstream side. The flow towards the edge is therefore simultaneously reduced, as can also be deduced from Table 9.3. This means that for any residue deposits resulting from solutions or suspensions, solid advection can be assumed to be more spread alongside the droplet's height, which in turn results in stepper slope and increased height of ring structures throughout this area. The overall outcome resulting from these phenomena is a more crescent- than ring-shaped deposit. The broadened portion is hereby located on the upstream side. An example for such an asymmetrical crescent structure can be seen in the μ-CT scan in Figure 7.9a.

In contrast to the above described spread, replenishing flows within the droplet are expected to be more strongly directed towards the edge with diminishing contact angle, and in addition are generally less shifted oppositely to the gas flow. This in turn means that the corresponding solid transportation shift is more pronounced and spread at higher angles, respectively (Bhardwaj et al.,

2009). Hence, droplets with smaller initial contact angle can be assumed to result in ring structures which are more uniform, less steep and reduced in height (Sondej et al., 2018). In consequence, such droplets are expected to be less affected by changes in forced convection. This behavior is also the reason for the experimentally observed reduction in slope and the flattening of residue structures towards the center, as the droplet's angle decreases with time and the structure formation begins at the outer edge of the formed spherical cap.

During the studies with varying droplet position, it could be seen that the respective flux profiles are also dependent on the conditions directly around each droplet, especially the formed boundary layers. This further implies that also the individual position on the substrate during convective drying influences intrinsic flows and subsequently formed structures. Hereby, the impact of a larger distance to the front edge is comparable to a slight reduction of ambient velocity.

The slight asymmetries of flux profiles that were observed in the binary purely diffusive case suggest that solid deposition structures can be expected to show modest asymmetry as well, if the droplets are simultaneously drying in proximity to each other. In binary cases involving forced convection, any flows inside the droplets and phenomena reasoned in the evaporation shift are expected to be slightly magnified for the upstream, and concurrently reduced for the downstream drop. This again can be assumed to result in strongly crescent shaped deposits formed from upstream droplets, with more symmetric ring structures resulting from droplets positioned in the wake of other drops. Similar to solitary setups, the observations above imply that the surrounding flow field's influence on the solid residues is hereby less severe with a decline in contact angle and less severe for the downstream droplet than for the one positioned upstream due to its higher distance towards the substrate edge.

9.3 Summary

After mesh and domain size tests and validation of the presented finite volume model at the limit of pure diffusion, different convectional influences were investigated for single and binary sessile droplet drying processes. In all cases, an increase in ambient gas velocity lead to an increase in evaporation on the upstream side of the respective droplet. At the maximum velocity tested in this study, over 65 % of the evaporation took place along the flow facing side. This shift phenomenon is generally decreased by a decline in contact angle, or an extension of the distance to the substrate's edge, and it is also influenced by other droplets nearby. Results which reflect the variation of upstream side evaporation with Reynolds number and contact angle are summarized in Figure 9.15. Furthermore, broadly speaking, the results show that any phenomena taking place in solitary droplet systems are further enhanced for upstream droplets in binary configurations and are simultaneously reduced for the respective downstream neighbors. Despite this, in most cases the changes decline with increasing dominance of advective forces and decreasing contact angle, or in other words, with decreasing interaction of the droplet with the flow. This result may be explained by the fact that under the present parameter variations, meaning laminar airflow and small droplets, only marginal vortex and circulation phenomena occur. The shape and limited height of the 1 μl

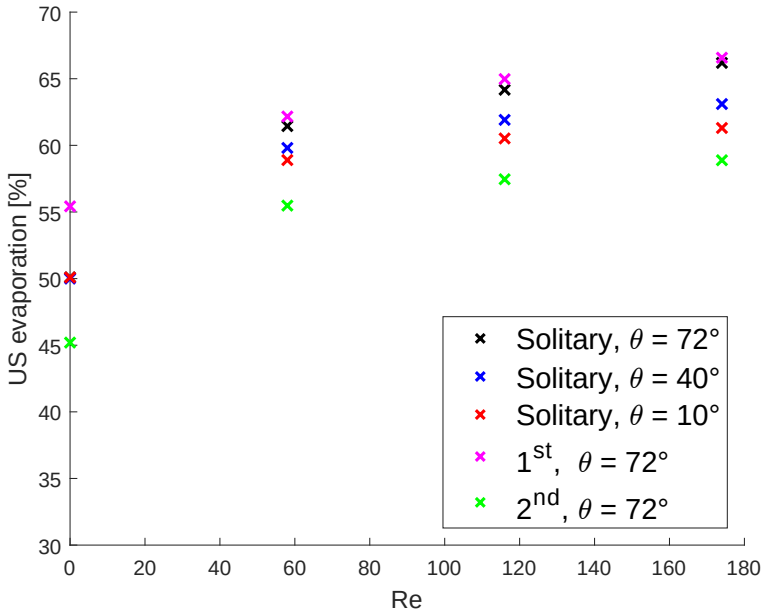

Figure 9.15: Summary of responses of upstream side evaporation on changes in Reynolds number and contact angle (binary combinations with same θ, 1^{st} droplet at $l = 10R$ from the substrate edge).

droplets imply that the droplets as a whole are always submerged in the flow's boundary layer which develops along the planar substrate. Any variation of temperature or humidity has large influence on total evaporation rate, but does not affect the flux distribution as it does not affect the boundary layer. Consequently, such investigations were not included in the present study.

9.4 Conclusions

A sessile droplet drying model capable of resolving local mass transfer at the interfacial boundary of evaporating droplets in presence of laminar overflow was developed via a finite volume approach. In this way, diffusive and foremost convective setups of sessile droplet drying could be simulated and evaluated. Under the assumption that evaporation is limited by mass transfer in the surrounding gas phase, evaporation flux distributions resulting at different ambient velocities and droplet contact angles were quantified for solitary droplets as well as binary droplet settings. Through these analyses it could be shown, that the attainable flux distribution strongly depends on the flow conditions within the system. In consequence, it can be stated that the convective drying conditions are crucial for the droplets' drying behavior, the thereby resulting flows within the droplet, as well as any solid transport or structure formation processes taking place during the drying process.

Exemplary for such structure formation phenomena are the asymmetries in the deposition of solids that are often observed during convective drying of sessile suspension or solution droplets. Due to enhanced internal flow towards the sections with higher evaporation, more solutes are expected to be deposited in the respective areas. Depending on ambient velocity, position on the planar substrate and contact angle, the morphology of such deposits is expected to be altered. This in

turn means that the evaporation flux distribution and thus the resulting structures are not only dependent on the overall applied convective conditions, but also on the droplet properties and the local conditions directly in front and around of each droplet.

The appearance of a local maximum on the upstream side of a convectively drying droplet on a substrate is a phenomenon that further influences any resulting deposition structures. Creating a more centered flow, this maximum can be assumed to result in more solid accumulation and steeper deposit slope around the middle of the upstream side of the droplet. In turn, a more crescent than ring shaped residue forms, as was experimentally shown in Section 7.7 and could be seen among others via experiments number 13 and 19 (Figures 7.8 and 7.9a).

Another focus of the present contribution was the development of the flux profile within the constant contact radius stage. Hereby again, significant dependencies of flux distribution on the actual contact angle as well as the position within the velocity boundary layer were found. Influences of temperature and humidity were tested, but showed much less effect on drying flux distribution in comparison with velocity, position or contact angle. However, the influence of forced convection is substantially weaker at low contact angles or great distances from the substrate edge.

Since solitary sessile droplets are rare in technical applications and in nature, cases of interacting droplet pairs were also investigated. It was shown that the presence of other simultaneously drying droplets in vicinity of each other greatly influences the individual drying and flux distribution behavior. It can thus be assumed to also have an influence on the resulting deposits, especially for droplets positioned in the wake of another one. This can be attributed to the thereby arising alteration of velocity and concentration boundary layers.

Chapter 10

Summary and outlook

10.1 Summary and outlook for the experimental results

Experiments mimicking the incremental coating layer build-up from deposited and subsequently dried colloidal and solution droplets have been presented. To experimentally simulate the transition from single deposit to coating layer structure, three layers, consisting of up to three droplet residues each, were applied on a planar, impermeable, partially wetting substrate in a droplet-by-droplet manner. Drying and structural analysis via white-light interferometry followed every droplet deposition. Convective drying conditions were kept constant during each layer build-up experiment, but varied from experiment to experiment, in order to study the dependence of structure formation on drying conditions. Three model substances, namely a silica-based nanofluid, a boron carbide microfluid and a sodium benzoate solution, were compared regarding their structural morphology as well as porosity during the incremental layer build-up.

In a follow-up study, further layer build-up experiments from sessile droplets were conducted. Within the same experimental setup and with the same execution as before, salt solution layers were incrementally built. Hereby, droplet properties were varied under the same drying conditions as in the prior investigation and complementary X-ray micro-computed tomography measurements were carried out to survey inner structure. Again, focus was laid on layer morphology and porosity.

All materials used in this study formed variants of ring structures commonly associated with sessile droplet drying in constant contact radius mode. This distinct morphology was observed to persist also beyond the initial droplet depositions. The degree of solid accumulation within a surrounding ring was hereby found to depend on size of the incorporated solids. It is clearly pronounced for solutes, but distinctively less pronounced for larger particles. It was also found to be dependent on the drying conditions, to some degree. Hereby, conditions that promote a fast drying process produce less pronounced ring structures. For cases with high drying airflow velocity, increased solid accumulation on the upstream side of the deposited droplets could be observed.

Through the experimental series different effects have been distinguished from each other and the

influence of several process parameters, especially drying conditions, on structural build-up could be resolved. For all substances it was found that fast drying conditions, id est high temperature and airflow velocity promote a more porous structure. Furthermore, layer porosity increases with decreasing influence of the substrate, or in other words with an increasement in the number of layers or layer thickness. This was found to be especially pronounced for solutions and lesser for colloids. Higher solid content was also discovered to result in more porous structures, while an influence of droplet size could not be clearly made out. All experiments showed relatively high residue porosities, as is commonly associated with this kind of impulse-free deposition and cautious handling of the resulting structures.

The studies of individual sublayer porosity together with the μ-CT visualization of inner structure showed that if one considers the droplets or sublayers as building blocks of a greater structure, it can be said that each block is structured relatively similar. Consequently, if there are only few inclusions in the structure, as it was the case exempli gratia for nanoparticles, the entire coating layer is relatively homogeneous. Through drying conditions, properties not only of the layer, but of individual sublayers could therefore be controlled. If, however, the material tends to include many cavities, this effect must be permanently taken into account and possibly counteracted, when one wants to specifically design the coating layer or an individual sublayer. It then may even be impossible to create certain sublayer porosities.

In addition to these major investigations on sessile droplet drying and structure formation, complementary coating experiments were carried out within a fluidized bed. Hereby, similarities between the incremental layer build-up from deposited droplets and sprayed-on droplets in industrial processes were ascertained. It was shown that similar trends regarding dependency on process and especially drying conditions do exist. This includes the increase in layer porosity at higher airflow velocity and temperature, as well as the increase alongside layer thickness, id est process time. Consequently, the reasons for certain trends and behaviors in such industrial applications could be identified through the present study on sessile droplets and the direct comparison with the fluidized bed. Nevertheless the attained porosities and morphologies during fluidized bed coating were found to differ significantly from their comparable sessile droplet counterparts. This is due to the presence of additional effects.

As is the nature of research, there are always further effects that can be investigated and possibilities that may shed more light on the matter at hand. To be mentioned here, among others, experimental investigations regarding the influence of spray-on droplet impact and correspondingly different spreading on the structure formation, as well as the influence of interparticle collisions within a fluidized bed on existing structures could be interesting as well as beneficial to investigate. For the former, experimental studies featuring a compressed-air-based droplet dispensing within a similar sessile droplet drying setup as used in this thesis would be conceivable. For the latter, as well as for the general transition from layers carefully created within a laboratory setup to layers from industrial processes, more experimental studies directly comparing process conditions and focusing on effects and phenomena during the build-up are necessary, which poses both opportunities and

challenges for future research.

10.2 Summary and outlook for the simulative results

The simulative part of this dissertation dealt with convective drying of sessile pure water droplets in air. From this investigation, both, insights on the evaporation flux distribution of convectively drying sessile droplets were brought, and conclusions regarding the preceding experimental investigations were drawn. It was found that forced convection induces an evaporation flux shift to the upstream side of deposited droplets. Thereby, a new local maximum in the evaporation flux distribution is created on the upstream side and the proportion of evaporation along the edge is reduced. Binary droplet systems showed flux shift phenomena already in the purely diffusive case. Furthermore, such systems of droplets placed after each other in flow direction caused slight effect enhancements for upstream droplets and a significant reduction of effects for the downstream counterparts, in the presence of forced convection. In general, an amplification of the effects of forced convection on drying sessile droplets was observed at higher Reynolds numbers, higher contact angles or a reduction of the droplets' distance to the substrate edge. The evaporation flux shift induced through forced convection, that was discovered during this simulative study, gave reason to the shift in solid accumulation and the corresponding distortion of the deposits towards the upstream side, which were observed during the experimental investigations.

To accurately simulate ring formation in a droplet's internal flow field in addition to the drying process of pure liquid droplets, a great amount of further studies is necessary in order to better understand the structure formation process in different colloidal and solute systems. As these processes, including among others the layering of particles, or the crystallization of solutes, still remain mostly unknown, such a comprising simulation remains illusive. Nevertheless, there are numerous further extensions or alterations conceivable for further in silico investigations of non-solid-laden droplet drying. Among these, and of further interest for several applications, are the influence of alternating convection and the influence of already present solid residues on follow-up droplet drying (non-planar substrate).

For a simulation of structure formation from deposited droplets, further coupling of the present CFD model with other methods is necessary. A generally very popular approach is the coupling of computational fluid dynamics for simulating the continuous phase with a discrete element method (DEM) for the discrete phase. It was first proposed by Tsuji et al. (1993) to simulate fluidization, and since then is one of the most common approaches to study the fundamentals of particle-fluid flow. Hereby, the flow of the continuous phase is modelled via momentum and mass conservation equations, as it is common, and also the case in the simulative part of the present dissertation. The motion of discrete particles within the flow is described by Newton's laws of motion. The results of both approaches are then continuously coupled in order to resolve the flow's effect on the included solids and vice versa. The interactions between solids and fluid phase are modeled by use of Newton's third law. CFD-DEM coupling is therefore the natural next step in extending the present simulative droplet drying investigation, because it is capable of simulating internal flows

and with this the internal transport of solids, induced through the evaporation flux distribution. The goal would therefore be a three phase simulation, including the gasflow around the droplet and the advection of vapor, the droplet's internal flows induced by the simulated evaporation profile's influence, and the movement of solids within the droplet. Intermediate steps may include the simulation of a one-dimensional, homogeneous flow field composed of particles and fluid against a boundary layer only permeable for the fluid, as well as the simulation of the particles' Brownian movement superimposed by an external flow field towards a boundary.

10.3 Synopsis

Evaluating the results that are summarized above, it can be concluded that the priorly formulated goals were largely achieved. Broadly speaking, the investigations brought new insights regarding droplet drying and layer formation. Although comparison of small layers created in the present experimental setup and large coating layers created within technical processes still needs to be handled carefully, the present dissertation can be considered as a first step of the investigation on transition from the former to the latter. The influences and correlations presented herein can further be seen as first means and guidelines that are expected to contribute to the overall understanding of droplet-based coating processes and in turn lead to a more purposeful design of coating layers. Furthermore, as the structure formation behavior of different classes of materials was analyzed and directly compared, the present deliberations may consequently serve as a guideline for associated coating material selection or the choosing of appropriate conditions for related coating processes, as well. Nevertheless, precise predictions still bear many challenges of further experimental investigation and structural characterization, and, in the end, of advanced modeling.

Appendix A

Basic principles

A.1 Principles of solid-laden droplet drying and crust formation

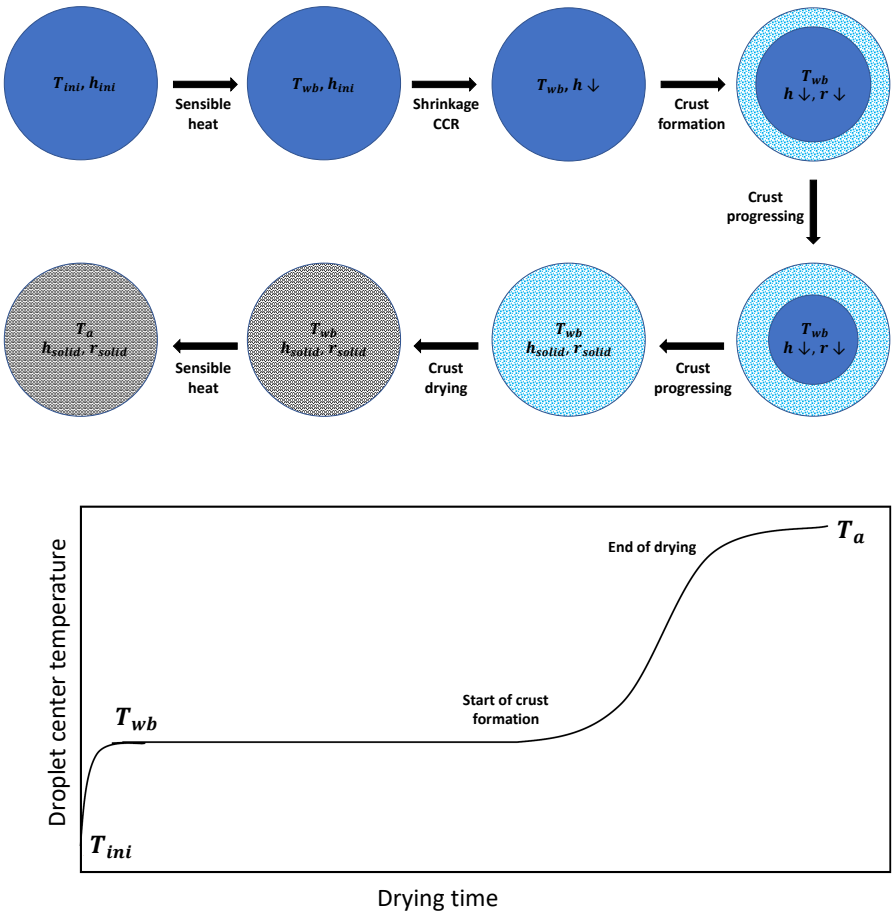

Figure A.1: Schematic illustration of sessile solid-laden droplet behavior during drying and crust formation with corresponding temperature development adapted from Farid (2003).

A.2 Principles of fluidized bed technology

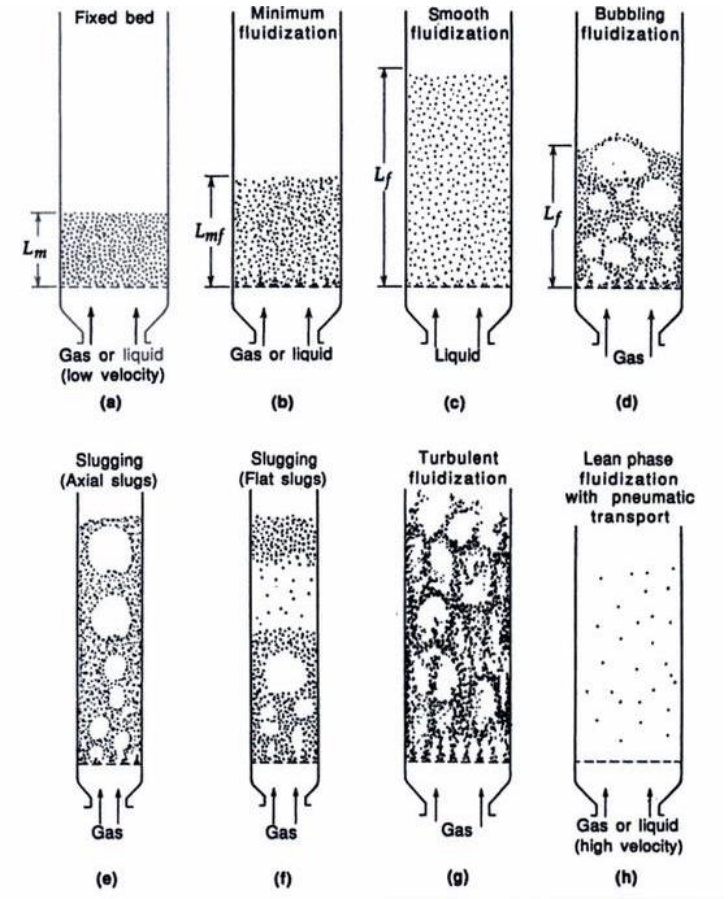

Figure A.2: Fluidization stages in dependence of fluid velocity, taken from Schmidt (2018), who adapted it from Kunii and Levenspiel (1991).

Appendix B

Experimental setup

B.1 Schematics of the sessile droplet drying air control unit

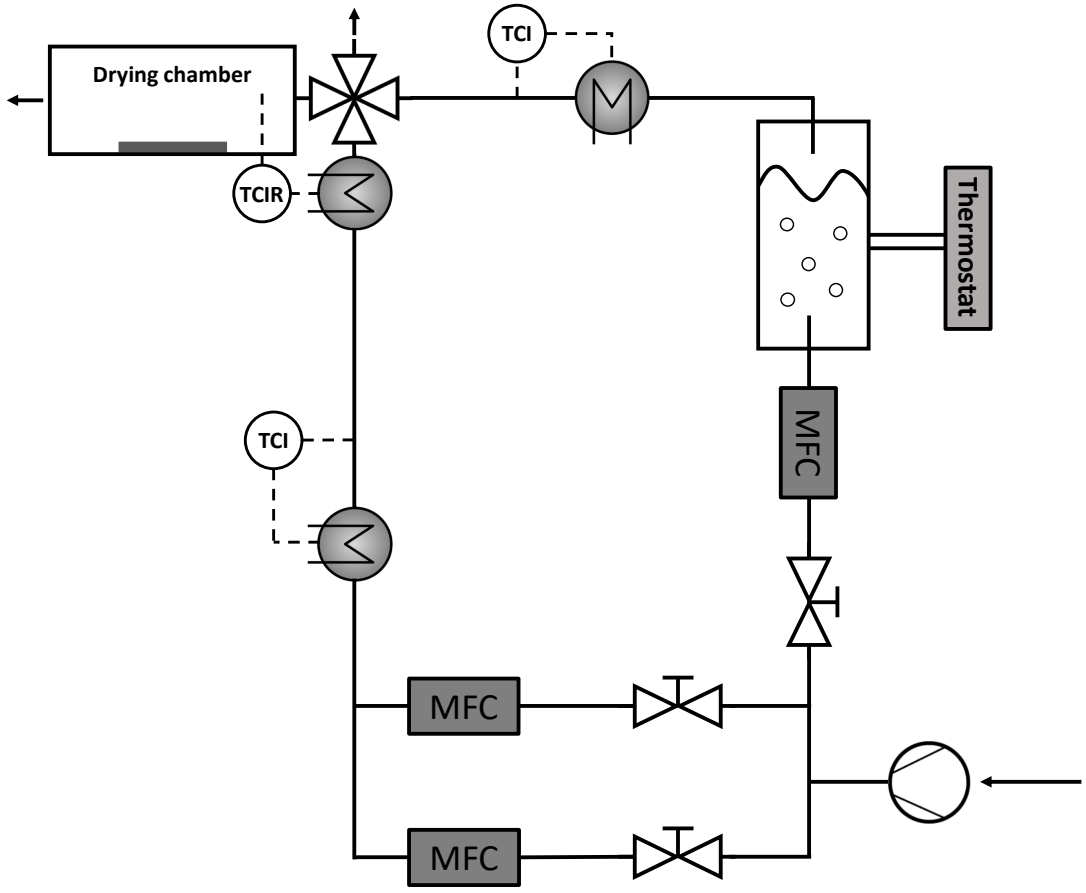

Figure B.1: Schematics of the installed air supply and control unit for sessile droplet drying.

B.2 Accuracy of the droplet dispenser

Table B.1: Results of the droplet dispenser accuracy test through weight measurements of the residue structures.

Test	Material	ω_{solid} [wt%]	Injection speed [nl/s]	$V_{drop,target}$ [nl]	m_{solid} [μg]	V_{drop} [nl]
1	SiO_2/TiO_2	40	50	1000	570	778
2	SiO_2/TiO_2	40	50	1000	540	737
3	SiO_2/TiO_2	40	50	1000	590	806
4	SiO_2/TiO_2	40	50	1000	590	806
	Mean				573	782
5	B_4C	5	50	1000	50	931
6	B_4C	5	50	1000	40	745
7	B_4C	5	50	1000	50	931
8	B_4C	5	50	1000	30	559
	Mean				42.5	791
9	NaB	30	50	1000	280	854
10	NaB	30	50	1000	260	793
11	NaB	30	50	1000	240	732
12	NaB	30	50	1000	240	732
	Mean				255	777
13	SiO_2/TiO_2	40	100	1000	680	923
14	SiO_2/TiO_2	40	100	1000	740	1010
15	SiO_2/TiO_2	40	100	1000	720	983
16	SiO_2/TiO_2	40	100	1000	750	1024
	Mean				723	987
17	B_4C	5	100	1000	60	1117
18	B_4C	5	100	1000	60	1117
19	B_4C	5	100	1000	30	559
20	B_4C	5	100	1000	60	1117
	Mean				52.5	978
21	NaB	30	100	1000	340	1037
22	NaB	30	100	1000	370	1129
23	NaB	30	100	1000	350	1068
24	NaB	30	100	1000	350	1068
	Mean				353	1076

B.3 Accuracy of the white-light interferometer

Table B.2: Results of the WLI accuracy test through repeated structural measurements.

Material	$V_{WLI,1}$ [μl]	$V_{WLI,2}$ [μl]	$V_{WLI,3}$ [μl]	$V_{WLI,4}$ [μl]	$V_{WLI,5}$ [μl]	$V_{WLI,mean}$ [μl]	σ_{RSTD} [%]
SiO_2/TiO_2	551	593	605	481	556	557	8.7
B_4C	46.8	39.9	45.9	54.9	51.2	47.7	11.9
NaB	511	539	597	610	461	544	11.3
NaB	6.2	6.3	6.9	7.1	5.8	6.5	8.2

Appendix C

Material properties

C.1 Correlations

C.1.1 Density of gases

$$\rho_{gas} = \frac{p_{tot}\,\tilde{M}_{gas}}{\tilde{R}\,(T + 273.15)} \tag{C.1}$$

with

$[T] = \,^{\circ}\mathrm{C}$
$\tilde{R} = 8314.4\,\mathrm{J\,kmol^{-1}\,K^{-1}}$

Source: Glück (1991)

C.1.2 Dynamic viscosity

$$\eta = \nu\rho \tag{C.2}$$

Source: Glück (1991)

C.1.3 Kinematic viscosity of air

$$\nu_{gas} = a_0 + a_1 T + a_2 T^2 + a_3 T^3 \tag{C.3}$$

with

$[T] = \,^{\circ}\mathrm{C}$
$[\nu] = \mathrm{m^2\,s^{-1}}$
$a_0 = 1.351980 \cdot 10^{-5}$
$a_1 = 8.930841 \cdot 10^{-8}$
$a_2 = 1.094808 \cdot 10^{-10}$
$a_3 = -3.659345 \cdot 10^{-14}$

Source: Glück (1991)

C.1.4 Diffusion coefficient of vapor in large excess of air

$$D = 0.00144 \frac{(T + 273.15)^{1.75} \left[\frac{1}{\tilde{M}_{vapor}} + \frac{1}{\tilde{M}_{air}}\right]^{1/2}}{\sqrt{2}\, p_{tot} \left[V_{diff,vapor}^{1/3} + V_{diff,air}^{1/3}\right]^2} \tag{C.4}$$

with

$[D] = \mathrm{cm^2\,s^{-1}}$
$[T] = \mathrm{°C}$
$[p_{tot}] = \mathrm{bar}$
$V_{diff,vapor} = 13$
$V_{diff,air} = 19$

Source: Poling et al. (2000), Marrero and Mason (1972)

C.1.5 Saturation water vapor pressure in air

$$p_{sat} = exp\left(A - \frac{B}{T + C}\right), \tag{C.5}$$

with

$[T] = \mathrm{K}$
$\tilde{R}_{vapor} = 461.5\,\mathrm{J\,kg^{-1}\,K^{-1}}$
$A = 23.1946$
$B = 3813.98$
$C = -46.29$

Source: Glück (1991)

C.1.6 Density of water

$$\rho_{water} = b_0 + b_1 T + b_2 T^2 + b_3 T^3 \tag{C.6}$$

with

$[T] = \mathrm{°C}$
$[\rho] = \mathrm{kg\,m^{-3}}$
$b_0 = 1.002045 \cdot 10^3$
$b_1 = -1.029905 \cdot 10^{-1}$
$b_2 = -3.698162 \cdot 10^{-3}$
$b_3 = 3.991053 \cdot 10^{-6}$

Source: Glück (1991)

C.1.7 Density of solutions and suspensions

$$\rho_{sol,sus} = \frac{\rho_{liquid}}{1 + \frac{\omega_{solid}\rho_{liquid}}{\rho_{solid}} - \omega_{solid}} \tag{C.7}$$

Source: Budeanu et al. (2010)

C.2 Properties of dry air

Table C.1: Properties of dry air at temperatures used in the experimental and simulative study, calculated with the correlations of Glück (1991) (Appendix C.1.1, C.1.3 and C.1.2).

Property	Temperature	Value	Unit
$\tilde{M}_{air}$	–	28.96	$\mathrm{kg\,kmol^{-1}}$
ρ_{air}	21 °C	1.1995	$\mathrm{kg\,m^{-3}}$
ρ_{air}	25 °C	1.1839	$\mathrm{kg\,m^{-3}}$
ρ_{air}	50 °C	1.0919	$\mathrm{kg\,m^{-3}}$
ρ_{air}	75 °C	1.0135	$\mathrm{kg\,m^{-3}}$
ν_{air}	21 °C	$1.5443 \cdot 10^{-5}$	$\mathrm{m^2\,s^{-1}}$
ν_{air}	25 °C	$1.5820 \cdot 10^{-5}$	$\mathrm{m^2\,s^{-1}}$
ν_{air}	50 °C	$1.8254 \cdot 10^{-5}$	$\mathrm{m^2\,s^{-1}}$
ν_{air}	75 °C	$2.0818 \cdot 10^{-5}$	$\mathrm{m^2\,s^{-1}}$
η_{air}	21 °C	$1.8524 \cdot 10^{-5}$	Pa s
η_{air}	25 °C	$1.8729 \cdot 10^{-5}$	Pa s
η_{air}	50 °C	$1.9932 \cdot 10^{-5}$	Pa s
η_{air}	75 °C	$1.8373 \cdot 10^{-5}$	Pa s

C.3 Properties of water vapor

Table C.2: Properties of water vapor at temperatures used in the experimental and simulative study, calculated with the correlations of Poling et al. (2000) (Appendix C.1.4) and Glück (1991) (Appendix C.1.5).

Property	Temperature	Value	Unit
$\tilde{M}_{vapor}$	–	28.96	$\mathrm{kg\,kmol^{-1}}$
$\tilde{R}_{vapor}$	–	461.5	$\mathrm{J\,kg^{-1}\,K^{-1}}$
D	8.3 °C	$23.4 \cdot 10^{-6}$	$\mathrm{m^2\,s^{-1}}$
D	21 °C	$25.3 \cdot 10^{-6}$	$\mathrm{m^2\,s^{-1}}$
D	25 °C	$26.1 \cdot 10^{-6}$	$\mathrm{m^2\,s^{-1}}$
D	50 °C	$29.9 \cdot 10^{-6}$	$\mathrm{m^2\,s^{-1}}$
D	75 °C	$34.0 \cdot 10^{-6}$	$\mathrm{m^2\,s^{-1}}$
p_{sat}	8.3 °C	1070	Pa
p_{sat}	21 °C	2457	Pa
p_{sat}	25 °C	3138	Pa
p_{sat}	50 °C	12317	Pa
p_{sat}	75 °C	38548	Pa

C.4 Properties of water

Table C.3: Properties of water at temperatures used in the experimental and simulative study, calculated with the correlation of Glück (1991) (Appendix C.1.6).

Property	Temperature	Value	Unit
$\tilde{M}_{water}$	–	28.96	$\mathrm{kg\,kmol^{-1}}$
η_{water}	25 °C	$8.91 \cdot 10^{-4}$	Pa s
σ_{water}	25 °C	74.1	$\mathrm{mN\,m^{-1}}$
ρ_{water}	8.3 °C	1000	$\mathrm{kg\,m^{-3}}$
ρ_{water}	21 °C	998	$\mathrm{kg\,m^{-3}}$
ρ_{water}	25 °C	997	$\mathrm{kg\,m^{-3}}$
ρ_{water}	50 °C	988	$\mathrm{kg\,m^{-3}}$
ρ_{water}	75 °C	975	$\mathrm{kg\,m^{-3}}$

C.5 Properties of aqueous silica-based nanofluid

Table C.4: Properties of the nanosuspension used in the experimental study at 25 °C.

Property	Solid mass fraction	Value	Unit	Source
$\tilde{M}_{SiO_2}$	–	60.08	$\mathrm{kg\,kmol^{-1}}$	Lide (2004)
$\tilde{M}_{TiO_2}$	–	79.87	$\mathrm{kg\,kmol^{-1}}$	Lide (2004)
ρ_{SiO_2}	–	2650	$\mathrm{kg\,m^{-3}}$	Manufacturer information
ρ_{TiO_2}	–	4260	$\mathrm{kg\,m^{-3}}$	Manufacturer information
$\rho_{SiO_2/TiO_2,sus}$	40 wt%	1831	$\mathrm{kg\,m^{-3}}$	Calculation
d_{part,SiO_2}	–	22	nm	Manufacturer information
d_{part,TiO_2}	–	21	nm	Manufacturer information
$\eta_{SiO_2/TiO_2,sus}$	40 wt%	$42.47 \cdot 10^{-4}$	Pa s	Rotational rheometer
$\sigma_{SiO_2/TiO_2,sus}$	40 wt%	79.84	$\mathrm{mN\,m^{-1}}$	Du Noüy tensiometer

C.6 Properties of aqueous boron carbide microfluid

Table C.5: Properties of the microsuspension used in the experimental study at 25 °C.

Property	Solid mass fraction	Value	Unit	Source
$\tilde{M}_{B_4C}$	–	55.25	$\mathrm{kg\,kmol^{-1}}$	Lide (2004)
ρ_{B_4C}	–	2510	$\mathrm{kg\,m^{-3}}$	Manufacturer information
$\rho_{B_4C,sus}$	5 wt%	1074	$\mathrm{kg\,m^{-3}}$	Calculation
d_{part,B_4C}	–	0.67	μm	Laser scattering
$\eta_{B_4C,sus}$	5 wt%	$14.61 \cdot 10^{-4}$	Pa s	Rotational rheometer
$\sigma_{B_4C,sus}$	5 wt%	76.66	$\mathrm{mN\,m^{-1}}$	Du Noüy tensiometer

C.7 Properties of aqueous sodium benzoate solution

Table C.6: Properties of the aqueous sodium benzoate solution used in the experimental study at 25 °C.

Property	Solid mass fraction	Value	Unit	Source
$\tilde{M}_{NaB}$	–	144.11	$\mathrm{kg\,kmol^{-1}}$	Lide (2004)
ρ_{NaB}	–	1440	$\mathrm{kg\,m^{-3}}$	Jang et al. (2001)
$\rho_{NaB,sol}$	5 wt%	1012	$\mathrm{kg\,m^{-3}}$	Budeanu et al. (2010)
$\rho_{NaB,sol}$	20 wt%	1062	$\mathrm{kg\,m^{-3}}$	Budeanu et al. (2010)
$\rho_{NaB,sol}$	30 wt%	1098	$\mathrm{kg\,m^{-3}}$	Budeanu et al. (2010)
$\eta_{NaB,sol}$	5 wt%	$11.98 \cdot 10^{-4}$	Pa s	Rotational rheometer
$\eta_{NaB,sol}$	20 wt%	$16.24 \cdot 10^{-4}$	Pa s	Rotational rheometer
$\eta_{NaB,sol}$	30 wt%	$26.21 \cdot 10^{-4}$	Pa s	Rotational rheometer
$\sigma_{NAB,sol}$	5 wt%	71.35	$\mathrm{mN\,m^{-1}}$	Du Noüy tensiometer
$\sigma_{NAB,sol}$	20 wt%	57.83	$\mathrm{mN\,m^{-1}}$	Du Noüy tensiometer
$\sigma_{NAB,sol}$	30 wt%	57.03	$\mathrm{mN\,m^{-1}}$	Du Noüy tensiometer

C.8 Contact angles on borosilicate glass

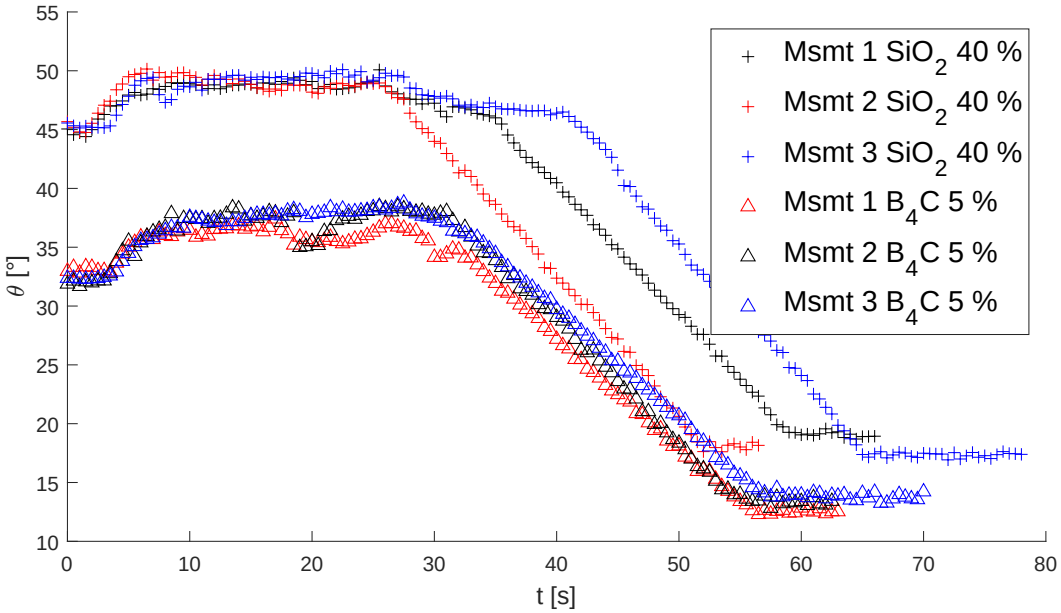

Figure C.1: Data of the dynamic contact angle measurements with SiO_2/TiO_2 and B_4C.

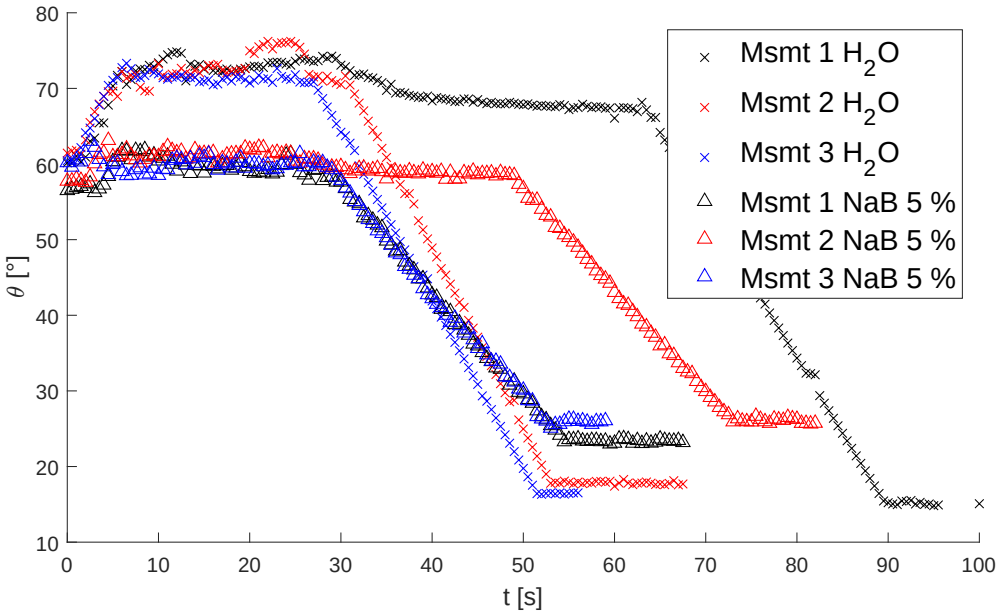

Figure C.2: Data of the dynamic contact angle measurements with water and NaB.

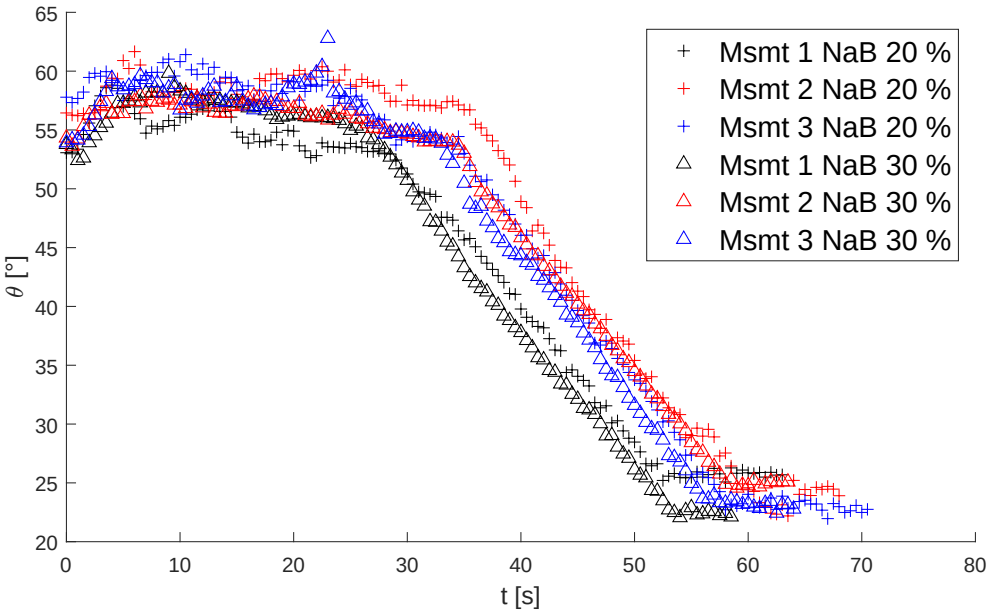

Figure C.3: Data of the dynamic contact angle measurements with NaB.

Appendix D

Sessile droplets in the experimental and simulative studies

D.1 Spatial dimensions and Bond numbers of sessile droplets

Table D.1: Spatial dimensions of the droplets used in the experimental studies and the simulative investigation at 25 °C.

Material	V_{drop} [μm]	ω_{solid} wt%	θ[°]	d_{drop} [mm]	h_{drop} [mm]	Bo
SiO_2/TiO_2	1	40	48.3	2.1998	0.49	0.0332
B_4C	1	5	36.9	2.4507	0.41	0.0319
H_2O	1	–	72.1	1.8117	0.66	0.0394
NaB	0.1	5	60.3	0.9237	0.27	0.0085
NaB	1	5	60.3	1.9901	0.58	0.0394
NaB	0.1	20	58.1	0.9403	0.26	0.0104
NaB	1	20	58.1	2.0258	0.56	0.0481
NaB	0.1	30	56.9	0.9496	0.26	0.0105
NaB	1	30	56.9	2.0458	0.55	0.0486

D.2 Camera recordings of structure formation during sessile solid-laden droplet drying

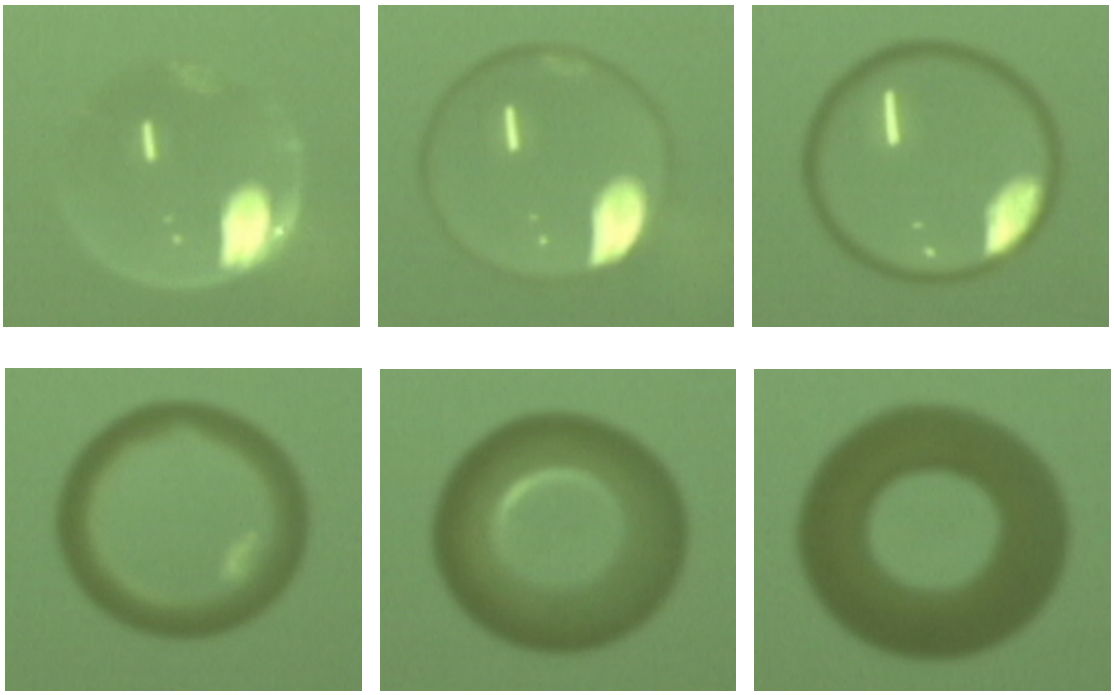

Figure D.1: Top-view camera recordings of the drying and ring-structure formation process of a deposited sodium benzoate droplet.

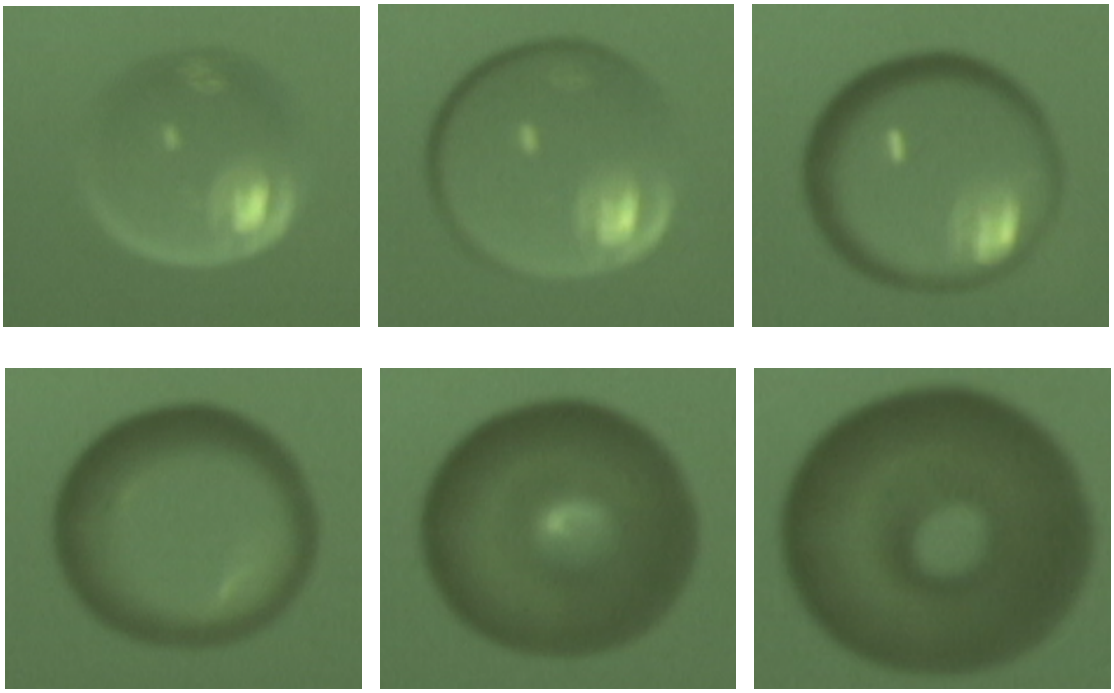

Figure D.2: Top-view camera recordings of the drying and crescent-structure formation process of a deposited sodium benzoate droplet.

D.3 Solitary deposit porosities

Table D.2: List of obtained solitary deposit porosities.

Exp. No.	Material	ω_{solid} [wt%]	V_{drop} [μl]	U [m/s]	T [°C]	$\varepsilon_{soli,1}$	$\varepsilon_{soli,2}$	$\varepsilon_{soli,3}$
1	SiO_2/TiO_2	40	1.0	0.1	21	0.56	0.45	0.52
2	SiO_2/TiO_2	40	1.0	1.0	21	0.54	0.57	0.50
3	SiO_2/TiO_2	40	1.0	1.5	21	0.67	0.62	0.52
4	SiO_2/TiO_2	40	1.0	1.5	50	0.56	0.58	0.74
5	SiO_2/TiO_2	40	1.0	1.5	75	0.69	0.50	0.64
6	B_4C	5	1.0	0.1	21	0.51	0.59	0.56
7	B_4C	5	1.0	1.0	21	0.69	0.59	0.64
8	B_4C	5	1.0	1.5	21	0.69	0.62	0.66
9	B_4C	5	1.0	1.5	50	0.67	0.73	0.70
10	B_4C	5	1.0	1.5	75	0.65	0.63	0.72
11	NaB	30	1.0	0.1	21	0.49	0.57	0.52
12	NaB	30	1.0	1.0	21	0.59	0.65	0.59
13	NaB	30	1.0	1.5	21	0.74	0.60	0.57
14	NaB	30	1.0	1.5	50	0.71	0.59	0.65
15	NaB	30	1.0	1.5	75	0.71	0.54	0.62
16	NaB	5	1.0	0.0	21	0.28	0.33	0.38
17	NaB	5	1.0	0.1	21	0.42	0.55	0.49
18	NaB	5	1.0	1.0	21	0.49	0.53	0.56
19	NaB	5	1.0	1.5	21	0.71	0.67	0.63
20	NaB	5	0.1	0.0	21	0.39	0.38	0.31
21	NaB	20	1.0	0.0	21	0.51	0.44	0.48
22	NaB	20	1.0	1.5	75	0.54	0.54	0.69
23	NaB	20	0.1	0.0	21	0.49	0.40	0.41
24	NaB	20	0.1	1.5	75	0.67	0.70	0.72
25	NaB	30	1.0	0.0	21	0.58	0.51	0.51
26	NaB	30	1.0	1.0	50	0.61	0.66	0.65
27	NaB	30	0.1	0.0	21	0.55	0.44	0.46
28	NaB	30	0.1	1.5	21	0.65	0.50	0.63
29	NaB	30	0.1	1.5	50	0.66	0.49	0.58
30	NaB	30	0.1	1.5	75	0.75	0.72	0.70

Appendix E

CFD simulation of sessile droplet drying

E.1 Development of boundary layer and mass transfer coefficient at different distances from the substrate edge

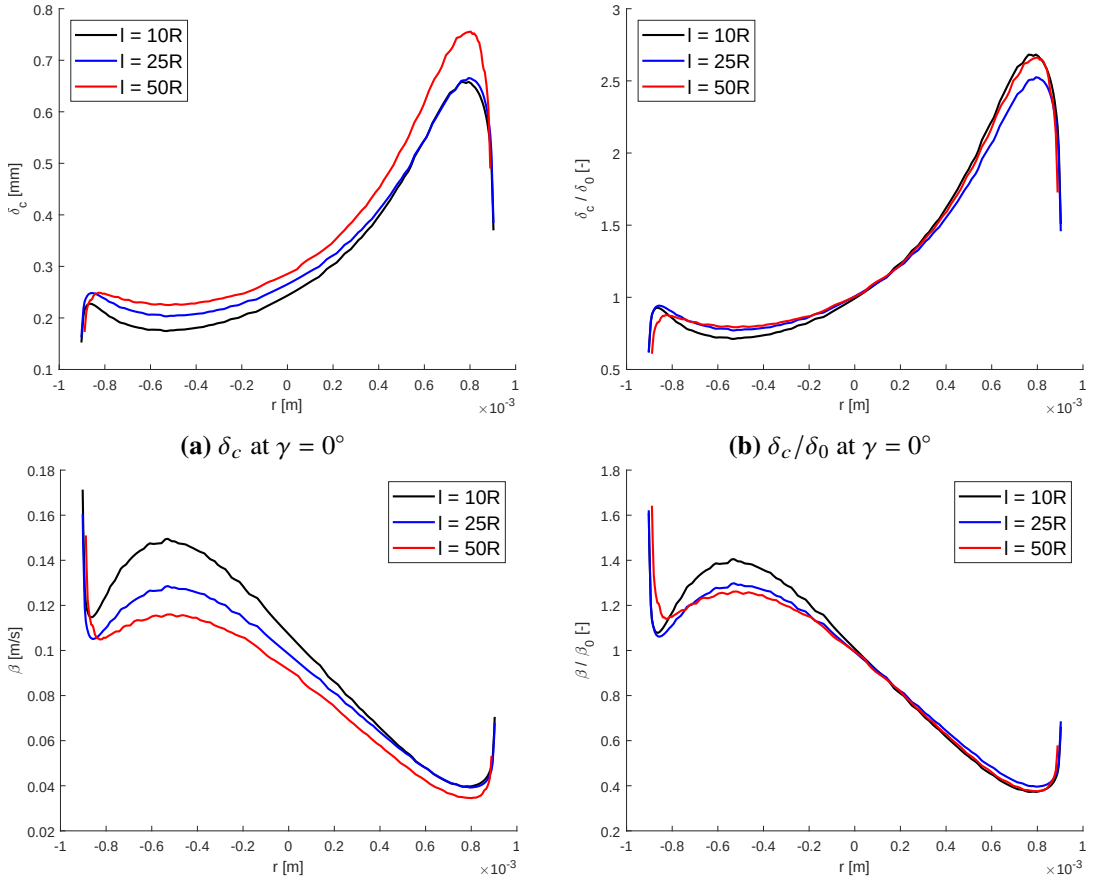

(a) δ_c at $\gamma = 0°$

(b) δ_c/δ_0 at $\gamma = 0°$

(c) β at $\gamma = 0°$

(d) β/β_0 at $\gamma = 0°$

Figure E.1: Development of boundary layer and mass transfer for $Re = 116$ at different distances from the substrate edge in flow direction.

E.2 Development of boundary layer and mass transfer coefficient at different contact angles

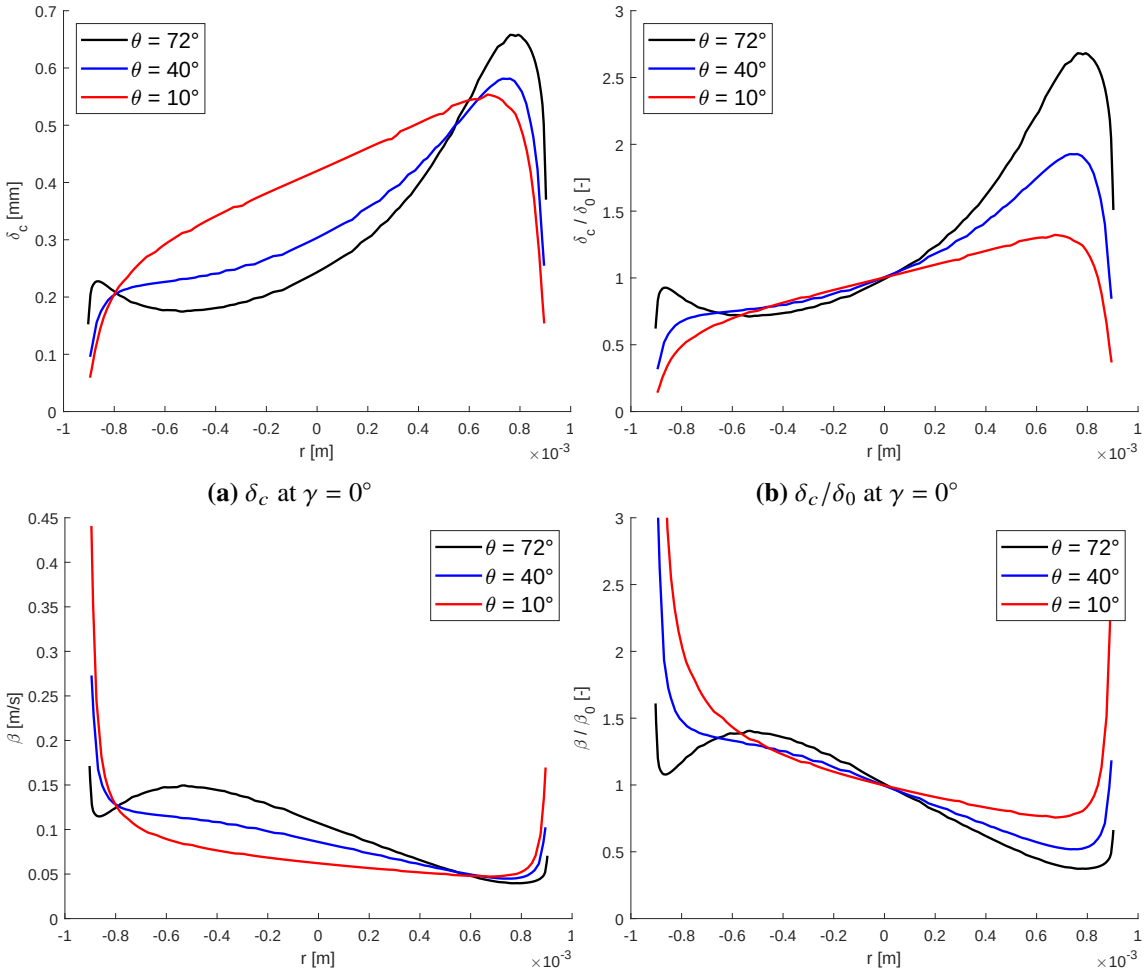

(a) δ_c at $\gamma = 0°$

(b) δ_c/δ_0 at $\gamma = 0°$

(c) β at $\gamma = 0°$

(d) β/β_0 at $\gamma = 0°$

Figure E.2: Development of boundary layer thickness and local mass transfer coefficient for $Re = 116$ at different droplet contact angles along the maximal cord in gas flow direction.

E.3 Evaporation along the maximal surface cord of two droplets placed one after the other in flow direction for different diffusive and convective cases.

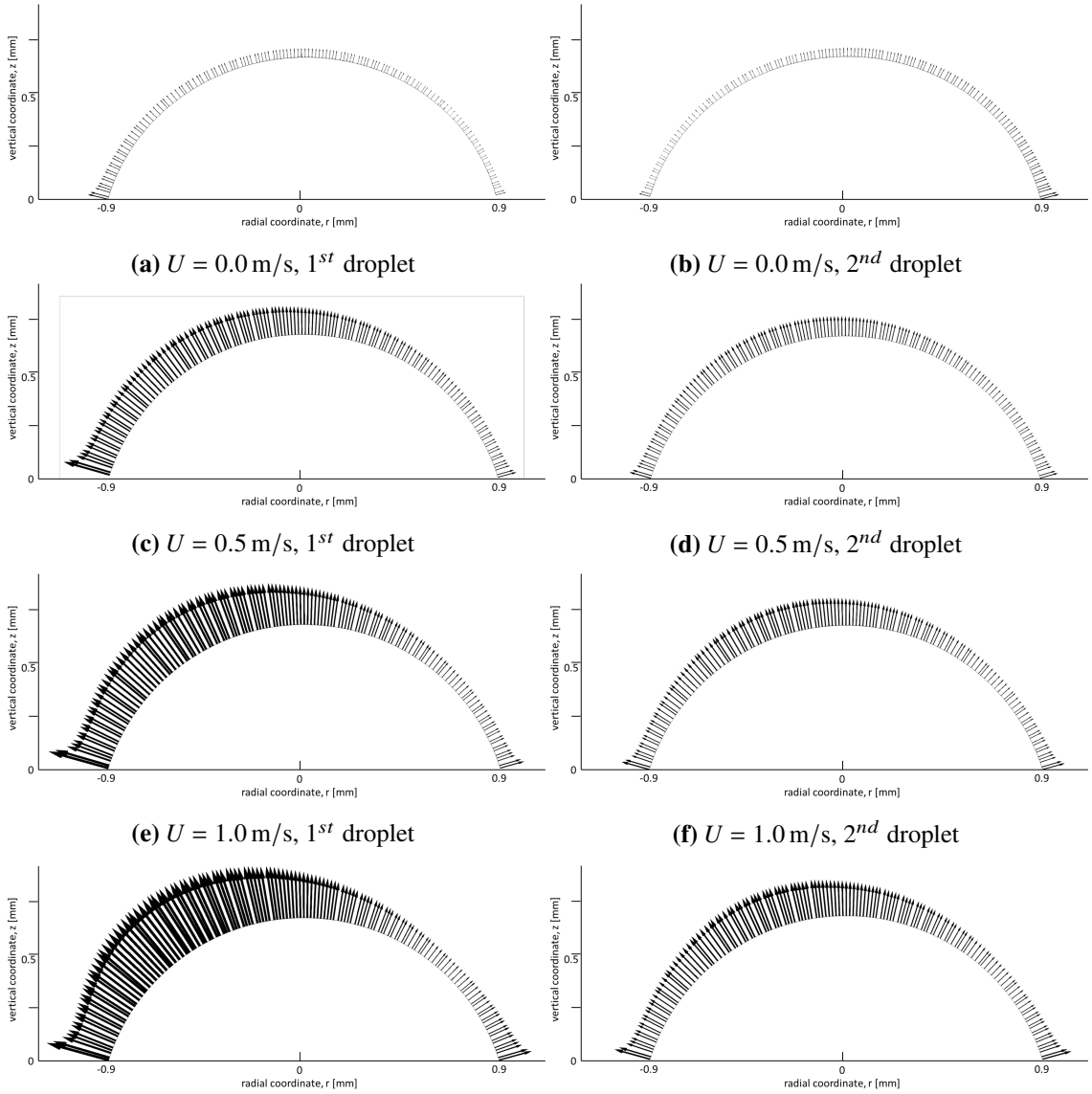

(a) $U = 0.0\,\mathrm{m/s}$, 1^{st} droplet

(b) $U = 0.0\,\mathrm{m/s}$, 2^{nd} droplet

(c) $U = 0.5\,\mathrm{m/s}$, 1^{st} droplet

(d) $U = 0.5\,\mathrm{m/s}$, 2^{nd} droplet

(e) $U = 1.0\,\mathrm{m/s}$, 1^{st} droplet

(f) $U = 1.0\,\mathrm{m/s}$, 2^{nd} droplet

(g) $U = 1.5\,\mathrm{m/s}$, 1^{st} droplet

(h) $U = 1.5\,\mathrm{m/s}$, 2^{nd} droplet

Figure E.3: Evaporation along the surfaces of two droplets placed one after the other in flow direction for different diffusive and convective cases at $\gamma = 0°$.

E.4 Normed flux profiles for the comparison between solitary and binary droplet setups

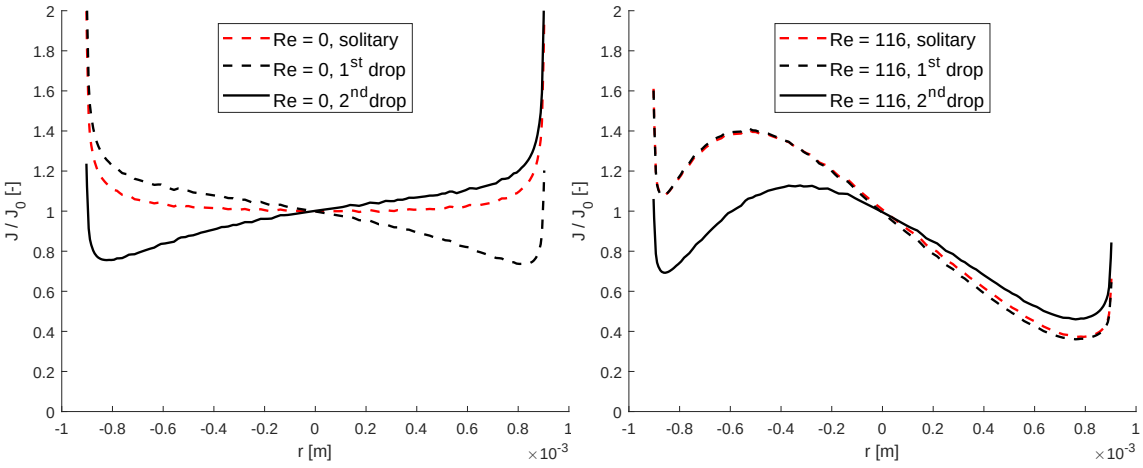

Figure E.4: Comparison of surface flux distribution along $\gamma = 0°$ of binary and solitary droplet setups for the purely diffusive case (left) and under forced convection at $Re = 116$ (right).

E.5 Boundary layer and mass transfer coefficient for binary droplet systems

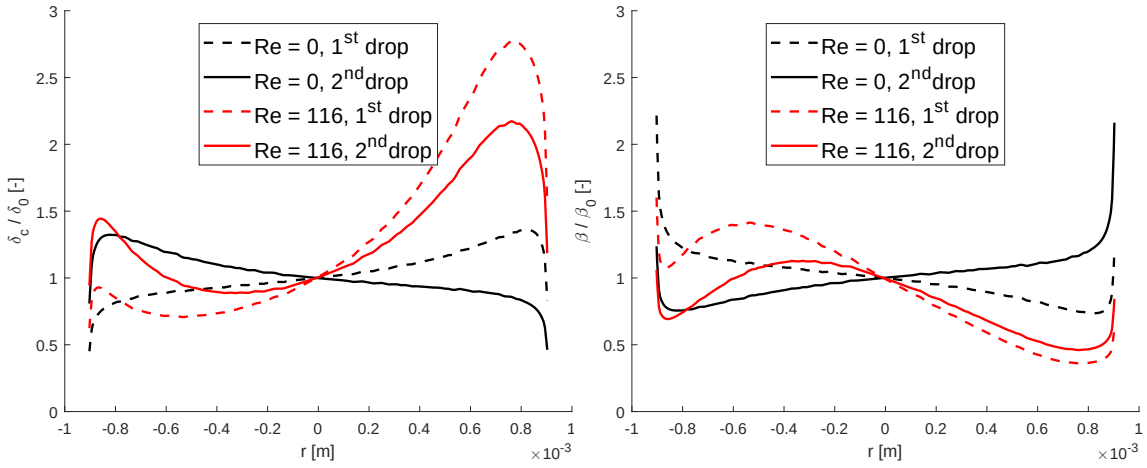

(a) δ_c/δ_0 at $\gamma = 0°$ **(b)** β/β_0 at $\gamma = 0°$

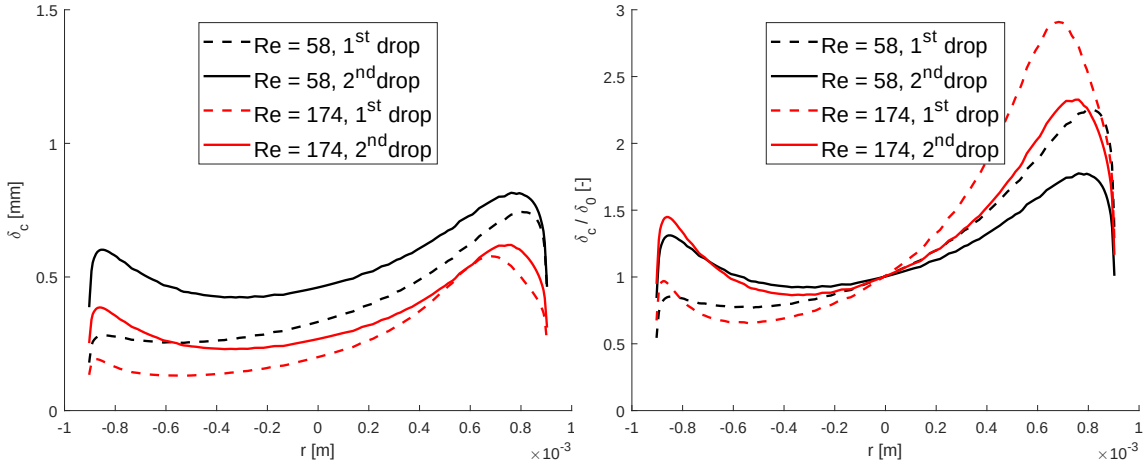

(c) δ_c at $\gamma = 0°$ **(d)** δ_c/δ_0 at $\gamma = 0°$

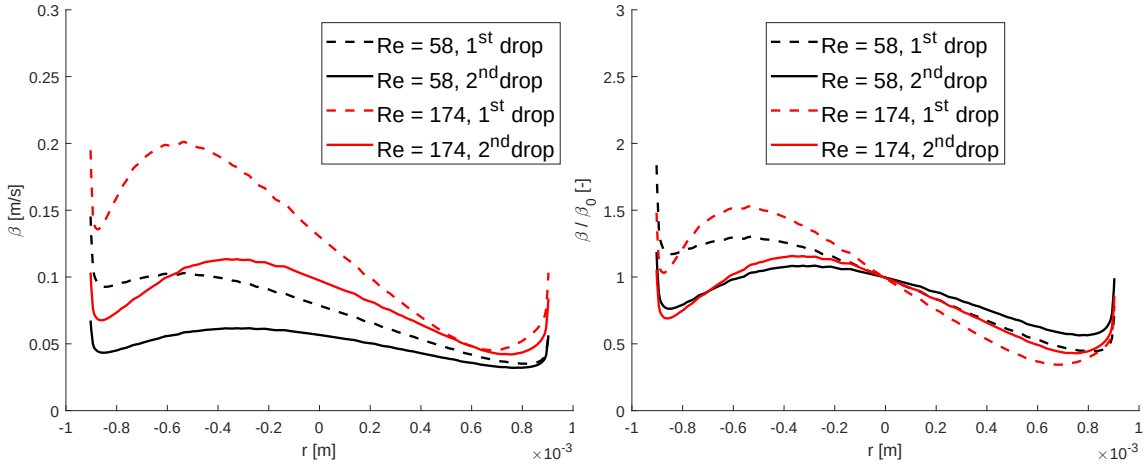

(e) β at $\gamma = 0°$ **(f)** β/β_0 at $\gamma = 0°$

Figure E.5: Boundary layer thickness and mass transfer coefficient with corresponding normalizations for various Reynolds numbers along $\gamma = 0°$.

E.6 Glyph illustrations of flux profiles at different contact angles

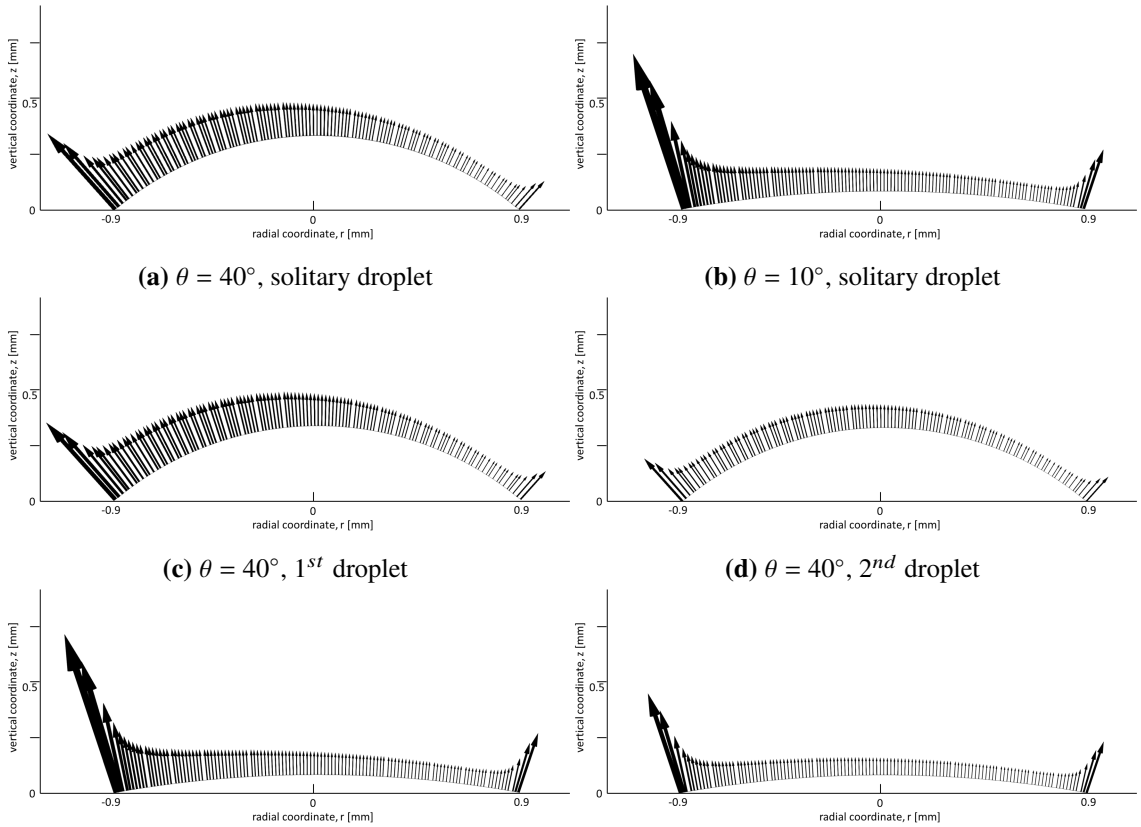

(a) $\theta = 40°$, solitary droplet

(b) $\theta = 10°$, solitary droplet

(c) $\theta = 40°$, 1^{st} droplet

(d) $\theta = 40°$, 2^{nd} droplet

(e) $\theta = 10°$, 1^{st} droplet

(f) $\theta = 10°$, 2^{nd} droplet

Figure E.6: Evaporation flux along the surface of solitary and binary droplets with various contact angles at $\gamma = 0°$ and $Re = 116$.

E.7 Development of boundary layer and mass transfer coefficient at different contact angles for binary droplet systems

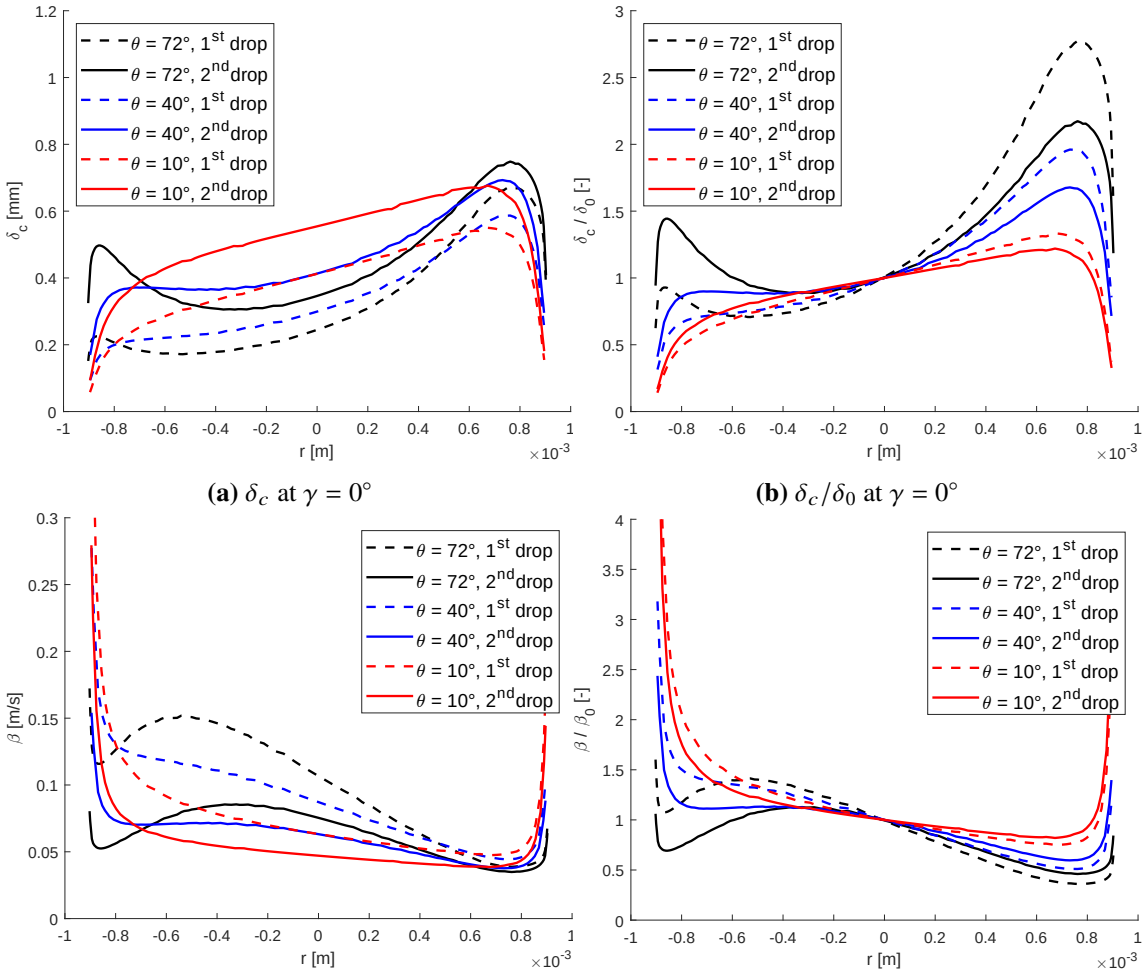

(a) δ_c at $\gamma = 0°$

(b) δ_c/δ_0 at $\gamma = 0°$

(c) β at $\gamma = 0°$

(d) β/β_0 at $\gamma = 0°$

Figure E.7: Binary setup development of boundary layer thickness and local mass transfer coefficient at $Re = 116$ for different droplet contact angles along the maximal cord in gas flow direction.

Bibliography

Ariyasu, A., Hattori, Y. and Otsuka, M. (2017). Non-destructive prediction of enteric coating layer thickness and drug dissolution rate by near-infrared spectroscopy and X-ray computed tomography. In: *International Journal of Pharmaceutics* 525 (1), pp. 282–290. DOI: 10.1016/j.ijpharm.2017.04.017.

Atarés, L., Depypere, F., Pieters, J. G. and Dewettinck, K. (2012). Coating quality as affected by core particle segregation in fluidized bed processing. In: *Journal of Food Engineering* 113 (3), pp. 415–421. DOI: 10.1016/j.jfoodeng.2012.06.012.

Attinger, D., Haferl, S., Zhao, Z. and Poulikakos, D. (2000). Transport phenomena in the impact of a molten droplet on a surface: Macroscopic phenomenology and microscopic considerations, Part 2: Heat transfer and solidification. In: *Annual Review of Heat Transfer* 11, pp. 65–143. DOI: 10.1615/AnnualRevHeatTransfer.v11.40.

Bachmann, P., Chen, K., Bück, A. and Tsotsas, E. (2020). Prediction of particle size and layer-thickness distributions in a continuous horizontal fluidized-bed coating process. In: *Particuology* 50, pp. 1–12. DOI: 10.1016/j.partic.2019.06.005.

Baines, W. D. and James, D. F. (1994). Evaporation of a droplet on a surface. In: *Industrial & Engineering Chemistry Research* 33 (2), pp. 411–416. DOI: 10.1021/ie00026a036.

Barthlott, W., Cerman, Z. and Stosch, A. (2004). Der Lotus-Effekt: Selbstreinigende Oberflächen und ihre Übertragung in die Technik. In: *Biologie in unserer Zeit* 34, pp. 290–296. DOI: 10.1002/biuz.200410260.

Bazargan, V. (2014). *Effect of substrate cooling and droplet shape and composition on the droplet evaporation and the deposition of particles*. Vancouver (BC), Canada: Dissertation University of British Columbia. DOI: 10.14288/1.0166865.

Bhardwaj, R. (2018). Analysis of an evaporating sessile droplet on a non-wetted surface. In: *Colloid and Interface Science Communications* 24, pp. 49–53. DOI: 10.1016/j.colcom.2018.02.004.

Bhardwaj, R., Fang, X. and Attinger, D. (2009). Pattern formation during the evaporation of a colloidal nanoliter drop: A numerical and experimental study. In: *New Journal of Physics* 11 (7), p. 075020. DOI: 10.1088/1367-2630/11/7/075020.

Bhardwaj, R., Fang, X., Somasundaran, P. and Attinger, D. (2010). Self-assembly of colloidal particles from evaporating droplets: Role of DLVO interactions and proposition of a phase diagram. In: *Langmuir* 26 (11), pp. 7833–7842. DOI: 10.1021/la9047227.

Birdi, K. S., Vu, D. T. and Winter, A. (1988). Interfacial tension of liquids from the height and contact angle of a single sessile drop. In: *Colloid & Polymer Science* 266 (9), pp. 849–854. DOI: 10.1007/BF01417869.

Black, D. L., McQuay, M. Q. and Bonin, M. P. (1996). Laser-based techniques for particle-size measurement: A review of sizing methods and their industrial applications. In: *Progress in Energy and Combustion Science* 22 (3), pp. 267–306. DOI: 10.1016/S0360-1285(96)00008-1.

Bouchenna, C., Ait Saada, M., Chikh, S. and Tadrist, L. (2017). Generalized formulation for evaporation rate and flow pattern prediction inside an evaporating pinned sessile drop. In: *International Journal of Heat and Mass Transfer* 109, pp. 482–500. DOI: 10.1016/j.ijheatmasstransfer.2017.01.114.

Bourges-Monnier, C. and Shanahan, M. E. R. (1995). Influence of evaporation on contact angle. In: *Langmuir* 11 (7), pp. 2820–2829. DOI: 10.1021/la00007a076.

Bradley, R. S. and Fuchs, N. A., eds. (1959). *Evaporation and Droplet Growth in Gaseous Media*. London, Oxford: Pergamon Press. DOI: 10.1016/B978-1-4832-0060-6.50001-6.

Breinlinger, T. and Kraft, T. (2014). A simple method for simulating the coffee stain effect. In: *Powder Technology* 256, pp. 279–284. DOI: 10.1016/j.powtec.2014.02.024.

Bruning, M. A., Loeffen, L. and Marin, A. (2020). Particle monolayer assembly in evaporating salty colloidal droplets. In: *Physical Review Fluids* 5 (8), p. 083603. DOI: 10.1103/PhysRevFluids.5.083603.

Brutin, D., Sobac, B., Loquet, B. and Sampol, J. (2011). Pattern formation in drying drops of blood. In: *Journal of Fluid Mechanics* 667, pp. 85–95. DOI: 10.1017/S0022112010005070.

Brutin, D., ed. (2015). *Droplet Wetting and Evaporation: From Pure to Complex Fluids*. Amsterdam, Boston and Heidelberg: Elsevier/AP Academic Press. DOI: 10.1016/C2013-0-18955-6.

Bück, A., Peglow, M., Naumann, M. and Tsotsas, E. (2012). Population balance model for drying of droplets containing aggregating nanoparticles. In: *AIChE Journal* 58 (11), pp. 3318–3328. DOI: 10.1002/aic.13726.

Budeanu, M., Radu, S. and Vasile, D. (2010). Comparing some models for predicting the density of liquid mixtures. In: *Revista de Chimie* 61 (3), pp. 322–327. DOI: 10/RCB2010-287580587.

Butterhof, C., Milius, W. and Breu, J. (2012). Co-crystallisation of benzoic acid with sodium benzoate: The significance of stoichiometry. In: *CrystEngComm* 14 (11), pp. 3945–3950. DOI: 10.1039/C2CE25185J.

Clarke, A., Blake, T. D., Carruthers, K. and Woodward, A. (2002). Spreading and imbibition of liquid droplets on porous surfaces. In: *Langmuir* 18 (8), pp. 2980–2984. DOI: 10.1021/la0117810.

Clayton, W. (1926). Capillary and colloid chemistry. In: *Journal of the Society of Chemical Industry* 45 (44), pp. 797–798. DOI: 10.1002/jctb.5000454407.

Crivoi, A. and Duan, F. (2013a). Evaporation-induced branched structures from sessile nanofluid droplets. In: *The Journal of Physical Chemistry C* 117 (15), pp. 7835–7843. DOI: 10.1021/jp312021w.

Crivoi, A. and Duan, F. (2013b). Fingering structures inside the coffee-ring pattern. In: *Colloids and Surfaces A: Physicochemical and Engineering Aspects* 432, pp. 119–126. DOI: 10.1016/j.colsurfa.2013.04.051.

Crivoi, A. and Duan, F. (2014). Three-dimensional Monte Carlo model of the coffee-ring effect in evaporating colloidal droplets. In: *Scientific Reports* 4, p. 4310. DOI: 10.1038/srep04310.

Dadkhah, M. (2014). *Morphological characterization of agglomerates produced in a spray fluidized bed by X-ray tomography*. Magdeburg, Germany: Dissertation Otto von Guericke University.

Dadkhah, M., Peglow, M. and Tsotsas, E. (2012). Characterization of the internal morphology of agglomerates produced in a spray fluidized bed by X-ray tomography. In: *Powder Technology* 228, pp. 349–358. DOI: 10.1016/j.powtec.2012.05.051.

Dal Pont, J. P., ed. (2013). *Process Engineering and Industrial Management*. London: Wiley-ISTE. DOI: 10.1002/9781118562130.

Dam, D. van and Kuerten, J. (2008). Modeling the drying of ink-jet-printed structures and experimental verification. In: *Langmuir: The ACS Journal of Surfaces and Colloids* 24, pp. 582–589. DOI: 10.1021/la701862a.

Dash, S. and Garimella, S. V. (2013). Droplet evaporation dynamics on a superhydrophobic surface with negligible hysteresis. In: *Langmuir* 29 (34), pp. 10785–10795. DOI: 10.1021/la402784c.

David, S., Sefiane, K. and Tadrist, L. (2007). Experimental investigation of the effect of thermal properties of the substrate in the wetting and evaporation of sessile drops. In: *Colloids and Surfaces A: Physicochemical and Engineering Aspects* 298 (1-2), pp. 108–114. DOI: 10.1016/J.COLSURFA.2006.12.018.

Deegan, R. D. (2000). Pattern formation in drying drops. In: *Physical Review E* 61 (1), pp. 475–485. DOI: 10.1103/PhysRevE.61.475.

Deegan, R. D., Bakajin, O., Dupont, T. F., Huber, G., Nagel, S. R. and Witten, T. A. (1997). Capillary flow as the cause of ring stains from dried liquid drops. In: *Nature* 389, pp. 827–828. DOI: 10.1038/39827.

Deegan, R. D., Bakajin, O., Dupont, T. F., Huber, G., Nagel, S. R. and Witten, T. A. (2000). Contact line deposits in an evaporating drop. In: *Physical Review E, Statistical Physics, Plasmas, Fluids, and Related Interdisciplinary Topics* 62 (1 Pt B), pp. 756–765. DOI: 10.1103/physreve.62.756.

Delele, M. A., Nuyttens, D., Duga, A. T., Ambaw, A., Lebeau, F., Nicolai, B. M. and Verboven, P. (2016). Predicting the dynamic impact behaviour of spray droplets on flat plant surfaces. In: *Soft Matter* 12 (34), pp. 7195–7211. DOI: 10.1039/C6SM00933F.

Dewettinck, K. and Huyghebaert, A. (1999). Fluidized bed coating in food technology. In: *Trends in Food Science & Technology* 10 (4), pp. 163–168. DOI: 10.1016/S0924-2244(99)00041-2.

Dewettinck, K., Deroo, L., Messens, W. and Huyghebaert, A. (1998). Agglomeration tendency during top-spray fluidized bed coating with gums. In: *LWT - Food Science and Technology* 31 (6), pp. 576–584. DOI: 10.1006/fstl.1998.0421.

Dufresne, E. R., Corwin, E. I., Greenblatt, N. A., Ashmore, J., Wang, D. Y., Dinsmore, A. D., Cheng, J. X., Xie, X. S., Hutchinson, J. W. and Weitz, D. A. (2003). Flow and fracture in

drying nanoparticle suspensions. In: *Physical Review Letters* 91 (22), p. 224501. DOI: 10.1103/PhysRevLett.91.224501.

Dufresne, E. R., Stark, D. J., Greenblatt, N. A., Cheng, J. X., Hutchinson, J. W., Mahadevan, L. and Weitz, D. A. (2006). Dynamics of fracture in drying suspensions. In: *Langmuir* 22 (17), pp. 7144–7147. DOI: 10.1021/la061251+.

Dugyala, V. R. and Basavaraj, M. G. (2014). Control over coffee-ring formation in evaporating liquid drops containing ellipsoids. In: *Langmuir* 30 (29), pp. 8680–8686. DOI: 10.1021/la500803h.

Dunn, G. J., Wilson, S. K., Duffy, B. R., David, S. and Sefiane, K. (2008). A mathematical model for the evaporation of a thin sessile liquid droplet: Comparison between experiment and theory. In: *Colloids and Surfaces A: Physicochemical and Engineering Aspects* 323 (1-3), pp. 50–55. DOI: 10.1016/j.colsurfa.2007.09.031.

Eral, H. B., Mannetje, D. and Oh, J. M. (2013). Contact angle hysteresis: A review of fundamentals and applications. In: *Colloid and Polymer Science* 291 (2), pp. 247–260. DOI: 10.1007/s00396-012-2796-6.

Erbil, H. Y. (2012). Evaporation of pure liquid sessile and spherical suspended drops: A review. In: *Advances in Colloid and Interface Science* 170 (1-2), pp. 67–86. DOI: 10.1016/j.cis.2011.12.006.

Farber, L., Tardos, G. and Michaels, J. N. (2003). Use of X-ray tomography to study the porosity and morphology of granules. In: *Powder Technology* 132 (1), pp. 57–63. DOI: 10.1016/S0032-5910(03)00043-3.

Farid, M. (2003). A new approach to modeling of single droplet drying. In: *Chemical Engineering Science* 58, pp. 2985–2993. DOI: 10.1016/S0009-2509(03)00161-1.

Gatapova, E. Y., Shonina, A. M., Safonov, A. I., Sulyaeva, V. S. and Kabov, O. A. (2018). Evaporation dynamics of a sessile droplet on glass surfaces with fluoropolymer coatings: Focusing on the final stage of thin droplet evaporation. In: *Soft Matter* 14 (10), pp. 1811–1821. DOI: 10.1039/c7sm02192e.

Gelderblom, H. (2013). *Fluid flow in drying drops*. Enschede, Twente, Netherlands: Dissertation University of Twente. DOI: 10.3990/1.9789036535250.

Girard, F., Antoni, M., Faure, S. and Steinchen, A. (2008). Influence of heating temperature and relative humidity in the evaporation of pinned droplets. In: *Colloids and Surfaces A: Physicochemical and Engineering Aspects* 323 (1-3), pp. 36–49. DOI: 10.1016/j.colsurfa.2007.12.022.

Gleason, K., Voota, H. and Putnam, S. (2016). Steady-state droplet evaporation: Contact angle influence on the evaporation efficiency. In: *International Journal of Heat and Mass Transfer* 101, pp. 418–426. DOI: 10.1016/j.ijheatmasstransfer.2016.04.075.

Glück, B. (1991). Zustands und Stoffwerte - Wasser Dampf Luft - Verbrennungsrechnung. In: *Bausteine der Heizungstechnik: Berechnung, Software*. 2nd ed. Understanding Complex Systems. Berlin: Verlag fuer Bauwesen. DOI: 10.1007/978-3-642-34070-3-26.

Golovko, D. S., Butt, H.-J. and Bonaccurso, E. (2009). Transition in the evaporation kinetics of water microdrops on hydrophilic surfaces. In: *Langmuir* 25 (1), pp. 75–78. DOI: 10.1021/la803474x.

Gorr, H., Zueger, J., McAdams, D. and Barnard, J. (2012). Salt-induced pattern formation in evaporating droplets of lysozyme solutions. In: *Colloids and Surfaces B, Biointerfaces* 103C, pp. 59–66. DOI: 10.1016/j.colsurfb.2012.09.043.

Gray, T. W. and Mann, N. (2012). *The Elements: A Visual Exploration of Every Known Atom in the Universe*. Philadelphia, New York: Running Press. DOI: 10/9781579128951.

Groot, P. de and Deck, L. (1995). Surface profiling by analysis of white-light interferograms in the spatial frequency domain. In: *Journal of Modern Optics* 42 (2), pp. 389–401. DOI: 10.1080/09500349514550341.

Guo, Q. and Cheng, P. (2019). Direct numerical simulations of sessile droplet evaporation on a heated horizontal surface surrounded by moist air. In: *International Journal of Heat and Mass Transfer* 134, pp. 828–841. DOI: 10.1016/j.ijheatmasstransfer.2019.01.049.

Haferl, S., Attinger, D., Zhao, Z. Z., Giannakouros, J. and Poulikakos, D. (2000). Transport phenomena in the impact of a molten droplet on a surface: Macroscopic Phenomenology and microscopic considerations, Part 1: Fluid Dynamics. In: *Annual Review of Heat Transfer* 11, pp. 145–205. DOI: 10.1615/AnnualRevHeatTransfer.v11.40.

Hampel, N., Bück, A., Peglow, M. and Tsotsas, E. (2013). Continuous pellet coating in a Wurster fluidized bed process. In: *Chemical Engineering Science* 86, pp. 87–98. DOI: 10.1016/j.ces.2012.05.034.

Hampel, R. (2010). *Beitrag zur Analyse von kinetischen Einflüssen auf die Wirbelschicht- Sprühagglomeration*. Magdeburg, Germany: Dissertation Otto von Guericke University.

Handscomb, C., Kraft, M. and Bayly, A. E. (2009). A new model for the drying of droplets containing suspended solids. In: *Chemical Engineering Science* 64, pp. 628–637. DOI: 10.1016/J.CES.2008.04.051.

Harris, D. J., Hu, H., Conrad, J. C. and Lewis, J. A. (2007). Patterning colloidal films via evaporative lithography. In: *Physical Review Letters* 98 (14), p. 148301. DOI: 10.1103/PhysRevLett.98.148301.

Hede, P. D., Bach, P. and Jensen, A. D. (2008). Top-spray fluid bed coating: Scale-up in terms of relative droplet size and drying force. In: *Powder Technology* 184 (3), pp. 318–332. DOI: 10.1016/j.powtec.2007.09.009.

Hu, H. and Larson, R. G. (2002). Evaporation of a sessile droplet on a substrate. In: *The Journal of Physical Chemistry B* 106 (6), pp. 1334–1344. DOI: 10.1021/jp0118322.

Hu, H. and Larson, R. G. (2006). Marangoni effect reverses coffee-ring depositions. In: *The Journal of Physical Chemistry B* 110 (14), pp. 7090–7094. DOI: 10.1021/jp0609232.

Huang, L., Kumar, K. and Mujumdar, A. (2004). Computational fluid dynamic simulation of droplet drying in a spray dryer. In: *Proceedings of the 14th International Drying Symposium*, pp. 326–332. DOI: 10/9788590457312.

Jang, G. S., Cho, W. J. and Ha, C. S. (2001). Crystallization behavior of polypropylene with or without sodium benzoate as a nucleating agent. In: *Journal of Polymer Science Part B: Polymer Physics* 39 (10), pp. 1001–1016. DOI: 10.1002/polb.1077.

Janocha, M. and Tsotsas, E. (2021a). In silico investigation of the evaporation flux distribution along sessile droplet surfaces during convective drying. In: *Chemical Engineering Science* 238, p. 116590. DOI: 10.1016/j.ces.2021.116590.

Janocha, M. and Tsotsas, E. (2021b). In-depth investigation of incremental layer build-up from dried deposited droplets. In: *AIChE Journal* 2021, e17445. DOI: 10.1002/aic.17445.

Janocha, M. and Tsotsas, E. (2022). Coating layer formation from deposited droplets: A comparison of nanofluid, microfluid and solution. In: *Powder Technology* 399, p. 117202. DOI: 10.1016/j.powtec.2022.117202.

Javed, S. and Rahman, A.-U. (2014). Aloe Vera gel in food, health products, and cosmetics industry. In: Studies in Natural Products Chemistry. Elsevier, pp. 261–285. DOI: 10.1016/B978-0-444-63294-4.00009-7.

Jiang, Z., Rieck, C., Bück, A. and Tsotsas, E. (2019). Modeling of inter- and intra-particle coating uniformity in a Wurster fluidized bed by a coupled CFD-DEM-Monte Carlo approach. In: *Chemical Engineering Science* 211, p. 115289. DOI: 10.1016/j.ces.2019.115289.

Jing, G. and Ma, J. (2012). Formation of circular crack pattern in deposition self-assembled by drying nanoparticle suspension. In: *The Journal of Physical Chemistry B* 116 (21), pp. 6225–6231. DOI: 10.1021/jp301872r.

Kaplan, C. and Mahadevan, L. (2014). Evaporation-driven ring and film deposition from colloidal droplets. In: *Journal of Fluid Mechanics* 781. DOI: 10.1017/jfm.2015.496.

Kaya, D., Belyi, V. A. and Muthukumar, M. (2010). Pattern formation in drying droplets of polyelectrolyte and salt. In: *The Journal of Chemical Physics* 133 (11), p. 114905. DOI: 10.1063/1.3493687.

Kelly-Zion, P. L., Pursell, C. J., Vaidya, S. and Batra, J. (2011). Evaporation of sessile drops under combined diffusion and natural convection. In: *Colloids and Surfaces A: Physicochemical and Engineering Aspects* 381 (1-3), pp. 31–36. DOI: 10.1016/j.colsurfa.2011.03.020.

Kleinbach, E. and Riede, T. (1995). Coating of solids. In: *Chemical Engineering and Processing: Process Intensification* 34.3, pp. 329–337. DOI: 10.1016/0255-2701(94)04021-4.

Korenchenko, A. E. and Zhukova, A. A. (2022). Sessile droplet evaporation in the atmosphere of different gases under forced convection. In: *Physics of Fluids* 34 (4), p. 042102. DOI: 10.1063/5.0084830.

Kovalchuk, N. M., Trybala, A. and Starov, V. M. (2014). Evaporation of sessile droplets. In: *Current Opinion in Colloid & Interface Science* 19 (4), pp. 336–342. DOI: 10.1016/j.cocis.2014.07.005.

Kunii, D. and Levenspiel, O. (1991). *Fluidization Engineering*. Second Edition. Boston: Butterworth - Heinemann. DOI: 10.1016/B978-0-08-050664-7.50009-3.

Larson, R. G. (2014). Transport and deposition patterns in drying sessile droplets. In: *AIChE Journal* 60 (5), pp. 1538–1571. DOI: 10.1002/aic.14338.

Lebedev, N. N. (1965). *Special Functions and their Applications*. Englewood Cliffs, New Jersey: Prentice-Hall International, Incorporated. DOI: 10.1137/1007133.

Lee, D., Omolade, D., Cohen, R. E. and Rubner, M. F. (2007). pH-Dependent structure and properties of TiO2/SiO2 nanoparticle multilayer thin films. In: *Chemistry of Materials* 19 (6), pp. 1427–1433. DOI: 10.1021/cm070111y.

Lee, D. Y. and Chung, B. J. (2017). Visualization of natural convection heat transfer on a sphere. In: *Heat and Mass Transfer* 53 (12), pp. 3613–3620. DOI: 10.1007/s00231-017-2097-1.

Lee, W. P. and Routh, A. F. (2004). Why do drying films crack? In: *Langmuir* 20 (23), pp. 9885–9888. DOI: 10.1021/la049020v.

Li, J., Freireich, B., Wassgren, C. and Litster, J. (2012). A general compartment-based population balance model for particle coating and layered granulation. In: *AIChE Journal* 58, pp. 1397–1408. DOI: 10.1002/aic.12678.

Lide, D. R. (2004). *CRC Handbook of Chemistry and Physics*. 85th ed. Washington D.C., London, New York: CRC press. DOI: 978-0849304842.

Liu, R., Li, L., Yin, W., Xu, D. and Zang, H. (2017). Near-infrared spectroscopy monitoring and control of the fluidized bed granulation and coating processes: A review. In: *International Journal of Pharmaceutics* 530 (1), pp. 308–315. DOI: 10.1016/j.ijpharm.2017.07.051.

Lubarda, V. A. and Talke, K. A. (2011). Analysis of the equilibrium droplet shape based on an ellipsoidal droplet model. In: *Langmuir: The ACS Journal of Surfaces and Colloids* 27 (17), pp. 10705–10713. DOI: 10.1021/la202077w.

Maenosono, S., Dushkin, C. D., Saita, S. and Yamaguchi, Y. (1999). Growth of a semiconductor nanoparticle ring during the drying of a suspension droplet. In: *Langmuir* 15 (4), pp. 957–965. DOI: 10.1021/la980702q.

Mampallil, D. and Eral, H. B. (2018). A review on suppression and utilization of the coffee-ring effect. In: *Advances in Colloid and Interface Science* 252, pp. 38–54. DOI: 10.1016/j.cis.2017.12.008.

Mampallil, D. (2014). Some physics inside drying droplets. In: *Resonance* 19, pp. 123–134. DOI: 10.1007/s12045-014-0016-z.

Marrero, T. R. and Mason, E. A. (1972). Gaseous diffusion coefficients. In: *Journal of Physical and Chemical Reference Data* 1 (1), pp. 3–118. DOI: 10.1063/1.3253094.

Maurice, U., Mezhericher, M., Levy, A. and Borde, I. (2015). Drying of droplets containing insoluble nanoscale particles: Second drying stage. In: *Drying Technology* 33 (15–16), pp. 1837–1848. DOI: 10.1080/07373937.2015.1039540.

Maxwell, J. C. (1890). In: *The Scientific Papers of James Clerk Maxwell*. Cambridge Library Collection - Physical Sciences. Cambridge: Cambridge University Press. DOI: 10.1017/CBO9780511710377.

Melik, D. H. and Fogler, H. S. (1984). Effect of gravity on Brownian flocculation. In: *Journal of Colloid and Interface Science* 101 (1), pp. 84–97. DOI: 10.1016/0021-9797(84)90010-9.

Mezhericher, M., Levy, A. and Borde, I. (2008). Heat and mass transfer of single droplet/wet particle drying. In: *Chemical Engineering Science* 63, pp. 12–23. DOI: 10.1016/j.ces.2007.08.052.

Mezhericher, M., Levy, A. and Borde, I. (2010). Theoretical models of single droplet drying kinetics: A review. In: *Drying Technology* 28 (2), pp. 278–293. DOI: 10.1080/07373930903530337.

Mikulencak, D. R. and Morris, J. F. (2004). Stationary shear flow around fixed and free bodies at finite Reynolds number. In: *Journal of Fluid Mechanics* 520, pp. 215–242. DOI: 10.1017/S0022112004001648.

Mokhtari, A., Mebrouk, A., Chikh, S. and Tadrist, L. (2021). Impact of internal flow and particle-substrate interaction on deposit patterns during evaporation of a colloidal sessile droplet. In: *Proceedings of the 2021 International Conference On Heat Transfer, Fluid Mechanics and Thermodynamics*, pp. 1–6. DOI: 10.1010/354653021.

Molchanov, S. P., Roldughin, V. I. and Chernova-Kharaeva, I. A. (2015). Three scenarios of evaporation of microliter droplets of dispersions and structure of formed ring-shaped deposits. In: *Colloid Journal* 77, pp. 770–779. DOI: 10.1134/S1061933X15060162.

Monse, K., Koch, M. and Walzel, P. (2006). Migration der kontinuierlichen Phase beim Trocknen von Suspensionstropfen in einer Trocknungskammer. In: *Chemie-Ingenieur-Technik* 78 (5), pp. 78–82. DOI: 10.1002/cite.200500103.

Msambwa, Y., Shackleford, A., Ouali, F. and Fairhurst, D. (2016). Controlling and characterising the deposits from polymer droplets containing microparticles and salt. In: *The European Physical Journal E* 39, pp. 1–8. DOI: 10.1140/epje/i2016-16021-x.

Nguyen, T. A. H., Hampton, M. A. and Nguyen, A. V. (2013). Evaporation of nanoparticle droplets on smooth hydrophobic surfaces: The inner coffee ring deposits. In: *The Journal of Physical Chemistry C* 117 (9), pp. 4707–4716. DOI: 10.1021/jp3126939.

Nguyen, T. A., Biggs, S. R. and Nguyen, A. V. (2017). Manipulating colloidal residue deposit from drying droplets: Air/liquid interface capture competes with coffee-ring effect. In: *Chemical Engineering Science* 167, pp. 78–87. DOI: 10.1016/j.ces.2017.04.001.

Peglow, M., Antonyuk, S., Jacob, M., Palzer, S., Heinrich, S. and Tsotsas, E. (2011). Particle Formulation in Spray Fluidized Beds. In: *Modern Drying Technology*. Ed. by E. Tsotsas and A. S. Mujumdar. John Wiley & Sons, Ltd. Chap. 7, pp. 295–378. DOI: 10.1002/9783527631667.ch7.

Perdana, J., Fox, M. B., Schutyser, M. A. I. and Boom, R. M. (2011). Single-droplet experimentation on spray drying: Evaporation of a sessile droplet. In: *Chemical Engineering & Technology* 34 (7), pp. 1151–1158. DOI: 10.1002/ceat.201100040.

Perfetti, G., Van de Casteele, E., Rieger, B., Wildeboer, W. and Meesters, G. (2010). X-ray micro tomography and image analysis as complementary methods for morphological characterization and coating thickness measurement of coated particles. In: *Advanced Powder Technology* 21, pp. 663–675. DOI: 10.1016/j.apt.2010.08.002.

Picknett, R. and Bexon, R. (1977). The evaporation of sessile or pendant drops in still air. In: *Journal of Colloid and Interface Science* 61 (2), pp. 336–350. DOI: 10.1016/0021-9797(77)90396-4.

Poling, B., Prausnitz, J. M. and O'Connell, J. P. (2000). *The Properties of Gases and Liquids*. 5th ed. New York: McGraw-Hill Education. DOI: 10/97800-71499996.

Popov, Y. O. (2005). Evaporative deposition patterns: Spatial dimensions of the deposit. In: *Physical Review E, Statistical, Nonlinear, and Soft Matter Physics* 71 (3 Pt 2B), p. 036313. DOI: 10.1103/PhysRevE.71.036313.

Prosser, J. H., Brugarolas, T., Lee, S., Nolte, A. J. and Lee, D. (2012). Avoiding cracks in nanoparticle films. In: *Nano Letters* 12 (10), pp. 5287–5291. DOI: 10.1021/nl302555k.

Rieck, C. (2020). *Microscopic and macroscopic modeling of particle formation processes in spray fluidized beds*. Magdeburg, Germany: Dissertation Otto von Guericke University. DOI: 10.25673/35295.

Rieck, C., Bück, A. and Tsotsas, E. (2016). Monte Carlo modeling of fluidized bed coating and layering processes. In: *AIChE Journal* 62 (8), pp. 2670–2680. DOI: 10.1002/aic.15237.

Rieck, C., Bück, A. and Tsotsas, E. (2020). Estimation of the dominant size enlargement mechanism in spray fluidized bed processes. In: *AIChE Journal* 66 (5), e16920. DOI: 10.1002/aic.16920.

Rieck, C., Hoffmann, T., Bück, A., Peglow, M. and Tsotsas, E. (2015). Influence of drying conditions on layer porosity in fluidized bed spray granulation. In: *Powder Technology* 272, pp. 120–131. DOI: 10.1016/j.powtec.2014.11.019.

Rowan, S. M., Newton, M. I. and McHale, G. (1995). Evaporation of microdroplets and the wetting of solid surfaces. In: *The Journal of Physical Chemistry* 99 (35), pp. 13268–13271. DOI: 10.1021/j100035a034.

Ruiz, O. and Black, W. Z. (2002). Evaporation of water droplets placed on a heated horizontal surface. In: *Journal of Heat Transfer* 124 (5), pp. 854–861. DOI: 10.1115/1.1494092.

Sadek, C., Schuck, P., Fallourd, Y., Pradeau, N., Le Floch-Fouéré, C. and Jeantet, R. (2014). Drying of a single droplet to investigate process–structure– function relationships: A review. In: *Dairy Science and Technology* 95, pp. 1–24. DOI: 10.1007/s13594-014-0186-1.

Sadek, C., Tabuteau, H., Schuck, P., Fallourd, Y., Pradeau, N., Le Floch-Fouéré, C. and Jeantet, R. (2013). Shape, shell, and vacuole formation during the drying of a single concentrated whey protein droplet. In: *Langmuir* 29 (50), pp. 15606–15613. DOI: 10.1021/la404108v.

Sanden, S. C. T. (2003). *A fundamental study of spray drying fluid catalytic cracking catalyst*. Eindhoven: Dissertation Eindhoven University of Technology. DOI: 10.6100/IR565285.

Sanyal, A., Basu, S. and Chaudhuri, S. (2015). Agglomeration front dynamics: Drying in sessile nano-particle laden droplets. In: *Chemical Engineering Science* 123, pp. 164–169. DOI: 10.1016/j.ces.2014.11.020.

Schlottke, J. and Weigand, B. (2008). Direct numerical simulation of evaporating droplets. In: *Journal of Computational Physics* 227, pp. 5215–5237. DOI: 10.1016/j.jcp.2008.01.042.

Schmidt, M. (2018). *Process dynamics and structure formation in continuous spray fluidized bed processes*. Magdeburg, Germany: Dissertation Otto von Guericke University.

Schomberg, A. K., Diener, A., Wünsch, I., Finke, J. H. and Kwade, A. (2021). The use of X-ray microtomography to investigate the microstructure of pharmaceutical tablets: Potentials and comparison to common physical methods. In: *International Journal of Pharmaceutics: X* 3, p. 100090. DOI: 10.1016/j.ijpx.2021.100090.

Schönfeld, F., Graf, K.-H., Hardt, S. and Butt, H.-J. (2008). Evaporation dynamics of sessile liquid drops in still air with constant contact radius. In: *International Journal of Heat and Mass Transfer* 51 (13-14), pp. 3696–3699. DOI: 10.1016/j.ijheatmasstransfer.2007.12.027.

Schutyser, M. A., Perdana, J. and Boom, R. M. (2012). Single droplet drying for optimal spray drying of enzymes and probiotics. In: *Trends in Food Science & Technology* 27 (2), pp. 73–82. DOI: 10.1016/j.tifs.2012.05.006.

Semenov, S., Starov, V. M., Velarde, M. G. and Rubio, R. G. (2013). Evaporation of Sessile Droplets of Liquid on Solid Substrates. In: *Without Bounds: A Scientific Canvas of Nonlinearity and Complex Dynamics*. Ed. by R. G. Rubio, Y. S. Ryazantsev, V. M. Starov, G.-X. Huang, A. P. Chetverikov, P. Arena, A. A. Nepomnyashchy, A. Ferrus and E. G. Morozov. Berlin, Heidelberg: Springer, pp. 285–300. DOI: 10.1007/978-3-642-34070-3-26.

Shah, R. K. and London, A. L. (1978). Dimensionless groups and generalized solutions. In: *Laminar Flow Forced Convection in Ducts*. New York, Stanford: Academic Press, pp. 37–60. DOI: 10.1016/B978-0-12-020051-1.50008-5.

Shahidzadeh, N., Schut, M. F. L., Desarnaud, J., Prat, M. and Bonn, D. (2015). Salt stains from evaporating droplets. In: *Scientific Reports* 5, p. 10335. DOI: 10.1038/srep10335.

Shahidzadeh-Bonn, N., Rafai, S., Azouni, A. and Bonn, D. (2006). Evaporating droplets. In: *Journal of Fluid Mechanics* 549, pp. 307–313. DOI: 10.1017/S0022112005008190.

Shen, X., Ho, C.-M. and Wong, T.-S. (2010). Minimal size of coffee ring structure. In: *The Journal of Physical Chemistry B* 114 (16), pp. 5269–5274. DOI: 10.1021/jp912190v.

Sliz, R., Czajkowski, J. and Fabritius, T. (2020). Taming the coffee ring effect: Enhanced thermal control as a method for thin-film nanopatterning. In: *Langmuir* 36 (32), pp. 9562–9570. DOI: 10.1021/acs.langmuir.0c01560.

Sloth, J., Jorgensen, K., Bach, P., Jensen, A. D., Kiil, S. and Dam-Johansen, K. (2009). Spray drying of suspensions for pharma and bio products: Drying kinetics and morphology. In: *Industrial & Engineering Chemistry Research* 48 (7), pp. 3657–3664. DOI: 10.1021/ie800983w.

Sondej, F. (2019). *Morphologische Charakterisierung beschichteter Partikel und feststoffhaltiger Mikrotropfen*. Magdeburg, Germany: Dissertation Otto von Guericke University. DOI: 10.25673/25927.

Sondej, F., Bück, A. and Tsotsas, E. (2016). Comparative analysis of the coating thickness on single particles using X-ray micro-computed tomography and confocal laser-scanning microscopy. In: *Powder Technology* 287, pp. 330–340. DOI: 10.1016/j.powtec.2015.09.039.

Sondej, F., Peglow, M., Bück, A. and Tsotsas, E. (2018). Experimental investigation of the morphology of salt deposits from drying sessile droplets by white-light interferometry. In: *AIChE Journal* 64 (6), pp. 2002–2016. DOI: 10.1002/aic.16085.

Soulié, V., Karpitschka, S., Lequien, F., Prene, P., Zemb, T., Moehwald, H. and Hans, R. (2015). The evaporation behavior of sessile droplets from aqueous saline solutions. In: *Physical Chemistry Chemical Physics* 17. DOI: 10.1039/C5CP02444G.

Strenzke, G., Dürr, R., Bück, A. and Tsotsas, E. (2020). Influence of operating parameters on process behavior and product quality in continuous spray fluidized bed agglomeration. In: *Powder Technology* 375, pp. 210–220. DOI: 10.1016/j.powtec.2020.07.083.

Sun, Y. (2014). *Liquid imbibition in porous media investigated by pore network models and pore-scale experiments*. Magdeburg, Germany: Dissertation Otto von Guericke University. DOI: 10.978-3-86912-111-6.

Takhistov, P. and Chang, H.-C. (2002). Complex stain morphologies. In: *Industrial & Engineering Chemistry Research* 41 (25), pp. 6256–6269. DOI: 10.1021/ie010788+.

Tokudome, Y., Ohshima, H. and Otsuka, M. (2009). Non-invasive and rapid analysis for observation of internal structure of press-coated tablet using X-ray computed tomography. In: *Drug Development and Industrial Pharmacy* 35, pp. 678–682. DOI: 10.1080/03639040802587807.

Tran, T. T. H., Avila-Acevedo, J. G. and Tsotsas, E. (2016). Enhanced methods for experimental investigation of single droplet drying kinetics and application to lactose/water. In: *Drying Technology* 34 (10), pp. 1185–1195. DOI: 10.1080/07373937.2015.1100202.

Tsotsas, E. (2012). Influence of drying kinetics on particle formation: A personal perspective. In: *Drying Technology* 30, pp. 1167–1175. DOI: 10.1080/07373937.2012.685139.

Tsoumpas, Y., Dehaeck, S., Rednikov, A. and Colinet, P. (2015). Effect of Marangoni flows on the shape of thin sessile droplets evaporating into air. In: *Langmuir* 31 (49), pp. 13334–13340. DOI: 10.1021/acs.langmuir.5b02673.

Tsuji, Y., Kawaguchi, T. and Tanaka, T. (1993). Discrete particle simulation of two-dimensional fluidized bed. In: *Powder Technology* 77 (1), pp. 79–87. DOI: 10.1016/0032-5910(93)85010-7.

Uhlemann, H. and Mörl, L. (2000). *Wirbelschicht-Sprühgranulation*. Berlin, Heidelberg: Springer. DOI: 10.978-3540669852.

Wang, Y., Ma, L., Xu, X. and Luo, J. (2016). Expressions for the evaporation of sessile liquid droplets incorporating the evaporative cooling effect. In: *Journal of Colloid and Interface Science* 484, pp. 291–297. DOI: 10.1016/j.jcis.2016.09.011.

Wang, Z., Orejon, D., Takata, Y. and Sefiane, K. (2022). Wetting and evaporation of multicomponent droplets. In: *Physics Reports* 960, pp. 1–37. DOI: 10.1016/j.physrep.2022.02.005.

Ward-Smith, A. J. (1980). *Internal Fluid Flow: The Fluid Dynamics of Flow in Pipes and Ducts*. Oxford: Clarendon Press. DOI: 10.1017/S0022112081213625.

Wenzel, R. N. (1936). Resistance of solid surfaces to wetting by water. In: *Industrial & Engineering Chemistry* 28 (8), pp. 988–994. DOI: 10.1021/ie50320a024.

Widati, A. A., Nuryono, N. and Kartini, I. (2019). Water-repellent glass coated with SiO2 – TiO2 – methyltrimethoxysilane through sol–gel coating. In: *AIMS Materials Science* 6 (1), pp. 10–24. DOI: 10.3934/matersci.2019.1.10.

Willmer, D., Baldwin, K., Kwartnik, C. and Fairhurst, D. (2010). Growth of solid conical structures during multistage drying of sessile poly(ethylene oxide) droplets. In: *Physical Chemistry Chemical Physics* 12, pp. 3998–4004. DOI: 10.1039/b922727j.

Woo, M. W., Daud, W. R. W., Mujumdar, A. S., Talib, M. Z. M., Hua, W. Z. and Tasirin, S. M. (2008). Comparative study of droplet drying models for CFD modelling. In: *Chemical Engineering Research and Design* 86 (9), pp. 1038–1048. DOI: 10.1016/j.cherd.2008.04.003.

Xu, P., Mujumdar, A. S. and Yu, B. (2009). Drying-induced cracks in thin film fabricated from colloidal dispersions. In: *Drying Technology* 27 (5), pp. 636–652. DOI: 10.1080/07373930-902820804.

Xu, T., Lam, M. L. and Chen, T.-H. (2017). Discrete element model for suppression of coffee-ring effect. In: *Scientific Reports* 7, p. 42817. DOI: 10.1038/srep42817.

Yadav, A., Kumar, A. and Tripathi, A. (2016). Sodium benzoate, a food preservative, affects the functional and activation status of splenocytes at non cytotoxic dose. In: *Food and Chemical Toxicology* 88, pp. 40–47. DOI: 10.1016/j.fct.2015.12.016.

Young, T. (1805). An essay on the cohesion of fluids. In: *Philosophical Transactions of the Royal Society* 95 (3), pp. 65–87. DOI: 10.1098/rstl.1805.0005.

Yuan, Y. and Lee, T. R. (2013). *Contact Angle and Wetting Properties*. Ed. by G. Bracco and B. Holst. Berlin, Heidelberg: Springer. DOI: 10.1007/978-3-642-34243-1.

Yunker, P., Still, T., Lohr, M. and Yodh, A. (2011). Suppression of the coffee-ring effect by shape-dependent capillary interactions. In: *Nature* 476, pp. 308–11. DOI: 10.1038/nature10344.

Al-Zaitone, B., Al-Zahrani, A., Al-Shahrani, S. and Lamprecht, A. (2020). Drying of a single droplet of dextrin: Drying kinetics modeling and particle formation. In: *International Journal of Pharmaceutics* 574, p. 118888. DOI: 10.1016/j.ijpharm.2019.118888.

Zang, D., Tarafdar, S., Tarasevich, Y. Y., Dutta Choudhury, M. and Dutta, T. (2019). Evaporation of a droplet: From physics to applications. In: *Physics Reports* 804, pp. 1–56. DOI: 10.1016/j.physrep.2019.01.008.

Zhang, N., Zheng, Z. C. and Eckels, S. (2008). Study of heat-transfer on the surface of a circular cylinder in flow using an immersed-boundary method. In: *International Journal of Heat and Fluid Flow* 29 (6), pp. 1558–1566. DOI: 10.1016/j.ijheatfluidflow.2008.08.009.

Zhang, W., Tu, J., Long, W., Lai, W., Sheng, Y. and Guo, T. (2017). Preparation of SiO2 anti-reflection coatings by sol-gel method. In: *Energy Procedia* 130, pp. 72–76. DOI: 10.1016/j.egypro.2017.09.398.

Zhong, X., Crivoi, A. and Duan, F. (2015). Sessile nanofluid droplet drying. In: *Advances in Colloid and Interface Science* 217, pp. 13–30. DOI: 10.1016/j.cis.2014.12.003.

Publications

Peer-review journal publications

Janocha, M.; Tsotsas, E. (2021): In silico investigation of the evaporation flux distribution along sessile droplet surfaces during convective drying. In: *Chemical Engineering Science* 238, 116590. DOI: 10.1016/j.ces.2021.116590.

Janocha, M.; Tsotsas, E. (2021): In-depth investigation of incremental layer build-up from dried deposited droplets. In: *AIChE Journal* 68(2), e17445. DOI: 10.1002/aic.17445.

Strenzke, G.; **Janocha, M.**; Tsotsas, E. (2022): Morphological descriptors of agglomerates produced in continuously operated spray fluidized beds. In: *Powder Technology* 397, 117111. DOI: 10.1016/j.powtec.2022.117111.

Janocha, M.; Tsotsas, E. (2022): Coating layer formation from deposited droplets: A comparison of nanofluid, microfluid and solution. In: *Powder Technology* 399, 117202. DOI: 10.1016/j.powtec.2022.117202.

Conference proceeding publications

Janocha, M.; Tsotsas, E. (2021): Analysis of drying parameter effects on porosity evolution during successive layer build-up from dried deposited droplets. In: *Proceedings of the 13th International Conference on Fluidized Bed Technology (CFB13)*. Vancouver, Canada, May 10–14, 2021. ISBN: 978-1-77136-850-6.

Janocha, M.; Tsotsas, E. (2022): Direct numerical simulation of sessile droplet drying under varying convective conditions. In: *Proceedings of the 22nd International Drying Symposium (IDS22)*. Worcester, USA, June 26–29, 2022.

Oral and poster presentations

Janocha, M.; Tsotsas, E.: Direkte numerische Simulation der Trocknung liegender Wassertropfen unter variierenden konvektiven Bedingungen. Poster auf dem *Jahrestreffen der ProcessNet-Fachgruppen Mischvorgänge, Trocknungstechnik und Wärme- und Stoffübertragung*. Essen, Deutschland, 18.−20. März, 2019.

Janocha, M.; Tsotsas, E.: Structure analysis of sodium benzoate layers from dried deposited droplets. Poster presentation on *9th International Granulation Workshop*. Lausanne, Switzerland, June 26−28, 2019.

Janocha, M.; Tsotsas, E.: Untersuchung der Trocknungsgeschwindigkeitsverteilung auf der Oberfläche ruhender Tropfen unter konvektiven Bedingungen. Vortrag auf dem *Jahrestreffen der ProcessNet-Fachgruppen Hochdruckverfahrenstechnik, Trocknungstechnik und Phytoextrakte*. Frankfurt, Deutschland, 15.−16. März, 2021.

Janocha, M.; Tsotsas, E.: Analysis of drying parameter effects on porosity evolution during successive layer build-up from dried deposited droplets. Oral presentation on *13th International Conference on Fluidized Bed Technology (CFB13)*. Vancouver, Canada, May 10−14, 2021.

Supervised student theses

The following theses were co-supervised by the author of this thesis:

Jothimani, J. *Simulative investigation of sessile droplet drying times under varying convective conditions*. Master thesis. Otto von Guericke University Magdeburg, November 2019.

Heydari, E. *Experimental investigation of convective sessile droplet drying processes and analysis of the resulting residue structures*. Master thesis. Otto von Guericke University Magdeburg, December 2020.